



N° d'ordre: 42523

Université Lille 1
Laboratoire d'Optique Atmosphérique

Thèse de Doctorat

Présentée par
Lucia-Timea DEACONU

Pour obtenir le grade de Docteur de l'Université Lille 1

Spécialité:
Optique, Lasers, Physico-Chimie, Atmosphère

ÉTUDE DES SITUATIONS MULTI-COUCHES "AÉROSOLS" ET DES INTERACTIONS «AÉROSOLS - NUAGES »

Soutenance prévue le 19 décembre 2017 devant le jury composé de:

FLAMANT Cyrille	Directeur de recherche CNRS, LATMOS, Univ. Pierre et Marie Curie, Paris	RAPPORTEUR
ZUIDEMA Paquita	Professeur, Rosenstiel School of Marine and Atmospheric Science, Miami, USA	RAPPORTEUR
TANRÉ Didier	Directeur de Recherche CNRS, LOA, Univ. Lille 1	EXAMINATEUR
MALLET Marc	Chercheur CNRM, Météo France, Toulouse	EXAMINATEUR
BELLOUIN Nicolas	Chercheur, Univ. of Reading, Reading, UK	EXAMINATEUR
GOLOUB Philippe	Professeur, LOA, Univ. Lille 1	DIRECTEUR
WAQUET Fabien	Maître de Conférences, LOA, Univ. Lille 1	CODIRECTEUR
FERLAY Nicolas	Maître de Conférences, LOA, Univ. Lille 1	CODIRECTEUR
JOSSET Damien	Chercheur U.S. Naval Research Laboratory, NASA Stennis Space Center, USA	MEMBRE INVITÉ



N° d'ordre: 42523

Université Lille 1
Laboratoire d'Optique Atmosphérique

THESIS

Presented by
Lucia-Timea DEACONU

To obtain the grade of PhD of Lille 1 University

Specialty:
Optics and Lasers, Physics and chemistry of the Atmosphere

STUDY ON MULTI-LAYER “AEROSOL” SITUATIONS AND OF « AEROSOL – CLOUD » INTERACTIONS

Defense expected for 19 December 2017 in front of the jury composed of:

FLAMANT Cyrille	Research Director CNRS, LATMOS, Univ. Pierre et Marie Curie, Paris	REVIWER
ZUIDEMA Paquita	Professor, Rosenstiel School of Marine and Atmospheric Science, Miami, USA	REVIWER
TANRÉ Didier	Research Director CNRS, LOA, Univ. Lille 1	EXAMINATOR
MALLET Marc	Researcher CNRM, Météo France, Toulouse	EXAMINATOR
BELLOUIN Nicolas	Researcher, Univ. of Reading, Reading, UK	EXAMINATOR
GOLOUB Philippe	Professor, LOA, Univ. Lille 1	DIRECTOR
WAQUET Fabien	Lecturer, LOA, Univ. Lille 1	CO-DIRECTOR
FERLAY Nicolas	Lecturer, LOA, Univ. Lille 1	CO-DIRECTOR
JOSSET Damien	Researcher, U.S. Naval Research Laboratory, NASA Stennis Space Center, USA	INVITED MEMBER

Résumé

Les aérosols ont un impact sur le bilan radiatif et les nuages de la Terre. Leurs effets sur le climat et les nuages sont associés à de fortes incertitudes, notamment dans le cas d'aérosols situés au-dessus ou à l'intérieur des nuages (IPCC, 2013). Il est indispensable d'améliorer la compréhension de ces situations pour une meilleure caractérisation des aérosols et de leurs effets dans les modèles climatiques.

L'un des principaux objectifs de cette étude est d'analyser la cohérence entre les restitutions d'aérosols au-dessus des nuages (AAC) réalisées à partir des mesures spatiales passive et active. Nous avons considéré la méthode basée sur les mesures polarisées de POLDER, la méthode développée pour le lidar spatial CALIOP et la méthode basée sur le rapport de dépolarisation CALIOP (DRM), pour laquelle nous proposons également une version re-calibrée. Nous effectuons une analyse régionale et une analyse pluriannuelle globale pour fournir des résultats de statistiques robustes. Nos résultats montrent un bon accord entre les restitutions DRM et POLDER AOT ($R^2 = 0,68$ à l'échelle mondiale), avec une différence moyenne de 0,07 sur l'épaisseur optique en aérosol à 532 nm (AOT). Ce résultat nous donne confiance dans notre capacité à mesurer les propriétés de l'AAC. La méthode opérationnelle de CALIOP sous-estime largement l'AOT, par rapport aux deux autres méthodes, sous-estimant ainsi l'impact radiatif des AACs au niveau global. Des différences plus importantes entre les méthodes DRM et POLDER se produisent lorsque les couches d'aérosols et de nuages sont en contact. Deux hypothèses ont été considérées: (i) les aérosols présents dans les nuages peuvent affecter la luminance polarisée réfléchi par les nuages, et par conséquent les restitutions de l'instrument POLDER, (ii) les aérosols, riches en suie, présents dans les gouttelettes des nuages pourraient modifier leur capacité de rétrodiffusion, affectant la méthode lidar (DRM).

Le deuxième objectif de cette étude porte sur l'impact des aérosols sur les propriétés des nuages et leur forçage radiatif, sur l'océan Atlantique Sud, une région présentant de fortes charges en aérosols carbonés ainsi que des nuages stratiformes. Nous avons considérée une approche combinant les restitutions CALIOP (profils verticaux) et POLDER (propriétés des aérosols et des nuages), avec des paramètres météorologiques co-localisés. Notre étude est centrée sur une zone d'échantillonnage localisée au large de l'Angola et s'étendant sur la période juin-août 2008. Nous réalisons des calculs de transfert radiatif dans les domaines visible et infrarouge thermique dans cette région à différents niveaux dans l'atmosphère. Nous analysons l'effet de la charge en aérosol sur les propriétés des nuages en fonction de la météorologie, et pour des cas de grandes et de faibles quantités en AAC absorbants. Nous avons montré que les aérosols réchauffent la couche où ils se trouvent (environ 6 K/jour) et affectent la stabilité atmosphérique. Ces couches d'aérosols sont constamment accompagnées d'une quantité importante de vapeur d'eau. Cette vapeur d'eau diminue l'effet de refroidissement se produisant au sommet des nuages dans l'infrarouge thermique. Ces deux effets cumulés pourraient avoir un impact sur la convection des nuages. Ces processus pourraient diminuer l'entraînement d'air sec au sommet du nuage, préservant ainsi l'humidité

dans la couche nuageuse et limitant son développement vertical. Nos résultats montrent que sous de fortes charges de AAC, les nuages deviennent optiquement plus épais, avec une augmentation du contenu en eau liquide (intégré entre la base et le sommet du nuage) de 20 g.m⁻². Les altitudes du sommet des nuages sont également plus basses en présence d'aérosols, en moyenne d'environ 200 m. Ces résultats indiquent un effet potentiel semi-direct des aérosols au-dessus des nuages.

Une validation de nos résultats est possible en utilisant les mesures de la campagne aéroportée AEROCLO-sA (récemment réalisée en Namibie, septembre 2017), et en utilisant un modèle afin de mieux contraindre les effets météorologiques et les séparer des effets des aérosols sur les nuages.

Mots-clés: atmosphère, aérosol au-dessus des nuages, télédétection, POLDER, CALIOP, forçage radiative, effet semi-direct

Abstract

Aerosols impact the Earth's radiative budget and clouds. Their effects on climate and clouds are associated with high uncertainties, especially in case of aerosols situated above or within the clouds (IPCC, 2013). It is prerequisite to improve the understanding of these situations for a better characterization of aerosols and their effects in climate models.

One of the main objectives of this study is to analyze the consistency between the aerosol above clouds (AAC) retrievals from passive and active satellite measurements. We consider the method based on the passive polarization measurements provided by the POLDER instrument, the operational method developed for the space borne lidar CALIOP, and the CALIOP-based depolarization ratio method (DRM), for which we also propose a calibrated version. We perform a regional analysis and a global multi-annual analysis to provide robust statistics results. Our findings show good agreement between DRM and POLDER AOT retrievals ($R^2 = 0.68$ at global scale), with a main difference of 0.07 in AOT at 532 nm. This result gives confidence in our ability to measure the properties of AAC. CALIOP operational method is largely underestimating the above cloud AOT, compared to the other two methods. Larger differences between DRM and POLDER occur when the aerosol and cloud layers are in contact. Two hypotheses were considered: (i) aerosols within the clouds can affect the polarization measurements, and consequently the POLDER AOT retrievals; (ii) aerosols in internal mixture with cloud droplets modify their backscatter ability, affecting the lidar method (DRM).

The second objective is to study the impact of aerosols on the cloud properties and their radiative forcing, over the South Atlantic Ocean. We perform a synergy between CALIOP vertical profiles and POLDER retrievals of AAC and cloud properties, with collocated meteorological parameters. Our study is focused on a sample area located off the coast of Angola, for the June-August 2008 period, for which we performed radiative transfer calculations in the visible and thermal infrared domains. We analyzed the effect of aerosol loading on the cloud properties and meteorology, in case of large and low amounts of absorbing AACs. We found that aerosols warm the layer where they reside (by around 6 K/day) and have an effect on the atmospheric stability. They come together with larger amounts of water vapor, which has an effect on the longwave cooling of the cloud top. These two cumulated effects could impact the cloud convection, preserving the humidity of the cloud layer and inhibiting its vertical development. Our results show that under large loads of AACs, clouds become optically thicker, with an increase in liquid water path of 20 g.m^{-2} and their cloud top altitudes are lower by 200 m. These results may indicate a potential semi-direct effect of aerosols above clouds. A validation of our results is possible using the AEROCLO-sA airborne campaign measurements, recently performed in Namibia (September 2017), and a model to better constrain the meteorological effects and separate them from the aerosol effects on clouds.

Keywords: atmosphere, aerosol above clouds, remote sensing, POLDER, CALIOP, radiative forcing, semi-direct effect

Table of Contents

CHAPTER 1	GENERAL INTRODUCTION	1
1.1	Generalities on atmospheric aerosols	1
1.2	The impact of aerosols	8
1.2.1	Effects on environment, health and visibility	8
1.2.2	Impact on climate	9
1.2.2.1	Direct effect	12
1.2.2.2	Semi-direct effect	12
1.2.2.3	Indirect effect	14
1.3	Aerosol and cloud properties	14
1.3.1	Aerosol optical properties	14
1.3.1.1	Scattering, absorption and extinction processes	14
1.3.2	Clouds properties	20
1.3.2.1	Macroscopic form of clouds	20
1.3.2.1	Microphysical and optical properties of cloud droplets	20
1.4	Methods used for the study of aerosols and clouds	22
1.4.1	Different methodologies and measurements	22
1.4.2	The constellation of satellites A-Train	24
1.4.3	Satellite retrievals of aerosol above cloud properties	25
1.5	Aerosols above clouds	28
1.6	Thesis objectives	30
CHAPTER 2	METHODOLOGY AND COMPUTATION TOOLS	31
2.1	Passive observations	31
2.1.1	Theoretical concepts	31
2.1.2	Radiative transfer equation	37
2.1.2.1	Successive Order of Scattering	37
2.1.2.2	GAME radiative transfer code	38
2.1.2.3	3DMCPOL and 3DCLOUD	39
2.1.3	POLDER / PARASOL instrument	40
2.1.4	POLDER methodology for aerosols above clouds retrieval	41
2.1.4.1	POLDER polarization method	41
2.1.4.2	POLDER absorption method	44
2.2	Active observations	46
2.2.1	Lidar equation	46

2.2.2	CALIOP / CALIPSO instrument	48
2.2.2.1	CALIOP Operational method	48
2.2.2.2	CALIOP Depolarization Ratio Method	49
2.2.2.3	The re-calibrated version of DRM: the SODA algorithm	51
2.3	ECMWF reanalysis for climate monitoring	54
CHAPTER 3 COMPARISON OF ACTIVE AND PASSIVE AEROSOL ABOVE CLOUDS MEASUREMENTS		55
3.1	Research strategy	55
3.1.1	Collocation	56
3.1.2	Distinction between vertical profiles	57
3.2	Regional analysis and case studies	58
3.2.1	African biomass-burning aerosols	60
3.2.2	Saharan desert dust aerosols	64
3.2.3	East Asian mixture of aerosols	67
3.3	Global analysis on different types of scenes	69
3.3.1	Detached, attached, undetermined	69
3.3.2	Evolution of the above cloud AOT retrievals with cloud properties	72
3.3.2.1	AOT versus r_{eff}	73
3.3.2.2	AOT versus COT	76
3.4	Discussion	78
3.5	Conclusions	85
CHAPTER 4 STUDY OF THE IMPACT OF AEROSOLS ABOVE CLOUDS OVER THE SOUTH ATLANTIC OCEAN		87
4.1	Aerosol effect in cloudy scenes over South Atlantic Ocean: a quick review	88
4.2	Description of aerosols, clouds and meteorology at the large regional scale	90
4.2.1	Aerosol optical and microphysical properties	91
4.2.2	Cloud optical and microphysical properties	94
4.2.3	Evolution of cloud and aerosol altitudes with longitude	96
4.2.4	Air circulation patterns and meteorology	98
4.3	Aerosol effect at a local scale	99
4.3.1	Strategy of observation and selection of a small area	100
4.3.2	Covariance between humidity and aerosol loadings	102
4.3.3	Strategy for an insight: the thread of thought	103
4.3.4	Calculation of radiative forcing of aerosols above clouds	104
4.3.4.1	Biomass-burning study case	104
4.3.4.2	Radiative effect over the sampled area	110
4.4	High and low aerosol loading approach	113
4.4.1	Meteorological parameters in the absence and presence of aerosols	114

4.4.2	Co-variation between cloud parameters, aerosol loads and meteorological parameters	118
4.5	Typical radiative transfer simulations of polluted and quasi-pristine scenarios	122
4.5.1	Diurnal variation of radiative forcing and heating rates	122
4.5.2	Temporal variation of the heating rate profiles for HIGH and LOW simulations	124
4.5.3	Distinction between aerosol versus water vapor radiative effects	129
CHAPTER 5	CONCLUSIONS AND PERSPECTIVES	135
ANNEX A		139
ANNEX B		143
BIBLIOGRAPHY		167

Chapter 1

General introduction

1.1 Generalities on atmospheric aerosols

Aerosols are all the solid and liquid particles, suspended in the atmosphere, having diameters in the range of 0.001 to 10 microns, with the exception of the hydrometeors (cloud droplets or ice crystals that form the clouds). These particles are originated from various sources and are generated by different mechanical or chemical processes. They can be transported over long distances at various altitudes. The aerosols are always present in the atmosphere, but their concentration strongly varies in time and space. For example, extreme phenomena such as sand storms, volcanic eruptions or forest fires can inject millions of tones of particles in the atmosphere in a short period of time. Depending on their sources, and on the atmospheric processes that affect them, these particles show different properties. When these particles are sufficiently abundant in the atmosphere, we notice their presence, as they scatter and absorb sunlight, limiting the visibility. Aerosols interact with the Earth's radiative budget and climate both directly (i.e. by scattering, absorbing and emitting electromagnetic radiations) and indirectly by serving as condensation or ice nuclei in the cloud formation. These particles also have several other important environmental impacts; they may, for instance, affect the human health, the atmospheric chemistry and air quality as well as the hydrological cycle. In this section, we describe the sources and the microphysical and optical properties of these particles and the processes that influence them, as well as their main impacts.

Aerosol types and sources

The anthropogenic aerosols are the particles that are generated by human activities (the industry, agricultural activities, domestic heating, cooking and transportation). Aerosols can also result from natural phenomena. The majority of aerosols resulting from natural

sources are mineral dust particles and sea salt, both being the product of mechanical erosion of surfaces due to wind. The other main natural aerosols include volcanic ash, biogenic aerosols (pollen, bacteria) and the biomass burning aerosols emitted from wildfires. Figure 1.1 presents some examples of aerosol emission sources into the atmosphere.

Another distinction can be also made in function of how the particles are formed. The particles that are generated and injected directly through the atmosphere, such as mineral dust, are called primary aerosols. The secondary aerosols designate particles resulting from the condensation of gas-phase species. These gas species are called aerosol precursors, and can also originate from both natural and anthropogenic sources (e.g. the sulfur dioxide, which can be injected through the atmosphere by industrial activities or by volcanoes). Table 1.1 summarizes the amount of aerosols and aerosol precursors emitted by different sources in one year. We observe that the sea spray (sea salt) is the main source of natural aerosols in the atmosphere, with 1000 to 6000 Tg/year (i.e. 1 million tons per year), along with the desert dust and the biogenic aerosols. For the anthropogenic aerosols, the industrial dust and the biomass burning aerosols mainly contribute to the total amount of aerosols, with amounts that reach 130 and 90 Tg/year, respectively.



a) Smog in Lianyungang, China, on December 8, 2013.



b) Sand Storm in Khartoum, Sudan



c) Volcanic eruption in Karo Regency, Indonesia, on February 9, 2015.



d) Smoke from vegetation fires

Figure 1.1 – Example of different emission sources resulted in high aerosol concentration: (a) smog, (b) dust storm, (c) volcanic eruption and (d) biomass fire.

Table 1.1 – Approximate emission flux of main primary aerosols and of aerosol precursors. Tg = 10¹² g, C = carbon, S = sulfur, N = nitrogen (Source: Boucher, 2015).

Aerosol type	Emission flux (Tg/year)
Natural primary aerosols	
Desert dust	1000 - 3000
Sea spray	1000 - 6000
Biomass burning aerosols	20 - 35
Biogenic aerosols	≈ 1000
- including bacteria	0.040 – 1.800
- including spores	30
Precursors of natural secondary aerosols	
Dimethylsulphide (DMS)	20 – 40 S
Volcanic SO ₂	6 – 20 S
Terpenes	40 - 400
Anthropogenic primary aerosols	
Industrial dust	40 – 130
Biomass-burning aerosols	50 – 90
Black carbon (from fossil fuel)	6 – 10
Organic carbon (from fossil fuel)	20 – 30
Anthropogenic secondary aerosols	
SO ₂	70 – 90 S
Volatile organic compounds (VOCs)	100 – 560 C
NH ₃	20 – 50 N
NO _x	30 – 40 N

Size of aerosols

Typically, the mass-based particles size distribution of aerosols is bimodal: the fine mode (or accumulation mode) and the coarse mode. The accumulation mode typically corresponds to particles with radius ranging between 0.05 and 1 µm, whereas the coarse mode corresponds to particles associated with radius larger than 1 µm. Natural aerosols typically exhibit size larger than 1 micron, and mainly contribute to the coarse mode. The mineral dust and volcanic ashes are the largest coarse particles. It should be noted that submicronic particle size (i.e. particles smaller than one micron in size) also exists in nature, such as the particles emitted by wildfires in boreal forests. Most of the anthropogenic particles belong to the fine mode and are generally associated with submicron particles size, with the exception of the dust particles generated by agricultural and industrial activities.

We can also distinguish two other modes to classify the aerosol size in function of their radius (r): the nucleation mode ($r \leq 0.01 \mu\text{m}$) and the Aitken mode ($0.01 \mu\text{m} \leq r \leq 0.05$

μm). The Aitken and nucleation modes allow describing the so-called “ultra fine” particles, which are encountered, for instance, during the formation of secondary aerosols. The first step of the gas-to-particle conversion is the nucleation process that can be homogeneous or heterogeneous, during which the gas phase changes into a condensed phase. In the first case the nucleation is made between the molecules available in the environment, while a heterogeneous nucleation requires the presence of an external solid or ionic support. Then, the particles reach the dimensions of an Aitken particle. After further coagulation (adhesion between the particles) with other particles, these aerosols can grow up to few tenths of microns and reach the size of the accumulation mode particles. In Figure 1.2, we present a schematic view of the multi-modal particle size distribution that shows the different growth processes and give some examples of aerosols that belong to the different modes.

The aerosols classified in the nucleation mode are subject to various processes (coagulation or impaction onto surfaces) and have a very short lifetime (order of minutes to hours). The Aitken mode aerosols act as condensation nuclei for water vapor (CCN) and other gaseous species. Their lifetime is also short due to their rapid coagulation. It should be noted that certain combustion processes could also inject ultra fine particles directly into the atmosphere (e.g. burning of wood, oil or gasoline). In the atmosphere, even if the particles that belong to the nucleation and the Aitken modes are the most numerous, the majority of particle mass consists of fine and coarse aerosols with sizes between 0.05 to 10 μm . Due to their size, the fine and coarse mode particles are also the ones that are the most relevant for climate studies since they efficiently interact with the solar and thermal electromagnetic radiations.

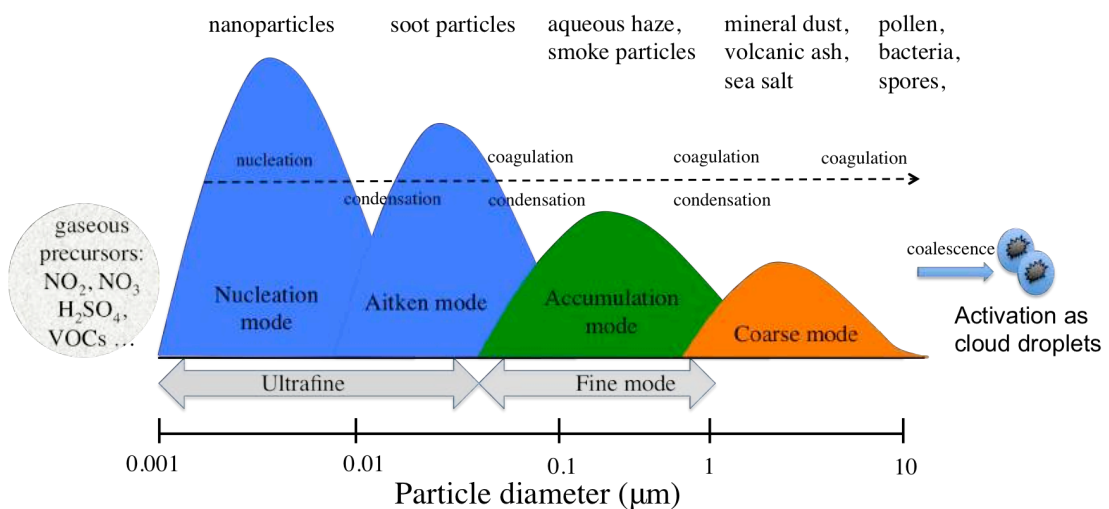


Figure 1.2 – Schematic multi-modal particle size distribution with typical transformations and examples of particle types within each mode.

The knowledge of the particles size is critical to describe their interactions with radiation. There are multiple mathematical models that allow the granulometric representation of a group of particles (Gamma number size distribution, Junge power-law distribution), but for the size distribution of aerosols, the lognormal distribution is commonly used. A multimodal lognormal size distribution for k modes can be written as a sum of each lognormal mode distribution:

$$n(r) = \sum_{i=1}^k \frac{N}{\sigma_i \sqrt{2\pi}} \exp \left[-\frac{\ln^2 r / r_{g,i}}{2\sigma_i^2} \right] \quad (\text{Eq. 1.1})$$

where $n(r)dr$ represents the number of particles per μm^{-3} for which r is between r and $r+dr$, N is the total number of particle, $r_{g,i}$ and σ_i are the mean granulometric radius (μm) and the standard deviation for each mode i .

Considering the large range of particles size, their size distribution is generally given in logarithm scale. In this case we define $n'(r)$ as the number of particles with radius between $\ln r$ and $\ln r + d \ln r$. Depending on the applications, it is sometimes necessary to convert the number distribution $n(\ln r)$ into surface $s(\ln r)$ or volume $v(\ln r)$ distributions:

$$s(\ln r) = \frac{dS}{d \ln r} = \pi r^2 n(\ln r) \quad \text{and} \quad v(\ln r) = \frac{dV}{d \ln r} = \frac{4\pi}{3} r^3 n(\ln r) \quad (\text{Eq. 1.2})$$

Figure 1.3 shows $n(\ln r)$, $s(\ln r)$ and $v(\ln r)$ computed for a population of freshly emitted particles and for the same particles after aging processes. In case of aged particles, the number distribution shifts to the right, as the size of the particles becomes larger. The surface and volume size distributions are also shifted towards larger particle sizes and their maximum increases.

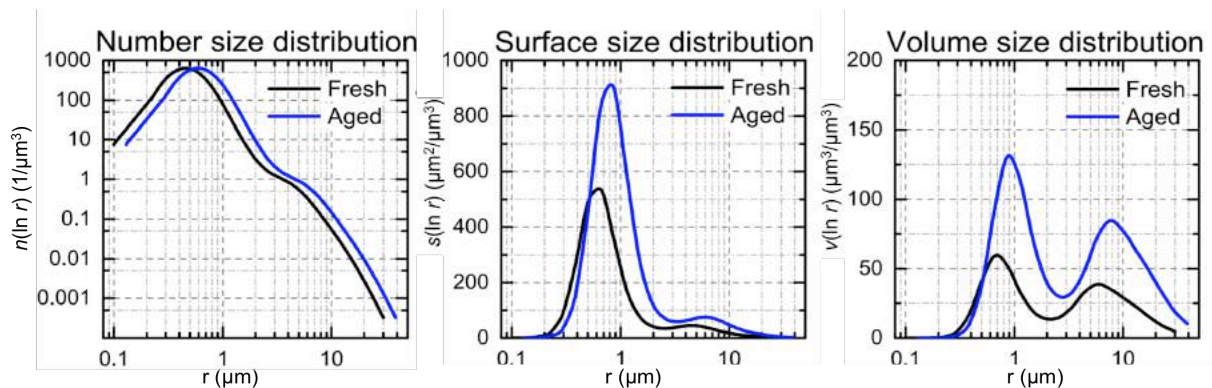


Figure 1.3 – Left to right: number, surface and volume size distribution for a population of freshly emitted particles with radius between 0.1 and 30 μm (black line). When the same particles suffer atmospheric aging processes (blue line), we observe a right shift in the distributions, as the size of the particles is increased towards larger particles (Source: Unga, 2017).

Composition of aerosols

The atmospheric aerosols have a very complex and variable chemical composition. Each particle has individual composition. Fine particles may contain different amounts of sulfate, nitrate, ammonium, carbonaceous components (soot or organic carbon) and certain trace metals (e.g. lead, cadmium, copper). Oxides (e.g. hematite, Fe_2O_3) and carbonates (e.g. calcium carbonate, CaCO_3) are the main components of mineral dust particles. Other coarse aerosols may contain, among other things, nitrate, sodium, chloride and biogenic organic components. From a chemical point of view, we differentiate water-soluble aerosol particles from the insoluble ones. Most water-soluble aerosol components are hygroscopic and they can absorb water. The absorption of water modifies the chemical composition of the particle and also potentially its size and shape (i.e. hygroscopic growth). Highly soluble particles are made, for instance, of ammonium, sulfate compounds or sulfate chloride. These soluble particles are generally likely to be considered as efficient cloud condensation nuclei (CCN). Most of the mineral dust, volcanic ash and anthropogenic soot particles are classified as insoluble particles. Recent studies however underlined that some of these insoluble particles could still act as good CCN. Mineral dust particles, for instance, could become hygroscopic and also act as CCN due to moisture adsorption onto their surfaces (Sullivan et al., 2009; Tang et al., 2016).

Shape of aerosols

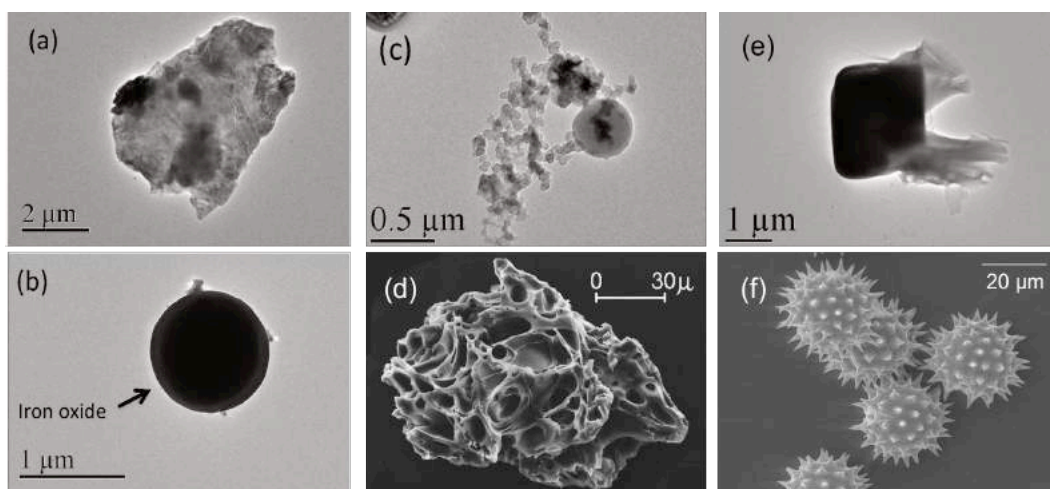


Figure 1.4 – Different types of aerosol particles found in the atmosphere obtained from a SEM instrument: (a) urban desert dust, (b) metallic aerosol (iron oxide), (c) soot, (d) volcanic ash, (e) sea salt and (f) grains of pollen (Source: UMBC, LASIR and Unga, 2017).

The morphology of the aerosols is not easy to describe, as there is a large variability of shapes observed for the particles that depends on the mechanisms that generated them. Scanning electron microscopy (SEM) analyses revealed that although spherical shaped

aerosols are found in nature (such as the secondary aerosols or the ones originating from anthropogenic activities), a large number of aerosol types fall into different categories (see Figure 1.4): cubic (salts), lattice (dust) or even fractal shapes given by agglomerates of spheres (soot). The shape of aerosols strongly impacts the way they scatter light and also their optical properties. We will see latter in this chapter how the shape of the particles impact their scattering and optical properties.

Deposition and transport of aerosols

Aerosols are subjected to different processes of deposition (dry or wet deposition) and removal processes. The *dry deposition* depends on the size of the particles. The largest particles usually have a short life in the atmosphere, as they are subject to gravitational sedimentation, but they can also be exposed to re-entrainment during windy days. On the contrary, the fine particles can be suspended for a long time and their deposition is mainly due to Brownian diffusion. They may accumulate in the atmosphere until eventually removed by precipitations. Precipitating clouds largely contribute in the removal process of aerosols from the atmosphere. The *wet deposition* is mostly due to precipitation (the raindrops more than the snowflakes) that captures the particles and drops them down to the surface. This process is also known as *below-cloud scavenging* whereas *in-cloud scavenging* corresponds to scenario when the aerosols penetrate the water droplets before precipitation or act as CCN through the droplets formation.

As the aerosols are mainly produced and emitted at the surface, the largest concentrations of aerosols are generally found in the lowest part of the troposphere and in the Boundary Layer (BL), that is the layer of the atmosphere located nearby the surface. Aerosols can be also transported horizontally over long distances or injected vertically at various altitudes. Due to the physical processes that influence the emission and the injection of mineral dust and biomass-burning aerosols in the atmosphere, a large amount of these particles reach the free troposphere, above the BL, and can be also transported above low-level clouds. The vertical distribution of aerosols strongly influences their lifetime. The higher the injection height is, the less efficient are the deposition processes. If they are transported above the clouds, the *wet deposition* is also insubstantial. This favors the long-distance transit and their impacts on climate. The particle transported at high altitudes reside longer time in the atmosphere than in the boundary layer where the sedimentation and scavenging processes are more efficient at removing aerosols. If the aerosols reach the stratosphere, such as in case of major volcanic eruption (e.g. the Pinatubo eruption in 1992), their lifetime in the atmosphere can be of several months. Sometimes, they can stay in the stratosphere for years due to its stability.

Figure 1.5 presents the emission and transport of different aerosols on a global scale on 7 September 2006, determined using the Goddard Global Ozone Chemistry Aerosol Radiation and Transport (GOCART) model. This model result illustrates how spread and variable is the spatial distribution of aerosols and the large distances that these particles can

cross. Savanna fires in South Africa emit large amount of carbonaceous aerosols that passes over the Atlantic Ocean; mineral dust emitted from the Saharan desert and the Middle East are transported westwards forming a dust belt across the Atlantic Ocean; European, Asian and North American anthropogenic emissions are responsible for aerosol layers that are transported eastwards and polewards. Consequently, the impact of these particles on the climate and weather is not localized. These particles can interact with weather systems, scatter or absorb solar and terrestrial radiation and modify the cloud microphysical properties on a global scale.

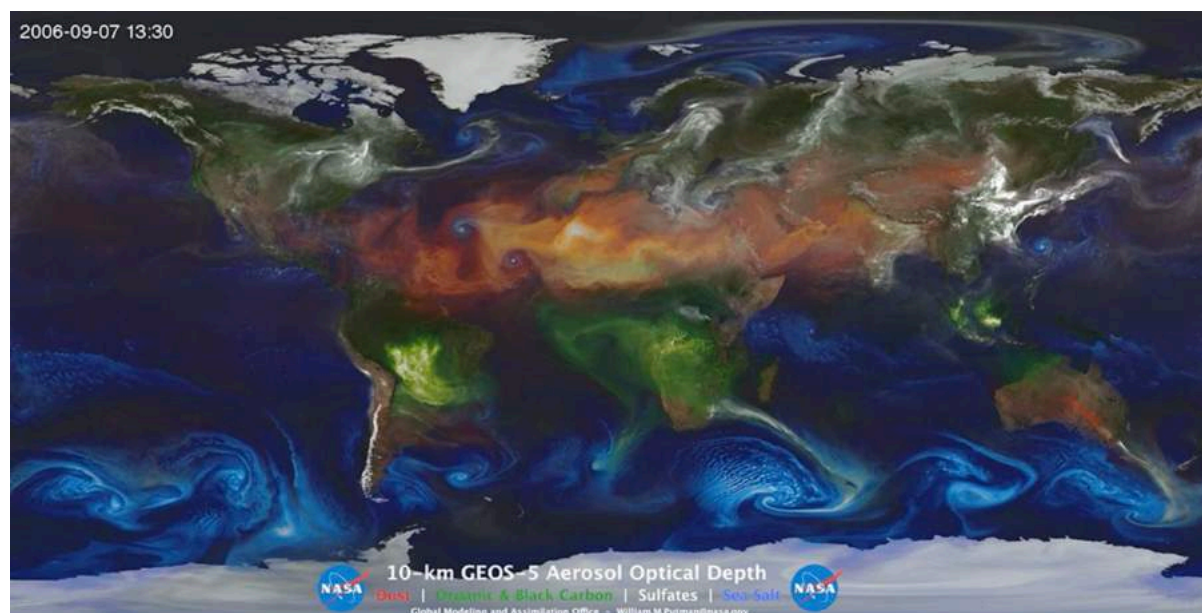


Figure 1.5 – Emission and transport of tropospheric aerosols on 7 September 2006: dust (red-orange), black and organic carbon (green), sulfates (white) and sea salt (blue) realized with the GOCART model (Source: W. Putman, NASA/Goddard; <https://gmao.gsfc.nasa.gov/>).

1.2 The impact of aerosols

1.2.1 Effects on environment, health and visibility

Aerosols have impacts on atmospheric pollution, health, environment and visibility. Aerosol precursors (SO_2 , NO_x) originated from natural (volcanic eruptions, biomass decomposition) and anthropogenic sources (domestic heating, transport, industry etc.) may cause acid rains. Driven by wet deposition, the rain brings acids (such as sulfuric: H_2SO_4 and nitric: HNO_3) at the ground level. Their effects on the environment are multiple and harmful (e.g. water acidification of lakes and soils with consequences on the fauna and aquatic flora). Aerosols may also have positive effects on the environment. Some of the aerosols can increase the productivity of an ecosystem by increasing the amount of nutrients. For instance,

mineral dust particles are rich in iron and phosphorus. After being deposited, these particles may become nutrient for the plankton.

Air quality monitoring networks define an air quality index using measurements of the main atmospheric pollutants such as nitrogen dioxide (NO₂), sulfur dioxide (SO₂), ozone from photochemical production processes (O₃) and also aerosols (mainly dust from natural and anthropogenic origins). The finest particles have the most adverse effects on the human health. Through them, toxic substances (such as sulfate, heavy metals and hydrocarbon), present at the surface of the aerosols, can be introduced into the respiratory tract. The health impacts of aerosols consist in both short-term acute symptoms (such as asthma or bronchitis) and long-term chronic irritation and inflammation of the respiratory tract, which can potentially lead to cancer. Aerosols might also have impacts on cardiovascular and reproductive systems. Some aerosols can also serve as vector to viruses and bacteria and promote epidemics (Chiapello, 2011).

By scattering and absorbing solar radiations, aerosols modify the distribution and intensity of the solar radiation available in the lowest parts of the atmosphere. The intensity of solar radiation directly drives the photochemistry of molecular gases, such as ozone and nitrogen dioxide. Aerosols may, therefore, indirectly impact the concentration of pollutant gases in the atmosphere. Due to their scattering and absorbing properties, aerosols also have an effect on the visibility. Hazes due to aerosols may occur during urban pollution events and strongly reduce the visibility in cities.

1.2.2 Impact on climate

Direct thermometer measurements performed from all around the globe indicate that the Earth's atmosphere is warming since 150 years. Temperatures have gone through natural cycles in the past, from cold periods (ice ages) to warm periods (interglacial ages). However, the analysis of ice-cores, tree-rings and other paleontological studies revealed that the warm temperatures that are presently measured have no precedent since the Holocene period (11.600 years ago), with the exception of the so-called medieval warm period.

Over the last hundred years, the Earth's average temperature has increased with approximately 0.75 °C (Figure 1.6). The current warming of the Earth is confirmed by an increasing number of indicators. For instance, at global scale, we observe a decrease in the ice land since 20 years, notably in Antarctica and Greenland where the mass loss in ice was six times larger in 1992 than in 2011. The elevation of the sea level (elevation of 19 cm between 1900 and 2010) is mainly to the thermal expansion of the ocean that progressively warms. This warming already amplified extreme events such as intense precipitation over the North continent and in Europe as well as tropical cyclones over the North Atlantic and drought in West Africa (IPCC, 2013).

Since the beginning of the industrial era (1750), the anthropic emissions have raised the concentrations of CO₂ and other green house gases (GHG) like CH₄ and N₂O. The current warming is, for most part, due to this additional GHG released through the atmosphere. The GHG, and also the water vapor, act as a screen that prevents the thermal infrared radiation to entirely escape back into space, causing the warming of the lower parts of the atmosphere and, as a consequence, the warming of the Earth's surface. As the greenhouse gases, the aerosols (natural or anthropogenic) can also have an impact on the Earth's radiative budget. However, the overall effect of aerosol is to cool the climate.

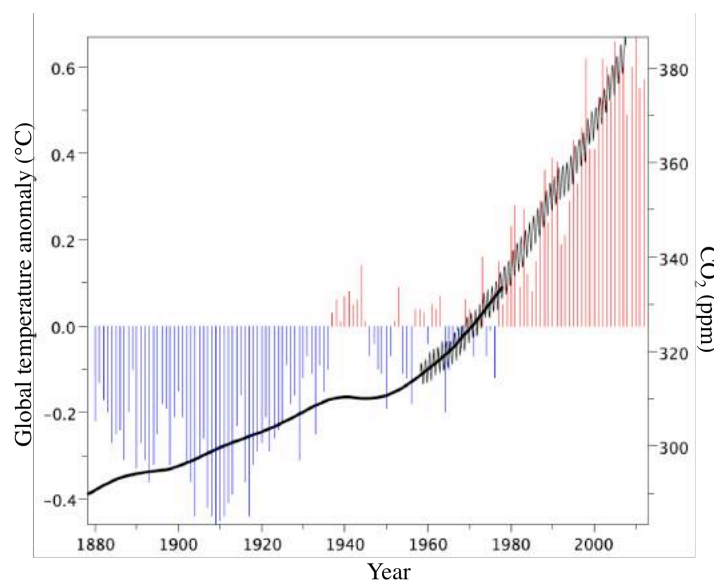


Figure 1.6 – Evolution of the global annual temperature measured over land and ocean (colored bars) and of the CO₂ concentration (black line) from 1880. The temperature anomaly is expressed in function of the reference temperature averaged between 1950 and 1980. The Global Historical Climatological Network (GHCN) provides the temperature data. The CO₂ concentrations from 1880 to 1975 result from polar ice core measurements, and observations at Mauna Loa (Hawaiï) by the Earth System Research Laboratory provide information on the CO₂ concentrations between 1958 and 2007 (Source: NOAA).

The Intergovernmental Panel on Climate Change (IPCC), an organization that aims to assess scientific information related to human-induced climate change and its potential impacts, quantifies the radiative effects of GHG and aerosols in terms of *radiative forcing* (RF). The radiative forcing is computed for a given perturbing agent and with respect to a reference state. It is expressed in $\text{W}\cdot\text{m}^{-2}$ and defined as the difference between the net radiative fluxes computed for the reference system and the ones computed for the same system including the perturbing agent. The RF calculation considers that all the atmospheric and surface properties are identical between the reference system and the system including the perturbing agent. The *effective radiative forcing* (ERF) is, however, a better indicator of

eventual responses of the atmospheric temperature, especially for aerosols, since it accounts for the adjustments of the atmospheric temperature, water vapor and clouds, but with surface temperature (or a portion of surface conditions) unchanged.

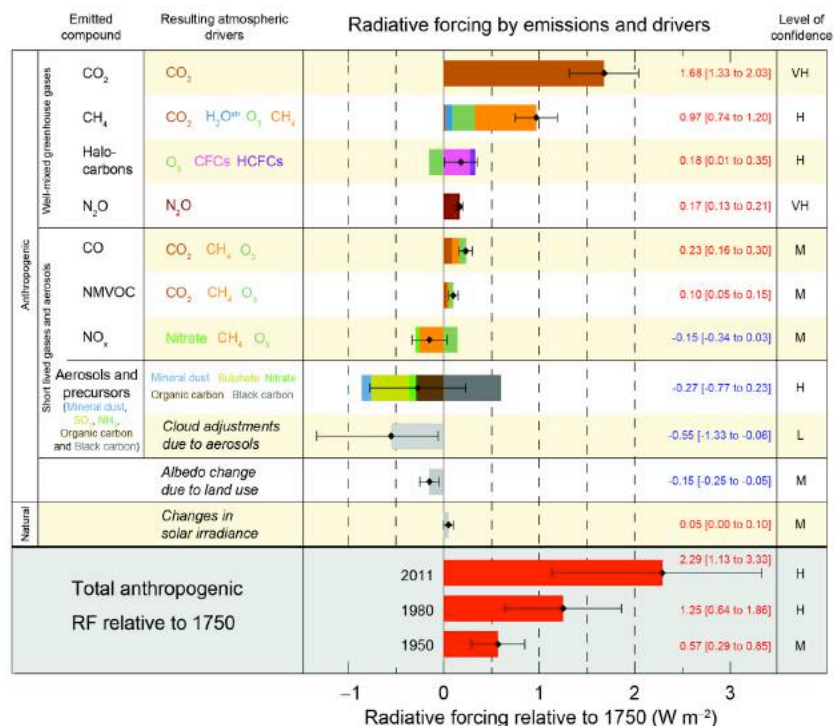


Figure 1.7 – Estimation of the effective anthropogenic radiative forcing in 2011 relative to 1750 and the associated uncertainties related to the main factors that drive climate change. The numerical values of the net radiative forcing are provided on the right of the figure. The confidence level varies from very high – VH to high – H, medium – M and low – L. (Source: IPCC, 2013).

Figure 1.7 presents the effective radiative forcing for various climate agents and the associated uncertainties from the IPCC 2013 report (Fifth Assessment Report – AR5). ERF was estimated using in-situ and remote sensing observations, aerosol and greenhouse gases properties, and numerical models calculations for representing the observed processes. The beginning of the industrial area, in 1750, was used as reference period for the ERF calculation, since the influence of the human activities on the atmospheric composition was then limited. The figure shows that the total anthropogenic ERF for 2011, relative to 1750, which includes all the type of anthropogenic agents, ranges between 1.13 to 3.33 W.m⁻². The ERF calculated for well-mixed GHG ranges between 2.22 and 3.78 W.m⁻² and is mainly responsible for the current global warming. Globally, the overall aerosol effect is associated to cooling (negative ERF values). The ERF of the total aerosol effect is -0.9 (-1.9 to -0.1) W.m⁻² and then is expected to partially compensate the warming effect of GHG. The aerosol

ERF due to aerosol-radiation interactions ranges between -0.77 to 0.23 W.m^{-2} whereas the aerosol ERF due to aerosol-cloud interactions ranges between -1.33 to -0.06 W.m^{-2} . The aerosols and their interaction with clouds continue to contribute the largest uncertainty to the estimation of the total radiative forcing. Despite the efforts, the scientific community encounters difficulties in assessing the aerosol effects on clouds and climate. Despite significant improvements in the modeling of the aerosol-radiation interactions in models, large disparities still remain on the estimate of the direct effect of aerosol on climate (Myhre et al., 2013b). These uncertainties are mainly explained by the fact the aerosol and cloud properties and their interactions processes are still not well represented in global climate models.

In the next section, we describe in more details the effects of aerosols on climate. Aerosols can exercise direct, semi-direct and indirect effects on the Earth's radiation budget (IPCC, 2013). It is worth mentioning that since the last Assessment Report of IPCC from 2013, these terminologies have changed into *aerosol-radiation interactions* (that includes the direct and the semi-direct effects) and *aerosol-cloud interactions* (which includes the indirect effects). However, throughout this thesis we will refer to these effects using the old nomenclature, as we will attempt to ultimately disentangle these effects.

1.2.2.1 Direct effect

By scattering a part of the solar radiation back to space, aerosols increase the albedo of the Earth, which reduces the amount of solar radiation reaching the surface, causing its cooling. This effect is called *direct radiative effect* (DRE) of aerosols or the *parasol* effect. At the top of the atmosphere, the sign and the amplitude of the DRE depends on the aerosol properties and on the reflective properties of the underlying surface (Lenoble et al., 1982; Peers et al., 2015). For instance, the presence of absorbing aerosols, such as biomass burning aerosols, above bright surfaces (such as snow, ice) causes a darkening of the scene, which leads to a positive DRE (i.e a warming effect). Also, when absorbing aerosols are located above clouds, the aerosol DRE can be positive or negative, depending on the cloud albedo and the aerosol type (e.g. biomass burning aerosols or dust) and its level of absorption (Keil and Haywood, 2003; Peers et al., 2015). The estimate of the DRE then requires an accurate knowledge of the properties of the aerosol layer as well as the radiative properties of the underlying surface or target.

1.2.2.2 Semi-direct effect

By absorbing sunlight, absorbing aerosols also warm the layer of the atmosphere where they reside. This may modify the profiles of temperature and humidity, and then potentially impact the formation and development of clouds. Hansen et al. have introduced the term *semi-direct effect* in 1997 to describe the evaporation of cloud droplets caused by the absorbing aerosols situated in the vicinity of the cloud (i.e. a cloud burning effect). Absorbing aerosols considered here are mainly the mineral dust particles and the biomass burning

aerosols that includes absorbing components such as soot (black carbon) or organic carbon (brown carbon). This effect is in fact even more complex and may, stabilize, promote or suppress the cloud formation. The semi-direct effect can be also seen as an adjustment of the climatic system to the direct effect according to Boucher et al. (2013). In 2010, Koch and Del Genio have synthesized the different types of possible semi-effect of aerosols on clouds (Figure 1.8).

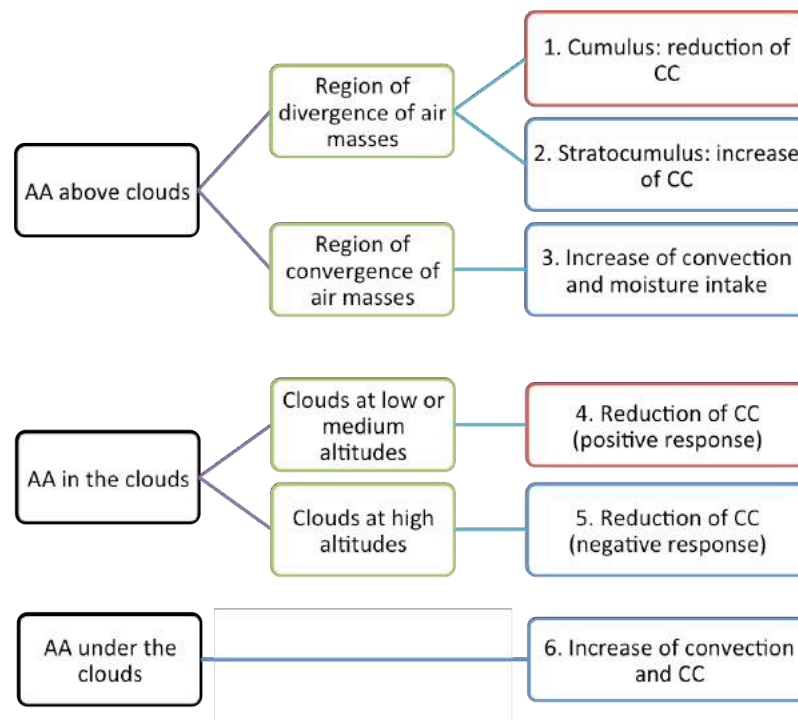


Figure 1.8 – Semi-direct radiative effect in function of the position of the aerosol layer relative to the cloud. The blue boxes correspond to effects associated to cooling and the red boxes correspond to warming effects. AA: Absorbing Aerosols. CC: Cloud Cover (Source: Koch and Del Genio, 2010).

In function of the position of the absorbing aerosol layer with respect with the cloud layer, and also in function of the cloud type, the aerosol semi-direct can lead to positive or negative RF:

- Absorbing aerosols within the clouds: in general, the warming of the atmospheric layer due to aerosol absorption tends to reduce relative humidity and the liquid water content (a so-called “cloud burning effect”), reducing the cloud cover in case of cumulus (Ackerman et al., 2000) and stratocumulus clouds (Hill et al., 2008).
- Absorbing aerosols below clouds: different studies suggest that a warming of the atmospheric layer located below the cloud tend to reinforce convection and water condensation. Therefore, it favors the development of cumuliform clouds (Feingold et al., 2005) (cumulus over land and pyrocumulus) and stratiform clouds (Johnson et al., 2004a) (marine stratocumulus mainly).

- Absorbing aerosols above clouds: in case of stratocumulus clouds, the warming of the layers located above the clouds would tend to increase the gradient of temperature above the inversion and stabilize the boundary layer. This stabilization would induce a diminution of the flux of dry air entrainment at the top of the cloud. The effects would be the preservation of the humidity of the cloud layer and the increase of its liquid water content, favoring the preservation of the cloud cover or its development (Brioude et al., 2009; Johnson et al., 2004a). In case of cumulus clouds, another study suggests that the presence of above cloud aerosols would inhibit the cloud formation when the cloud optical thickness is small and, conversely, would reinforce the convection when the cumulus optical thickness is important (Koren et al., 2004)

1.2.2.3 Indirect effect

The aerosols indirectly impact the Earth's radiative budget by modifying the cloud properties by acting as condensation and ice nuclei (CCN and IN). An increase in the number of aerosols (serving as cloud condensation nuclei) leads to a larger number of smaller cloud droplets (i.e. assuming that the amount of available water remains constant). Smaller cloud droplets lead to clouds that reflect more visible radiation back to space, inducing a cooling. This process is considered as the *first indirect effect*, also called the cloud albedo effect or Twomey effect (Twomey, 1974). Additionally, the reduction of cloud droplet size has other potential impacts on precipitation and cloud properties (Rosenfeld, 2000). Smaller cloud droplets might inhibit rainfall and increase cloud lifetime. These processes correspond to the so-called *second indirect effect* (Albrecht, 1989).

The understanding of the aerosol-radiation and aerosol-cloud interactions requires to accurately knowing the aerosol and cloud properties. The next section is dedicated to the description of the optical and microphysical parameters that need to be estimated in order to understand the impacts of aerosols on climate, as well as the methods used to retrieve or measure these parameters.

1.3 Aerosol and cloud properties

1.3.1 Aerosol optical properties

1.3.1.1 Scattering, absorption and extinction processes

When a radiation interacts with a particle, a part of the incident energy is absorbed whereas the other part is spatially redistributed in a non-isotropic way. These two processes correspond to the absorption and scattering processes, respectively. The extinction of radiation by a particle corresponds to the sum of these two processes. To characterize these

properties, one generally uses the extinction, the absorption and the scattering efficient factors:

$$\left\{ \begin{array}{l} Q_{\text{diff}} = \frac{S_{\text{diff}}}{S_g} \\ Q_{\text{abs}} = \frac{S_{\text{abs}}}{S_g} \\ Q_{\text{ext}} = \frac{S_{\text{ext}}}{S_g} \end{array} \right\} \quad (\text{Eq. 1.3})$$

where S_g is the geometrical section of the particle (m^2) and S_{diff} , S_{abs} and S_{ext} are the effective cross-sections of the particle (m^2), which represent the effective area of the particle that interacts with the radiation, respectively for the processes of scattering, absorption and extinction.

The following relation links the extinction coefficient to the scattering and absorption coefficients:

$$Q_{\text{ext}} = Q_{\text{abs}} + Q_{\text{diff}} \quad (\text{Eq. 1.4})$$

We also introduce the single scattering albedo, which characterizes the efficiency of the particle scattering with respect to its absorption. A non-absorbing particle has a value of $\omega_0 = 1$.

$$\omega_0 = \frac{Q_{\text{diff}}}{Q_{\text{ext}}} \quad (\text{Eq. 1.5})$$

The Mie theory

The scattering by a particle, for which the size is comparable to the wavelength of the incident radiation, is described by the Mie theory. The scattering process then depends on the Mie parameter, which quantifies the ratio between the size of the particle (with r the radius of the particle) and the wavelength of the incident radiation:

$$x = \frac{2\pi r}{\lambda} \quad (\text{Eq. 1.6})$$

The value of x yields to a classification of three domains of scattering: the Rayleigh scattering for $x \ll 1$ (Rayleigh, 1871), the Mie scattering for $x \approx 1$ (Mie, 1908) and the geometrical optics laws for the largest particles, when $x \gg 1$ (van de Hulst, 1957). The Rayleigh scattering theory applies for gas molecules. The scattered intensity is inversely proportional to λ^4 , and so the Rayleigh scattering is more efficient at shorter wavelengths. The Mie theory allows computing the scattering, absorbing and extinction effective cross sections of aerosols (van de Hulst, 1957).

The refractive index

The scattering by a particle depend on the Mie parameter but also on the refractive index of the particle, defined as:

$$n = m - ik \quad (\text{Eq. 1.7})$$

where m and k are the real and imaginary parts of the complex refractive index of the particle. The real part of the refractive index is linked to the speed of propagation of light in a given medium whereas the imaginary part of the refractive index corresponds to the particle absorption. The complex refractive index of a particle depends mainly on its chemical composition and is spectrally dependent. For aerosols, the real refractive index m varies between 1.35 and 1.60 for the visible part of the spectrum. Different values can be observed in case of dry biomass burning aerosols ($m > 1.60$) or in case of hydrated particles (marine aerosols $m < 1.37$). The biomass-burning aerosols typically show the highest values of imaginary refractive index, with k values varying between 0.005 and 0.06, depending on their concentration in soot. Mineral dust particles mainly absorb in the blue and in the UV spectral region (k is of about 0.005) due to iron.

Extinction coefficient

Let us now consider the propagation of radiation inside a homogenous medium and select a layer of a thickness dz perpendicular to a radiation beam of intensity I ($\text{W}\cdot\text{m}^{-2}$). Inside the matter, the radiant energy generally suffers some losses due to extinction processes and after the path dz , the radiance has been changed to $I + dI$, with:

$$dI = -I\sigma_{\text{ext}}(z)dz \quad (\text{Eq. 1.8})$$

where σ_{ext} is the extinction coefficient (km^{-1}).

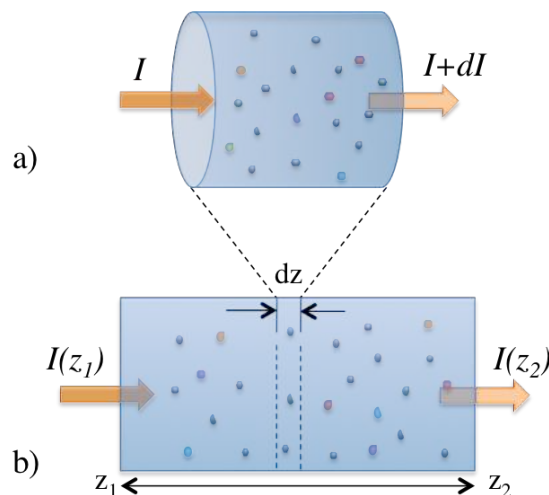


Figure 1.9 – Definition of extinction. (a) Intensity that passes through a thin layer suffers extinction proportional to the path length dz . (b) Intensity crossing a finite path length suffers exponential extinction.

For a particle population with a size distribution $n(r)$, the extinction coefficient is defined as:

$$\sigma_{\text{ext}} = \int_0^{\infty} \pi r^2 Q_{\text{ext}}(m, r, \lambda) n(r) dr \quad (\text{Eq. 1.9})$$

where Q_{ext} is the extinction efficiency. The same formula stands for the absorption coefficient σ_a and for the scattering coefficient σ_s , by replacing Q_{ext} in Eq. 1.9 by Q_{abs} and Q_{ext} , respectively.

After a finite path between z_1 and z_2 , integration of the above Eq. 1.8 gives:

$$I(z_2) = I(z_1) e^{-\tau_e} \quad (\text{Eq. 1.10})$$

with

$$\tau_e = \int_{z_1}^{z_2} \sigma_{\text{ext}}(z) dz \quad (\text{Eq. 1.11})$$

where τ_e is the extinction optical thickness of the layer between z_1 and z_2 and $e^{-\tau_e}$ is the transmittance of the layer. Equation 1.10 is known as the Beer's exponential extinction law.

Aerosol optical thickness

For the atmosphere, the aerosol optical thickness is calculated by integrating the σ_{ext} from the ground to the top of the atmosphere. The total column aerosol optical depth can be written as follows:

$$\tau_e = \int_0^z dz \left(\int_0^{\infty} \pi r^2 Q_{\text{ext}} \left(\frac{2\pi r}{\lambda}, m \right) n(r, z) dr \right) \quad (\text{Eq. 1.12})$$

where the particles size distribution $n(r, z)$ can be dependent on the altitude.

Single scattering albedo

The fractional contribution of the scattering to the total extinction is called single scattering albedo (SSA or ω_0). It describes the efficiency of particles to scatter or absorb light, and mainly depends on the imaginary part of the complex refractive index of the particle and also on the particles size distribution.

$$\omega_0 = \frac{\sigma_s}{\sigma_{\text{ext}}} = \frac{\sigma_s}{\sigma_a + \sigma_s} \quad (\text{Eq. 1.13})$$

Ångström exponent

In order to express the spectral dependency of the optical thickness τ_e , we define the Ångström exponent α . The values of the Ångström exponent increase when the particle size decreases. Therefore, for coarse aerosols, α is basically 0 (as there is no spectral dependence), while for a molecule the α is equal to 4.

$$\frac{\tau_{e,\lambda_1}}{\tau_{e,\lambda_2}} = \left(\frac{\lambda_1}{\lambda_2}\right)^{-\alpha} \Rightarrow \alpha = -\frac{\ln \frac{\tau_{e,\lambda_1}}{\tau_{e,\lambda_2}}}{\ln \frac{\lambda_1}{\lambda_2}} \quad (\text{Eq. 1.14})$$

Effective parameters

In radiative applications, we also consider the effective radius and the associated effective variance of the aerosols. These two quantities are defined in the following equations:

$$r_{\text{eff}} = \frac{\int_0^\infty r^3 n(r) dr}{\int_0^\infty r^2 n(r) dr} \quad \text{and} \quad v_{\text{eff}} = \frac{\int_0^\infty (r - r_{\text{eff}})^2 r^2 n(r) dr}{r_{\text{eff}}^2 \int_0^\infty r^2 n(r) dr} \quad (\text{Eq. 1.15})$$

Phase function

The phase function quantifies the angular distribution of light intensity after being scattered by a particle. It only depends on the scattering angle if the particles are spherical or randomly orientated. In that case the phase function is normalized such that the integral over 4π steradians is unity:

$$\int_0^{2\pi} \left\{ \int_0^\pi p(\Theta) \sin(\Theta) d\Theta \right\} d\phi = 1 \quad (\text{Eq. 1.16})$$

The phase function depends on the size and shape of the particle and on the wavelength. The phase function represents the probability for the incident radiation to be scattered in a solid angle $d\Omega$, following the scattering angle Θ , defined between the incident and scattering directions. The radiation scattered by a particle, in case of a natural incident radiation, is polarized with a polarized ratio equal to $P(\Theta) = q(\Theta)/p(\Theta)$, with $q(\Theta)$ the polarized phase function (i.e. the P12 element of the phase matrix).

The scattering in forward direction is encountered mostly at large particles (i.e. the peak of diffraction) and is more isotropic for smaller sizes, as observed in Figure 1.10. Although nearly spherical particles exist in nature, the majority of aerosols have complex morphologies that cause the Mie calculation to be inaccurate. In case of non-spherical particles, there are alternative computational methods, such as the T-matrix method, that allow to compute the optical properties of non-spherical particles, such as spheroids (Babenko et al., 2003; Dubovik et al., 2006; Mishchenko et al., 2002). Non-spherical particles typically

show a rather flat angular behavior in comparison with spherical particles (see Figure 1.10a) for scattering angles large than 80° and never exhibit bows such as spherical hydrated marine aerosols (Herman et al., 2005) or cloud droplets.

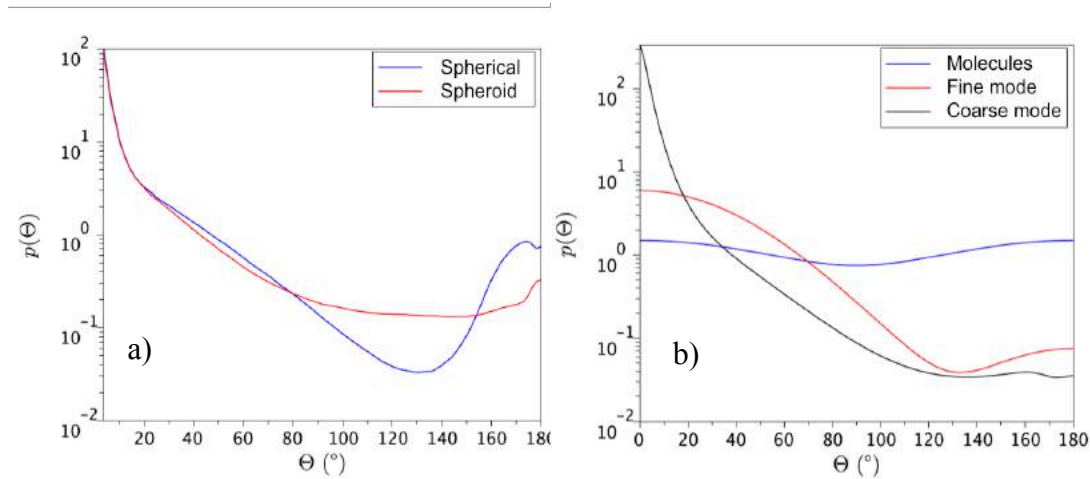


Figure 1.10 – Phase function $p(\Theta)$ for (a) spherical and spheroid particles (Dubovik et al., 2006) and (b) different size types of particles: molecules, fine mode particles and coarse mode particles (Source: Mortier, 2014).

Asymmetry parameter

The asymmetry parameter g depends on the shape of the phase function. Depending on the extent of the backward ($\Theta > 90^\circ$) or forward ($\Theta < 90^\circ$) scattering, the asymmetry parameter varies between -1 to 1.

$$g = 2\pi \int_{-1}^1 p(\cos\Theta) \cos\Theta d(\cos\Theta) \quad (\text{Eq. 1.17})$$

The parameter g is equal to 1 for a radiation that is entirely scattered in the forward direction. If g is negative, the radiation is scattered preponderantly backward. In case of molecules, the asymmetry factor is zero, since the scattering phase function is isotropic.

Backscatter coefficient

When the incident radiation is backscattered we can use the phase function at 180° to define the backscatter coefficient ($\text{km}^{-1} \cdot \text{sr}^{-1}$) as following:

$$\beta = \sigma_s \frac{p(180^\circ)}{4\pi} \quad (\text{Eq. 1.18})$$

This parameter is mainly used in active remote sensing techniques, as for instance Lidar (Light Detection and Ranging) systems.

1.3.2 Clouds properties

Clouds have a fundamental role in climate. Low-level clouds strongly reflect shortwave radiation back to space, which contribute to cooling the Earth's surface. High-level clouds, in the opposite, tend to reduce the longwave radiation emitted by the Earth-surface system back to space, trapping the heat (the thermal radiation) at the surface and in the low levels of atmosphere. Clouds are also very effective agents in cleaning the atmosphere of anthropogenic emissions and other gases and aerosols.

1.3.2.1 Macroscopic form of clouds

Luke Howard firstly made the classification of clouds in 1803. Since then, the World Meteorological Organization (WMO) has extended the list and has reassigned the clouds into ten main groups. These are divided into three clusters in function of the altitude of their base: low cloud (up to about 2 km above the surface), middle clouds (between 2 and 7 km) and high clouds (above 7 km). The cloud nomenclature is based on three terminologies:

- *stratus* (with a stratiform appearance, mainly horizontally developed)
- *cumulus* (extend farther vertically and tend to be convective clouds)
- *cirrus* (formed at very high altitudes, have a fibrous like appearance and are made of ice crystals)

Apart from these terms, the word *nimbus* is also used to describe precipitating clouds as well as *alto* for high altitude clouds.

The repartition of the different clouds in function of altitude is presented in Figure 1.11. The low clouds group include the Stratocumulus, Stratus, Cumulus and Cumulonimbus clouds, as their base is usually below 2 km. Mid level clouds are the Altocumulus, Altostratus and Nimbostratus clouds whereas the Cirrus, Cirrocumulus and Cirrostratus types are the high-level clouds. The Nimbostratus is another type of cloud that can be found at different altitude levels.

1.3.2.1 Microphysical and optical properties of cloud droplets

Cloud formation requires moisture (water vapor), aerosols that act as CCN, and a process of cooling. For instance, a parcel of warm air located above the ground may rise, cool and condensate, depending on the available water vapor and CCN, and also on the thermodynamic conditions of temperature and pressure. Due to the latent heating energy released by the condensation process, clouds may develop and become more convective. The droplets then may grow, for instance by colliding other droplets and coalescing with them, until they reach their precipitable size.

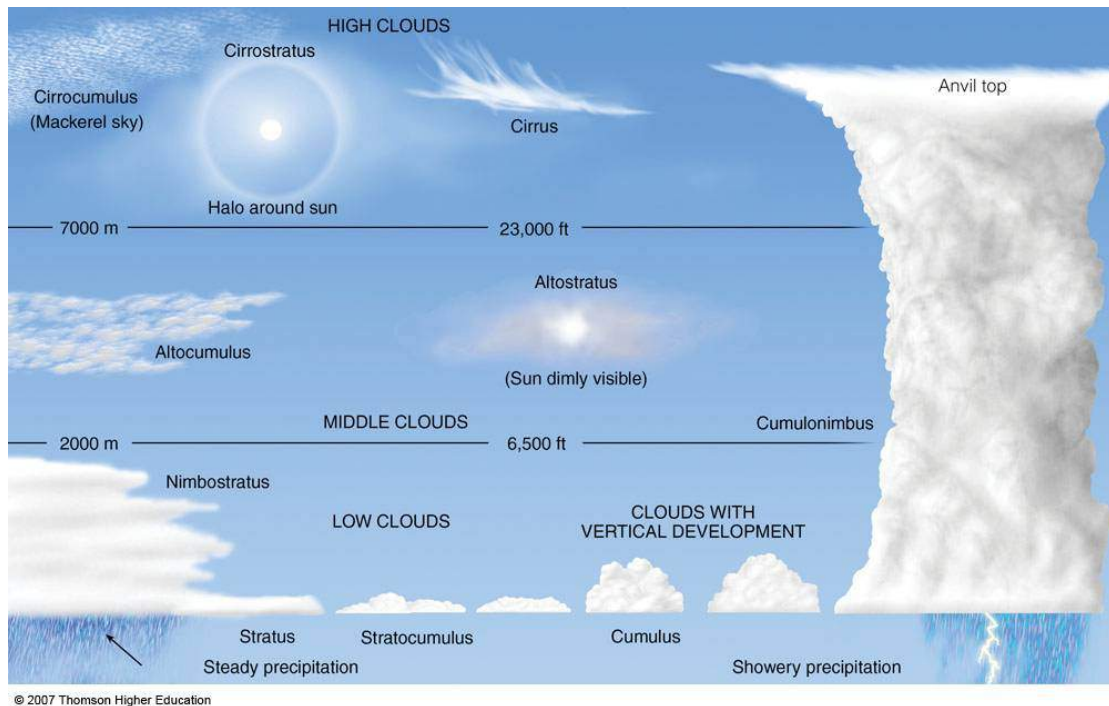


Figure 1.11 – Repartition of different types of clouds in function of altitude (Source: Ahrens, 2011).

We can distinguish also three categories of clouds in function of the type of cloudy particles:

- *Warm clouds*, or liquid water clouds, are found mainly at low altitudes where the temperature is higher. It should be noted that the distinction between “warm” and “cold” clouds is made in function of the cloud phase and not in function of the temperature (Lamb and Verlinde, 2011), since water droplets may exist at temperature lower than 0°C.
- *Cold clouds* are made solely of ice crystals, such as Cirrus clouds. The microstructure of ice crystals is very complex: from dendrites to columns (long, pencil-like forms) or plates (thin, flat hexagons), which requires specific microphysical models (Labonnote et al., 2000).
- *Mix-phase clouds* that incorporate liquid droplets and ice crystals as for instance clouds with strong vertical development, such as Cumulonimbus, that may exhibit liquid water droplets at its basis and ice crystal at its top. The middle part is often in mixed phase.

Important microphysical parameters used in describing the warm clouds are:

- the *cloud droplet concentration* in a unit volume of air (number.m^{-3}): $n = N/V$, where N is the total number of water droplets in the volume of the cloud V .

- the *liquid water content* (LWC) in a unit volume of air (g.m^{-3}) calculated as $LWC = (m_w \times n) N$, where m_w is the mass of air in the air parcel.
- the *liquid water path* (g.m^{-2}) is a measure of the total amount of liquid water between two points in the atmosphere, defines as:

$$LWP = \int \rho_{air} r_L dz \quad (\text{Eq. 1.19})$$

where ρ_{air} is the air density and r_L is the liquid water mixing ratio in the cloud.

- the size distribution of the cloud particles is usually described by a gamma particles size distribution, generally defined using three parameters, α , β and γ that depend on the cloud type and a constant C which depends on the total number of particles:

$$n(r) = Cr^\alpha \exp(-\beta r^\gamma) \quad (\text{Eq. 1.20})$$

- the cloud droplet effective radius (μm) and the effective variance as defined for the aerosols.
- the *cloud optical thickness* that describes the vertical optical thickness of a cloud, from the bottom to the top of the cloud, as for an aerosol layer. This quantity varies from about 1 to 40, depending on the cloud type.
- the *cloud albedo* is a ratio that describes the amount of solar radiation reflected back to space by the cloud. It depends on the cloud optical thickness and cloud particles microphysics. The cloud albedo and the cloud optical thickness are the optical quantities used to characterize the radiative effects of clouds.

1.4 Methods used for the study of aerosols and clouds

The scientific community is working on better monitoring the load and microphysical properties of aerosols in order to assess the influence of those particles on the Earth's radiative budget and clouds. We describe below the main methods and measurements used to depict the aerosol and cloud properties.

1.4.1 Different methodologies and measurements

In-Situ technics:

In-situ measurements allow sampling the particles in their environment. They typically allow measuring a large set of microphysical and optical aerosol parameters, but they remain limited in time and space. For instance, the particle counters and TEOM (Tapered

Element Oscillating Microbalance) provide instantaneous and continuous measurements of mass and number concentration of particles. Observations made by a scanning electron microscope (SEM) or by an accelerator mass spectrometry (AMS) may provide a detailed knowledge of the physical and chemical properties of the atmospheric particles (size, shape and composition). Optical methods are also used to analyze the aerosols properties from in-situ data. For example, nephelometers and aethalometers' measurements provide (after modeling) the aerosol scattering and absorption coefficients.

Remote sensing technics:

The radiation scattered and reflected by the Earth depends on the composition of its atmosphere and surface. The microphysical properties of aerosols and clouds are responsible for the processes of scattering, absorption and emission. The measurements of the radiation scattered or emitted by the atmospheric particles (i.e. passive remote sensing technics), and the accurate modeling of these radiations, allow the determination of a certain number of particle parameters. Active remote sensing techniques (which create their source of illumination) are also used to study aerosol and clouds and allow depicting the vertical structure of the atmosphere. Lidar system measures the radiation backscattered by the atmospheric particles. Lidar mainly provides the backscatter coefficient profiles and allows the retrieval of the extinction coefficient.

These radiations can be measured from space, at the surface or within the atmosphere and we distinguish different types of observations:

Ground-based observations: Sun-photometers directly measure the solar constant attenuation and also the downwelling radiation scattering by the molecules and aerosols. The measurements acquired at the ground allow to accurately retrieving the aerosol properties integrated over the atmospheric column, and are typically used for the validation of satellite retrievals. The AERONET (AERosol Robotic NETwork) sun-photometers network includes 350 sites distributed all over the world. It provides the aerosol optical properties in the absence of clouds in some visible, near-infrared and UV spectral bands. The lidar network, called EARLINET (European Aerosol Research Lidar Network), allows acquiring almost continuous measurements of the vertical distribution of aerosols, on 28 different sites distributed over Europe.

Airborne observations: such as the ones acquired during experimental field campaigns provide useful information on certain types of particles and processes at a regional scale. They can be combined for instance with in-situ measurements to provide a comprehensive characterization of the aerosol or cloud properties. For example, one can note the following field campaigns: "SAFARI 2000", that was dedicated to biomass-burning aerosols study over the South Atlantic Ocean, "SHADE", the SaHAran Dust Experiment, performed in 2000, and the most recent AEROCLO-SA (AERosol RadiatiON and CLOUDs in southern Africa), that allowed to measure the aerosol and cloud properties at different levels of the atmosphere,

using airborne in-situ and remote sensing measurements as well as ground-based in-situ measurements.

Space borne observations: the satellite measurements allow retrieving aerosol and cloud properties over large spatial-temporal scale and the study of their effects on climate.

1.4.2 The constellation of satellites A-Train

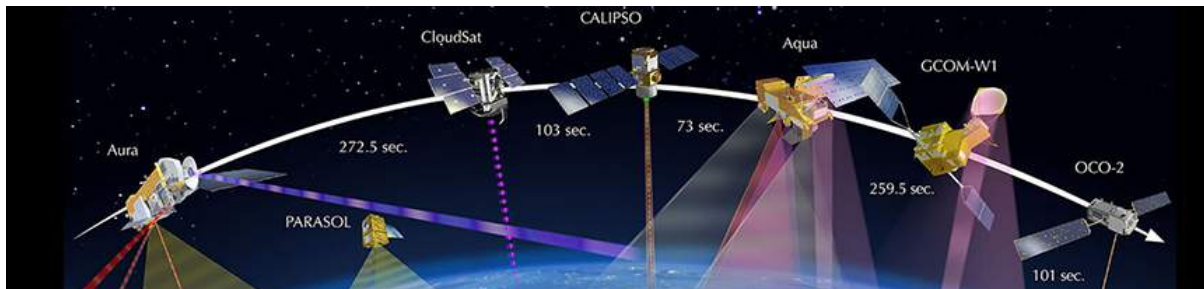


Figure 1.12 – A-Train satellite constellation in 2017 (Source: <https://atrain.nasa.gov/>)

The constellation of satellites called A-Train includes different passive and active sensors for monitoring clouds and aerosols properties (<http://atrain.nasa.gov/publications/A-TrainFactSheet.pdf>). A-Train sensors describe a geosynchronous orbit and provide quasi-simultaneous measurements, making possible the combination and comparison of various measurements and methods and also the possibility to perform instrumental synergies. AQUA was the first platform launched in 2002. The platforms CALIPSO and PARASOL joined the A-Train after January 2006.

The active sensor typically used to describe the aerosol and cloud properties is the Cloud-Aerosol Lidar with Orthogonal Polarization (CALIOP) installed on CALIPSO (Cloud-Aerosol Lidar and Infrared Pathfinder Satellite Observation) satellite. It provides high-resolution vertical profiles of aerosols and clouds (Chand et al., 2008; Winker et al., 2010). CALIOP provides the total attenuated backscatter signal ($\text{km}^{-1} \text{sr}^{-1}$) at 532 nm and 1064 nm. From the backscatter measurements, an operational aerosol algorithm allows for retrieval of the vertical extinction profiles as well as the aerosol optical thickness (AOT) by assuming an aerosol lidar ratio (extinction to backscatter) (Omar et al., 2009; Young and Vaughan, 2009). Moreover, two orthogonally polarized channels measure the parallel and perpendicular backscatter signal at 532 nm that allows calculating the depolarization ratio (i.e. the ratio of the two orthogonal polarization signals) (Hunt et al., 2009). Depolarization measurements are used for discrimination between spherical and non-spherical particles (Sassen, 1991). CALIOP provides exhaustive details on the vertical distribution of optical and microphysical properties of aerosols and clouds, including their shape, and a qualitative classification of aerosol type (via the wavelength dependence of the backscatter) (Winker et al., 2009; Young and Vaughan, 2009).

The main A-Train passive instruments used to characterize the aerosol and cloud properties are the Moderate Resolution Imaging Spectroradiometer (MODIS) instrument, the Polarization and Directionality of Earth Reflectances (POLDER) instrument and the Ozone Monitoring Instrument (OMI). The MODIS instrument onboard Aqua uses multi-spectral measurements to enable the separation of the fine and coarse aerosols properties (Tanré et al., 1997). The OMI instrument onboard Aura satellite uses the properties of aerosols to absorb UV radiations to retrieve their properties in the UV (Torres et al., 2007). The POLDER instrument, aboard PARASOL (Polarization and Anisotropy of Reflectances for Atmospheric Science coupled with Observations from a Lidar), detects the aerosols by measuring the angular, polarized and spectral properties of the radiations in some visible and near-infrared bands (Tanré et al., 2011). The main retrieved parameters for aerosols are the AOT and the Ångström Exponent (AE), which is a parameter indicative of the particles size (Kaufman et al., 2002). Recent methods also allow retrieving the aerosol Single Scattering Albedo (SSA) over clear-sky ocean scenes (Dubovik et al., 2008; Torres et al., 2013; Waquet et al., 2016). The directional observations of POLDER allowed evaluating the non-sphericity of the particles (Herman et al., 2005). The aerosol properties are typically more accurately retrieved over dark ocean scenes than over land where the surface contribution is typically larger than the aerosol one. A new method (GRASP) that allows to simultaneously retrieving the aerosol and surface properties was recently developed. This method use multi-pixel and multi-temporal observations. This method was shown to significantly enhance the accuracy of the aerosol retrievals performed over land with POLDER/PARASOL in clear-sky scenes (Dubovik et al., 2011). The study of the aerosols located in cloudy scenes from space is also challenging. The difficulty for the passive instruments is to separate the aerosol contribution from that of the clouds, which is much more intense. This is the reason why most of the operational retrieval methods based on passive remote sensing are currently restricted to “clear-sky” situations.

For clouds, the current operational methods developed for the A-Train sensors mainly provide the cloud optical thickness and the cloud droplet effective radius. King et al. (1997) described the algorithm of retrieving the optical thickness, effective radius and thermodynamic phase with the MODIS instrument. Buriez et al. (1997) described the detection of cloud properties from POLDER, using the multidirectional measurements. The POLDER angular polarized signal allows the retrieval of the thermodynamic phase of the cloud (Goloub et al., 2000; Riedi et al., 2010). The measurements are also sensible to the water droplet size distribution (Bréon and Goloub, 1998) and to the presence of ice clouds (Chepfer et al., 2000).

1.4.3 Satellite retrievals of aerosol above cloud properties

The study of the aerosols located above clouds from space is a relatively recent topic in the field of remote sensing. Until now, different innovative methods and instruments were used for the retrieval of the Aerosol Above Clouds (AAC) properties.

Lidar instruments that depict the vertical profile of the atmosphere are dedicated instruments for the study of multi-layer situations and aerosol above cloud scenes. The operational method developed for CALIOP allows the retrieval of the aerosol properties (i.e. mainly the AOT) for scenes with aerosol above clouds. However, the method relies on assumptions and alternative CALIOP-based research methods have also been introduced to retrieve the above-cloud AOT. The depolarization ratio method (DRM) (Hu et al., 2007a) and the color ratio method (CRM) (Chand et al., 2008) use fewer assumptions for the retrieval of aerosol properties. These methods are based on light transmission methods and treat the liquid water clouds situated underneath the aerosol layer as a target. Hu et al. (2007b) have shown that, in the case of opaque water clouds, the layer integrated attenuated backscatter at 532 nm and layer integrated attenuated depolarization ratio at 532 nm can be used to retrieve the aerosol optical depth of the overlaying aerosol or optically thin cloud layers. The CRM uses the layer integrated attenuated color ratio, which is the ratio of integrated attenuated backscatter at 1064 nm to 532 nm. Over the visible to near-infrared spectral region, fine-mode absorbing aerosols above clouds exhibit a strong wavelength dependence color ratio (Chand et al., 2008). This makes possible the detection of absorbing biomass-burning aerosols transported above clouds. The color ratio observed in the case of coarse mode particles or purely scattering fine mode aerosols transported above clouds exhibits little or no wavelength dependence and thus, these particles can be less accurately detected with the CRM method.

Passive sensors have also been used to obtain information on aerosols above clouds. Torres et al. (2012) have developed an algorithm to retrieve the ACAOT and the underlying aerosol-corrected cloud optical depth, using radiance measurements performed in the ultra violet (UV) by OMI instrument. The method takes advantage of the ability of biomass burning and mineral dust aerosols to strongly absorb UV radiations. Another method that can retrieve the ACAOT and, simultaneously, the aerosol-corrected COT is the “color ratio” method proposed by Jethva et al. (2013) that employs measurements in visible and shortwave infrared (SWIR) channels from the MODIS instrument. Also, Meyer et al. (2015) developed an algorithm that employs reflectance measurements from six MODIS channels (from the visible to the shortwave infrared) to retrieve the ACAOT, as well as the COT and droplet effective radius (r_{eff}) of the underlying cloud. Using the measurements of the satellite instrument SCIAMACHY, de Graaf et al. (2012) have developed an algorithm used to calculate the instantaneous radiative effect of aerosols above clouds, using the reflectance spectrum measured by SCIAMACHY.

The multi-directional polarization measurements have shown sensitivity to AAC scenes (Waquet et al., 2009, Hasekamp, 2010; Knobelspiesse et al., 2011). The aerosols generate an additional polarized light at forward and side scattering angles (70° to 130°) and reduce the polarized signal of the cloud bow (i.e. a strong polarized rainbow feature observed near 140° in scattering angle). Mineral dust particles do not much polarize light, but they strongly minimize the cloud bow magnitude. Based on these effects, Waquet et al. (2009) have developed a method for retrieving the properties of aerosols above clouds that relies on the polarized radiances measured by POLDER. Because polarized radiances are not affected

by the optical thickness of the cloud (i.e. the polarized radiance reflected by the cloud is saturated when the cloud is optically thick enough), the method is able to retrieve the scattering ACAOT at two wavelengths (670 nm and 865 nm) without much assumption on cloud properties. An analysis of the global results obtained with the operational algorithm is given in Waquet et al. (2013a). Furthermore, Peers et al. (2015) have developed a complementary method that uses additional total multidirectional radiances measured by POLDER. The method provides the aerosol SSA and the aerosol-corrected cloud optical thickness. So far, the algorithm of Peers et al. (2015) is a research method, only applied for regional studies (Peers et al., 2016). Table 1.2 summarize the list of the satellite methods developed until now to measure AAC and below-cloud properties.

Table 1.2 – List of methods developed to measure AAC properties and below-cloud properties, along with the input information and the retrieved parameters.

Methods	Input parameters	Retrieved parameters
CALIOP operational method (Winker et al., 2009, Young and Vaughan, 2009)	Attenuated backscatter profile at 532 nm and 1064 nm	AOT Cloud top altitude Aerosol top and base altitude
CALIOP Depolarization Ratio Method (Hu et al., 2007) + SODA Method (Deaconu et al., 2017)	Layer integrated attenuated backscatter profile, depolarization ratio at 532 nm	AOT and Ångström exponent
CALIOP Color ratio method (Chand et al., 2008)	Layer integrated attenuated backscatter, color ratio	AOT and Ångström exponent
POLDER polarization method (Waquet et al., 2009)	Polarized Reflectance at 865 and 670 nm	AOT and Ångström exponent
POLDER absorption method (Peers et al., 2015)	Total radiance at 490 and 865 nm	Absorption AOT and COT corrected for absorption
OMI (Torres et al., 2012)	Reflectance at 388 nm, measured UVAI	AOT and COT (aerosol models assumed)
MODIS color ratio (Jethva et al., 2013)	Reflectance at 470 and 860 nm	AOT and COT (aerosol models assumed)
MODIS (Meyer et al., 2015)	Reflectance at 470, 550, 660, 860, 1240 et 2100 nm	AOT, COT and r_{eff}
Schiamachy (De Graaf et al., 2012)	Reflectance spectrum	DRE

1.5 Aerosols above clouds

The lack of knowledge of aerosol properties in case of aerosols above clouds (AAC) scenes has been recently highlighted as a source of uncertainty for the estimation of all-sky DRE of aerosols (Peers et al., 2016). Different approaches have been developed to quantify the DRE of AAC using satellite observations. But despite recent observational and modeling studies (De Graaf et al., 2014; Peers et al., 2015; Zhang et al., 2016), the aerosol DRE for AAC remains a subject of large uncertainty. In the process of quantification and interpretation of the aerosol impact on climate, the aerosol interactions with clouds constitute the largest uncertainty in global climate models (Myhre et al., 2013a, 2013b). Figure 1.13 shows the results Peers et al. (2016) obtained in the framework of the AEROCOM (Aerosol Comparisons between Observations and Models, (Kinne et al., 2006; Textor et al., 2006) project, which aims to improve the representation of aerosols in global climate models.

This figure compares the above cloud AOT and the Single Scattering albedo (SSA) retrieved by POLDER-3 at 550 nm with the ones modeled by five climate models. Figure 1.13 highlights the biases in climate models, for both the particles load (AOT) and absorption (SSA) and can explain the current difficulties in accurately estimating the DRE of aerosols in this region of the world, as previously noted by Myhre et al. (2013b).

The study of AAC may also contribute to reduce the uncertainties associated with the semi-direct and indirect effects. For instance, in case of absorbing AAC, the warming of the atmosphere occurring above stratocumulus clouds might reduce the strength of the convection and consequently impact the vertical development and the cloud properties. This warming might increase the liquid water content and the persistence of clouds (Johnson et al., 2004b; Wilcox, 2010). Evidence of the first indirect effect was also found over the South Atlantic region, where AAC events are frequently observed. Costantino and Bréon, (2013) notably found a strong decrease in the droplet effective radius when the aerosol layers are in contact with the top altitude of the cloud deck. Also, the understanding of AAC aerosols would allow a better description and characterization of the underlying cloud properties, which are biased in many studies due to the presence of aerosols.

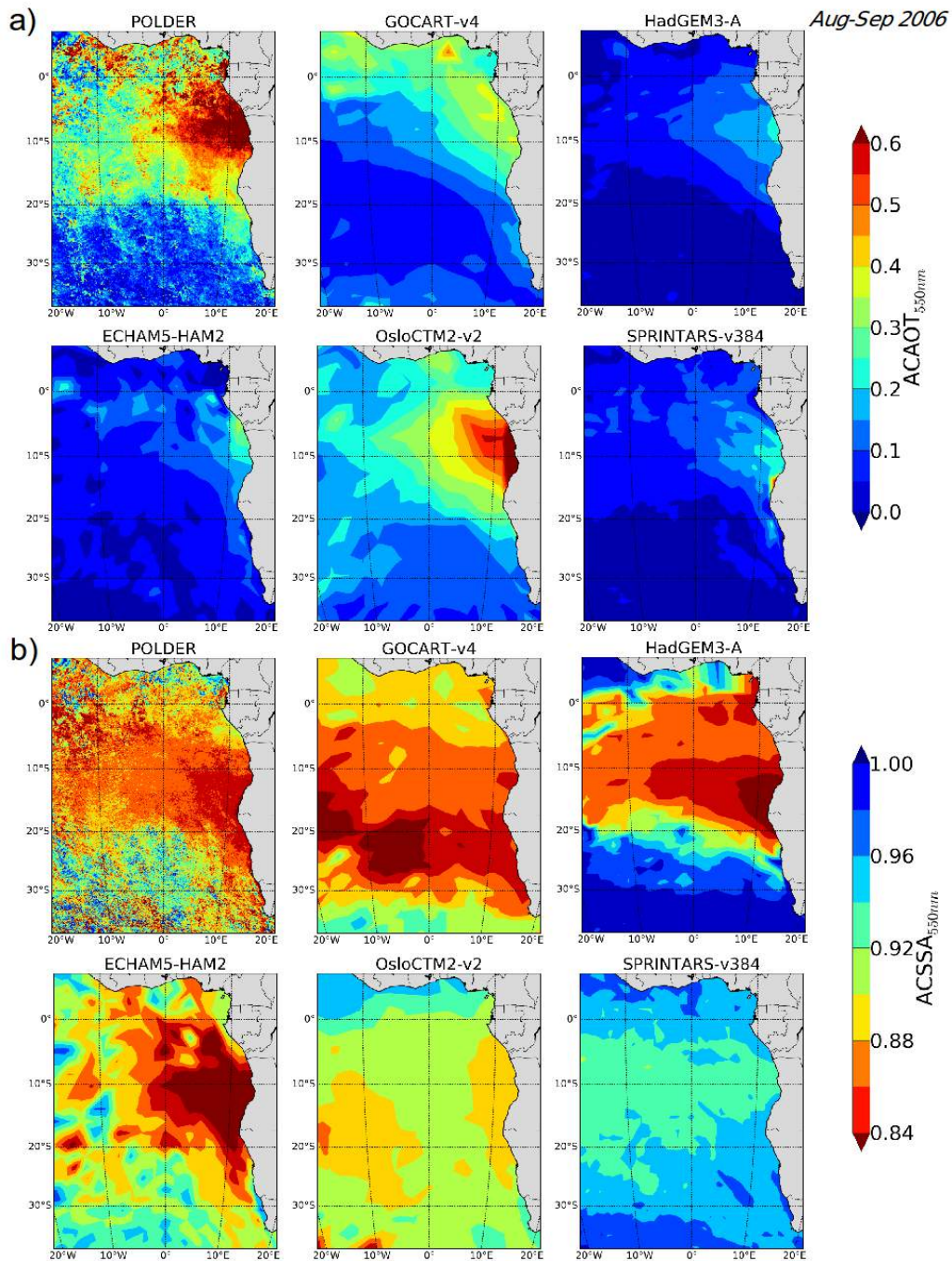


Figure 1.13 – Average on the period August-September 2006 of aerosol optical thickness above clouds (ACAOT) (a) and single scattering albedo above clouds (ACSSA) (b) at 550 nm retrieved by POLDER-3 instrument in the South Atlantic Region, along with 5 other simulations by climate models (Source: Peers et al., 2016).

1.6 Thesis objectives

The work presented in this manuscript is focused on the analysis of aerosol above cloud properties and radiative impacts as well as the study of their potential interactions or effects with the underlying clouds.

The validation of aerosols above clouds is not possible using regular sun-photometer measurements (i.e. ground-based sun-photometer can't perform measurements in case of cloudy skies). The first objective of this thesis is to perform an inter-comparison of the above cloud aerosol properties retrieved with three of the aforementioned methods in order to assess their consistency. We compare the above clouds AOT and the Ångström Exponent retrieved from active and the passive measurements. We considered the following methods: (a) the CALIOP operational method (CALIOP_{OM}) because of the numerous studies in which it was used, (b) the DRM developed by Hu et al. (2007a), (c) a calibrated version of the DRM algorithm and (d) the POLDER polarization method. The DRM and POLDER methods were chosen because both are measuring AAC properties above the same type of cloudy scenes (i.e. optically thick and homogeneous liquid water clouds). Moreover, both techniques are sensitive to all types of particles (scattering or absorbing particles, fine or coarse ones), which is not the case for CRM that can operate only for absorbing aerosols. It is also interesting to compare these two approaches since the POLDER method requires a hypothesized aerosol microphysics, while DRM doesn't require any hypothesis for the aerosols but requires assumptions and an approximate model to estimate the signal backscattered by clouds. We will perform the comparison for three regional study cases and also a global analysis. A discussion related to the limitations of each method and improvements will be also presented. The analysis takes into account the vertical repartitions of aerosol layers relative to the cloud layers (i.e. aerosol and cloud in contact).

The second objective is to study the radiative impact and the potential semi-direct effect of biomass-burning aerosols over the South Atlantic Ocean. The collocated properties of AAC provided by POLDER (AOT, SSA, particles size and absorption and cloud optical thickness) and the MODIS cloud droplets effective radius are collocated with the vertical profiles provided by CALIOP for aerosols and clouds and the meteorological re-analysis data provided by the ECMWF weather model. Using this original database, that includes new retrieved parameters, such as the absorption of the aerosols and the corrected cloud optical thickness, we calculate the aerosol direct radiative effect at the top of the atmosphere and show the cloud properties observed by POLDER in case of low and high load of AAC loadings. By combining CALIOP and POLDER, we calculate the profiles of heating rates in the shortwave and longwave spectral domains and evaluate the radiative impacts of aerosols within the atmosphere. Then, we propose a strategy to separate the meteorological effects from the potential effects of aerosols on clouds properties to ultimately estimate the semi-direct effect of aerosols over this region.

Chapter 2

Methodology and computation tools

In this section, we present the radiative quantities typically used in passive and active remote sensing problems. We present the instruments used to measure the field of radiation reflected or backscattered by the surface-atmosphere system as well as the equations and tools used to model these radiations. Finally, we present the theoretical basis of the algorithms used to retrieve the aerosols above clouds properties from passive and active measurements.

2.1 Passive observations

2.1.1 Theoretical concepts

Normalized radiance

Passive radiometers measure the radiations scattered and/or reflected by the Earth-atmosphere system. These instruments are equipped with sensors and measure the power of the electromagnetic wave (W) emitted by a target. This power is measured for a solid angle characterized by the geometry of the instrument, and when divided by the apparent surface of the detector, it gives the radiance in $\text{W}\cdot\text{m}^{-2}\cdot\text{sr}^{-1}$. If filters are used, then the instrument measures a spectral radiance in $\text{W}\cdot\text{m}^{-2}\cdot\text{sr}^{-1}\cdot\mu\text{m}^{-1}$. The quantity that is typically used in remote sensing applications is the normalized total radiance defined as:

$$L(\theta_s, \theta_v, \varphi_r) = \frac{\pi L^*(\theta_s, \theta_v, \varphi_r)}{E_s} \quad (\text{Eq. 2.1})$$

where L^* is the spectral radiance, E_s is the solar irradiance incident upon the Earth's atmosphere ($\text{W}\cdot\text{sr}^{-1}\cdot\text{m}^{-2}\cdot\mu\text{m}^{-1}$), θ_s et θ_v are sun and view zenithal angles, and φ_s et φ_v are the

azimuth angles. The relative azimuth angle φ_r is calculated as the difference between the observation azimuth φ_v and the solar azimuth φ_s .

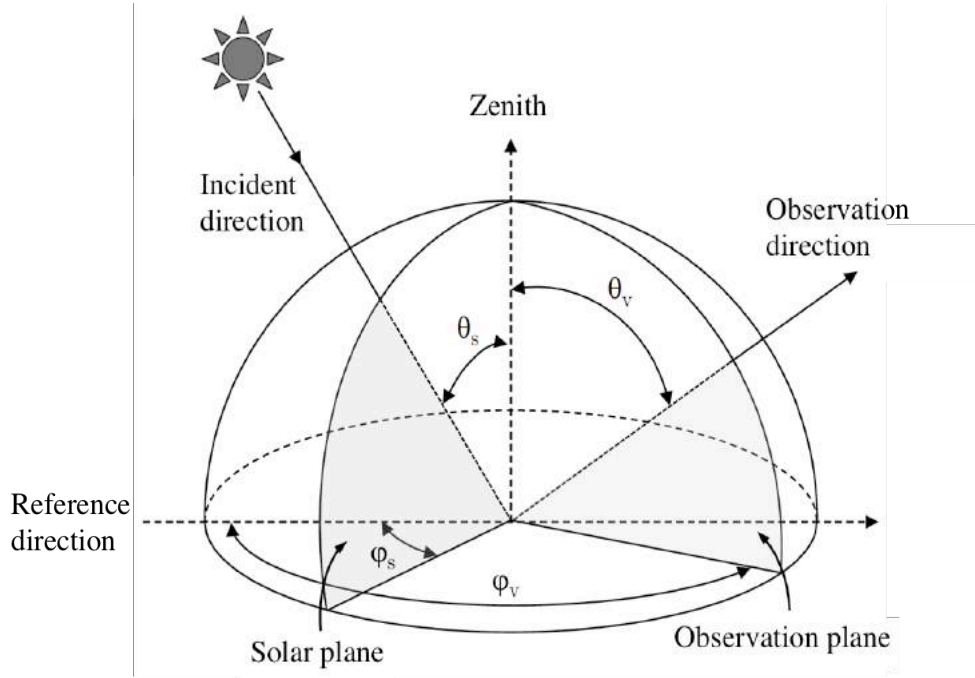


Figure 2.1 – Geometry of illumination and observation

Reflectance and Albedo

The bidirectional reflectance r is defined as the fraction of radiation reflected under a directional incident irradiation:

$$r(\theta_s, \theta_v, \varphi_r) = \frac{L(\theta_s, \theta_v, \varphi_r)}{\cos\theta_s} = \frac{\pi L^*(\theta_s, \theta_v, \varphi_r)}{E_s \cos\theta_s} \quad (\text{Eq. 2.2})$$

Radiative Flux

The net flux is calculated by integrating the spectral radiance L^* over all the directions and it is expressed in $\text{W}\cdot\text{m}^{-2}$:

$$F(\theta_s) = \int_{4\pi} L^* \cos\theta_v d\omega \quad (\text{Eq. 2.3})$$

where $d\omega$ is the elementary solid angle.

We can separate the net flux into two fluxes integrated over each hemisphere: the upwelling flux F^\uparrow and downwelling flux F^\downarrow , defined as:

$$F = F^\uparrow - F^\downarrow \quad (\text{Eq. 2.4})$$

At the top of the atmosphere the incident flux is equal to $E_s \cos\theta_s$. For a perfectly reflecting surface (Lambertian reflector) the upwelling flux can be written as $F_{reflected} = \pi L^*$ when the radiance is isotropic (i.e. the radiance doesn't depend on θ_v or ϕ_v).

The planar albedo for a surface is defined as the ratio between the upwelling flux F^\uparrow (in W.m^{-2}) and the downwelling flux F^\downarrow . Its values range between 0 and 1:

$$\rho_p = \frac{F_{reflected}}{F_{incident}} = \frac{F^\uparrow}{F^\downarrow} \quad (\text{Eq. 2.5})$$

Lastly, we can define the spherical albedo ρ , by integrating the albedo ρ_p over all the directions of solar incident radiation:

$$\rho = 2 \int_0^1 \mu_s \rho_p(\mu_s) d\mu_s \quad (\text{Eq. 2.6})$$

where μ_s is the cosine of the solar angle.

Radiative forcing

The aerosol radiative forcing measured in W.m^{-2} is defined as the difference between the net radiative fluxes computed with aerosols (F_{aer}) and without aerosols (F_{clean}):

$$\Delta F = F_{aer} - F_{clean} = (F_{aer}^\downarrow - F_{aer}^\uparrow) - (F_{clean}^\downarrow - F_{clean}^\uparrow) \quad (\text{Eq. 2.7})$$

At the top of the atmosphere, the downwelling flux doesn't depend on the aerosol loading, therefore $F_{aer}^\downarrow = F_{clean}^\downarrow$. Then, we can define the aerosol radiative forcing at the top of the atmosphere as:

$$\Delta F = F_{clean}^\uparrow - F_{aer}^\uparrow \quad (\text{Eq. 2.8})$$

A negative aerosol radiative forcing means that the aerosol layer contribute to increase the albedo of the Earth-atmosphere system causing a cooling whereas a positive value means the opposite effect.

Heating rate

The heating (or cooling) rate is used to characterize the radiative impact of the aerosol within the atmosphere.

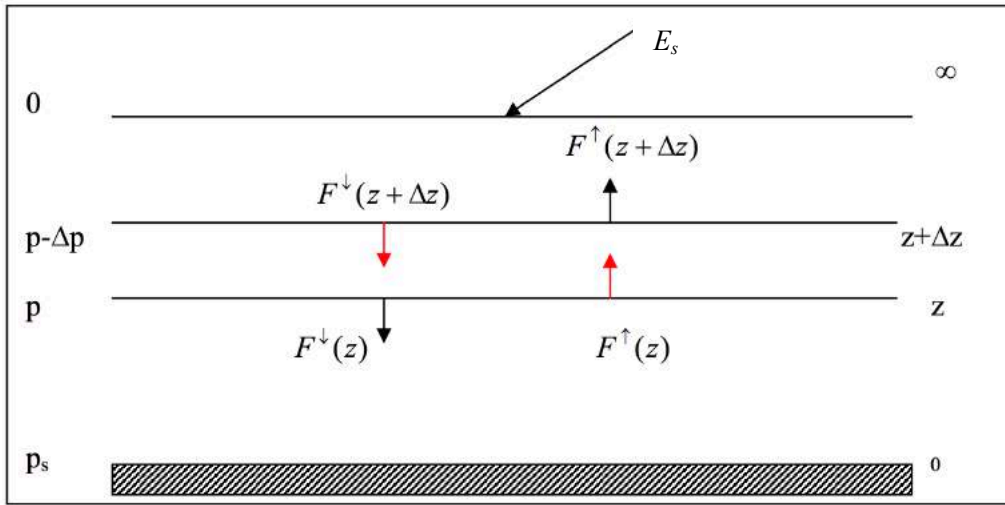


Figure 2.2 – Schematic of calculating heating rates in the atmosphere. p stands for pressure, F_0 is the incident solar irradiance.

The instantaneous gain of radiative energy G of a thin layer of geometrical thickness Δz located at the altitude z in the atmosphere, can be calculated as:

$$G(z) = \sum F_{ingoing} - \sum F_{outgoing} = [F^\uparrow(z) + F^\downarrow(z + \Delta z)] - [F^\uparrow(z + \Delta z) - F^\downarrow(z)]$$

$$G(z) = -[F_{net}(z + \Delta z) - F_{net}(z)]$$

$$G(z) = -\frac{\partial F_{net}}{\partial z} \Delta z = h(z) \Delta z \quad (\text{Eq. 2.9})$$

where $h(z)$ is the heating (or cooling) radiative rate expressed in W.m^{-2} . This quantity is equal to the divergence of the net flux for a given layer of atmosphere. It corresponds to the radiative energy trapped (or lost) by the layer.

Then, we can define the heating rate (in K.day^{-1}) as:

$$\frac{\partial T}{\partial t} = \frac{1}{c_p \rho} h(z) = -\frac{1}{c_p \rho} \frac{dF_{net}(z)}{dz} \quad (\text{Eq. 2.10})$$

where ρ is the air density (Kg.m^{-3}) and c_p is the air specific heat ($\text{J.K}^{-1}.\text{Kg}^{-1}$)

Polarization and Stokes parameters

In a general description, the light consists of a superposition of plane and monochromatic electromagnetic waves. Each single wave corresponds to a transverse wave that is characterized by an electric field \vec{E} and a magnetic field \vec{B} . The Maxwell equations link the two fields, and the knowledge of the electric field is sufficient to characterize the wave

properties. The complex electric field vector can be expressed for a single wave with the following equation:

$$\vec{E}(\vec{r}, t) = E_0 e^{i(\omega t - \vec{k} \cdot \vec{r})} \quad (\text{Eq. 2.11})$$

where \vec{r} represents the position of the vector at the observation point, t is the time, E_0 is the amplitude, $i = \sqrt{-1}$, ω is the angular frequency and \vec{k} is the direction of the wave propagation.

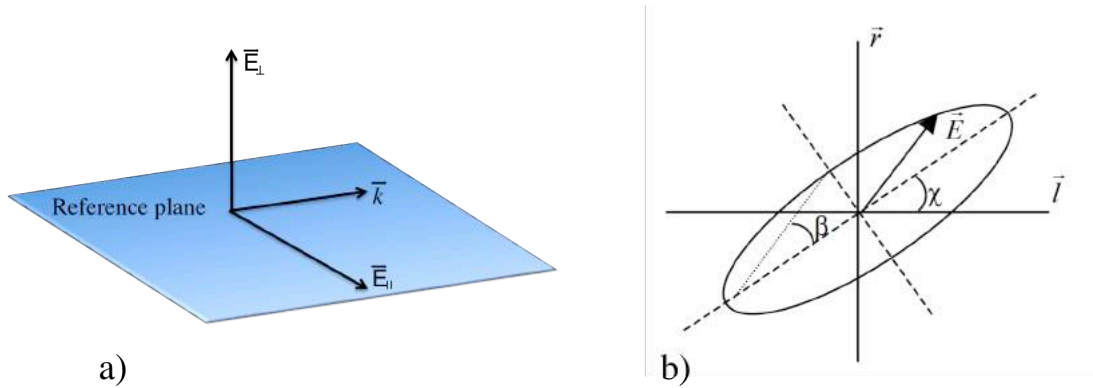


Figure 2.3 – (a) The parallel and perpendicular electric field components: \vec{E}_{\parallel} and \vec{E}_{\perp} in the axis system $(\vec{r}, \vec{l}, \vec{k})$. (b) Elliptic polarization in the vector basis (\vec{l}, \vec{r}) . β and χ are the ellipticity and the angle that defines the direction of the main axis, respectively.

In the axis system $(\vec{r}, \vec{l}, \vec{k})$, where \vec{l} and \vec{r} define two directions in the wave plane that is perpendicular to the direction of propagation \vec{k} (see Figure 2.3a), the vector \vec{E} can be decomposed into a parallel component \vec{E}_{\parallel} and a perpendicular component \vec{E}_{\perp} , written as:

$$\vec{E}_{\parallel} = E_{\parallel 0} e^{i(\omega t - kz - \phi_{\parallel})} \quad (\text{Eq. 2.12})$$

$$\vec{E}_{\perp} = E_{\perp 0} e^{i(\omega t - kz - \phi_{\perp})} \quad (\text{Eq. 2.13})$$

where $E_{\parallel 0}$ and $E_{\perp 0}$ are the amplitudes of the parallel and the perpendicular components of the electric field, ϕ_{\parallel} and ϕ_{\perp} are their respective phase, k is the wave number ($k = \frac{2\pi}{\lambda}$, where λ is the wavelength) and z is the direction of propagation.

In the general case, the extremity of the electric field vector describes an ellipse in the wave plane (see Figure 2.3b). This trajectory describes the state of polarization of the wave. When $\phi_{\parallel} - \phi_{\perp}$ is equal to zero, the trajectory is a segment and the polarization is linear. The polarization is circular for the specific case when:

$$\phi_{\parallel} - \phi_{\perp} = +/\!-\frac{\pi}{2} \quad \text{and} \quad E_{\parallel 0} = E_{\perp 0}$$

The Stokes parameters are typically used to describe the intensity and the state of polarization of the electromagnetic radiations (Chandrasekhar, 1950; van de Hulst, 1957; Stokes, 1852). The so-called Stokes column vector \mathbf{I} is a four-element vector, defined as:

$$\mathbf{I} = \begin{pmatrix} I \\ Q \\ U \\ V \end{pmatrix} = \frac{\varepsilon_0 c}{2} \begin{pmatrix} \langle E_{\parallel 0}^2 \rangle + \langle E_{\perp 0}^2 \rangle \\ \langle E_{\parallel 0}^2 \rangle - \langle E_{\perp 0}^2 \rangle \\ \langle 2E_{\parallel 0}E_{\perp 0}\cos\delta \rangle \\ \langle 2E_{\parallel 0}E_{\perp 0}\sin\delta \rangle \end{pmatrix} \quad (\text{Eq. 2.14})$$

The brackets $\langle \dots \rangle$ indicate a time averaging, δ is the retardation in the phase between the two components: $\delta = \phi_{\parallel} - \phi_{\perp}$, c is the speed of light in vacuum and ε_0 is the dielectric constant of a vacuum.

The Stokes vector element I represents the total intensity associated with the radiation. The second and the third Stokes parameters, Q and U , describe the linear polarization, while the fourth component V corresponds to the circular polarization. These parameters have an array of energy and can be added if they are defined in the same basis of vector. The Stokes parameter V can be neglected in the atmosphere (Kawata, 1978). The natural light coming from the sun is un-polarized. The radiation emerging from the Earth-atmosphere system is however partially linearly polarized due to scattering and surface reflection processes (i.e. driven by the Fresnel equations). For our study, the radiation measured by a passive radiometer can be considered as linearly partially polarized and can be fully described by the parameters I , Q and U .

The following equations summarize the quantity that describe the radiation:

$$I = I_{nat} + I_p \quad (\text{Eq. 2.15})$$

$$P = \frac{I_p}{I} = \frac{\sqrt{Q^2 + U^2}}{I} \quad (\text{Eq. 2.16})$$

$$\tan(2\chi) = U/Q \quad (\text{Eq. 2.17})$$

where I_{nat} and I_{pol} are the natural and polarized component of the radiation. The quantity P is the linear polarization ratio and χ the angle that defines the direction of polarization with respect with a given axis.

Polarized radiance

The total radiance L is proportional to the first Stokes parameter I . We can rewrite Eq. 2.15 as $L = L_{nat} + L_p$, where L_{nat} and L_p are the natural and polarized radiances, respectively. The polarized radiance L_p can be calculated using the Q and U Stokes parameters as follows:

$$L_p = +/\sqrt{Q^2 + U^2} \quad (\text{Eq. 2.18})$$

The polarized radiance is signed positive when the electric field is perpendicular to the scattering plane (i.e. the plane that contains the incident and scattering directions). It is signed negative when the electric field is parallel to the scattering plane.

2.1.2 Radiative transfer equation

The radiative transfer equation must be solve in order to model the total and polarized radiances.

The vector of the radiative transfer equation (RTE) that describes the propagation of radiation in a scattering and absorbing medium is:

$$\mu_v \frac{d\mathbf{L}(\tau, \mu_v, \varphi_v)}{d\tau} = \mathbf{L}(\tau, \mu_v, \varphi_v) - \mathbf{S}(\tau, \mu_v, \varphi_v) \quad (\text{Eq. 2.19})$$

where the source vector \mathbf{S} is described as:

$$\begin{aligned} \mathbf{S}(\tau, \mu_v, \varphi_v) = & \frac{\varpi(\tau)}{4\pi} \mathbf{P}(\tau, \mu_v, \varphi_v, \mu_s, \varphi_s) E_0 \exp\left(\frac{\tau}{\mu_s}\right) + \\ & + \frac{\varpi(\pi)}{4\pi} \int_{-1}^1 \int_0^{2\pi} \mathbf{P}(\tau, \mu_v, \varphi_v; \mu'_v, \varphi'_v) \mathbf{L}(\tau, \mu_v, \varphi_v; \mu'_v, \varphi'_v) d\mu'_v d\varphi'_v \end{aligned} \quad (\text{Eq. 2.20})$$

where μ_v and μ_s are the cosine of the viewing and zenith solar angles, respectively; φ_v and φ_s are the azimuth viewing and solar angles; \mathbf{L} is the Stokes vector, \mathbf{P} is the 3×3 phase matrix.

This integral-differential equation gives exact analytic results only in case of the single scattering. The third part of Eq. 2.20 corresponds to the multiple scattering processes (i.e. radiation scattered more than one time) and must be computed for an accurate modeling of the radiances.

Different methods and codes were developed to solve this equation. Two categories of code were developed: the «1D» codes or «plan-parallel» codes that separate the atmosphere into horizontal and parallel homogeneous infinite layers. These codes assume that the atmospheric columns are independent. The so-called «3D» codes consider the spatial heterogeneity of the atmosphere and provide more accurate results in case of heterogeneous cloudy atmosphere.

2.1.2.1 Successive Order of Scattering

The Successive Order of Scattering (SOS) method is a 1D code that allows computing the Stokes parameters of the radiation fields reflected by the surface-atmosphere, assuming no

gaseous absorption. The method is based on the separation of radiances into the contributions of radiations scattered n times:

$$\mathbf{L}(\tau, \mu_v, \varphi_v) = \sum_{n=1}^{+\infty} \mathbf{L}_n(\tau, \mu_v, \varphi_v) \quad (\text{Eq. 2.21})$$

where \mathbf{L}_n is the radiance vector at the diffusion order n . The single scattering contribution is first computed and then used to compute the contribution of the second order of scattering and so on. The summation will continue until the contribution of the n order becomes negligible.

In this study, we use the version of the SOS code developed at the Laboratoire d'Optique Atmosphérique (LOA). More information can also be found in the paper of Lenoble et al. (2007). The code accounts for the polarization and directional effects of ocean surface (i.e. glitter) and its diffuse contribution, assuming a Lambertian reflectance. This code will be used to simulate the polarized radiances computed for scenes with aerosol above clouds located over ocean.

2.1.2.2 GAME radiative transfer code

The Global Atmospheric Model (GAME) is a fast and high spectral resolution radiative transfer code that allows the calculations of radiances (and fluxes) in horizontal and plan-parallel atmospheric layers (Dubuisson, P., J. C. Roger, M. Mallet, 2006). GAME uses the DISORT method (DIScrete ORDinaTes) (Stamnes et al., 1988) to solve the radiative transfer equation. This method allows discretizing the radiation field in a finite number of propagation directions. Therefore, the integral part of the radiative transfer equation can be replaced by a summation and can be written as:

$$\int_{-1}^{+1} \mathbf{P}(\tau, \mu_v; \mu'_v) \mathbf{L}(\tau, \mu'_v) d\mu'_v = \sum_{\substack{i=-n \\ i \neq 0}}^n w_i \mathbf{P}(\tau, \mu_v; \mu_{v,i}) \mathbf{L}(\tau, \mu_{v,i}) \quad (\text{Eq. 2.22})$$

where w_i is a weight of the Gauss-Legendre quadrature and the index i denotes a discrete ordinate.

This method allows to efficiently compute the multiple scattering processes occurring in the atmosphere whatever the value of the optical thickness is. So far, this method however does not incorporate the Stokes formalism and cannot be used to simulate the polarized radiance.

The absorption coefficients for gases are computed with a line-by-line code (Scott, 1974). The code takes into account the molecular absorption for various species (CO_2 , O_2 , O_3 , CH_4 , CO , N_2) and includes the water vapor absorption continuum. GAME splits the longwave spectrum (from 4 to 50 μm) into 115 spectral intervals, whereas 208 spectral intervals are

considered for the shortwave spectrum (from 220 nm to 4 μm). Different vertical profiles are available for ozone and water vapor and for the thermodynamic quantities (e.g. tropical or mid-latitude atmosphere). These profiles can be also adjusted based on meteorological sounding if available. The atmosphere is vertically divided into 33 or 50 layers depending on the considered spectral domain (shortwave or longwave). In our study, we increased this number for the sake of accuracy. GAME accounts for the Rayleigh scattering effects and for the scattering and absorbing properties of clouds and aerosols that have to be computed over the different spectral intervals. The GAME code is primarily used in our study to compute the fluxes at different levels in the atmosphere, in the visible and also in the thermal infrared.

2.1.2.3 3DMCPOL and 3DCLOUD

Different studies shown that the homogeneous 1-D cloud assumption may lead to errors in the retrieved cloud parameters from total visible radiance (Marshak and Davis, 2005). Clouds are heterogeneous systems both in terms of shape and microphysical properties. These heterogeneities may impact the propagation of the radiation depending on the scale of the problem. In case of a cloudy atmosphere, significant biases in 1D calculations rise at pixel size smaller than 1 km, because of the independent columns approximation considered in the 1D codes. For larger pixels, the so-called “plan-parallel” bias becomes the main source of biases. This effect is due to the non-linear relationship that links the total radiance to the cloud optical thickness.

The radiative transfer code 3DMCPOL (Cornet et al., 2010) is based on the Monte-Carlo method (Metropolis and Ulam, 1949). It simulates the radiative transfer of the solar radiation in a tridimensional atmosphere by propagating the radiation in homogeneous 3D pixels of various scales. The computations of the total and polarized radiances are performed by following the trajectories of individual photons, starting from the source, and according to the physical and geometrical properties of the considered system. The directions of the photons are defined relatively to the position of the sun, and the interactions of the photons with the atmosphere (absorption and scattering) and with the surface (reflection) are defined with statistical laws. A complementary method, called 3DCLOUD, was employed for the generation of a realistic 3D cloudy structure used in the 3DMCPOL code (Szczap et al., 2014).

The operational algorithm developed for retrieving the properties of aerosol above clouds with POLDER/PARASOL is currently restricted to homogenous and optically thick clouds. In this study, we will use this 3D code to generate synthetic data of polarized radiances emerging from a complex scene with broken-field clouds. These simulations will be use to evaluate the response of the algorithm and its potential limitations when aerosols overlay fractional cloud covers.

2.1.3 POLDER / PARASOL instrument

The PARASOL mission was launched in December 2004, as part of the A-Train Sun-synchronous satellite formation. POLDER/PARASOL left the A-Train orbit in 2009 but still acquired measurements until December 2013. This instrument measures the total and polarized radiances in different spectral bands for various viewing geometries (Tanré et al., 2001).

The POLDER instrument, onboard on the PARASOL satellite, consists in a telecentric optic with a wide field of view, a rotational filter wheel and a two-dimensional CCD matrix array detector. The wheel filter has 16 positions, for which 7 positions are dedicated to total radiance measurements and 9 positions to polarized measurements. Total radiance measurements are performed in 9 spectral bands from the visible (440 nm) to the near-infrared (1020 nm). Polarized measurements are performed in 3 spectral bands including 490, 670 and 865 nm. The objective aperture is $\pm 51^\circ$ and $\pm 43^\circ$ depending on the axis, leading to a swath of 2100 km along the orbit track and 1600 km in the perpendicular direction. The CCD matrix consists in 242×274 pixels and allows the acquisition of two-dimensional images with a spatial resolution of around 6 km per 7 km at nadir viewing direction. This instrumental concept enables acquiring successive images that partially overlap each other. Hence, the same target is observed in different viewing geometries along the satellite track (Figure 2.4).

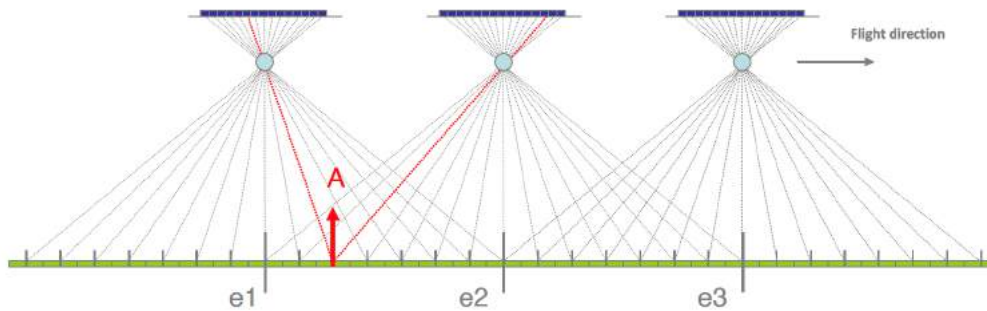


Figure 2.4 – Principle of multidirectional measurements of the POLDER instrument (Source: CNES). The instrument registers three images ($e1$, $e2$ and $e3$) along the track. The image $e1$ is overlapped by the image $e2$, therefore the observation point A is seen two times, from different angles.

In order to measure the polarized signal, it is necessary to perform three different acquisitions with three analyzers in order to retrieve the total radiance, the polarized radiance as well as the direction of polarization. Hence, the same filter appears three times, doubled by a polarizer which is crossed by 60° compared to the two others. The Malus law gives the signal measured for each combination:

$$\begin{aligned}
L_1 &= \frac{L_{nat}}{2} + L_p \cos^2(60^\circ + \chi) \\
L_2 &= \frac{L_{nat}}{2} + L_p \cos^2(\chi) \\
L_3 &= \frac{L_{nat}}{2} + L_p \cos^2(60^\circ - \chi)
\end{aligned} \tag{Eq. 2.23}$$

where χ is the polarization angle of the electric field with respect to a reference direction. We can compute the total and polarized radiances as well as the angle that defines the direction of polarization as follow:

$$L = \frac{2}{3}(L_1 + L_2 + L_3) \tag{Eq. 2.24}$$

$$L_p = \frac{2\sqrt{2}}{3} \sqrt{(L_1 - L_2)^2 + (L_2 - L_3)^2 + (L_1 - L_3)^2} \tag{Eq. 2.25}$$

$$\tan(2\chi) = \sqrt{3} \frac{L_3 - L_1}{2L_2 - L_1 - L_3} \tag{Eq. 2.26}$$

MODIS instrument

The MODIS instruments was developed by the American Space Agency (NASA) and was launched aboard NASA's Terra and Aqua satellites in December 1999 and May 2002, respectively. The mission objective is the observation of the atmosphere, the ocean, the biosphere, the cryosphere and the continental surfaces over a long period of time. MODIS is a scanning radiometer that measures the radiance in 36 spectral channels (from visible to thermal infrared between 405 nm and 14.4 μm). This instrument provides measurements at different spatial resolution depending of the considered spectral channels: 250 m (2 channels), 500 m (5 channels) and 1 km (29 channels). In our study, we mainly used the MODIS level 1 data (radiances and brightness temperature) and level-2 data (retrieved parameters) to characterize the properties of clouds observed within the POLDER pixel at a high spatial resolution (1 km \times 1 km).

2.1.4 POLDER methodology for aerosols above clouds retrieval

2.1.4.1 POLDER polarization method

The presence of aerosols above clouds strongly affect the polarized radiance reflected back to space by the clouds. Figure 2.5 shows simulated polarized radiances for different Aerosol Above Cloud (AAC) scenes: including fine-mode aerosols and non-spherical coarse-

mode particles. The radiances were processed with a Successive Order of Scattering (SOS) code.

Calculations were also performed for a single cloud layer without aerosols. Then, the main feature is a strong peak (the primary cloud-bow) located at a scattering angle of approximately 140° , which is characteristic of liquid water clouds. The polarized radiance measured for scattering angles smaller than 130° is typically weak and almost constant (i.e. saturated) for cloud optical thickness larger than 3.0.

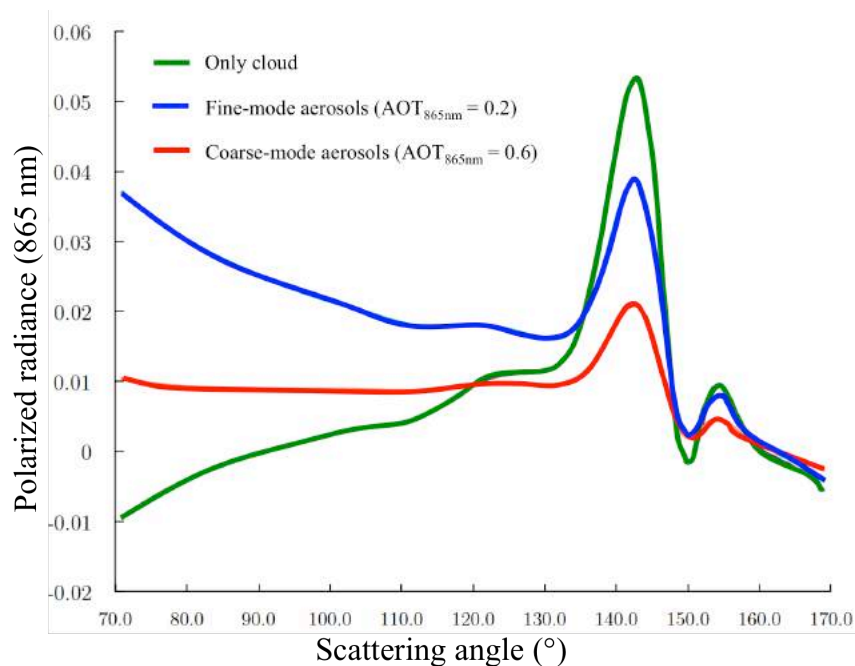


Figure 2.5 – Polarized radiance at 865 nm processed with the SOS code for a liquid water cloud (green), fine-mode aerosols with AOT_{865nm} of 0.2 situated above the cloud (blue) and coarse-mode particles located above cloud with AOT_{865nm} of 0.6 (red). The cloud effective radius (r_{eff}) is considered equal to $10 \mu m$ and the cloud optical thickness (COT) is equal to 10 (Waquet et al., 2013b).

In case of AAC scenes, the magnitude of the cloud-bow decreases and an additional polarization signal appears for scattering angles smaller than 130° . Fine mode particles efficiently polarize light through the process of scattering, which explains the creation of polarization for scattering angles smaller than 130° . In case of non-spherical coarse particles, one can note smaller amount of polarization since those particles less efficiently polarize light. However, the two types of aerosols significantly attenuate the primary bow. The creation of polarization by scattering and the attenuation of the cloud-bow, are the main

physical processes that allow detecting aerosol above clouds from passive polarimetric observations.

Based on these effects, Waquet et al. (2013) have developed a method for retrieving aerosol above cloud properties from the POLDER polarization measurements. The method for retrieving the above-cloud scattering AOT consists of a comparison between polarized radiances measured by POLDER at 670 nm and 865 nm and polarized radiances pre-computed with the SOS code (Deuzé et al., 1989). This is a look-up table (LUT) algorithm where polarized radiances are computed and stored for various load, viewing geometries as well as cloud and aerosol microphysical models. Interpolation processes are considered and a minimization procedure is used to estimate the AOT and aerosol model that best fit the data. Seven aerosol models are considered for the aerosols. They follow a single lognormal particles size distribution. Six models correspond to spherical aerosols (fine-mode particles) with radius from 0.06 to 0.16 μm , for which a complex refractive index of 1.47-0.01i is assumed. The seventh model is bimodal and characteristic of non-spherical aerosols (dust) with a refractive index of 1.47-0.0007i. The properties of aerosols and clouds models are summarized in Table 2.1.

Table 2.1 – Properties of aerosols and clouds used in LUT for the POLDER polarization method. r_g is the granulometric radius, r_{eff} is the effective radius, v_{eff} is the effective variance and σ is the standard deviation.

	Aerosols		Clouds
	Fine mode	Dust	
Vertical distribution	Gaussian layer with a mean altitude of 4 km		Homogeneous layer between 0 and 0.75 km
Size distribution	lognormal distribution with $r_g = 0.06$ to $0.16 \mu\text{m}$ (with a step of $0.02 \mu\text{m}$) and $\sigma = 0.4$	bimodal lognormal distribution with $r_{\text{eff},\text{fine}} = 0.35 \mu\text{m}$ $r_{\text{eff},\text{coarse}} = 2.55 \mu\text{m}$ and $\sigma = 0.4$	Gamma law with $r_{\text{eff}} = 5$ to $26 \mu\text{m}$ (with a step of $1 \mu\text{m}$) and $v_{\text{eff}} = 0.06$
Refractive index	1.47 – 0.01i	1.47 – 0.0007i	$m_r, 670 \text{ nm} = 1.331$ $m_r, 865 \text{ nm} = 1.330$

In the search for the best fitting aerosol model, the operational algorithm follows the strategy described by Waquet et al. (2013). After a first step, the algorithm produces an approximation of the AOT at 865 nm. As a function of this AOT value, a decision tree is applied: if the AOT is larger than 0.1 then the algorithm will search the best fitting model within all the seven models without any angular constraint for the selection of the POLDER

data (scattering angle ranging from 0° to 180°). Next, if the mineral dust model fails to reproduce the data or if the AOT retrieved in the first step is smaller than 0.1, then only fine-mode models are considered in the retrieval scheme and the viewing geometries are restricted to side or forward viewing geometries ($< 130^\circ$). The AOT threshold of 0.1 at 865 nm is empirical and was introduced since the retrieval of the aerosol type (dust or fine mode particles) becomes difficult for small AOT.

Collocated cloud properties retrieved from MODIS at high resolution ($1 \times 1 \text{ km}^2$ at nadir) are used to characterize and to select the cloudy scenes within a POLDER pixel ($6 \text{ km} \times 6 \text{ km}$ at nadir). We only consider fully covered cloudy pixels associated with optically thick liquid water clouds: the cloud optical thickness retrieved by MODIS has to be larger than three and a cloud phase algorithm is applied to select liquid water clouds (Riedi et al., 2010). Moreover, Waquet et al. (2013) have introduced a mask to eliminate cirrus above liquid clouds that makes use of the MODIS Brightness Temperature Difference (BTD) between 8.5 and 11 μm wavelength bands as well as MODIS and POLDER cloud top pressure estimates. Lastly, the AOT retrievals at the $6 \text{ km} \times 6 \text{ km}$ spatial resolution are aggregated to $18 \text{ km} \times 18 \text{ km}$ spatial grid. The retrieved solution is kept if the number of $6 \text{ km} \times 6 \text{ km}$ pixels is larger than 5 and if the standard deviation computed for the mean AOT is smaller than 0.1. This latter procedure allows removing edges of clouds. More information on the operational algorithm can be found in Waquet et al. (2013). In our study, we use the version 3.00 of the official output product PARASOL_PM02-L2 for AAC scenes available at ICARE website (<http://www.icare.univ-lille1.fr/parasol/products/>).

2.1.4.2 POLDER absorption method

Polarized radiances are primarily generated by the single scattering process and, for this reason, the so-called polarization method mainly provides the scattering AOT. The method is also sensitive to the particle size (via the retrieval of the Angström exponent between 670 and 865 nm). In a pristine atmosphere, the radiance scattered by water droplets is weakly dependent on the wavelength from the UV to the near infrared. When biomass-burning aerosols are located above clouds, they strongly attenuate the total radiances reflected by the cloud layer, modifying the apparent color of the cloud (De Graaf et al., 2012). This is the so-called “color effect” that can be used to detect absorbing aerosol above clouds using for instance MODIS or OMI total radiance measurements. This effect is primarily related to the absorbing properties of the aerosols and can’t be used, for instance, to detect purely scattering aerosols transported above clouds. The POLDER instrument measures both the total radiances and the polarized radiances, which allowed the development of a complementary method used to determine the absorbing properties of the aerosols situated above clouds.

The POLDER absorption method was developed by Peers et al. (2015). The input data used in this retrieval algorithm are the POLDER total radiances at 490 nm and 865 nm (at $6 \text{ km} \times 6 \text{ km}$ spatial resolution), and the previously calculated scattering AOT above cloud and

the associated aerosol model. Figure 2.6 presents the ratio of two total radiances modeled at 490 and at 865 nm in function of the total radiance at 865 nm. These radiances were simulated for different level of aerosol absorption and different values of cloud optical thickness. For this example, the scattering AOT is fixed at 0.18 and the absorption AOT varies with the imaginary part of the refractive index k . The figure shows that the radiance at 865 nm increases with the COT increasing whereas the ratio of the two radiances changes with the absorbing AOT. These two effects can be used to derive the aerosol absorption and the corrected cloud optical thickness, once the scattering AOT and the aerosol size are known.

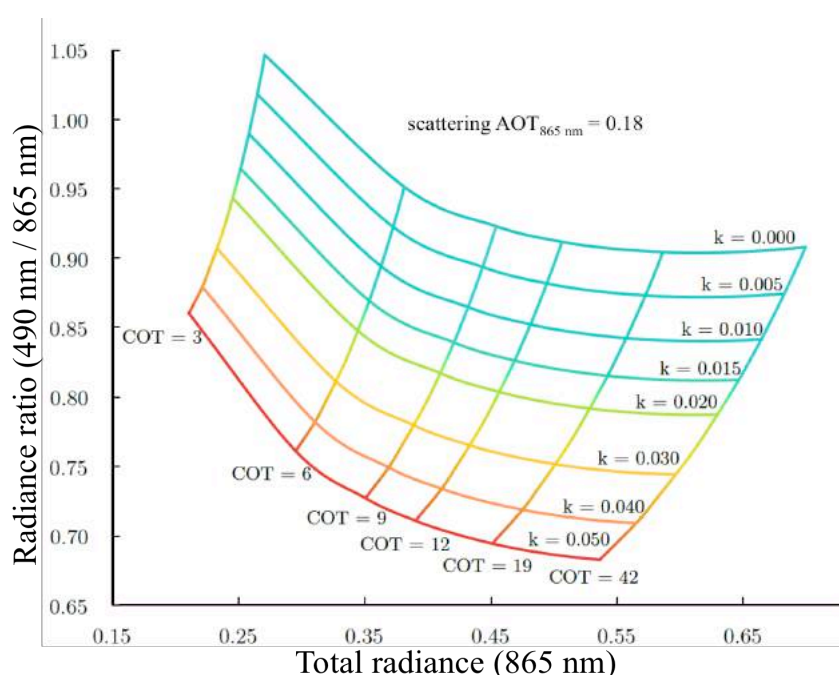


Figure 2.6 – Ratio of 490 nm and 865 nm radiances in function of total radiance at 865 nm. The aerosol layer considered has a fix scattering AOT equal to 0.18 at 865 nm. The aerosol effective radius is $0.1 \mu\text{m}$ and the cloud droplet effective radius is $10 \mu\text{m}$. The simulation was made for different cloud optical thicknesses (COT) and multiple imaginary part of the refractive index (k) for absorbing aerosols (Source: Peers et al., 2015).

The POLDER absorption method uses a LUT algorithm. The surface wind speed is also included in the simulation of the total radiance since it may slightly impact the retrieval of the cloud optical thickness. The wind speed is estimated based on the ECMWF re-analysis data. The aerosol models considered in the LUT are the same models considered earlier in Table 2.1, but with additional information on the imaginary part of the refractive index (k). Because of the weak wavelength dependency for fine-mode particles, k is assumed to be equal at 490 nm and 865 nm and varies from 0.00 to 0.05. On the other hand, for dust particles k is set at a value of 0.0007 at 865 nm and varies between 0.00 and 0.004 at 490 nm, due to iron

oxide absorption in the blue and UV bands. The clouds droplet effective radius is set to 10.0 μm and the cloud effective variance is equal to 0.06. After all these assumptions, the $\text{AOT}_{865\text{nm}}$ and the $\text{SSA}_{865\text{nm}}$ can be underestimated by 0.055 in case of extreme events of aerosols above clouds (i.e. AOT of 0.6 and SSA of 0.77). Otherwise, the bias of the SSA is under 0.03, and the AOT is biased around 20 % for values lower than 0.2 in AOT. The aerosol and cloud information used to model the absorption LUT are presented in Table 2.2. More information on the description of the algorithm, results and retrieval accuracy can be found in Peers et al., (2015).

Table 2.2 – Properties of aerosols and clouds used in LUT for the POLDER absorption method.

	Aerosols		Clouds
	Fine mode	Dust	
Vertical distribution	Homogeneous layer between 2 and 3 km		Homogeneous layer between 0 and 0.75 km
Size distribution	lognormal distribution with $r_g = 0.06$ to $0.16 \mu\text{m}$ (with a step of $0.02 \mu\text{m}$) and $v_{\text{eff}} = 0.4$	bimodal lognormal distribution with $r_{\text{eff, fine}} = 0.35 \mu\text{m}$ and $r_{\text{eff, coarse}} = 2.55 \mu\text{m}$ and $v_{\text{eff}} = 0.4$	Gamma law with $r_{\text{eff}} = 10 \mu\text{m}$ and $v_{\text{eff}} = 0.06$
Refractive index	$1.47 - k.i$ with $k = 0.00$ to 0.005 (step of 0.0025)	$1.47 - k.i$ with $k_{865 \text{ nm}} = 0.0007$ and $k_{490 \text{ nm}} = 0.00$ to 0.004 (step of 0.0005)	$m_{r, 490 \text{ nm}} = 1.338$ $m_{r, 865 \text{ nm}} = 1.330$

2.2 Active observations

2.2.1 Lidar equation

Active remote sensing instruments measure the signal backscattered by the particles present in the atmosphere. Lidar systems emit an electromagnetic wave in the atmosphere. The energy associated with this wave is scattered by a parcel of air located at a distance z and a receiver (e.g. telescope) measures the energy of the backscattered wave.

The lidar typically measures the attenuated lidar signal $P(z)$ (W) as a function of the altitude z . In case of aerosols and molecules, without gaseous absorption, this quantity can be written as:

$$P(z) = \frac{KP_0}{z^2} (\beta_{mol}(z) + \beta_{aer}(z)) \exp \left[-2 \int_{z_{min}}^z (\sigma_{mol}(z') + \eta(z')\sigma_{aer}(z')) dz' \right] \quad (\text{Eq. 2.27})$$

The suffixes _{aer} and _{mol} denote parameters related to aerosols and molecules, respectively. The parameters β and σ are the backscatter ($\text{km}^{-1} \cdot \text{sr}^{-1}$) and extinction (km^{-1}) coefficients, respectively. K is an instrumental constant. P_0 is the power emitted by the laser (W). The variable z is the distance between the lidar and the target in meters. $\eta(z)$ accounts for the multiple scattering processes occurring through the aerosol layer. The wavelength dependence of the different quantities involved in this equation has been omitted for sake of clarity.

We also introduce the molecular two-way transmittance derived from the lidar equation:

$$T_{mol}^2(z_{min}, z) = \exp \left[-2 \int_{z_{min}}^z \sigma_{mol}(z') dz' \right] \quad (\text{Eq. 2.28})$$

The backscatter molecular profile is proportional to the extinction profile:

$$S_{mol} = \frac{\sigma_{mol}}{\beta_{mol}} = \frac{8\pi}{3} \quad (\text{Eq. 2.29})$$

where S_{mol} is the molecular extinction-to-backscatter ratio (sr) (or lidar ratio).

The aerosol two-way transmittance is defines as :

$$T_{aer}^2(z_{min}, z) = \exp[-2\eta(z)\tau_{aer}(z_{min}, z)] \quad (\text{Eq. 2.30})$$

where $\eta(z)$ is the multiple scattering factor. This coefficient can't be neglected in case of optically dense medium such as a cloud. This quantity is however generally assumed to be equal to 1 in case of aerosol layers. $\tau_{aer}(z_{min}, z)$ describes the aerosol optical thickness computed between z_{min} and z , where z_{min} could be the basis of the aerosols layer and, z , its top altitude :

$$\tau_{aer}(z_{min}, z) = \int_{z_{min}}^z \sigma_{aer}(z') dz' \quad (\text{Eq. 2.31})$$

We also introduce:

$$S_c = \frac{\sigma_{aer}}{\beta_{aer}} \quad (\text{Eq. 2.32})$$

where S_c is the particulate lidar ratio (sr), assumed to be constant within the identified aerosol layer.

2.2.2 CALIOP / CALIPSO instrument

The CALIOP was launched onboard CALIPSO in June 2006 and is still in the A-Train constellation. The CALIOP is a frequency-doubled Nd:YAG laser, dual-wavelength, dual-polarization, elastic backscatter lidar equipped with a one meter-diameter telescope and a field of view of $135 \mu\text{rad}$ (Winker et al., 2009). The retrievals of the vertical atmospheric profiles are made at high resolution (30 to 60 m), the native horizontal resolution is 333 m and the footprint of each profile in the lower atmosphere is 90 m.

The directed laser beam is linearly polarized at 532 and at 1064 nm, and the instrument measures the attenuated backscattering coefficients at these two wavelengths. Two polarization-sensitive receivers are used at 532 nm, which allows the calculation of the depolarization ratio at 532 nm.

The lidar returned signal is first geolocated and calibrated. The data are then normalized and range-corrected to provide the altitude-resolved profiles of total attenuated backscatter coefficient ($\text{km}^{-1} \text{sr}^{-1}$). These are the level 1 data. These data are then processed with various algorithms to derive the optical and microphysical properties of aerosols and clouds (Vaughan et al., 2009; Winker et al., 2009).

2.2.2.1 CALIOP Operational method

In order to retrieve the attenuated backscatter data and the columnar AOT at 532 nm and 1064 nm, the operational CALIOP algorithm combines the feature and layer detection scheme (Vaughan et al., 2009) with the extinction retrieval algorithm (Young and Vaughan, 2009) that employs assumptions on the extinction-to-backscatter ratio of aerosols. There are several steps involved in the operational data processing: 1) cloud and aerosol layers are detected in the backscattered signal along with their altitudes, 2) the algorithm determines which layers have cloud or aerosol features, 3) the cloud ice-water phase is estimated and the aerosol lidar-ratio is determined, using assumptions on the aerosol models, and finally, 4) the extinction coefficients and AOT are retrieved at 532 and 1064 nm.

Lidar systems have a limited capability to determine the composition and size of aerosols. Hypotheses are then used on the aerosol phase function at 180° and on the aerosol single scattering albedo (SSA) in order to calculate the aerosol lidar ratio.

In the operational algorithm, the aerosol models consist in a mixture of aerosol components characteristic of a region or an air mass. It should be noted that an incorrect assumption for the lidar ratio could be a source of substantial errors in the AOT retrieved with this method. The values of CALIOP lidar ratio used for different types of aerosols is presented in Table 2.3 (Winker et al., 2009):

Table 2.3 – CALIOP aerosol types and associated lidar ratios S_c .

Lidar ratio S_c (sr)	Dust	Smoke	Clean continental	Polluted continental	Clean marine	Polluted dust
532 nm	40	70	35	70	20	65
1064 nm	30	40	30	30	45	30

For our study we use the level 2 version 3.01 of the inversion products, officially named CAL_LID_L2_05kmALay (ALay) and CAL_LID_L2_05kmCLay (CLay) (that can be found at <http://www.icare.univ-lille1.fr/calipso/products/>), which provide respectively the aerosol and cloud layer parameters at a nominal horizontal resolution of 5 km. From these products we used the AOTs retrieved at 532 nm and 1064 nm, the aerosol base and top altitudes, the cloud top altitude, the ice-water cloud phase and the feature type. We also use CALIOP level 1 dataset, labeled CAL_LID_L1-ValStage1 (link above) that provides the attenuated backscatter coefficient calculated at a vertical resolution of 30 m from -0.5 to 8.2 km altitude and at a horizontal resolution of 333 m (Winker et al., 2007).

2.2.2.2 CALIOP Depolarization Ratio Method

For retrieving the optical thickness of a thin high layer (aerosols or clouds) above a lower and optically thick water cloud layer, Hu et al. (2007a) and Chand et al. (2008) describe the depolarization ratio method applied to CALIOP measurements. An opaque cloud with a minimum optical depth of three will attenuate the lidar beam completely. For optically thick clouds, we estimate the optical thickness of the above thin aerosol or cloud layer by treating the opaque cloud as a target and by using the Beer-Lambert law to estimate the direct transmission of light above this cloud layer. We will refer to this product hereafter as DRM_{Hu} .

The physical properties used in this method are the cloud attenuated backscatter coefficient (γ'_{water}) integrated from the base to the top of the cloud layer at 532 nm and the integrated attenuated depolarization ratio (δ') at 532 nm. When Rayleigh scattering contribution has been corrected for, the definition of γ'_{water} is given by the following equation:

$$\gamma'_{\text{water}} = \int_{z_{\text{top}}}^{z_{\text{base}}} \beta'(z) dz \quad (\text{Eq. 2.33})$$

where β' is the total attenuated backscatter coefficient ($\text{km}^{-1} \text{sr}^{-1}$).

In situations where the cloud is optically thick and there are no aerosol above the cloud, the lidar equation simplifies to the following definition, expressed as a function of the lidar ratio (S_c) and layer effective multiple scattering factor (η_c) (Platt, 1979):

$$\gamma'_{\text{water,calc}} = \int_{z_{\text{top}}}^{z_{\text{base}}} \beta'(z) dz = (2\eta_c S_c)^{-1} \quad (\text{Eq. 2.34})$$

S_c is narrowly constrained to about 19 sr at a wavelength of 532 nm. This value is typically used for liquid water clouds with droplets smaller than about 50 μm (O'Connor et al., 2004; Pinnick et al., 1983). η_c , which takes values between 0 and 1, is strongly related to the cloud depolarization ratio δ' (defined as the ratio of the parallel and perpendicular polarization signals), since multiple scattering processes tend to depolarize light. An approximate relation was derived from Monte Carlo simulations (Hu et al., 2006):

$$\eta_c = \left(\frac{1 - \delta'}{1 + \delta'} \right)^2 \quad (\text{Eq. 2.35})$$

After γ'_{water} is corrected for molecular and gaseous attenuation, the ratio between γ'_{water} and $\gamma'_{\text{water,calc}}$ should be equal to 1 in the absence of higher aerosol or cloud layer, and with an accurate lidar calibration. Instead, in case of an overlying aerosol or cloud layer, this ratio can be written as:

$$\frac{\gamma'_{\text{water}}}{\gamma'_{\text{water,calc}}} = T^2 = \exp(-2\tau_{\text{top,DR}}) \quad (\text{Eq. 2.36})$$

where T^2 is the transmission of light after a two-way propagation between the sensor and the targeted cloud, and $\tau_{\text{top,DR}}$ is the higher layer's optical thickness. It follows from Eq. 2.36 that the optical depth ($\tau_{\text{top,DR}}$) is given by:

$$\tau_{\text{top,DR}} = \frac{-1}{2} \ln(2S_c \gamma'_{\text{water}} \eta_c) \quad (\text{Eq. 2.37})$$

DRM_{Hu} differs from the operational method by the fact that it does not rely on assumptions related to aerosol microphysical properties (aerosol phase function and SSA) and does not require accurate layer detection for the overlying aerosol layer in order to estimate the AOT integrated over the atmospheric column. The main uncertainties of the DRM_{Hu} are linked to the calibration of the lidar, which impact the estimate of the parameters in Eq. 2.37.

2.2.2.3 The re-calibrated version of DRM: the SODA algorithm

Providing a robust, self calibrated method, working at global scale, and for the whole CALIPSO dataset is not trivial. A re-calibrated version of the DRM method was introduced and evaluated during this study. We describe here below the modifications and improvements applied to the DRM method, which have permitted to obtain an efficient operational algorithm and to perform a global treatment.

In order to improve the estimate of the AOT with the DR method, the developers of the Synergized Optical Depth of Aerosols and ICE clouds (SODA & ICE, available at the ICARE thematic center), Josset et al. (2010; 2012), modified the original formalism of DRM_{Hu} . The main reason for these modifications is that the relationship between the multiple scattering factor and the depolarization by the cloud shows a systematic deviation from the theory (see Fig. 2 in Hu, 2007). The multiple scattering–depolarization relationship has been confirmed by laboratory experiments (Cao et al., 2009). Even if it has to be modified in presence of sub-micrometer or non-spherical particles, the origin of the discrepancy between theory and observation points towards an instrumental issue. The long transient response of the receiver has been proposed as an explanation and a correction was also proposed (Hu et al., 2007b). There are, however other issues related to the calibration of the polarization channel that could explain the discrepancy. The low gain/ high gain merging scheme and the day/night calibration transfer are a significant source of uncertainty. Previous research (Sassen and Zhu, 2009) found a bias in the linear depolarization of cirrus clouds of around 30%.

In order to overcome these difficulties and improve the accuracy of the method, SODA takes advantage of the high number of CALIOP observations of liquid water clouds in the absence of AAC. Practically, the SODA algorithm introduces global scale correction factors in the multiple scattering coefficient to depolarization relationship and a recalibrated value of the liquid water cloud lidar ratio as a function of latitudes. These two corrections come from the fact that, when the liquid water clouds are optically dense and in absence of AAC, the lidar equation can be reduced to Eq. 2.34. Over the ocean, the lidar ratio of most liquid water clouds is relatively constant (Hu et al., 2006) and the multiple scattering coefficient can be measured directly if the lidar is well calibrated. This correction follows the original intent of DRM_{Hu} (Hu et al., 2007a), which has always been to be a self calibrated method, unaffected by instrumental or geophysical uncertainties (see Eq. (4) of Hu et al. (2007a) and related discussion). However, because the discrepancy between theory and observations is due to an instrumental artifact linked to the receiver electronics, SODA introduces a clearer separation between the parallel and perpendicular channel than in DRM_{Hu} (Hu et al., 2007b). DRM_{Hu} relates the total backscatter coefficient to the ratio of perpendicular and parallel backscatter coefficient while SODA links the parallel backscatter coefficient to this ratio. This approach is supported by the theory of light propagation in dense medium where the contribution of multiple scattering to the perpendicular and parallel channel is identical (Xu and Alfano, 2005) and by the analysis of CALIOP data.

A preliminary and mandatory step of the calibration procedure is to select optically opaque liquid water clouds with no AAC. The calibration modules of SODA use the following criteria. Note that there is some level of redundancy in order to increase data quality selection.

a) Criteria of optical density:

- the top and bottom of the cloud is given by the 333 m CALIPSO cloud product. This ensures a minimum level of signal strength and the presence of a transparent atmosphere above it. Note that SODA corrects the molecular attenuation above the cloud, but does not contain an explicit correction of it within the cloud because of the high scattering ratio of liquid water clouds. Nonetheless, the molecular contribution is statistically taken into account by the calibration procedure.
- the maximum of the lidar signal is above the base of the cloud. This ensures an adequate level of attenuation of the surface return.
- the ocean surface integrated attenuated backscatter is below a detectability threshold of $7.5 \times 10^{-6} \text{ sr}^{-1}$ for nighttime data and $1 \times 10^{-3} \text{ sr}^{-1}$ for daytime data. This corresponds to a cloud optical thickness of around 2 during daytime and 4-5 during nighttime, which is when this filter is the most useful. The intent of this threshold is the same as the previous criteria. More specifically, the goal is to use a threshold such that half the shots are below the noise sensitivity of the instrument.

b) Criteria of cloud in liquid phase

- the temperature at the top of the cloud is higher than 0°C . The isotherm is defined by the GMAO (Global Modeling and Assimilation Office) temperature when interpolated on the CALIPSO vertical grid.
- the total cloud liquid water contained in a vertical column of atmosphere retrieved from collocated pixels of AMSR-E/ AMSR2 is larger than 0 mm.

c) Criteria of clear air above the cloud

- the total 532 nm integrated attenuated backscatter coefficient from 20 km of altitude to the top of the cloud is below the following threshold:

$$\int_{z_{\text{top}}}^{20\text{km}} \beta'(z) dz < \frac{1 - \exp(-2\tau_{\text{air,mol}})}{2 \frac{8\pi}{3} 1.5} \quad (\text{Eq. 2.38})$$

where $\tau_{\text{air,mol}}$ is the optical depth due to air Rayleigh scattering and ozone absorption. The factor 1.5 allows reducing the occurrences of false positives due to noise. It also allows to simplify the formalism as the King factor (Bates, 1984; King, 1923) can be neglected with no

expected impact on the results. As this filter introduces more aerosol contamination during daytime (similar to Josset et al. (2010), Fig. 4), it could be desirable to consider the shot-to-shot CALIOP cloud mask for future version of the algorithm as SODA already uses this information for the scene classification flag.

As previously mentioned, even if the multiple scattering–depolarization relationship has been confirmed by laboratory experiments (Cao et al., 2009), the relationship between the multiple scattering factor and the depolarization by the cloud shows a systematic deviation from the theory. It has to be corrected, as it would introduce a bias in aerosol optical depth with the particularly undesirable trait to correlate with cloud microphysical properties. As a first step, SODA calibrates the multiple scattering to depolarization relationship for nighttime data on a monthly basis. The data of interest are based on Eq. 2.34 and can be written as:

$$\eta_{\text{geo}} = \frac{1}{2 \times 19 \times \gamma'_{\text{water,parallel}}} \quad (\text{Eq. 2.39})$$

where $\gamma'_{\text{water,parallel}}$ is the parallel-integrated backscatter coefficient. This equation provides a direct measurement of the multiple scattering coefficient of liquid water clouds (η_{geo}) when their lidar ratio is constant. The constant value of 19 sr used in the SODA algorithm is based on Hu et al. (2006) who found a lidar ratio equal to 19.1 ± 0.21 sr when the 41 droplet size distributions of Miles et al. (2000) are used as inputs of a Mie scattering code.

For all opaque liquid water clouds defined with the above criteria, SODA then compares the direct measurement of the multiple scattering coefficient (η_{geo}) and the theory (η_c) to find the second order polynomial that best fit the data in the least square fit sense. This defines the calibrated multiple scattering coefficient (η_{calibr}):

$$\eta_{\text{calibr}} = \text{fit}[\eta_{\text{geo}}(\eta_c)] = A\eta_c + B\eta_c^2 \quad (\text{Eq. 2.40})$$

This procedure allows us to use a relationship between depolarization and multiple scattering that fits the observation. Using Eq. 2.35 instead of Eq. 2.40 would create an aerosol optical depth bias that would typically range between 0.02 and 0.08. Although this is not always significant, this correction is necessary as the resulting ACAOT bias does correlate with the clouds microphysical properties. This is particularly undesirable as the link between aerosol and cloud microphysical properties is an active topic of research.

As a second step, SODA calculates the apparent lidar ratio $S_{c,\text{lat}}$ of all opaque liquid water clouds as a function of each degree of latitude and for both 532 and 1064 nm. This procedure is done separately for daytime and nighttime data. The latitudinal dependency is aimed at correcting the calibration inaccuracies of CALIOP, which are dependent on latitude (Powell et al., 2010) and possible geophysical variations of cloud microphysical properties between the northern and southern hemisphere.

$$S_{c,lat} = \frac{1}{2 \times \eta_{calibr} \times \gamma'_{water,parallel}} \quad (\text{Eq. 2.41})$$

For the four and a half years of data we considered in this study, the median of $S_{c,lat}$ for the nighttime data is 19.36 sr, which is interestingly close from the theoretical value determined by Hu et al. (2006). For daytime data, $S_{c,lat}$ is systematically higher and with a median of 20.64 sr. The systematic daytime/nighttime difference could be geophysical. However, it is premature to reach such conclusion until all nighttime/daytime differences in the CALIPSO data have been addressed.

Lastly, all these coefficients are finally integrated in the AOT retrieval equation:

$$\tau_{top,DRcalibr} = -\frac{1}{2} \ln(2S_{c,lat} \eta_{calibr} \gamma'_{water,parallel}) \quad (\text{Eq. 2.42})$$

Through this study, we will refer to this product as DRM_{SODA} and can be found at ICARE data center (<http://www.icare.univ-lille1.fr/projects/soda/>).

2.3 ECMWF reanalysis for climate monitoring

In this study, we also used reanalysis meteorological data in order to estimate the main thermodynamic quantities as well as the amount of water vapor and ozone present in the atmosphere. A meteorological reanalysis is a meteorological data assimilation which aims to combine models and historical observational data (such as radio sounding measurements) spanning over an extended period, to better predict the temperature, pressure or wind patterns of the atmosphere.

We used the product ERA-Interim provided by the European Centre for Medium-Range Weather Forecast (ECMWF) model (Berrisford et al., 2011), which provided various profiles, including profiles of temperature (K), specific humidity (g/kg), pressure (hPa), wind (speed and direction), and ozone (atm-cm). The assimilating model is configured for 60 vertical levels divided in pressure units, from the surface up to 0.1 hPa. The horizontal resolution of the products is 0.5 degree and the reanalysis data are provided every 3 or 6 hours (Dee et al., 2011).

These data were collocated with the POLDER observations in space and time, therefore an interpolation processes was used in function of the POLDER time overpass. In our study, the meteorological database was used to describe the meteorological tendencies over the South Atlantic Ocean, and to calculate realistic fluxes and heating rates.

It should be noted that models have difficulties to take into account the effects and properties of aerosols. Therefore, the potential feedback effects of aerosols on the thermodynamic quantities are not necessarily well reflected in reanalysis meteorological data.

Chapter 3

Comparison of active and passive aerosol above clouds measurements

This chapter presents a comparison between the retrieval of optical properties of aerosol above clouds (AAC) from different techniques developed for the A-Train sensors CALIOP/CALIPSO and POLDER/PARASOL. The main objective is to analyze the consistency between the results derived from the active and the passive measurements in order to improve our understanding of the AAC properties. We compare the aerosol optical thickness (AOT) retrieved above optically thick clouds and their Ångström exponent (AE). We perform a regional analysis and a global and multi-annual analysis to provide robust statistics results. The vertical distribution of the aerosol and cloud layer is also considered. The comparison is made along the CALIOP track, which will result in less available data for POLDER. However, we analyze in details the differences observed between the methods and point out the limitations of each technique.

Most of the results presented here after were recently published in the Atmospheric and Measurements Technic (AMT) journal (Deaconu et al., 2017, <https://www.atmos-meas-tech.net/10/3499/2017/>).

3.1 Research strategy

As we have seen in the previous chapter, the active and passive methods designed for the AAC retrievals are entirely independent and employ different assumptions. In order to assess the consistency between these methods, Jethva et al. (2014) already performed an intercomparative analysis of the above clouds AOT retrieved with six of the aforementioned methods (see Chapter 1, Table 1.2). The results were encouraging and, despite the use of

different assumptions and measurements, a close agreement was reported over homogeneous clouds. Similarly to this analysis, we will focus on the comparison between the AAC retrievals performed with the active and passive techniques. However, In comparison with (Jethva et al., 2014), which only present two case studies, we perform a regional analysis as well as a global and multi-year analysis to provide robust statistics results. The vertical distribution of the aerosol and cloud layer is also considered (i.e. aerosol and cloud layers in contact or well separated).

We concentrate on the following methods: (a) the CALIOP operational method, because of the numerous studies in which it was used, (b) the DRM method developed by Hu et al., (2007a), (c) the calibrated version of the DRM method called SODA and (d) the POLDER polarization method. The DRM and POLDER methods were chosen because both are measuring AAC properties above the same type of cloudy scenes (i.e. optically thick and homogeneous liquid water clouds). Moreover, both techniques are sensitive to all types of particles (scattering or absorbing particles, fine or coarse ones), which is not the case of the other technics.

We first analyze six months of data over three distinctive regions characterized by different types of aerosols and clouds. Additionally, for these regions, we select three case studies: a biomass-burning event over the South Atlantic Ocean, a Saharan dust case over the North Atlantic Ocean and a Siberian biomass-burning event over the North Pacific Ocean. Four and a half years of data are studied over the entire globe for distinct situations where aerosol and cloud layers are in contact or vertically separated. Potential biases on the retrieved AOT as a function of cloud properties are also investigated. For different types of scenes, the retrieval of above-cloud AOT from POLDER and from DRM are compared for different underlying cloud properties (droplet effective radius (r_{eff}) and COT retrieved with MODIS).

The next sections present the strategy considered for the AOT inter-comparison and the classification used for the ACC scenes (aerosol and cloud layers in contact or well separated). The results for the regional analysis are presented in section 3.2. Section 3.3 presents the global analysis and the results obtained in function of the type of AAC scenes. Section 3.4 discusses the sensitivity of the methods to the properties of the below cloud layer and the peculiar results obtained for the cases of contact. The intermediate conclusions for this chapter are given in section 3.5.

3.1.1 Collocation

The A-Train satellites pass through close orbits within several minutes, providing coincident observations of POLDER, MODIS and CALIOP instruments. Using the nearest pixel approximation, CALIOP files are used as a space reference for sampling POLDER and MODIS products. CALTRACK is the output dataset and can be found at ICARE data and service center. It contains coincident data from POLDER at $18 \text{ km} \times 18 \text{ km}$ and MODIS, extracted under the CALIOP track at 5 km horizontal resolution (see Figure 3.1). The DRM_{Hu} and DRM_{SODA} optical depth retrievals are processed at the CALIOP native resolution of 333

m and aggregated afterwards at 5 km horizontal resolution. Moreover, for a better consistency of the AOT comparison, the POLDER AOT was extrapolated at 532 nm using the AE retrieved with the POLDER algorithm.

We also limited the cloud top altitude at 5 km because we are interested in low-level clouds. Likewise, we eliminated from our data analysis all situations in which the aerosol top altitude exceeds 10 km. This maximal value should be sufficient, since most of the biomass burning and dust aerosol layers are typically observed between 0.5 and 4.0 km over ocean (Torres et al., 2013).

3.1.2 Distinction between vertical profiles

Additionally, we have employed an approach that is similar to the concept of Costantino and Bréon (2012) to classify the type of AAC scenes. The respective positions of the aerosol and cloud layers are defined using the CALIOP ALay and CLay products. We classify the AAC scenes into five categories: “detached”, “attached”, “across”, “within” and “undetermined”.

The so-called “attached cases” correspond to situations where the aerosol layer touches the top of the beneath cloud layer. For these cases, we assume that the vertical distance of the aerosol bottom altitude from cloud top altitude must be lower than 100 meters, without penetrating the cloud layer for more than 50 meters. Inversely, the “detached cases” correspond to aerosol and cloud layers that are considered well separated, considering a distance higher than 500 m between the aerosol base altitude and the cloud top. Aerosol layers with the base altitude within a distance between 100 and 500 meters above the cloud layer are considered uncertain, as they are not contained within the definition of the above situations, and are excluded from our study.

We also distinguished two other situations for which the aerosol layer top height and/or the aerosol layer bottom height are detected below the cloud top. The “across” category corresponds to cases for which the bottom height of the aerosol layer is located below the cloud top height by more than 50 meters. This is rather similar to “attached” cases excepted that the base height of the aerosol layer can be located deeper into the cloud. The “within” cases are situations for which the aerosols are entirely located within the cloud (see Figure 3.1). In theory, the lidar signal does not much penetrate the cloud layer when the cloud optical thickness is large (>3), and then should not provide reliable information. These situations are therefore considered to be highly uncertain. However, these situations are sometimes associated with valid POLDER and SODA AOT retrievals and we therefore decided to keep this data in our analysis. Note that these two later situations were not initially discussed in the article published in AMT (Deaconu et al., 2017). These additional cases will be only discussed in the section 3.4 of this chapter that focuses on the AAC scenes for which the aerosol and the cloud layers are in contact.

The last category, “undetermined” corresponds to situations for which the respective position of the aerosol or cloud layer is not identified by the CALIOP layer detection algorithm (i.e. missing data), even though POLDER and DRM_{SODA} AAC AOT retrievals are valid. We chose to keep these data in our analysis as they cover the majority of POLDER AAC detected cases with a non-negligible AOT (even if CALIOP classifies them as invalid or noise), as the purpose of the study is to better comprehend the disparities between the methods.

We also distinguish the “two layer situation” (i.e. one aerosol layer and one cloud layer) from the “multiple layer situations” (more than one aerosol layer and/or more than one cloud layer). These latter situations are filtered in our analysis for the sake of simplicity (see Sect. 3.2 and Sect. 3.3).

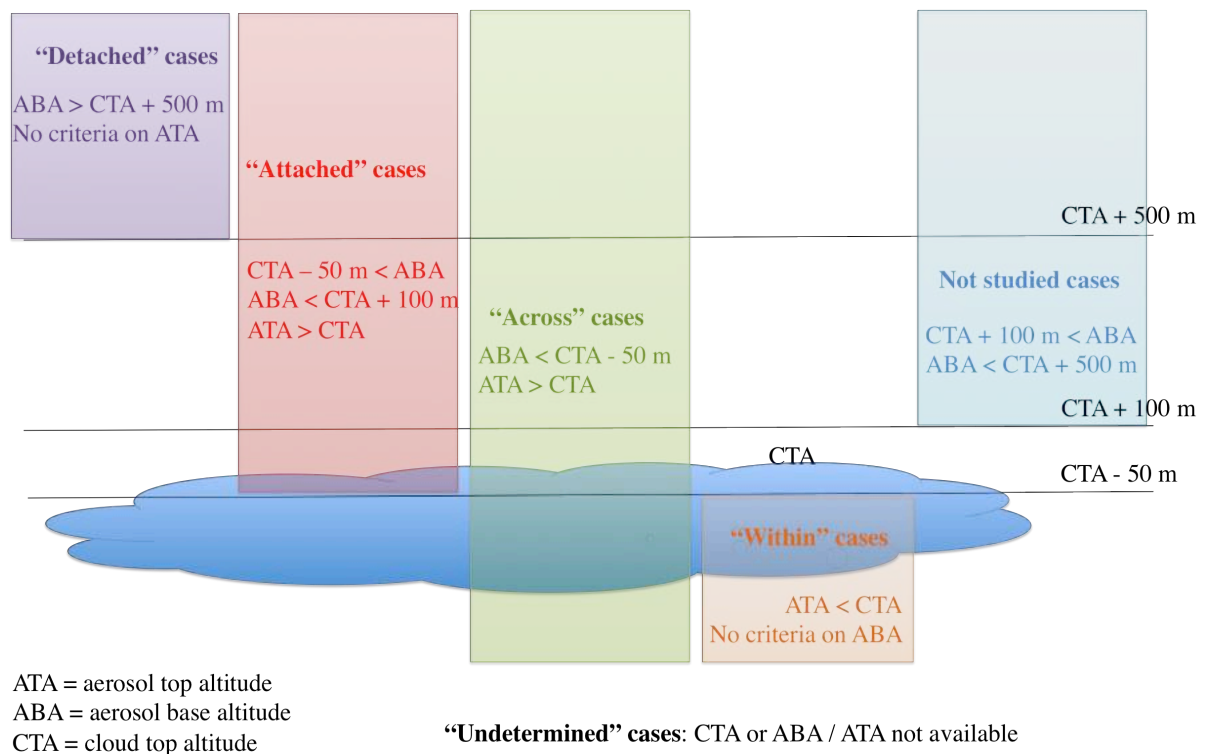


Figure 3.1 – Schematic characterization of the methodology used for data selection in case of different vertical positions of the aerosol and cloud layers.

3.2 Regional analysis and case studies

In the regional analysis and the study cases we used the entire set of data, without differentiating between the vertical distributions of aerosols related to the cloud top altitude. The results presented in this section were acquired from May to October 2008. We selected

three distinctive regions (see Figure 3.2) that are under the influence of various aerosol species and different types of clouds: a) an area that extends from 30° S to 5° N and 12° W to 14° E over the South Atlantic Ocean (SAO), b) an area between 10 to 35° N and 10 to 40° W over the North Atlantic Ocean (NAO) and c) an area located between 35 to 60° N and 140 to 170° E over the North Pacific Ocean (NPO). The south of the African continent is the main contributor to biomass-burning aerosols above clouds, originating from man-made crops fires (Waquet et al., 2013b). These aerosols are highly absorbing (SSA of approximately 0.84 at 865 nm) and associated with high AE values; they mainly contribute to the fine mode. The NAO area is mainly under the influence of dust aerosols originating from the Saharan Desert for the time period of interest. These particles are mainly non-spherical and contribute primary to the coarse mode. They are moderately absorbing at the wavelength of CALIOP (532 nm) and almost non-absorbing at 865 nm (SSA of approximately 0.98) (Balkanski et al., 2007; Dubovik et al., 2002; Peers et al., 2015). The North Pacific Ocean (NPO) is associated with various types of particles: fine mode aerosols with rather scattering properties originating from man-made pollution (Waquet et al., 2013a; Yu et al., 2008), biomass-burning from forest fires (Peers et al., 2015; Zhang et al., 2003) and dust originated from the Asian deserts. Potential mixture of these different species is also possible for this area (Yu et al., 2006).

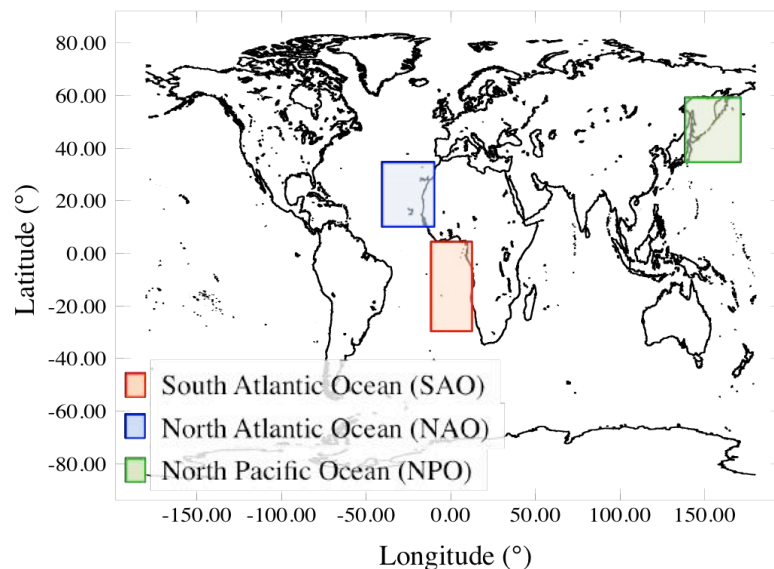


Figure 3.2 – The map presents the latitudinal and longitudinal boundaries of the three regions used in the regional study (Sect. 3): South Atlantic Ocean (SAO) extends from 30° S to 5° N and 12° W to 14° E, North Atlantic Ocean (NAO) is situated between 10 to 35° N and 10 to 40° W and North Pacific Ocean (NPO) is located between 35 to 60° N and 140 to 170° E.

Cloud types and their associated optical and microphysical properties are expected to be different in these three regions (Warren et al. 1988). Low-level stratocumulus clouds typically cover the SAO, with some occurrences of cumulus and altostratus clouds. Cumulus, altostratus clouds and some stratocumulus clouds generally cover the NAO. The cloud cover is generally fractional over this part of the Atlantic Ocean. Stratocumulus clouds also frequently cover the NPO. Higher altostratus and cumulus clouds are also often observed over this area. Cirrus clouds can be frequently found at mid-latitudes and also in the intertropical convergence zone, which includes the NPO and the NAO regions.

We studied six months of data over each region to observe the consistency between different techniques for various types of aerosols. For this part of the study, we mixed the “two-layer” and “multiple layer” situations and we analyzed all the data, disregarding the position of the aerosol and cloud layers. A case study was selected for each region in order to show the spatial variability of the AOT at 532 nm retrieved along the CALIOP transect. The first case is related to a biomass-burning event detected off the coast of Namibia on 13 August 2006. The second event concerns Saharan dust lifted above clouds westwards over the North Atlantic Ocean on 4 August 2008, and the third case concerns Siberian biomass-burning aerosols transported over the Okhotsk Sea, on 3 July 2008.

Figure 3.3 presents the backscatter profile at 532 nm and at 1064 nm ($\text{km}^{-1} \text{sr}^{-1}$) of the lidar CALIOP for the three case studies, which directly provides information on the aerosol and cloud vertical distribution. In addition, the AOT and AE values measured by different techniques are presented along the CALIOP track. Additional results for the study cases comparison are shown in Table 3.1.

Figure 3.4 shows the regional comparison between the AOT and AE retrieved with POLDER and DRM_{SODA} for a period of six months in 2008. The retrieval of aerosol type becomes difficult at small AOT. Therefore the AE comparison was performed only when the values of POLDER AOT at 865nm and DRM_{SODA} AOT at 532 nm were larger than 0.1. The AE mean value is shown with a dashed blue line. The lateral histograms show the data distribution. For the AOT comparison the color scale represents the POLDER $\text{AE}_{670/865}$. In the case of AE comparison, the POLDER $\text{AOT}_{532\text{nm}}$ was also reported with a color scale. The above-mentioned description is also considered in Figure 3.5, which presents the regional comparison between the AOT and AE retrieved with POLDER and $\text{CALIOP}_{\text{OM}}$ for the same period. Additional results for the regional inter-comparison are reported in Table 3.2.

3.2.1 African biomass-burning aerosols

According to the CALIOP vertical profile at 532 nm of the biomass-burning case (Figure 3.3a), the cloud top is at around 1.5 km and the aerosol layer is located between 3 and 5 km. The 1064 nm backscatter profile (Figure 3.3b) exhibits an aerosol layer with a larger vertical extent, showing up more potential contact area with the underlying cloud. We observe a thin cirrus cloud between 10° and 12° S that was not filtered, probably since the cirrus is optically too thin (Figure 3.3c and Figure 3.3d).

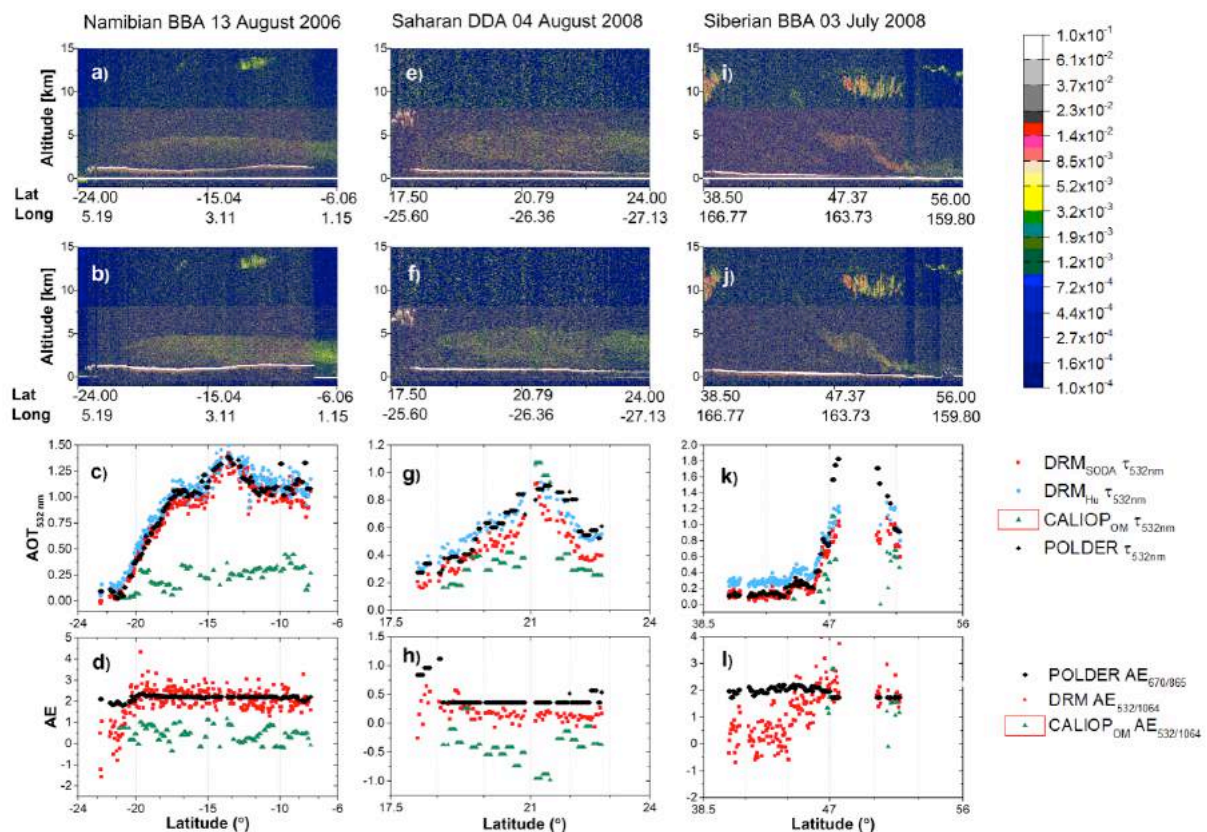


Figure 3.3 – The first row of the panel shows the lidar CALIOP attenuated backscatter coefficients at 532 nm ($\text{km}^{-1} \text{sr}^{-1}$) and the second row presents the CALIOP attenuated backscatter coefficients at 1064 nm for three case studies: African biomass-burning (BBA) aerosols above clouds on 13 August 2006 (a, b, c, d), Saharan dust (DDA) on 4 August 2008 (e, f, g, h) and Siberian biomass-burning aerosols over the Okhotsk Sea on 3 July 2008 (i, j, k, l). For these cases, the above-cloud AOT at 532 nm and the Ångström exponent (AE) as a function of latitude, measured with several techniques are displayed.

In general, there is an excellent agreement between POLDER, DRM_{Hu} and DRM_{SODA} AOT retrievals with a square correlation $R^2 = 0.93$ (see Table 3.1). High values of AOT are retrieved by the different methods, with AOT values as large as 1.5. The retrieved POLDER $\text{AE}_{670/865}$ is larger than 1.8 (Figure 3.3d), which is characteristic for fine mode particles (Dubovik et al., 2002). The DRM_{SODA} $\text{AE}_{532/1064}$ is consistent with the POLDER AE, with values higher than 1.5. AOT values retrieved by $\text{CALIOP}_{\text{OM}}$ are much lower than the ones retrieved by the three other techniques. The maximal AOT retrieved by $\text{CALIOP}_{\text{OM}}$ at 532 nm is 0.5. A possible explanation for this potential low bias was proposed by Jethva et al. (2014): in case of optically thick aerosol layer, the sensitivity of the backscattered signal to the altitude of the base of the aerosol layer would be reduced or lost, being strongly attenuated by the two-way transmission term. As a result, the operational algorithm may overestimate the aerosol base altitude and so underestimate the geometrical thickness of the aerosol layer and

consequently the AOT. The selection of an inappropriate aerosol model (i.e. aerosol lidar ratio S_a for biomass burning, varies between 70 ± 28 at 532 nm and 40 ± 24 sr at 1064 nm (Cattrall et al., 2005; Omar et al., 2005)) or the significant biases found in the V3.01 CALIOP 1064 nm calibration, might also contribute to the underestimation of the AOT for this case study. The CALIOP_{OM} mean $AE_{532/1064}$ seems quite low for fine mode particles (AE values are lower than 1). The selection of an inappropriate aerosol model might also contribute to the underestimation of the AOT for this case study.

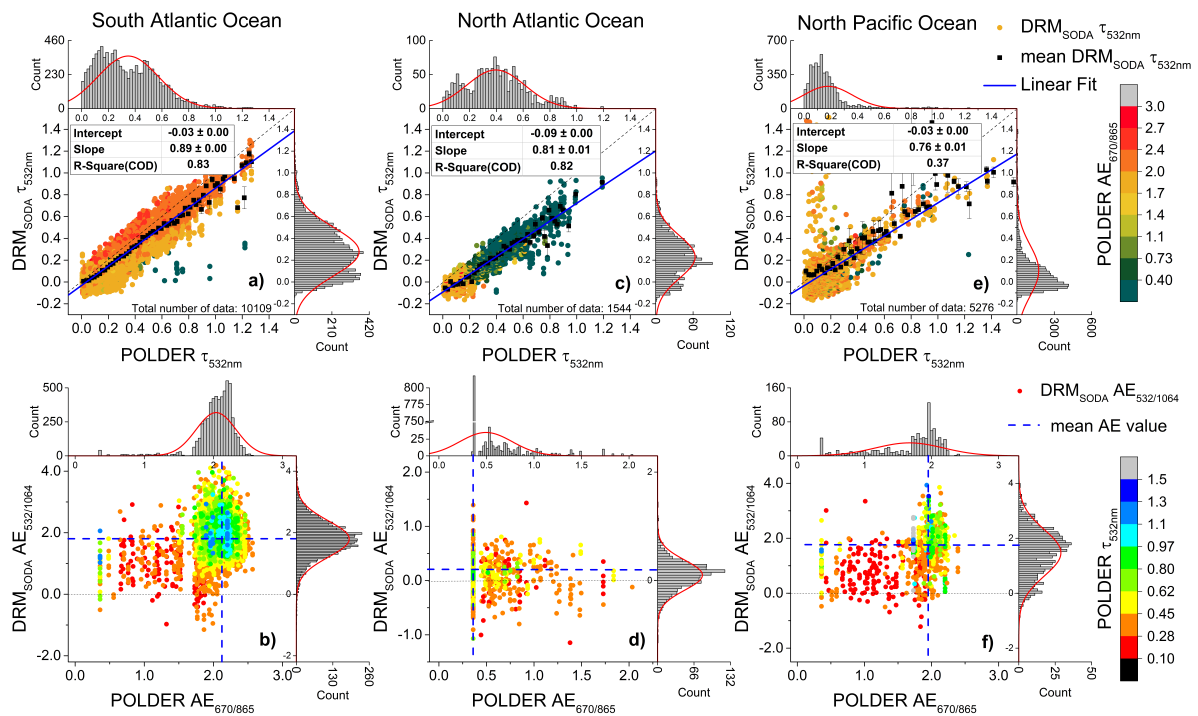


Figure 3.4 – The first row of the panel shows the comparison of AOT at 532 nm retrieved from DRM_{SODA} and POLDER methods, with the corresponding POLDER AE color scale, computed between 670 and 865 nm. The second row presents the Ångström exponent comparison for AOTs larger than 0.1, retrieved from DRM_{SODA} and POLDER methods, with the corresponding POLDER AOT at 532 nm color scale. The measurements were made over a period of six months (May to October 2008) and over three distinctive regions: South Atlantic Ocean - between 30° S to 5° N and 12° W to 14° E (a and b), North Atlantic Ocean - between 10 to 35° N and 10 to 40° W (c and d) and North Pacific Ocean - between 35 to 60° N and 140 to 170° E (e and f). The histograms present the data distribution. The error bars in figures (a), (c) and (e) represent the standard error of the mean (SEM).

Regional analysis shows that South Atlantic region is mostly characterized by biomass-burning aerosols with large AOT and AE (Figure 3.4a and Figure 3.4b). On average, the cloud top height is located below 1.5 km, while the aerosol layers are frequently located between 2.5 and 4 km (see Table 3.3). The AOT_{532nm} measured by DRM_{SODA} and POLDER may reach values as large as 1.30 (Figure 3.4a), with 80 % of the retrieved AOTs ranging between 0.05 and 0.8. This AOT inter-comparison shows close correlation between DRM_{SODA} and POLDER ($R^2 = 0.83$). The mean value of POLDER $AE_{670/865}$ is 2.05, whereas the mean DRM_{SODA} $AE_{532/1064}$ is 1.79 (Table 3.5) (both typical for BBA). DRM_{Hu} and DRM_{SODA} give rather same results. From the linear regressions performed (see Table 3.2) we can observe that the offset is always positive for DRM_{Hu} and systematically larger than the absolute value for DRM_{SODA} , when compared to POLDER method. The AOT estimated by POLDER is constantly between DRM_{Hu} and DRM_{SODA} .

We do not find a good correlation between the $CALIOP_{OM}$ and POLDER AOT and AE retrievals. The $CALIOP_{OM}$ mean AOT_{532nm} is 0.12 and the mean $AE_{532/1064}$ is 0.97. Comparing with POLDER and DRM_{SODA} , $CALIOP_{OM}$ is underestimating the ACAOT by a factor of 2.92.

Table 3.1 – Linear regressions of AOT calculated between different methods for three case studies: African biomass-burning aerosols (BBA), Saharan desert dust aerosols (DDA) and Siberian biomass-burning aerosols. R^2 represents the coefficient of determination (COD) between the two sets of data.

Linear regressions		African BBA (13.08.2006)	Saharan DDA (04.08.2008)	Siberian BBA (03.07.2008)
DRM_{SODA} vs. POLDER	Slope	0.89±0.01	0.74±0.04	0.56±0.01
	Intercept	0.04±0.01	0.01±0.02	0.07±0.009
	R^2 (COD)	0.93	0.79	0.90
DRM_{Hu} vs. POLDER	Slope	0.91±0.01	0.74±0.03	0.60±0.01
	Intercept	0.11±0.01	0.15±0.02	0.23±0.009
	R^2 (COD)	0.93	0.82	0.89
$CALIOP_{OM}$ vs. POLDER	Slope	0.19±0.01	0.86±0.11	0.47±0.08
	Intercept	0.05±0.01	-0.16±0.07	-0.04±0.08
	R^2 (COD)	0.35	0.41	0.45

3.2.2 Saharan desert dust aerosols

For the mineral dust case (Figure 3.3e), the cloud top altitude is located at approximately 1 km altitude whereas the aerosol layer is located between 2 and 5 km for latitudes between 18° and 23° N. Figure 3.3g shows that the POLDER, DRM_{SODA} and DRM_{Hu} AOT_{532nm} increase up to 0.92, following the same gradient. The correlation coefficients between POLDER parameters and DRM_{Hu} and DRM_{SODA} parameters are close (Table 3.1).

Table 3.2 – Linear regressions of AOT calculated between different methods for data acquired over six months (May to October 2008), over three different regions: South Atlantic Ocean (SAO), North Atlantic Ocean (NAO) and North Pacific Ocean (NPO).

Linear regressions		SAO	NAO	NPO
DRM _{SODA} vs. POLDER	Slope	0.89±0.004	0.81±0.009	0.76±0.01
	Intercept	-0.03±0.001	-0.09±0.004	-0.03±0.003
	R ² (COD)	0.83	0.82	0.37
DRM _{Hu} vs. POLDER	Slope	0.90±0.004	0.86±0.01	0.76±0.01
	Intercept	0.05±0.001	0.04±0.004	0.13±0.003
	R ² (COD)	0.82	0.82	0.44
CALIOP _{OM} vs. POLDER	Slope	0.34±0.004	0.52±0.02	0.28±0.02
	Intercept	-0.04±0.002	-0.01±0.01	0.01±0.01
	R ² (COD)	0.43	0.42	0.24
CALIOP _{OM} vs. DRM _{SODA}	Slope	0.34±0.002	0.62±0.01	0.35±0.01
	Intercept	-0.01±0.002	0.04±0.006	0.01±0.007
	R ² (COD)	0.42	0.48	0.28

The majority of POLDER AE_{670/865} and DRM_{SODA} AE_{532/1064} are associated with values lower than 0.4 (Figure 3.3h), which indicates that coarse mode particles are predominant (Dubovik et al., 2002). Except for few retrievals associated with an abrupt change in the AE and AOT measured by CALIOP_{OM} (around 21° N in latitude), 90 % of the CALIOP_{OM} AOT_{532nm} is lower than 0.45, being once again underestimated with respect to the other estimates. Most of CALIOP_{OM} AE_{532/1064} values are underestimated (i.e. overestimation of the particles size) in comparison with the AE retrieved by the two other algorithms. These low values of AOT and AE may be explained once more by a biased CALIOP calibration at 1064 nm combined with an unfitted model selection (i.e. for desert dust, S_a is equal to 40 ± 20 sr at 532 nm and 55 ± 17 sr at 1064 nm (Cattrall et al., 2005; Omar et al., 2005)).

A regional study shows similar AOT and AE results over the North Atlantic region (Figure 3.4c). On average, the aerosol layers are located between 3 and 4.5 km and the cloud top heights are typically around 1.4 km (see Table 3.3). The values of AOT_{532} retrieved from POLDER and DRM_{SODA} are well correlated ($R^2 = 0.82$), with maximum values of respectively 1.19 and 0.95. Nonetheless, we observe a larger offset between DRM_{SODA} and POLDER AOT_{532nm} for this region (-0.09) compared to the South Atlantic Ocean region (-0.03). The use of only one dust model in the LUT algorithm used for POLDER remains a limitation that might explain this larger offset. The introduction of additional dust models with larger or smaller effective radius values may contribute to improve the AOT retrievals for dust ACC events. Regarding the POLDER $AE_{670/865}$ retrievals, most of the values are lower than 0.4, which is expected for desert dust aerosols (Figure 3.4c and Figure 3.4d). However, for AOT values lower than 0.2, the $AE_{670/865}$ retrieved by POLDER is between 1.4 and 2.2. This is explained by the fact that the selection of the dust model is not permitted in the POLDER algorithm in case of low AOTs. Nonetheless, all three methods are consistent in revealing the predominance of the coarse mode. The mean values for the AE are 0.49 for POLDER, 0.10 for DRM_{SODA} and -0.19 for $CALIOP_{OM}$. The AOT_{532nm} correlation between $CALIOP_{OM}$ and POLDER is low, with $R^2 = 0.42$.

Table 3.3 – Regional analysis using CALIOP measurements over six months (May to October 2008), over South Atlantic Ocean (SAO), North Atlantic Ocean (NAO) and North Pacific Ocean (NPO): mean cloud altitude for altitudes smaller than 5 km; mean aerosol base and top altitudes for altitudes smaller than 10 km.

	SAO	NAO	NPO
Mean cloud top altitude [km]	1.24±0.43	1.35±0.5	1.09±0.84
	Min: 0.30	Min: 0.20	Min: 0.05
	Max: 4.95	Max: 3.25	Max: 5.0
Mean aerosol top altitude [km]	3.83±0.093	4.50±1.03	2.74±1.68
	Min: 0.50	Min: 0.44	Min: 0.47
	Max: 6.73	Max: 6.67	Max: 9.85
Mean aerosol base altitude [km]	2.90±0.97	2.97±1.12	3.48±1.78
	Min: 0.02	Min: 0.02	Min: 0.05
	Max: 5.80	Max: 5.74	Max: 9.31

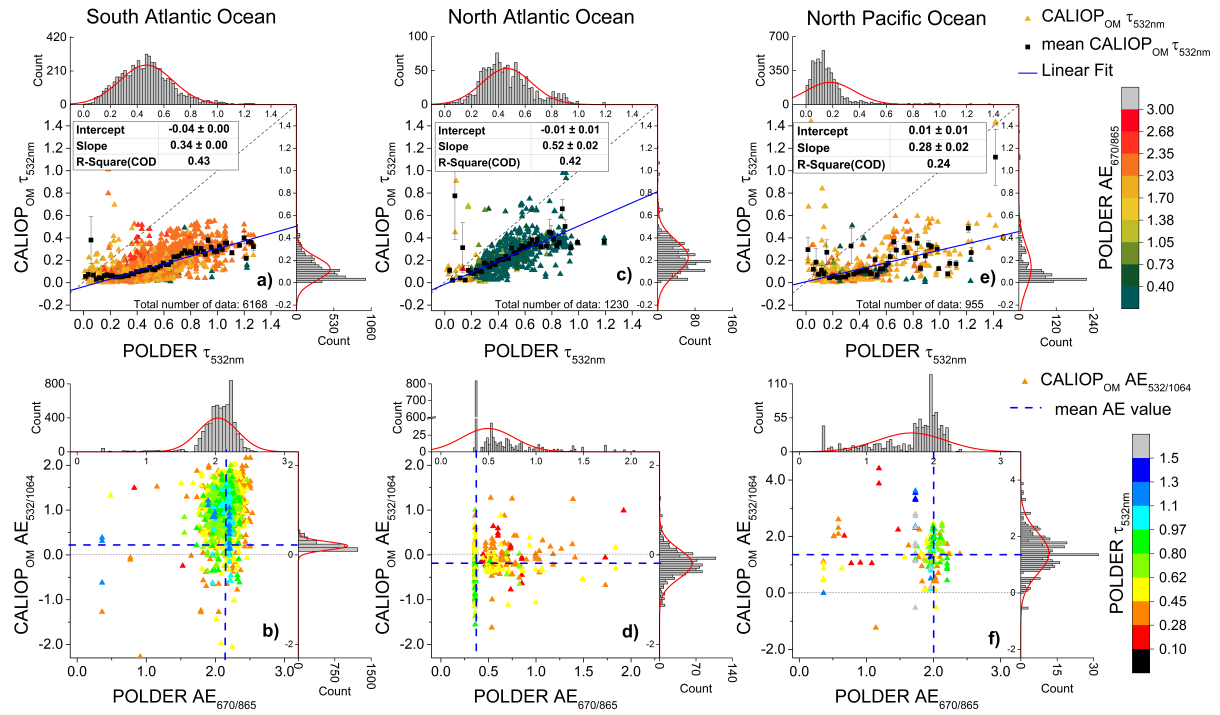


Figure 3.5 – Same as Figure 3.4, retrieved from CALIOP operational method and POLDER method.

Table 3.4 – Calculated mean, minimum value and maximum value of AOT_{532nm} over six months in 2008, for three regions (SAO, NAO, NPO) and for different methods.

AOT_{532nm}		SAO	NAO	NPO
POLDER	Mean	0.35 ± 0.23	0.39 ± 0.21	0.18 ± 0.21
	Min	0.005	0.005	0.005
	Max	1.27	1.19	2.17
DRM _{SODA}	Mean	0.28 ± 0.22	0.23 ± 0.19	0.15 ± 0.38
	Min	-0.13	-0.16	-0.16
	Max	1.30	0.95	3.26
DRM _{Hu}	Mean	0.37 ± 0.23	0.38 ± 0.20	0.32 ± 0.40
	Min	-0.07	-0.06	-0.06
	Max	1.50	1.17	3.68
CALIOP _{OM}	Mean	0.12 ± 0.11	0.23 ± 0.18	0.14 ± 0.23
	Min	0.001	0.005	0.001
	Max	1.88	2.38	2.01

3.2.3 East Asian mixture of aerosols

The CALIOP transect shows that Siberian biomass-burning case is located between 40° and 52° N, the cloud top altitude is constantly around 1 km, and the base of the aerosol layer decreases from 10 km in the south (at 45° N) to around 2 km in the north (at 54° N) (Figure 3.3i). We notice also cirrus clouds at high altitude (around 10 km) between 47° and 51° N, which were efficiently eliminated from the retrievals (Figure 3.3k). The maximum POLDER AOT value is as large as 1.9, while DRM reaches 1.3 in AOT. Nonetheless, Table 3.1 shows that POLDER and DRM methods AOT_{532nm} retrievals are consistent ($R^2 = 0.90$). POLDER AE_{670/865} values are between 1.7 and 2.3, indicating small particles of smoke, while DRM_{SODA} AE_{532/1064} has a large range of values (Figure 3.3l). The number of sampled ACAOT events by CALIOP_{OM} is 4.5 times less than of POLDER and DRM_{SODA}. For these, the CALIOP_{OM} AOTs are underestimated by a factor of 1.5 compared to ones retrieved by the other methods. Also the correlation coefficient with POLDER is 0.45. Table 3.5

Table 3.5 – Mean value of AE over six months in 2008, for three regions (SAO, NAO, NPO) and for different methods after filtering the POLDER AOT_{865nm} > 0.1 and DRM_{SODA} AOT_{532nm} > 0.1, respectively CALIOP_{OM} AOT_{532nm} > 0.1.

		SAO	NAO	NPO
POLDER	Mean AE _{670/865}	2.05±0.27	0.49±0.27	1.67±0.50
	Min	0.36	0.36	0.36
	Max	2.56	2.03	2.39
DRM _{SODA}	Mean AE _{532/1064}	1.79±0.58	0.10±0.27	1.47±0.84
	Min	-1.15	-1.14	-1.21
	Max	4.19	1.43	3.93
CALIOP _{OM}	Mean AE _{532/1064}	0.97±0.51	-0.19±0.32	0.41±0.72
	Min	-2.27	-1.62	-2.63
	Max	3.16	1.27	4.41

On a regional scale, this area is under the influence of various aerosols (BBA, DDA, pollution) and elevated cirrus clouds are frequent. The mean cloud top altitude is around 1 km and the aerosols are between 2.5 km and 4.0 km. As indicated in Table 3.3, the maximum aerosol altitude is 9.85 km, which might suggest cirrus misclassification. In some cases, DRM_{SODA} gives large values of AOT_{532nm} (larger than 1) whereas the POLDER estimates AOT_{532nm} smaller than 0.2. These situations could be explained by a misinterpretation of thin cirrus clouds as aerosols. Otherwise, the POLDER mean AOT_{532nm} and DRM_{SODA} AOT_{532nm}

are in rather close agreement (0.18 and 0.15, respectively, see Table 3.4), but the correlation between them is low ($R^2 = 0.37$, Table 3.2). All methods show a large variability for the retrieved AE, with values that correspond to particle size distributions dominated by coarse or fine modes and mixtures (Table 3.5). As previously mentioned, the algorithm developed for POLDER uses a bimodal aerosol model for dust. However, the possibility of mixing different fine and coarse aerosol models in various proportions is not yet included. This might explain why we found a lower correlation between the POLDER and DRM retrievals for this region. As for above, the CALIOP_{OM} and POLDER AOT_{532nm} are not correlated ($R^2 = 0.24$).

In general, there is a good agreement between POLDER and DRM_{SODA} AOTs, especially when the fine mode or coarse mode dominates the particle size distribution (i.e. BBA and DDA). Overall, DRM_{SODA} and DRM_{Hu} give similar results. However, the AOTs retrieved with DRM_{Hu} are generally larger than those of DRM_{SODA} for all the three regions (i.e. 0.37 compared to 0.28 for SAO, see Table 4). While DRM_{SODA} has a constant negative offset when compared to POLDER, DRM_{Hu} rarely retrieves null AOT values (offsets always larger than 0, see Table 3.2). This is likely to be a consequence of the calibration performed for the DRM_{SODA} method. Also, there is no obvious correlation between the CALIOP_{OM} and POLDER AOT_{532nm} retrievals for all regions.

Table 3.6 – Linear regression calculated between DRM_{SODA} AOT_{532nm} and POLDER AOT_{532nm} for situation when the aerosol layer is attached to the cloud top and when the aerosol layer is well separated from the cloud over three regions (South Atlantic Ocean, North Atlantic Ocean and North Pacific Ocean) and for a period of four and a half years.

	SAO		NAO		NPO	
	Attached	Detached	Attached	Detached	Attached	Detached
Slope	0.60 (±0.02)	0.77 (±0.003)	0.63 (±0.07)	0.59 (±0.01)	0.78 (±0.12)	0.80 (±0.02)
Intercept	0.04 (±0.006)	0.02 (±0.001)	-0.005 (±0.02)	-0.011 (±0.006)	-0.04 (±0.02)	-0.015 (±0.007)
R² (COD)	0.54	0.715	0.39	0.57	0.19	0.435

Finally, in addition to the six months regional study, we also examined the impact of the vertical aerosol-cloud profiles over the three regions using data acquired from May to October between 2006 and 2010. We systematically found higher correlation coefficients between the DRM_{SODA} and POLDER AOTs when the layers were well separated than when they were in contact (see Table 3.6). These results have led us to consider the vertical distribution of aerosols and clouds in the global comparison.

3.3 Global analysis on different types of scenes

3.3.1 Detached, attached, undetermined

Figure 3.6a shows the global comparison between the AOT_{532nm} and AE retrieved with POLDER and DRM_{SODA} for the detached cases. The AE comparison was only performed when the POLDER AOT at 865 nm and DRM_{SODA} AOT at 532 nm are larger than 0.1. The color scales used in Figure 3.6 represent either the POLDER $AE_{670/865}$ for the AOT comparison (Figure 3.6a) or the POLDER AOT_{532nm} for the AE comparison (Figure 3.6d). Considering the large amount of selected data (85.6 % of the two-layer cases) in terms of both spatial and temporal coverage, the comparison shows a good correlation between the two methods ($R^2 = 0.68$). A better agreement between the methods is found when the values of DRM_{SODA} and POLDER AE are larger than 1.8. This is likely due to the fact that the POLDER method is more sensitive to fine mode aerosols, due to polarization measurements, and also because an improved description of the fine mode properties was included in the LUT (i.e. six fine mode aerosol models are used).

Nevertheless, some of the “detached” cases considered in our study, mainly the ones associated with optically thick smoke layers, are likely to be incorrectly classified as “detached” due to the limitations of the CALIOP layer detection products. In the “detached” cases, the choice of 500 m between the cloud top altitude and aerosol base altitude was made as a compromise between keeping enough data to be statistically coherent and choosing a large enough distance to minimize the possible contact between the layers. Nonetheless, we can justify our choice of the altitudes for the “attached” and “detached” cases, by comparing the DRM_{SODA} and POLDER AOTs at 532 nm over a period of 4.5 years (June 2006 to December 2010) for two other situations:

- all valid AAC measurements that include “attached”, “detached” and intermediate cases (aerosol base altitude between 100 and 500 m above the cloud top)
- “detached” cases with the aerosol base altitude higher than 1.5 km above the cloud top.

Figure 3.7a shows that, when taking into account all the situations, the correlation between the two methods decreases to $R^2 = 0.48$. Moreover, the slope also decreases from 0.84 to 0.79, suggesting a larger offset between the data. Contrarily, when the distance increases, as shown in Figure 3.7b, the agreement increases to $R^2 = 0.70$, and the slope increases to 0.86. Thus, we can agree that when the aerosol and cloud layer are better separated, the DRM_{SODA} and POLDER AOT retrievals improve, while contact situations pose difficulties for both methods.

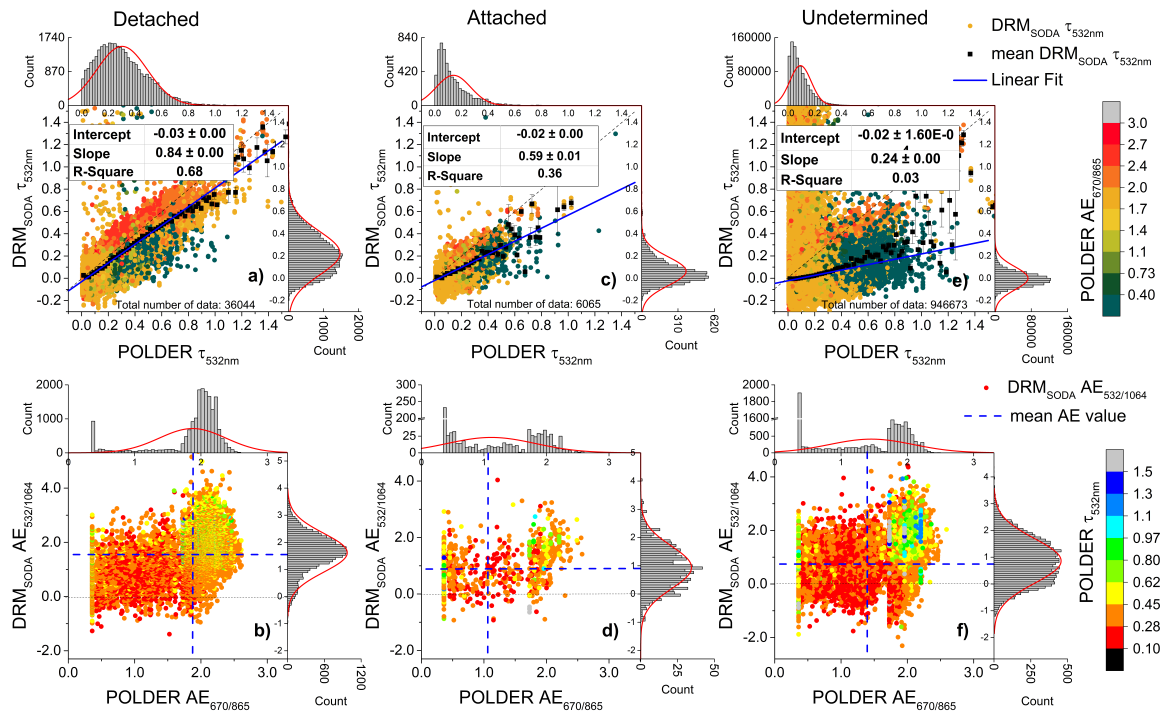


Figure 3.6 – Global comparison over a period of four and a half years (June 2006 to December 2010) for situations with aerosol layer well separated from the cloud top - detached (a and b), for cases where the aerosol layer is in contact with the cloud – attached (c and d) and for “undetermined” situations (e and f). The comparison of AOT at 532 nm retrieved from DRM_{SODA} and POLDER methods is shown in the first row. The color scale represents the corresponding POLDER AE computed between 670 and 865 nm. The second row presents the Ångström exponent for AOTs larger than 0.1, with a POLDER AOT at 532 nm color scale. The histograms present the data distribution. The error bars in figures (a), (c) and (e) represent the standard error of the mean (SEM).

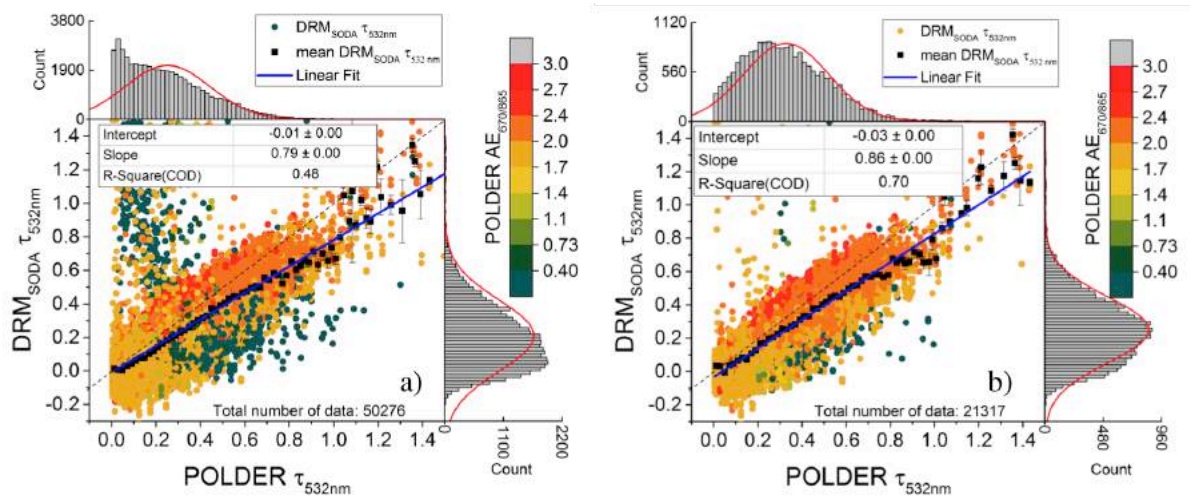


Figure 3.7 – Global comparison over a period of 4.5 years (June 2006 to December 2010) for (a) all valid AAC situations (in which the base of the aerosol layer penetrates the cloud maximum 50 m and (b) situations where the aerosol layer is well separated from the cloud top with a minimum distance of 1.5 km between the two layers. The color scale represents the corresponding POLDER AE computed between 670 and 865 nm. The histograms present the data distribution. The error bars in figures (a), (c) and (e) represent the standard error of the mean (SEM).

Events for which the aerosol layer is attached to the cloud top represent 14.4 % of the total number of two-layer cases. They are associated with lower AOT and the correlation between the two retrievals largely decreases (compare to the “detached” events). The correlation between the two AOT retrievals also decreases ($R^2 = 0.36$, Fig. 5c). The POLDER AOT is larger by a coefficient of 1.7 than the DRM_{SODA} AOT on average. The AE given by both methods is approximately 1.0 (when considering only AE values associated with $AOT > 0.1$). The lateral histogram shows that the POLDER method identifies AAC events associated with both low and high AE values resulting in a mean AE of about 1.0.

The “undetermined” situations correspond to retrievals when CALIOP does not give all the information regarding the layer altitudes. The number of cases is significant (approximately 92 % of the total number of global retrievals) but most of data (95 %) corresponds to AOT_{532nm} lower than 0.2. This probably explains why the layer detection algorithm has difficulties in estimating the base and top of the aerosol layer. For the “undetermined” cases, we observe that there is not much correlation between POLDER and DRM_{SODA} measurements. On average, the DRM_{SODA} AOTs are centred around zero for this category whereas POLDER has a non-negligible low AOT for most cases. In this category, the AE comparison shows a better consistency between the methods for $AOT_{532nm} > 0.5$ and for AE of approximately 2.0.

Table 3.7 – Linear regressions calculated between different methods for data acquired over June 2006 to December 2010, on a global scale above the ocean in the case of aerosol attached to the cloud top, detached from the cloud and undetermined situations for AOT smaller than 1.5.

Linear regressions		Detached	Attached	Undetermined
DRM _{SODA} vs. POLDER	Slope	0.84±0.003	0.59±0.01	0.24±0.001
	Intercept	-0.03±0.001	-0.02±0.002	-0.02
	R ² (COD)	0.68	0.36	0.03
DRM _{Hu} vs. POLDER	Slope	0.78±0.002	0.55±0.001	0.28±0.001
	Intercept	0.10±0.001	0.12±0.002	0.09
	R ² (COD)	0.68	0.36	0.05
CALIOP _{OM} vs. DRM _{SODA}	Slope	0.17±0.002	0.12±0.007	0.06±0.008
	Intercept	0.013	0.02±0.001	0.14±0.002
	R ² (COD)	0.15	0.047	0.003
CALIOP _{OM} vs. DRM _{SODA}	Slope	0.17±0.002	0.1±0.007	0.21±0.01
	Intercept	0.029	0.04±0.001	0.14±0.001
	R ² (COD)	0.15	0.03	0.01

Table 3.7 shows the results of the linear regressions performed between the AOTs retrieved with POLDER and the other active method considered in our study for each category (i.e. detached, attached and undetermined). We recapture the systematically larger offsets of DRM_{Hu} AOT_{532nm} compared to DRM_{SODA}, and the underestimation of CALIOP_{OM} AOT with respect to the other methods.

3.3.2 Evolution of the above cloud AOT retrievals with cloud properties

In principle, the retrieval of AAC properties from the methods considered in this study should not depend on the properties of the underlying clouds. However, hypotheses and empirical relations used in the retrieval methods to exploit the signal backscattered by the underlying cloud cover obviously have their limitations. In order to understand potential issues linked with diversity of cloud properties, we analyse in this section the difference between the AOT retrievals of POLDER, DRM_{SODA} and DRM_{Hu} by classes of cloud properties (COT and r_{eff} retrieved with MODIS). We considered global measurements acquired for four and a half years of data and used the classification defined in Sect. 3.1.2

Figure 3.9 presents POLDER and DRM_{SODA} AOT₅₃₂ retrievals as a function of the MODIS droplets effective radius (r_{eff}), while Figure 3.11 displays POLDER and DRM_{SODA} AOT_{532nm} as a function of the MODIS cloud optical thickness (COT). Histograms of the cloud

properties are also reported in Figure 3.9, Figure 3.10 and Figure 3.11. The results of the POLDER and DRM_{Hu} AOT₅₃₂ comparison as a function of the effective radius are shown in Figure 3.10. DRM_{SODA} and DRM_{HU} AOT_{532nm} generally exhibit rather similar behaviour, at least qualitatively. Therefore, we did not report the results found for the DRM_{Hu} AOT₅₃₂ as a function of MODIS COT.

3.3.2.1 AOT versus r_{eff}

The lateral histograms plotted in Figure 3.9 and Figure 3.11 show that most of the AAC scenes correspond to cloud droplets effective radius values between 8 and 15 μm (mean r_{eff} equal to 12 μm) and COT ranging from 5 to 15 (mean COT of 10). These mean values are expected since most of the AAC events are generally associated with low-level non-precipitating clouds, such as stratocumulus ones, which typically show rather small droplets (approximately 10 μm) and optical thickness values of approximately 10.

Figure 3.9a shows the POLDER and DRM_{SODA} AOTs for the “detached” situations. For the two methods, the retrieved AOTs are maximal for the smallest values of r_{eff} and progressively decrease with r_{eff} . Same tendencies are observed for the DRM_{Hu} (see Figure 3.10a). The two curves have however an offset. The histogram of the differences between POLDER and DRM_{SODA} AOT ($\Delta\tau$) is presented in Figure 3.9d. The mean $\Delta\tau$ value computed over the entire range of r_{eff} is equal to 0.073. This offset is not constant and slightly increases with r_{eff} , suggesting a sensitivity of one of the two methods to the cloud droplets effective radius. The DRM algorithm does not use an explicit parameterization of the lidar ratio as a function of the cloud droplets effective radius. An implicit dependence will arise from the latitudinal correction (Eq. 9) when clouds at different latitudes will exhibit different microphysical properties.

In order to understand the usefulness of adding an explicit parameterization, we recalculated the DRM_{SODA} AOT_{532nm} taking into account the dependence of S_c on r_{eff} . This calculation assumes a simplified and unique droplet size distribution and is based on MODIS r_{eff} retrieval. We expect that even if the cloud droplet size distribution is variable (Miles et al., 2000) and that the ACAOD creates a bias in r_{eff} , the results will still provide guidance for future algorithm development. As defined in Josset et al. (2011), S_c was computed using a Mie code with the following equation:

$$S_c = \frac{4\pi}{\omega_0 \times p(180^\circ)} \quad (\text{Eq. 3.1})$$

where $p(180^\circ)$ is the average value of the phase function in the backscatter direction computed over the size distribution. ω_0 is the Single Scattering Albedo of the particles, defined as the ratio between the mean scattering coefficient and the mean extinction coefficient computed over the particle size distribution. We used a two-parameter gamma size distribution with an effective variance of 0.088. The real refractive index was set to 1.337.

Liquid water droplets do not significantly absorb at 532 nm and the imaginary part of the complex refractive index was set to 0.

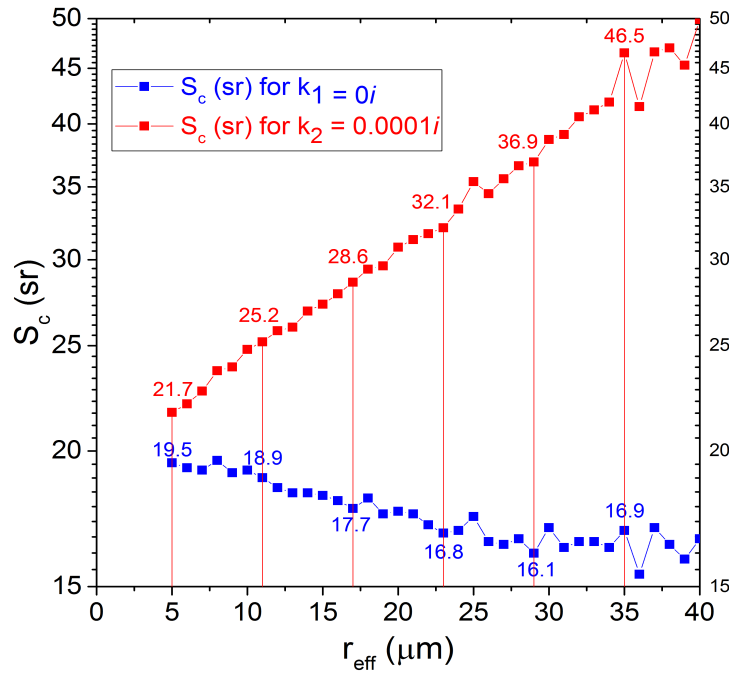


Figure 3.8 – Sensitivity study of lidar ratio (S_c , sr) as a function of the cloud droplets effective radius, using a two-parameter Gamma size distribution in Mie code. The effective variance, v_{eff} is set to 0.088. The real part of the refractive index is fixed to 1.337, while the imaginary part, k , was set to 0 (blue) and to 0.0001i (red).

As shown in Figure 3.8, S_c slightly decreases with r_{eff} from 19.5 to 15.5 as the effective radius values increases from 5 to 40 μm . With this correction, the mean difference between POLDER and the $\text{DRM}_{\text{SODA}} \text{AOT}_{532\text{nm}}$ ($\Delta\tau$ corr S_c in Figure 3.9d) decreases from 0.073 to 0.065. We found equivalent results for the “attached” and “undetermined” cases (Figure 3.9b and Figure 3.9c). After correction of S_c , the difference between POLDER and DRM_{SODA} decreases on average by 0.01, for the “attached” cases, and by 0.019 for the “undetermined” cases. We also observe that most of the negative AOT values retrieved by the DRM_{SODA} shift either to null values or weakly positive values when this correction is included (Figure 3.9a, b and c). We are aware that MODIS effective radius may be affected by the presence of aerosols above clouds. For example, Haywood et al. (2004) found biases of $\pm 2 \mu\text{m}$ for r_{eff} in case of strong dust events above clouds and Meyer et al. (2015) found an increase in the r_{eff} monthly mean of 2% in case of above-cloud absorbing aerosols. We expect that large biases on r_{eff} could be possible in case of high aerosol loading for “detached” cases. However, we consider that the impact of the biases on the retrieved r_{eff} on our findings and conclusions can be neglected, since the analysis hold for (i) a wide range of droplets effective radius (from 5 to 40 μm) and (ii) AAC events associated with low aerosol loadings (see the

results for the “undetermined” cases), where the impacts of the aerosols on the cloud retrievals are expected to be minimized or negligible.

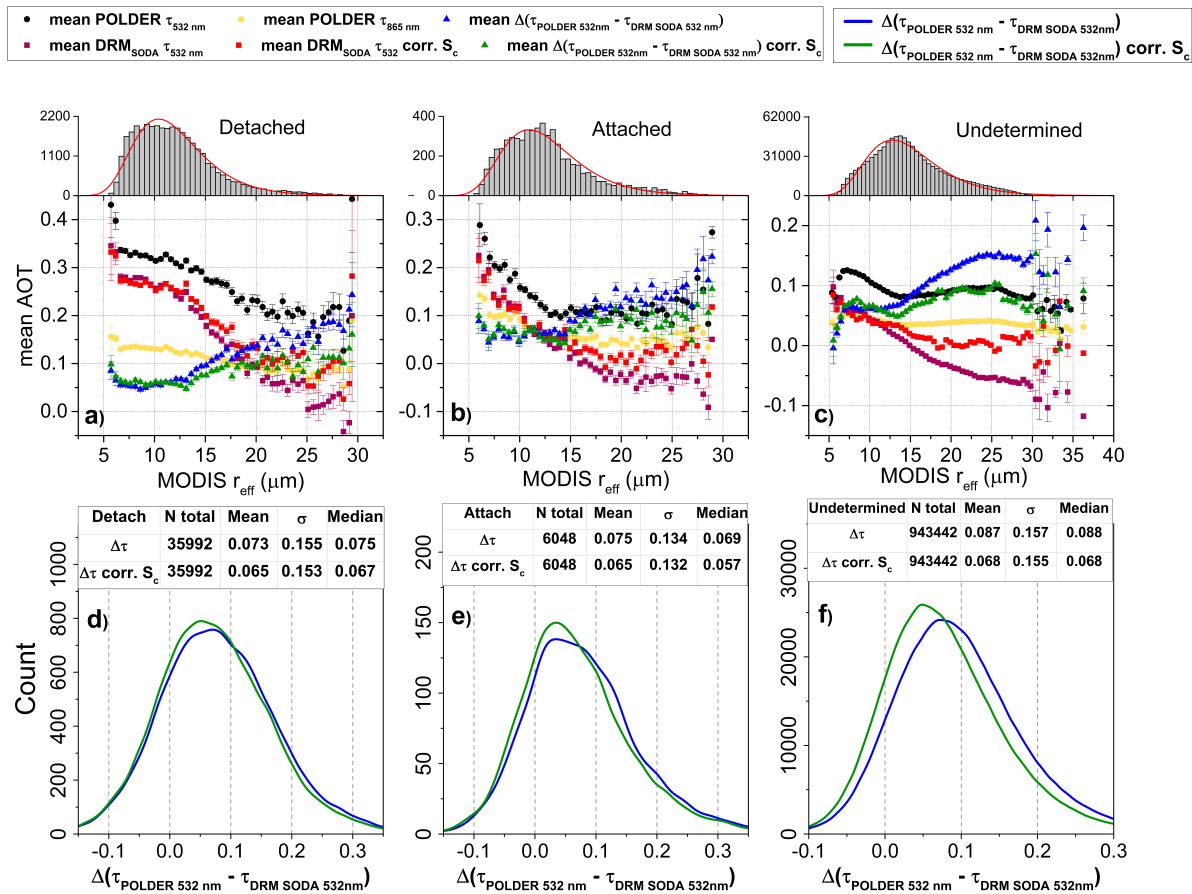


Figure 3.9 – Four and a half years of global study on the evolution of POLDER and DRM_{SODA} above cloud AOT retrievals as a function of MODIS effective radius (r_{eff} , μm) for situations where: the aerosol layer is detached from the cloud top ((a) and (d)), for cases where the aerosol layer is attached to the cloud top ((b) and (e)) and for undetermined situations (c) and (f)). The histograms from figures (a), (b) and (c) represent the distribution of r_{eff} . The histograms in figures (d), (e) and (f) present the difference between POLDER and DRM_{SODA} mean AOTs, before the correction of DRM_{SODA} AOT with r_{eff} ($\Delta\tau$) and after this correction ($\Delta\tau$ corr. S_c). The associated tables indicate the number of cases, mean, standard deviation (σ) and median values of these differences. The error bars in figures (a), (b) and (c) represent the standard error of the mean (SEM).

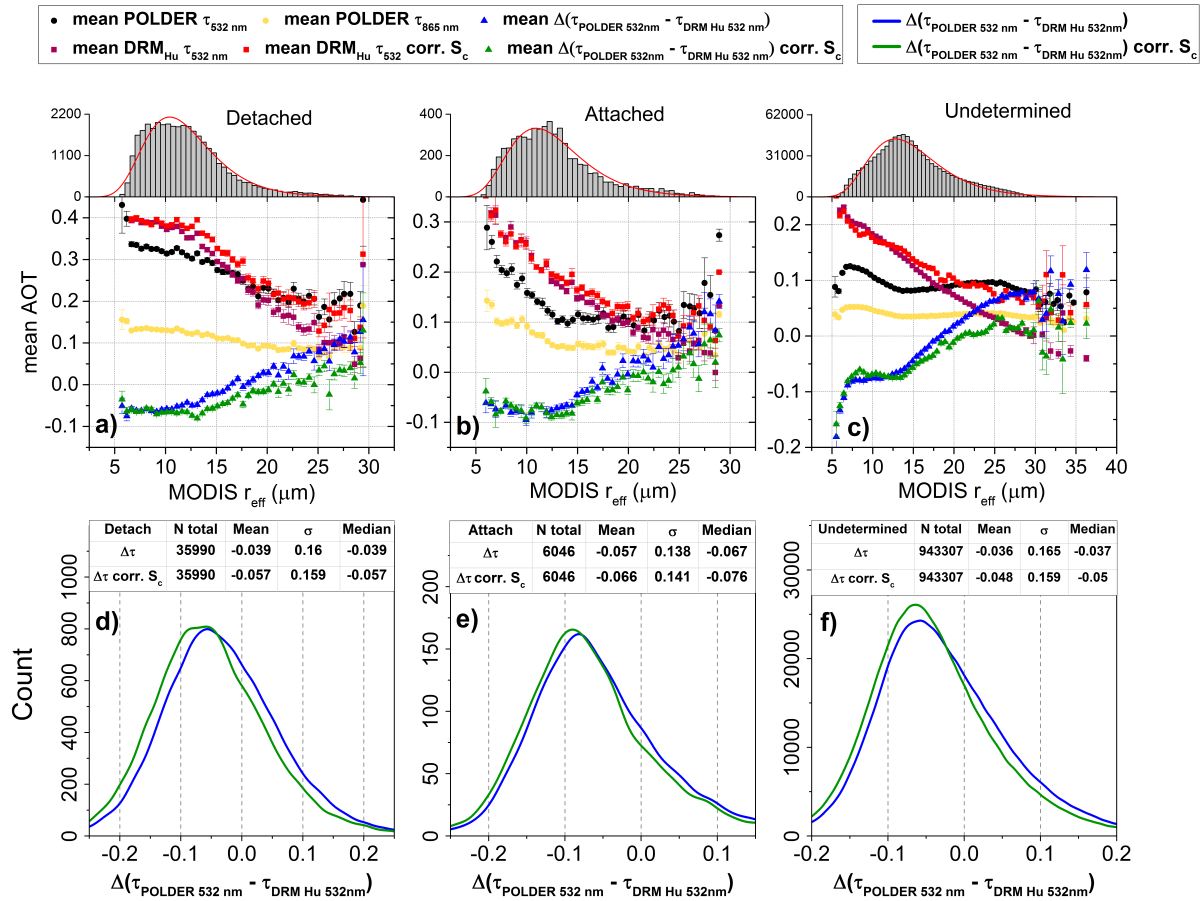


Figure 3.10 – Same as Figure 3.9, POLDER and DRM_{Hu} above cloud AOT retrievals as a function of MODIS effective radius (r_{eff} , μm).

3.3.2.2 AOT versus COT

The two methods were developed to detect AAC events in the case of optically thick and homogeneous liquid water clouds. In the following, we only discuss results obtained for large values of COT (larger than 5). If the clouds are optically thinner, the two methods are potentially less accurate since they become sensitive to the surface contribution. Hu et al. (2007a) noticed the surface impact on DRM_{Hu} when the underlying cloud is not entirely opaque, therefore the assumptions used in the DRM_{Hu} AOT retrievals are not met. For COTs ranging between 5 and 30 and for “detached” cases, the POLDER AOTs are almost constant and reach 0.3 on average at 532 nm (see Figure 3.11a). Most of the associated COT values are then ranging between 5 and 10. For these cases, DRM_{SODA} and POLDER AOTs are offset by around 0.07 on average, as noted above. However, the DRM_{SODA} AOT progressively increases with the COT, which is not observed for the POLDER AOT. Consequently, the differences in AOT between the two methods become almost negligible for the largest (and less frequent) values of COT (larger than 20). For COTs larger than 3, the polarized signal reflected by the cloud is saturated and the POLDER method should be insensitive to COT. DRM_{SODA} is sensitive to the multiple scattering processes occurring within the cloud layers

and might be impacted by the COT since multiple scattering increases with the optical thickness. The measured depolarization (δ) and the multiple scattering factor (η_{calibr}) plotted as a function of the COT are shown in Figure 3.11d. As expected, the depolarization and the multiple scattering factor respectively increase and decrease as COT increases. The increase in the DRM_{SODA} AOT observed at large COTs might be due to an increase in the multiple scattering.

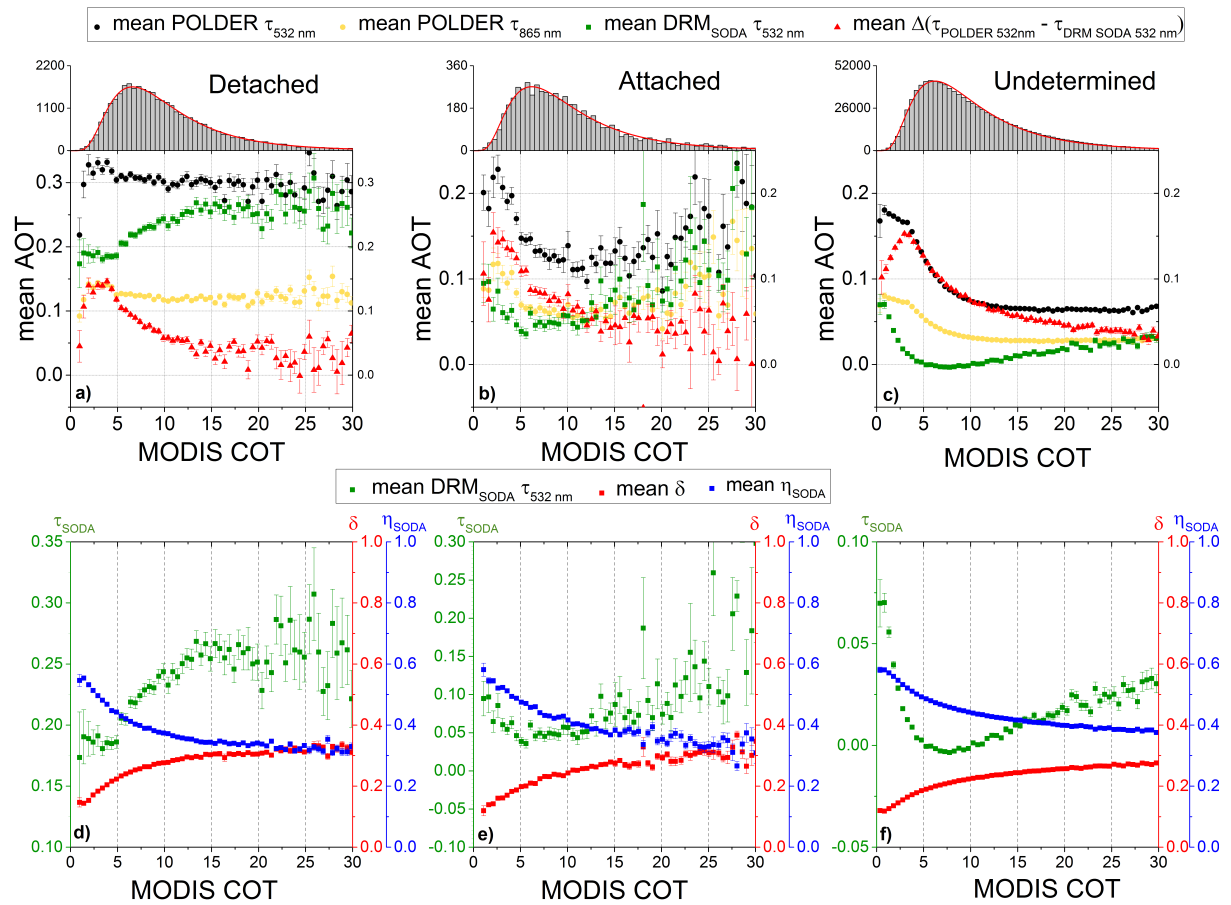


Figure 3.11 – Four and a half years of global study of the evolution of POLDER and DRM_{SODA} above cloud AOT retrievals, as well as the difference of these two methods as a function of MODIS cloud optical thickness (COT), for situations where: the aerosol layer is detached from the cloud top (a), for cases where the aerosol layer is attached to the cloud top (b) and for “undetermined” situations (c). The histograms represent the distribution of COT. The error bars show the standard error of the mean (SEM). Figures (d), (e) and (f) display the evolution of DRM_{SODA} AOT (τ_{SODA}), depolarization ratio (δ) and multiple scattering factor (η_{SODA}) as a function of MODIS COT, for the abovementioned situations.

We recall that DRM_{SODA} uses a relationship to connect the depolarization and the multiple scattering factor and that this relation is calibrated based on CALIOP data. The

calibration might be less accurate in case of AAC events associated with clouds for which the properties are statistically less representative. Again, we presume that our conclusions are not impacted by the fact that the MODIS COTs can be potentially biased in case of AAC events since the tendencies we observed hold for a large range of variability in COT (5 to 30) and also for AAC events associated with low AOT above clouds (see the results for the “undetermined” cases).

3.4 Discussion

In the first part of this section, we quantify and discuss the overall differences found between the active and passive methods in terms of the retrieved AOT. In the second part, we address more specifically the “attached” cases and make hypotheses regarding the meaning of these results.

On average, the difference between POLDER and DRM_{SODA} AOTs at 532 nm is equal to 0.073 for the “detached” cases and 0.087 for the “undetermined” cases. These differences slightly decrease to 0.065 and 0.068, respectively, when we account for the dependency of the cloud droplets lidar ratio (S_c) to r_{eff} in Eq. 10. The POLDER AOTs are systematically smaller than the ones retrieved with DRM_{Hu} . On average, these differences between these two methods are equal to -0.039 and -0.057, for the “detached” cases, and reach -0.036 and -0.048 for the “undetermined” cases, respectively without and with corrections for S_c . Thereby, the POLDER AOT estimates range, on average, between the DRM_{Hu} and DRM_{SODA} ones. The differences in AOTs found between the POLDER method and the two DRM ones could be set to zero by modifying the lidar calibration by roughly $\pm 10\%$. One another main difference between the three methods is their different responses in terms of AOT when the atmosphere above the clouds becomes pristine. The majority of AOT (94 %) is lower than 0.1 at 865 nm for the “undetermined” cases. For these cases, the POLDER algorithm retrieves a mean AOT of about 0.04 at 865 nm. The accuracy of the POLDER AOT product is in the same order of magnitude. For an $\text{AOT}_{865\text{nm}}$ of 0.2, the error for a real refractive index uncertainty of ± 0.06 would be about 0.05; for an imaginary refractive index uncertainty of ± 0.01 , the error would be of 0.02 (Peers et al., 2015). The impact of the assumed refractive index is lower at smaller AOT (especially for an AOT of 0.04). The background of the extrapolated POLDER AOT at 532 nm for the “undetermined” cases reaches 0.09. This latter value is only reported for the sake of comparison with the two other methods since the Ångström exponent retrieved by POLDER, (and consequently the AOT extrapolated at 532 nm) cannot be accurately retrieved for low AOTs. DRM_{SODA} found a mean AOT of about 0.005 at 532 nm for the “undetermined” cases (see Figure 3.9c). The result is likely due to the re-calibration process since DRM_{Hu} found a background even larger than the POLDER one, of about 0.12 at 532 nm. It is difficult to assess the truthfulness of this background, considering the given level of accuracy of the POLDER method and the uncertainties associated with the lidar calibration. We assume that these background values are not physical and could be due to some inherent limitations of the retrieval methods. From our data, however, we cannot exclude the

possibility that there is always a background loading of particles above clouds (e.g. aerosols or fine droplets in formation). Nevertheless, the main result of our investigation is that POLDER and DRM methods compare well for most situations with a mean difference of about ± 0.07 in AOT at 532 nm.

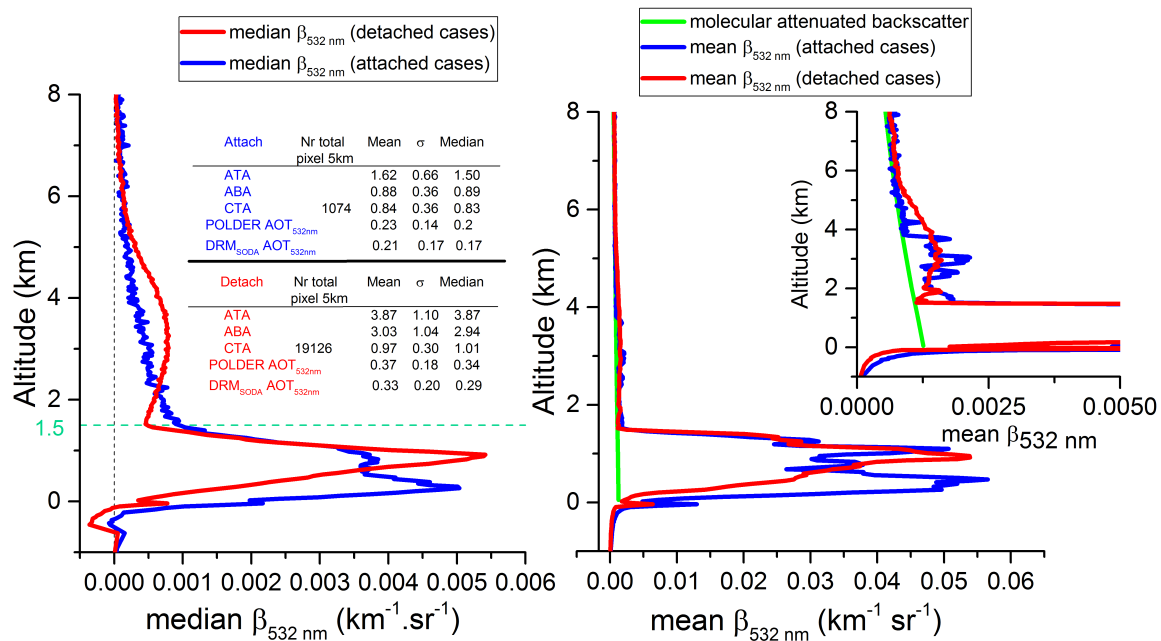


Figure 3.12 – Median (a) and averaged (b) backscatter profiles ($\text{km}^{-1}\text{sr}^{-1}$) for aerosol layer detached from the cloud layer (red) and aerosols attached to the top of the cloud (blue), for a period of four and a half years on the global scale. For comparison, the molecular attenuated backscatter profile is shown in green line. The data was filtered for a cloud top altitude lower than 1.5 km, a cloud optical thickness COT larger than 5 and for a DRM_{SODA} AOT at 532 nm larger than 0.1. The number of 5 km horizontal resolution pixels is also shown. The mean, standard deviation (σ) and median of aerosol top altitude (ATA), aerosol base altitude (ABA) and cloud top altitude (CTA) are given for each situation. Same values are shown for POLDER AOT at and DRM_{SODA} AOT at 532 nm.

Although the number of cases is small, the results of the “attached” cases are interesting. They suggest that the lidar CALIOP and POLDER could be affected by layers of aerosols that physically and locally interact with the upper part of the cloud. In order to understand how the vertical profiles differ from one situation to another, we compared the CALIOP attenuated backscatter coefficient for “attached” and “detached” cases. We considered the period 2006–2010 and used data acquired over the entire globe. We only select the “attached” and “detached” cases where the cloud top altitude is below 1.5 km, the COT is larger than 5 and the DRM_{SODA} AOT_{532nm} is larger than 0.1. These criteria allow for selection

of data that corresponds to AAC events associated with similar cloud vertical extents and with significant AOTs. For these cases, we computed the average and median of the CALIOP level 1 attenuated backscatter coefficients at 532 nm. Figure 3.12 presents these results and some information concerning the mean and median values of CALIOP level 2 products: cloud top altitude, aerosol layer's base and top altitudes. The mean and median values computed for the AOTs retrieved by POLDER and DRM_{SODA} and the numbers of sampled events are also reported.

Two different types of profiles can be observed for the “detached” and “attached” situations. For the “detached” cases, the aerosol and cloud backscattering profiles can be easily distinguished in both the median and mean profiles. The strong peaks in the backscatter profiles at around 1 km correspond to the top of the clouds, whereas the increase in the lidar backscatter signal observed between 2 and 4 km in altitude comes from the aerosols. For the “attached” situations, the backscatter profiles are noisier, which is likely due to the fact that the number of detected events is smaller compared to “detached” cases. The top of the cloud layer is still clearly visible in the mean and median backscattered lidar signals, but two maxima can be observed. We assume that we sampled two different regimes of clouds. In addition, there is a continuous transition in the backscatter signal between the top of the cloud and the above molecular atmosphere that is most clearly visible in the median profiles. This signal doesn't appear for the “detached” cases. This signal could explain the non-negligible above-cloud AOTs retrieved by POLDER and DRM_{SODA} for the “attached” cases (see Figure 3.6). It is difficult to assess the origin of this signal. This might be due to aerosols layers that penetrate the cloud layers at the top of the clouds. Natural aerosol or fine droplets in formation, commonly present in the vicinity of the clouds, might also create this additional signal.

Figure 3.13 compares the mean DRM_{SODA} AOT and mean POLDER AOT at 532 nm for the four determined situations described in Sect. 3.1.2 (see Figure 3.1). These situations are: aerosols “detached” from the cloud top, aerosols “attached” at the cloud top, aerosols “across” the cloud layer (rather same situation as “attached” but the aerosol layer bottom height is located deeper into the cloud layer) and aerosols “within” the cloud (aerosols entirely located within the cloud layer). Figure 3.14 shows mean results computed over four and a half years on a global scale for collocated DRM_{SODA} and POLDER AOT retrievals. We observe that the correlation between the two retrievals decreases as the position of the aerosol layer comes more and more into contact with the cloud layer (i.e. “attached” cases and “within” cases). A fairly nice agreement is observed between the mean AOTs for the detached cases ($R^2 = 0.99$) whereas the correlation progressively decreases for the “attached” and “across” situations, for which R^2 is equal to 0.95 and 0.88, respectively. Also, it is interesting to note that the slope values associated with the linear regressions decrease gradually from 0.84 for the “detached” cases to 0.02 for the within cases. For the “within” cases, the POLDER algorithm returns non-negligible AOT values, that can be as large as 0.8 at 532 nm, whereas while DRM_{SODA} retrieves an AOT lower than 0.1. The correlation between the two methods has further decreased for these cases ($R^2 = 0.50$). The results obtained for the “within” and “attached” cases suggest that the POLDER method could be sensitive to the

aerosols located within the cloud, as they could affect the polarized radiances measured by POLDER.

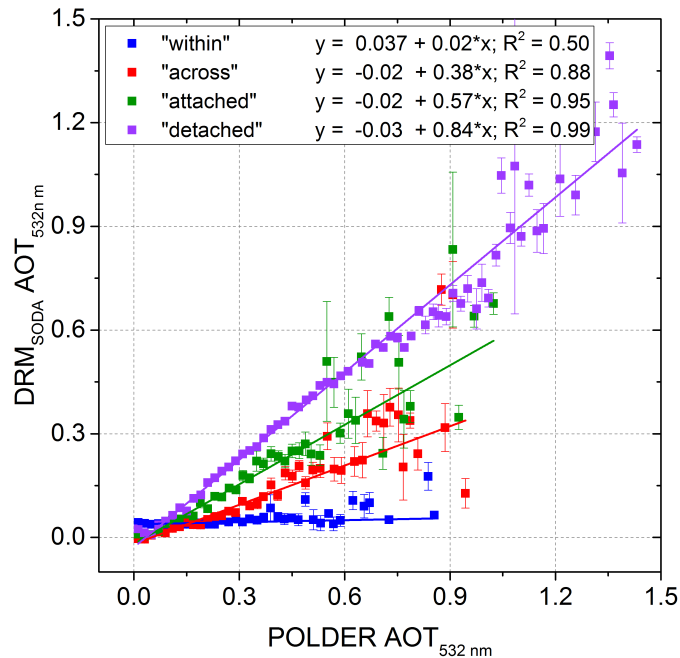


Figure 3.13 – Global comparison of average $DRM_{SODA} AOT_{532 \text{ nm}}$ and $POLDER AOT_{532 \text{ nm}}$ retrieved over a period of four and a half years (June 2006 to December 2010) along the CALIOP track for four different situations defined in Figure 3.1: aerosols “detached” from the cloud (violet), aerosols “attached” to the cloud top (green), aerosols “across” the cloud (red) and aerosols “within” the cloud (blue).

Since the operational algorithm developed for POLDER assumes that the entire aerosol layer is located above the clouds, an additional polarized signal coming from aerosol located within the cloud could lead to an overestimation of the above cloud AOT retrieved from POLDER. To test this assumption, we modeled the polarized radiance measured by POLDER for AAC scenes, considering different vertical locations of the aerosol layer (Figure 3.14). We used the Successive orders of scattering (SOS) radiative transfer code (Lenoble et al., 2007) for this simulation. We considered a liquid water cloud located between 0 and 1 km. The particles (aerosol and cloud) are vertically homogeneously mixed. The COT is equal to 10 and the effective radius and variance are equal to 10 μm and 0.08, respectively. The aerosol layer is characterized by an AOT of 0.25 at 865 nm, a refractive index of $m = 1.47 - 0.01i$ and an effective radius of 0.15 μm .

Figure 3.14 shows the typical polarized feature for AAC events in case of “detached” situations (i.e. aerosols located between 1.25 and 1.75 km): a creation of polarization is observed at side and forward scattering angles, whereas the cloud bow magnitude decreases.

For the “attached” case (aerosols between 0.75 and 1.25 km), the amount of polarization created at forward scattering angles decreases and the cloud bow attenuation is less significant in comparison with the “detached” scenario. When the aerosol layer is located within the upper part of the cloud layer (between 0.5 and 1 km) we still observe a weak polarized signal created at forward scattering angles. When the aerosol layer is located in the lower part of the cloud layer, the effects of the aerosols disappear since the polarized radiance scattered by the aerosols is lost due to multiple scattering occurring within the clouds. These simulations were processed with the POLDER algorithm (Waquet et al., 2013b). We recall that the LUTs used in this algorithm were built for “detached” situations. The algorithm retrieved an AOT of 0.09 at 865 nm when the aerosols are located within the upper part of the cloud layer. This demonstrates that polarized radiances are sensitive to aerosols situated within the clouds for the “attached” cases.

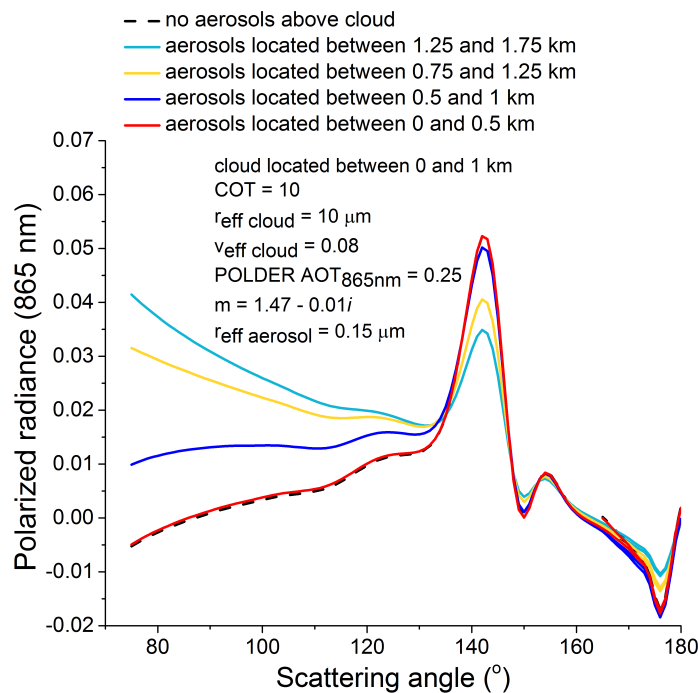


Figure 3.14 – Sensitivity study of polarized radiance at 865 nm to the relative position of the aerosol layer above the cloud. Simulation performed for a cloud layer located between 0 and 1 km and aerosol layers varying at different altitudes. The cloud droplet effective radius is fixed to 10 μm and the effective variance is 0.08. The aerosol layer is characterized by an AOT of 0.25 at 865 nm, a refractive index of 1.47-0.01i and an aerosol effective radius of 0.15 μm .

The DRM methods might also be impacted by the presence of aerosols within the clouds. Aerosols as a solution within the cloud droplets (i.e. internal mixture) might impact the chemical composition of the droplets and modify their ability to backscatter light. Figure 3.8 shows lidar ratio computed for absorbing cloud droplets. We used an imaginary part of 0.0001 for the complex refractive index of the droplets. This might simulate, for instance, the properties of brown clouds contaminated by absorbing aerosols. The chosen value is in agreement with the refractive indices given for water containing soot inclusions with volume

fractions ranging between 10^{-4} and 10^{-2} (Erlick, 2006). We observe a drastic increase of S_c with r_{eff} (from 21.7 sr at $5 \mu\text{m}$ to 50 sr at $40 \mu\text{m}$) when the water droplet is weakly absorbing. In the case of an external mixture, we assume that the presence of aerosols at the top of cloud might also modify the value of S_c . Any deviation from the 19 sr value assumed for the droplets lidar ratio in Eq. 3.1, will necessarily impact the retrieved AOT and the differences observed between the AOT estimates provided by the POLDER and DRM methods.

Until now, we tried to explain the differences, observed between DRM_{SODA} and POLDER in case of “within” or “attached” cases, by assuming that aerosols are present within the clouds or that these particles modify the ability to cloud droplets to backscatter light. However, we cannot ignore the possibility that these differences could be also due to some limitations inherent to the proposed methodologies. We assume that a misidentification of fractional cloud covers could also impact the passive POLDER retrievals. POLDER or MODIS cloud retrievals sometimes retrieves a cloud cover fraction of 100 % whereas the cloud cover is in fact partially fractional due to some sub-pixel heterogeneities (personal communication, Céline Cornet, LOA). Since the POLDER operational algorithm is applied only in case of homogeneous and fully cloudy pixels, the retrieved AOT could be potentially biased for such cases.

In order to test this assumption, we simulated the polarized radiance reflected by a biomass-burning aerosol layer (with an AOT of 0.15 at 865 nm) located above fractional cloud covers. A cloud fraction of 0.76 was used and the mean cloud optical thickness is equal to 10. The 3DCLOUD code, described in Chapter 2, was used to accurately account for the 3D radiative cloud effects. Calculations were also performed for homogeneous and fully cloudy scenes, as a reference. Then, we used these simulations as input data for the POLDER polarization algorithm.

The results showed that, for homogeneous clouds, the simulated polarized radiances reproduce well the input signals. The retrieved values of AOT are very close to the assumed one in the input simulations. For fractional cloud covers, the results depend on the solar zenith angle (θ_s). We recalled that the polarization radiances computed by the POLDER polarization algorithm are based on calculations performed with a plan-parallel code. At θ_s of 20° , the computed polarized radiance underestimate the input signal. There is a strong difference in the region of the primary bow (around 140° in scattering angle). The plan-parallel bias is responsible for this overestimation in the 1D calculations. At θ_s of 60° , the polarized radiances computed by the POLDER algorithm is overestimated in comparison with the input simulations. For this low solar elevation, we assume that some shadowing effects decrease the polarized signal for forward scattering viewing geometries. The AOT retrieved by the algorithm is then substantively overestimated (see Table 3.8). Therefore, depending on the solar elevation, the presence of undetected fractional clouds could impact the POLDER retrievals and might explain some of the differences found between the active and the passive methods.

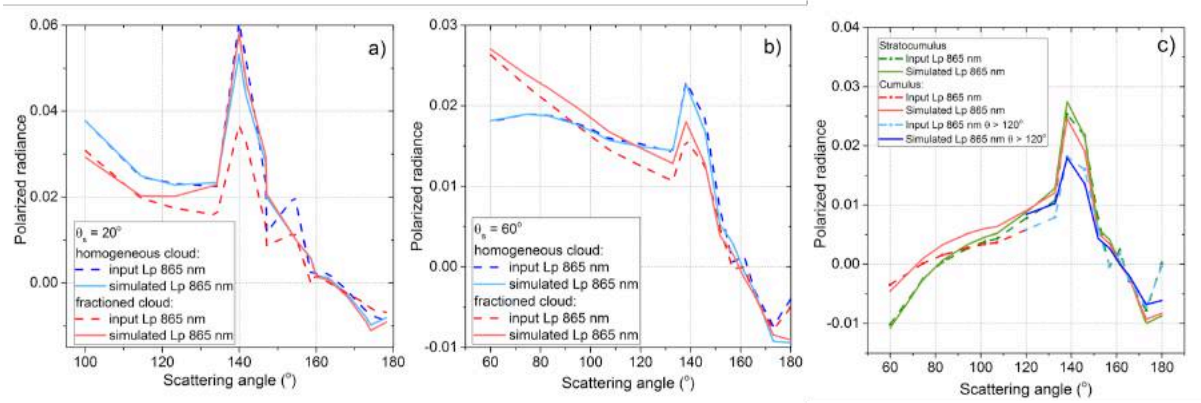


Figure 3.15 – Polarized radiance shown as a function of the scattering angle. Simulations performed for a biomass-burning aerosol layer ($AOT_{865\text{nm}} = 0.15$) located above homogeneous fully cloudy scenes (blue lines) and fractional cloud covers (red lines) (a, b). The dashed lines are the input synthetic data computed with a 3-D code in, while the solid lines are the polarized radiances simulated with the POLDER algorithm for (a) θ_s of 20° and (b) θ_s of 60° . (c) Same results for a fully cloudy scenes with no aerosols in case of stratocumulus and cumulus clouds, when the retrievals are performed with all the value of scattering angles (green and red) and when the retrieval process is restricted to angles larger than 120° (blue).

We also tested the potential effects of different types of cloud covers on the POLDER polarization method, when no aerosols above clouds are considered. Our purpose was to identify some limitations in the POLDER polarization method when the atmosphere above clouds becomes pristine. For stratocumulus clouds (flat and bumpy clouds) with fully cloud pixels and fractional cover with cumulus (76% cloudy), the polarization method works well and no aerosol were retrieved ($AOT = 0$). On some occurrences, the range of scattering angles sampled by the POLDER instrument can be also restricted, depending on the geographical position and viewing geometry. Therefore, we tested our retrieval method for a fractional cover with cumulus clouds, when POLDER data are only available for scattering angles larger than 120° (a less favorable case, see Figure 3.15c). In this peculiar case, the algorithm retrieves an erroneous AOT value of 0.28 instead of zero at 865 nm. This can explain certain differences occasionally observed between the POLDER method and the DRM_{SODA} method.

Table 3.8 – Aerosol properties retrieved using synthetic simulations performed for a biomass aerosol layer located above homogeneous fully cloudy scenes and for fractional cloud covers, for three values of solar zenith angles.

Input biomass-burning $AOT_{865\text{ nm}} = 0.15$	Homogeneous clouds			Fractioned clouds		
	$\theta_s = 20^\circ$	$\theta_s = 40^\circ$	$\theta_s = 60^\circ$	$\theta_s = 20^\circ$	$\theta_s = 40^\circ$	$\theta_s = 60^\circ$
POLDER $AOT_{865\text{ nm}}$ (output after simulation)	0.18	0.17	0.17	0.11	0.17	0.28

3.5 Conclusions

In this study, we compared and analyzed the consistency of the AOT and AE retrievals above clouds from different passive and active techniques. We used the CALIOP operational algorithm (Winker et al., 2009) the POLDER polarization method (Waquet et al., 2013b), and the CALIOP-based depolarization ratio method (DRM_{Hu}) (Hu et al., 2007a) – for which we proposed a re-calibrated version of the DRM algorithm (DRM_{SODA}). The observations were made for: a) three case studies corresponding to an African biomass-burning event, a Saharan dust event and a Siberian biomass-burning event; b) a regional scale analysis, over South Atlantic Ocean, North Atlantic Ocean and North Pacific Ocean for a period of six months in 2008 and c) a global scale analysis for different vertical layer distributions for the period 2006–2010.

In the regional analyze, we observed that POLDER method and DRM are in good agreement when the microphysics of aerosols is dominated by fine-mode particles of biomass-burning aerosols (in the South Atlantic region, $R^2 = 0.83$) or coarse-mode aerosols of dust (in the North Atlantic region, $R^2 = 0.82$). A good correlation between these methods ($R^2 = 0.68$) is also noticed in the global treatment, when the aerosol and cloud layers are well separated. Nevertheless, some of the “detached” cases considered in our study, mainly the ones associated with optically thick smoke layers, are likely to be incorrectly classified as “detached”. As a future perspective, the misclassified “detached” cases (due to strong attenuation of the CALIOP 532 nm signal) could be detected by controlling the CALIOP 1064 nm signal, which was shown to provide more sensitivity to the entire vertical extent of these absorbing aerosol layers. The CALIOP operational method largely underestimates the AOT above clouds in all situations, with respect to other methods.

The differences between the DRM and POLDER retrievals increase when a complex mixture of aerosols is expected (such as in the East Asia region). This is probably due to the fact that the current algorithm developed for POLDER uses a limited number of microphysical models of aerosols. Also, the relative position of the aerosol layer above the cloud impacts the AOT retrievals from both active and passive measurements: the correlation decreases when the layers are in contact ($R^2 = 0.36$), suggesting that aerosols at the top or within the cloud can affect the AOT retrievals. One hypothesis is that an additional polarized signal coming from aerosol located within the cloud could affect the polarization signal and method, which leads to an overestimation of the AOT retrieved with POLDER algorithm. The aerosols attached with or within the cloud also have the potential to impact the DRM retrievals, by modifying the lidar ratio (and consequently the AOT) as a result of internal or external mixture. The (undetected) fractional cloud covers could also impact the passive retrievals by modifying the angular polarized radiance used in the inversion method. This could result in significant underestimation or overestimation of the AOT, depending on the solar incident angle, which might also explain part of the differences between POLDER and DRM_{SODA} retrievals.

Furthermore, we investigated potential biases in the retrieved AOT measured by POLDER and DRM_{SODA} as a function of MODIS cloud properties (i.e. droplet effective radius (r_{eff}) and cloud optical thickness (COT)). The tendencies show an increase in the difference between the two methods for larger r_{eff} , suggesting sensitivity to the cloud droplet effective radius. For this reason, we recalculated the DRM_{SODA} $\text{AOT}_{532\text{nm}}$ taking into account the dependence of lidar ratio on r_{eff} , as this method assumes a constant lidar ratio regarding the droplet effective radius. By doing so, we observed a decrease in the difference between POLDER and DRM methods and a shift of the DRM AOT from negative (unphysical) to positive values. For a better accuracy of DRM retrievals in future studies, this correction should be taken into account. The results show also that the multiple scattering processes, which are more pronounced in optically thick clouds, could also slightly affect the DRM technique.

All of the aforementioned situations have revealed that DRM_{Hu} has larger mean AOT than that of DRM_{SODA} . This is likely to be a consequence of the re-calibration performed for the DRM_{SODA} method. Actually, POLDER $\text{AOT}_{532\text{nm}}$ values are consistently smaller than the ones of DRM_{Hu} and larger than those of DRM_{SODA} . The primary conclusion of our investigation is that POLDER and DRM techniques are comparable for the majority of cases, with a mean difference of about ± 0.07 in AOT at 532 nm, depending on lidar calibration.

Given the fact that each method relies upon different physical concepts, applied to different sensors and measurements, the high value of the correlation obtained for the AOT retrievals is a remarkable result that highlights the coherence between active and passive methods for aerosols above clouds.

Chapter 4

Study of the impact of aerosols above clouds over the South Atlantic Ocean

The fourth chapter is consecrated to the study of the impact of aerosol layers overlying low-level clouds, their associated radiative forcing and their effects on these underlying clouds, for the South Atlantic Ocean area. This region is well suited to investigate these effects, as large aerosol loadings from South-western Africa biomass fires are transported over the semi-permanent deck of stratocumulus clouds that typically cover this area, which constitutes one of the most extended cloudy regions on Earth. The main objective of the study is to evaluate the radiative forcing of aerosols above clouds (AAC), and to address the difficult question of the semi-direct effects of aerosols over this area, thanks to an original synergy of observations (PARASOL and CALIOP), combined with reanalyzed meteorological data. Our approach will attempt to separate the influence of the aerosols on the low cloud cover from the influence of the meteorological conditions.

First, we give a short review of previous studies whose objectives have been to analyze the impact of aerosols located above clouds on the cloud properties and radiative forcing. Afterwards, we describe the properties that characterize the aerosols and clouds that exist in the area of interest, along with their typical altitudes and the main meteorological conditions and trends observed in this region. We perform a set of radiative transfer calculations in order to compute the aerosol radiative forcing and its variation with the strength of the smoke episodes. Additionally, we attempt to disentangle the effect of biomass-burning aerosols on the radiative forcing in the region of interest from that of the water vapor, that comes together with the biomass-burning aerosol layers. Lastly, we show the covariance that we found between the aerosol loading, the meteorological conditions and the cloud parameters.

4.1 Aerosol effect in cloudy scenes over South Atlantic Ocean: a quick review

The South Atlantic Ocean is largely influenced by high biomass-burning aerosol loadings that can impact the local climate by inhibiting the precipitation, affecting the cloud formation and development, and can modify the radiative budget. Therefore, this region and the question of the direct, semi-direct and indirect effects of aerosols located above clouds have been the subject of previous studies based on the exploitation of satellite observations and modeling.

Costantino and Bréon (2013) used MODIS observations to retrieve aerosol and cloud parameters collocated with CALIOP layer altitude estimates. Their objective was to use the simultaneous satellite retrieved aerosol and cloud properties to contribute to the knowledge of aerosol-caused effect on cloud microphysics (r_{eff}), optical properties (COT) and liquid water path (LWP) of low-level stratocumulus clouds. The MODIS AOT at 550 nm and AE calculated between 550 and 860 nm were retrieved within broken field clouds and integrated over the entire atmospheric column. With these data the Aerosol Index (AI) was calculated for a qualitative detection of the aerosols above clouds. Using CALIOP retrievals, the aerosol layer was assumed well separated from the cloud top when the distance between the layers was at least 750 m. Also, the layers were considered in contact, when the vertical distance between the aerosol bottom and cloud top was less than 100 m. The results argued that the aerosol effects on the cloud microphysics are strong, when the layers are in contact, suggesting a potential indirect effect of aerosols. The effective radius can decrease from 15-16 μm down to 10-11 μm for an aerosol index that varies from 0.02 to 0.5. The aerosol effect on the optical properties and on the liquid water path does not show a significant dependence with the increase in AI. However, the MODIS r_{eff} and COT retrievals were not corrected for the effect of aerosols above clouds, which can introduce biases in the analysis (Haywood et al., 2004; Peers et al., 2016).

Wilcox (2010) also used the aerosol and cloud altitudes retrieved with CALIOP in combination with OMI aerosol index, in order to analyze the link between the absorbing aerosols located above clouds and the marine stratocumulus cloud properties. The sea surface temperature (SST) and the LWP were derived from the Advanced Microwave Scanning Radiometer-EOS (AMSR-E), as the effect of biomass-burning aerosols in the microwave is negligible. The data were used to analyze the response of the cloud to the changes in tropospheric temperature as result of above-cloud aerosol absorption of solar radiation. Their strategy was to analyze the satellite data for two different situations: when the smoke aerosol loading is large (OMI AI is greater than 2) and when the smoke amount is low (OMI AI is less than 1). The results showed that the presence of absorbing aerosol layers lead to a heating (by nearly 1 K at 700 hPa) in the lower troposphere that stabilizes the atmosphere. For an AOT of 1.0 at 550 nm the shortwave heating rate in the aerosol layer was found to reach 3.5 K/day. This warming coincides with LWP values for high-smoke cases that are greater by

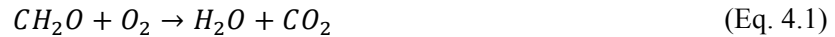
more than 20 g.m^{-2} compared to low smoke cases. This is true despite the different SST values. Also, the cloud top altitude derived from CALIOP is by 200 m lower for high-smoke cases. These higher LWP and lower cloud top altitude would be a consequence of the warming due to aerosol layer. This warming would tend to reduce the cloud convection and the entrainment of dry air at the cloud top, preserving the humidity of the cloud layer and limiting its vertical development. The work of Johnson et al. (2004) confirmed this possible mechanism. This study performed large-eddy simulations that showed an increase in LWP of stratocumulus clouds overcast by aerosols by 5 to 10 g.m^{-2} compared to situations without biomass-burning aerosol layer above clouds. They related this cloud thickening effect to the stabilization of the lower troposphere due to the aerosol warming. Wilcox (2010) concluded that the direct radiative effect of above-cloud absorbing aerosols is positive at the top of the atmosphere (warming), while the semi-direct effect yields a negative radiative forcing (cooling) due to the albedo enhancement of thicker clouds (i.e. larger LWP). The balance of these contrasting radiative forcing effects depends on the loading and optical properties of the aerosols, as well as the COT and coverage of the underlying cloud.

Some of these observations were also found by Sakaeda et al. (2011) that used the Community Atmospheric Model 3.0 (CAM) to simulate the regional direct and semi-direct effect of biomass-burning absorbing aerosols over the southern Atlantic, during the biomass-burning season. The model was adjusted using satellite observations. MODIS and CALIOP measurements were used to detect the aerosol layers above clouds and to constrain the AOT in the model. Their approach was similar with that of Wilcox (2010), simulating mean cloud properties for situations with and without carbonaceous aerosols and computing the radiative forcing for these cases. The results show that over the ocean the LWP increases by around 15 g.m^{-2} , notably when the low-level cloud cover increases (i.e. the model predicts more low-level clouds when overlying aerosols are present). The cloud changes could be induced by a surface cooling feedback due to the direct aerosol forcing and also by the increase in the lower tropospheric stability due to radiative heating by the aerosol layer. The primary conclusions are that the total aerosol radiative effect at the Top of the Atmosphere (TOA) is highly affected by the semi-direct effects, which are primary driven by the cloud cover and the liquid water path changes. They found that, over the ocean, the TOA semi-direct radiative effect due to cloud cover changes provides a significant offsetting of the cloudy-sky direct radiative effect.

Nonetheless, none of the above mentioned studies have tried to (or achieved to) rigorously disentangle the effect of meteorological conditions versus aerosol effects on the boundary layer cloud cover. Yet, cloud cover are both sensitive to meteorological conditions, and to the presence of aerosols. And aerosols themselves can affect the meteorological conditions by changing the temperature of the layer where they reside and stabilizing the lower tropospheric atmosphere.

Also, the aforementioned studies are typically depicting dry smoke plumes, while biomass-burning aerosol events are accompanied by varying water vapor production. Depending on of the moisture content of fresh biomass (Parmar et al., 2008), the natural or

anthropogenic biomass fires are indeed releasing water vapor in the atmosphere, in addition to organic and black carbon, CO_2 and CO . For biomass burning, the basic reaction is:



where CH_2O represents the average chemical composition of biomass material (Levine, 1991).

It might be important to account for the effect of this accompanying moisture, and to identify the different air circulation patterns that will lead the biomass-burning transportation off coast of South Africa. Adebisi et al. (2015) incorporated radiosondes measurements from St. Helena Island of temperature and specific humidity, MODIS $\text{AOT}_{550 \text{ nm}}$, CALIOP aerosol altitude data and reanalysis data (ERA-Interim) to provide a unique dataset of thermodynamic profiles linked to clear and polluted conditions. They also investigated the radiative effect of moisture and absorbing aerosol in different cloudy conditions at St. Helena. The results show a shift southward in circulation patterns and thermodynamics between July-August and September-October, as the southern African anticyclone strengthens. Also, the specific humidity (q_v) is higher within the aerosol plumes (around 700 hPa). This was previously observed during the UK-SAFARI 2000 campaign (Haywood et al., 2003) with q_v values larger than 2 to 4 g.kg^{-1} within the aerosol layer, while outside the smoke plume the q_v values are less than 1 g.kg^{-1} . The moisture may have a role in the aerosol aging and a radiative significance in both shortwave and longwave spectra. Besides aerosols, the water vapor also absorbs in shortwave, enhancing the warming of the above cloud atmosphere. Their radiative transfer calculations show that midtropospheric moisture generates a net diurnal cooling of approximately 0.45 K/day, decreasing the impact of the shortwave heating caused by the biomass-burning aerosols that reaches 1.5 K/day. As in Wilcox (2010), this study shows a decrease in the cloud top altitude of about 112 m near St. Helena under polluted conditions. Nevertheless, until present the changes are not attributable to meteorological effect or to the aerosol radiative heating.

Starting from all these observations, we have developed our own strategy in order to better understand the effect of aerosols and meteorological parameters on clouds and to calculate the radiative forcing. Before moving onward to data analysis and results, we describe the aerosol parameters and the cloud properties in the South Atlantic Ocean, as well as the general pattern of the air circulation and meteorological characteristics.

4.2 Description of aerosols, clouds and meteorology at the large regional scale

The southern African subcontinent is the main annual contributor of biomass burning aerosols, as most of this region is covered by savannah type ecosystem. Due to agricultural practices, the savannah vegetation is burned and large amount of aerosols is injected into the

atmosphere (Labonne et al., 2007). Due to favorable physical characteristics and meteorological processes these biomass-burning aerosols are lifted into the upper atmosphere (mostly above the clouds) and are transported long distances westwards, over the South Atlantic Ocean (Ichoku et al., 2003; Waquet et al., 2009). The insufficiently wet scavenging of the aerosols transported above the clouds leads to a near-persistent smoke layer above the stratocumulus deck, that can be suspended in the atmosphere for several days. The emission of smoke aerosols, ozone and other trace gases, varies with season, as the intensity of cropland fires and widespread biomass burning in the tropical and subtropical southern Africa is higher during August to November. During the rest of the year, dust and industrial pollution become the predominant aerosol types due to the decrease of man-made vegetation fires (Fishman et al., 1991; Piketh et al., 1999; Swap et al., 1996).

During the austral late winter and spring the dominant aerosol transported above clouds over the South Atlantic Ocean is smoke, which is mostly composed of organic carbon and black carbon, depending on the type of fuel, the combustion phase and oxygen availability (Andreae and Merlet, 2001). The strong absorbing property of these components can have a warming effect on the surrounding atmosphere and can impact the cloud development, the cloud formation (i.e. semi-direct effect) and can have a positive forcing at the top of the atmosphere (i.e. direct effect). Also, in case of contact between the aerosol layer and the cloud top, the smoke particles can be activated as CCN and can indirectly affect the cloud lifetime, by decreasing the water droplet size and inhibiting precipitation (i.e. indirect effect) (Costantino and Bréon, 2012).

For a comprehensive understanding of the impacts associated to aerosols on clouds and local climate, we will firstly investigate the average aerosol and cloud properties encountered over the South Atlantic Ocean, as well as the meteorological conditions.

The POLDER and MODIS aerosol and cloud retrievals were acquired from May to October 2006 to 2009 over an area that extends from 30°S to 5°N and from 12°W to 14°E in the South Atlantic Ocean (SAO). The following maps present the average values of different aerosol and cloud parameters for this region at a horizontal resolution of 6 km × 6 km.

4.2.1 Aerosol optical and microphysical properties

Large aerosol loadings are found close to the coast, where the average ACAOT exceeds 0.3 at 865 nm. Towards the west, the above-cloud AOT (ACAOT) decreases to an average of 0.2 at 865 nm due to transportation and deposition of aerosols (Figure 4.1a). As expected, the mean values of the Ångström exponent ($AE_{670/865}$) along the shoreline are larger than 2.0, characteristic of very fine particles of smoke (Dubovik et al., 2002), while westwards the mean $AE_{670/865}$ values slightly decrease to around 1.85 (Figure 4.1b). This implies an increase in the particle size that can also be observed in Figure 4.1c, where the aerosol granulometric radius, r_g , increases from 0.13 μm to 0.15 μm , as the plume is transported towards the open sea. The decrease (increase) of the mean AE (mean r_g) values

with longitude can suggest the evolution of the aerosol properties, such as growth of the smoke aerosols associated to aging (Müller et al., 2007; Reid et al., 1998). Dubovik et al. (2002) and Haywood et al. (2003) also found that the mean aerosol radius could increase with aging. To test the hypothesis of aerosol size evolution with longitude, we selected a relatively constant aerosol loading along the longitude, with values of POLDER AOT_{865nm} between 0.1 and 0.15, and we analyzed the associated POLDER $AE_{670/865}$ for a horizontal transect of 1° of latitude (between $12^\circ S$ and $13^\circ S$), supposing the aerosols are mainly transported westwards.

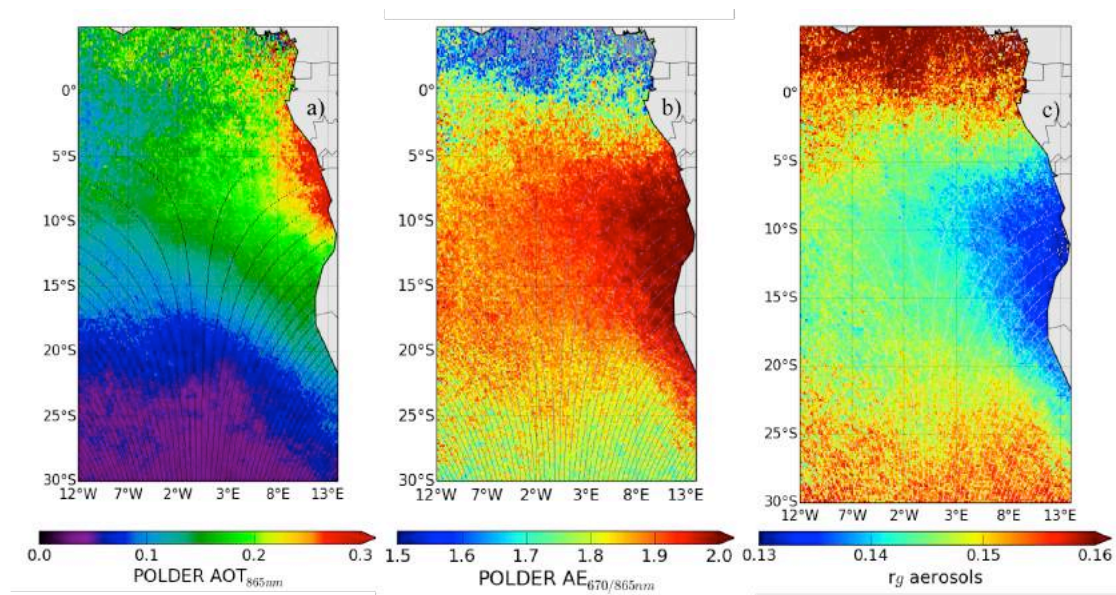


Figure 4.1 – POLDER mean values of aerosol above-cloud properties above the South Atlantic Ocean, for a period of six months (May to October) from 2006 to 2009: (a) AOT_{865nm} , (b) $AE_{670/865}$ and (c) aerosol granulometric radius (μm).

Figure 4.2 presents the evolution of the POLDER $AE_{670/865}$ with longitude. The color map (respectively the color bar) shows the 2D Kernel points density estimate: darker colored cells have more points around them than lighter colored cells. We observe that the majority of the $AE_{670/865}$ values are decreasing with longitude, for a constant AOT. This indicates a potential growth of the particle size due to aging as it is transported further away from the source, independently on aerosol load.

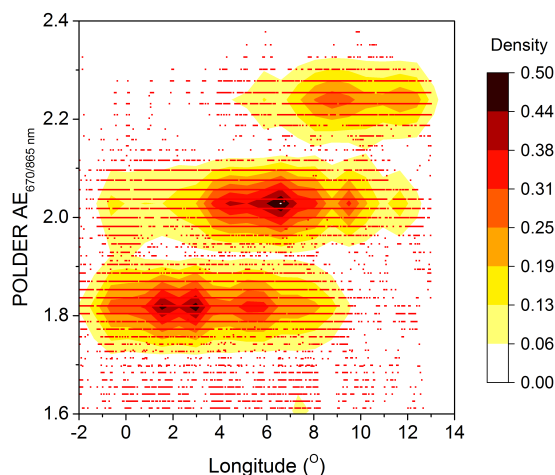


Figure 4.2 – POLDER $AE_{670/865 \text{ nm}}$ as a function of longitude for a horizontal transect of 1° of latitude and for a POLDER $AOT_{865 \text{ nm}}$ between 0.1 and 0.15. The color bar presents the 2D Kernel density estimate.

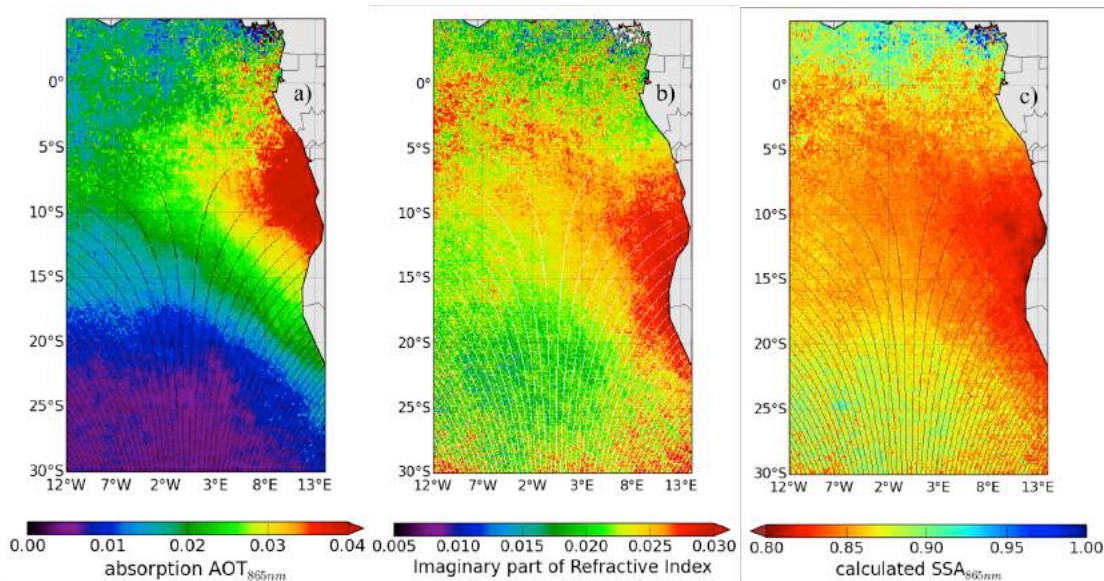


Figure 4.3 – Same as Fig. 4.1 for: (a) absorption $AOT_{865 \text{ nm}}$, (b) imaginary part of the refractive index and (c) aerosol single scattering albedo ($SSA_{865 \text{ nm}}$).

Information related to the absorption property of the aerosols is given by the absorption $AOT_{865 \text{ nm}}$, the imaginary part of the refractive index (k) and/or the single scattering albedo (SSA). For this region we observe high values of absorption $AOT_{865 \text{ nm}}$, which exceed 0.04 close to the coast (Figure 4.3a) and decrease progressively westwards. These estimates are consistent with the values calculated for the $SSA_{865 \text{ nm}}$ of 0.80 at seashore that increase to 0.87 around 12°W (Figure 4.3c) The observations are in agreement with the typical values provided by AERONET (Dubovik et al., 2002) and the field campaigns SAFARI-2000

(Leahy et al., 2007) and DABEX (Johnson et al., 2008) for the biomass-burning aerosols. The imaginary part of the refractive index, k , (Figure 4.3b) varies from 0.02 to 0.03 at 865 nm, and is an indicator of the chemical composition of the particles and their evolution in the presence of humidity (e.g. aging was found to modify the optical properties of aerosols by Jacobson (1999) and Lelieveld et al. (2002)).

North of the latitude 5°S, the SAO region is also under the influence of desert dust aerosols, as we can notice in Figure 4.3c. The $SSA_{865\text{ nm}}$ increases up to 0.97, which is characteristic to scattering type of particles (Dubovik et al., 2002), the size of the particles is also increasing with r_g surpassing 0.16 μm and the $AE_{670/865}$ is lower than 1.7 (Figure 4.1).

4.2.2 Cloud optical and microphysical properties

Low-level stratocumulus clouds, with some occurrences of cumulus and altostratus clouds typically cover the South Atlantic Ocean. Generally, the stratocumulus clouds are characterized by rather small droplets (r_{eff} of approximately 10 μm) and by optical thickness values of around 10-15 (Szczodrak et al., 2001). Haywood et al., (2004) found that, in the presence of above-cloud biomass-burning aerosols, the satellite retrieved COT can be underestimated by 20 % (especially over bright clouds with large COT) and r_{eff} can be overestimated by around 1-2 μm (especially for large droplets).

Figure 4.4a shows the mean COT retrieved with MODIS, while Figure 4.4b presents the mean POLDER COT that was corrected for the aerosol induced bias due to aerosol above-cloud absorption (Peers et al., 2015). We notice that MODIS COT values are lower compared to POLDER COT by about 5, where the overlying absorbing aerosols are located. This underestimation can impact the computation of the direct radiative effect (DRE) at the top of the atmosphere. Meyer et al. (2013) found an increase of the aerosol DRE at TOA of at least 2 $\text{W}\cdot\text{m}^{-2}$ when a corrected MODIS COT is used.

The MODIS cloud droplet effective radius (r_{eff}) (Figure 4.5a) is increasing from the coast towards the open sea, from 10 to 15 μm . As previously mentioned, these values are typical of stratocumulus clouds, but can include a bias of $\pm 2 \mu\text{m}$ in the retrievals, as the effect of aerosols above clouds was not corrected. The cloud altitude (Z_{O_2}) (Figure 4.5b) is calculated using the POLDER oxygen pressure method (P_{Oxygen}), which is determined from differential absorption between two spectral bands centered on the oxygen A-band (763 and 765 nm respectively) (Buriez et al., 1997; Vanbauce et al., 2003). This cloud pressure indicates mainly the cloud middle pressure (Ferlay et al., 2010), and in case of geometrically thicker clouds it is more distant from the cloud top pressure.

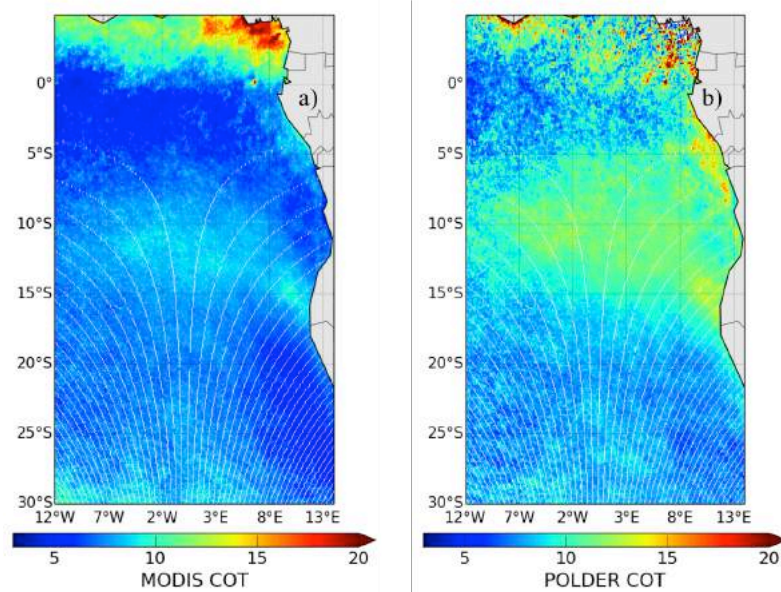


Figure 4.4 – (a) Mean cloud optical thickness retrieved with MODIS and (b) POLDER COT, over the South Atlantic Ocean for a period of six months (May to October) from 2006 to 2009.

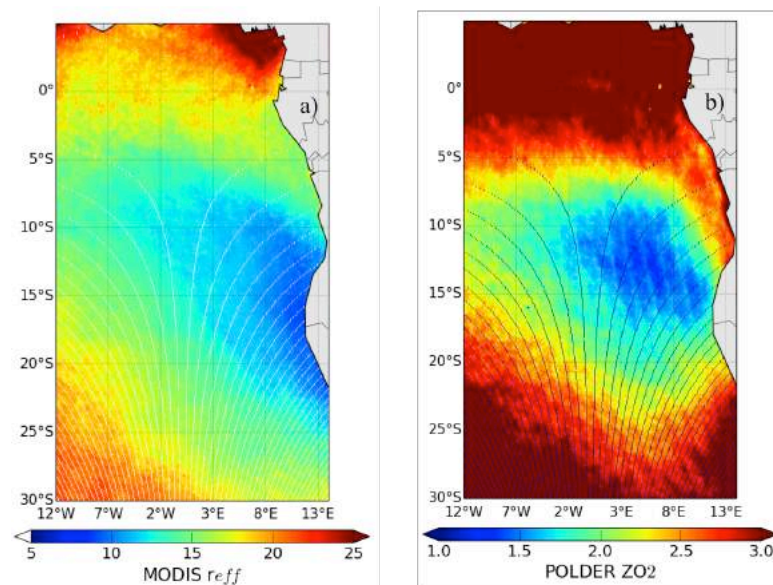


Figure 4.5 – (a) Mean cloud effective radius (μm) retrieved with MODIS and (b) cloud altitude (km) calculated from POLDER oxygen pressure, over the South Atlantic Ocean for a period of six months (May to October) from 2006 to 2009.

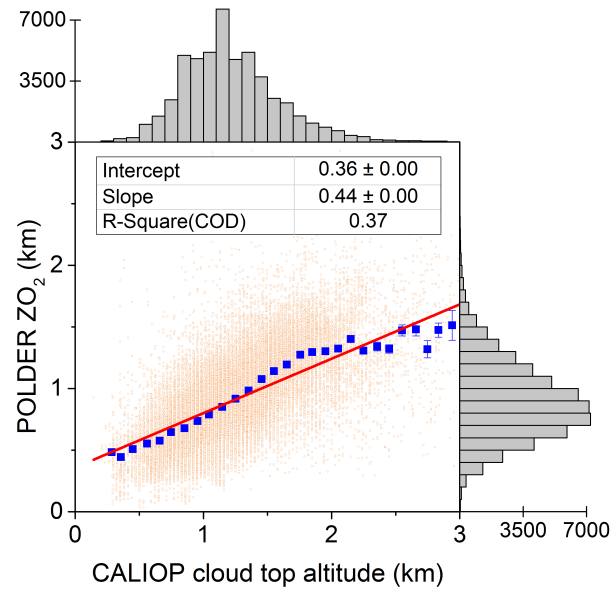


Figure 4.6 – POLDER cloud altitude (Z_{O_2}) is compared to CALIOP cloud top altitude. The data were retrieved over a period of six months (May to October) from 2006 to 2010 along the CALIOP track.

This explains the difference that we observed between POLDER Z_{O_2} and the CALIOP cloud top altitude (CTA) over a period of six months (May to October) from 2006 to 2010 along the CALIOP track (Figure 4.6): the two pressures are well correlated but Z_{O_2} is lower than CTA. From the lateral histograms, we notice that the majority of CTA values are centered around 1.25 km, while Z_{O_2} values are centered around 0.9 km. The difference between the products increases systematically when CTA exceeds 1.5 km. Nevertheless, the stratocumuli are low-level clouds, so, an underestimation of around 300 m by the POLDER product is more expected. In Figure 4.5b we observe a minimum cloud altitude of 1.2 km central to the stratocumulus deck, which increases radially as the stratocumulus become more fractioned (i.e. cumulus) or when the frequency of other types of clouds increases (Warren et al., 1988).

4.2.3 Evolution of cloud and aerosol altitudes with longitude

In this section we analyze the evolution of cloud and aerosol altitudes over the South Atlantic for a period of six months (May to October) from 2006 to 2010. The POLDER retrievals were collocated along the CALIOP track at 5 km horizontal resolution, following the approach described in Chapter 3, Section 3.1.1.

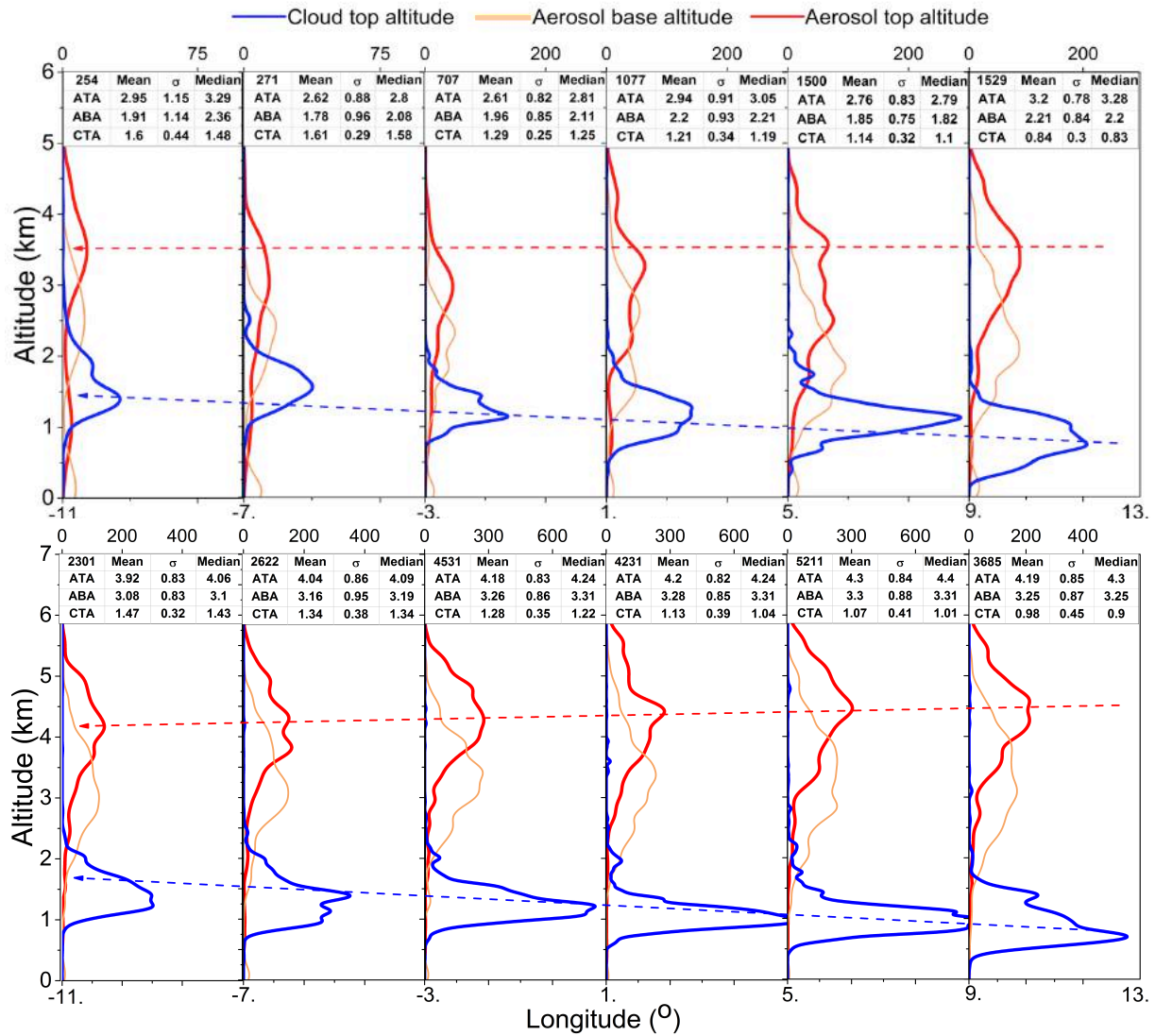


Figure 4.7 – First and second row of the panel present the histograms of the cloud top altitude (CTA), the aerosol top altitude (ATA) and the aerosol base altitude (ABA) as a function of longitude for two time periods: May to July and August to October, respectively, from 2006 to 2010. The mean, median and standard deviation over four degrees of longitude as well as the number of measurements are shown in the associated tables. The selected area extends from 30° S to 5° N and 12° W to 14° E over the South Atlantic Ocean (SAO).

We examined the evolution of the cloud and aerosol altitudes with longitude along the CALIOP track. Figure 4.7 presents the mean values of cloud top altitude, aerosol top altitude (ATA) and aerosol base altitude (ABA) for longitude bins of 4°. The data were retrieved with CALIOP operational method, for May-July in the first row and for August-October in the second row. The mean, standard deviation and median, as well as the number of measurements for each 4° bin of longitude are shown in the associated tables. For both time periods we notice the cloud top altitude increasing from 1.0 km to 1.5 km towards the west, implying that the clouds develop and become more convective further away from the coast. The average aerosol top altitude is higher during the second interval (August-October), and we observe a higher number of AAC situations. This is likely due to the fact that the biomass-

burning events that reach higher altitudes are most frequent during the late austral winter. It also seems that there might be an aerosol profile with two modes in the first period, mainly west of 1°E (upper left profiles): one mode around 3.0 km and another around 1 km, which may correspond to sea salt aerosols located in the boundary marine layer. Other aerosols, such as dust and pollutants could be also transported within the boundary layer. If in the first period the aerosol base and top altitudes are more or less stable, in the second period the average aerosol altitudes decreases from east to west. This suggests that contact situations between the cloud and the aerosol layers are less frequent close to the coast where the clouds are lower in altitude, and increase as the aerosols are transported westwards.

4.2.4 Air circulation patterns and meteorology

The pattern of the atmospheric circulation and meteorology play a determinant role in the transport of the low-level cloud cover and in the transport of aerosols emitted from the African continent. The air currents lift the aerosols at high altitudes and the horizontal winds carry them above the semi-permanent stratocumulus cloud deck above the South Atlantic Ocean. While the southern hemisphere trade winds consist of south-easterlies close to the surface, the atmospheric circulation is actually dominated by easterlies throughout the air column, as shown on Figure 4.8 (panels a, d and e) issued from Adebisi et al. (2015). The figure presents the average wind direction and speed for three pressure levels: 600 hPa (where aerosols mainly reside), 800 hPa (above clouds) and 1000 hPa (close to surface): from July to October the Southern Hemisphere is influenced by the Atlantic anticyclone in altitude, at 600 hPa and 800 hPa, and the trade winds at the surface (with winds stronger than $5 \text{ m}\cdot\text{s}^{-1}$).

During September-October (SO) we observe differences compared to July-August (JA) period (panels b, d, f). Around 600 hPa, the anticyclone is stronger during the austral spring over South of Africa (the geopotential height corresponding to 600 hPa is lower with 20 m during SO), which strengthens the 600-hPa easterlies at around 10°S. In the same time, the 800-hPa shallower anticyclone moves southwards (off the west coast of Africa), allowing the easterlies to strengthen even more. This process determines a maximum coverage of the stratocumulus clouds in SO and, more importantly, a maximum in the continental aerosol loading transported westwards over the Atlantic basin, around 10°S.

The Southern Hemisphere is also characterized by two different humidity and temperature regimes: larger values are found north of 20°S compared to the southern region. Adebisi et al. (2015) described also a general increase in the midtropospheric moisture at 600 hPa during September-October, suggesting an association between the aerosol loading and moisture.

This seasonal cycle of the meteorological parameters can also influence the cloud optical and microphysical changes observed in previous studies (Costantino and Bréon, 2013; Johnson et al., 2004b; Wilcox, 2010). These circulation patterns can impact the stratocumulus clouds by changing the thermodynamic environment, regarding of the presence (or absence) of aerosols above clouds. Therefore, to analyze the semi-direct effect of aerosols in the South

Atlantic Ocean, it is first necessary to separate (or constrain) the effects of meteorology on clouds from the variations caused by AAC. This brings us to our methodology and the first set of results that attempts to investigate if there is a connection between the aerosol loading, meteorological parameters and cloud adjustments over a sampled region in the SAO.

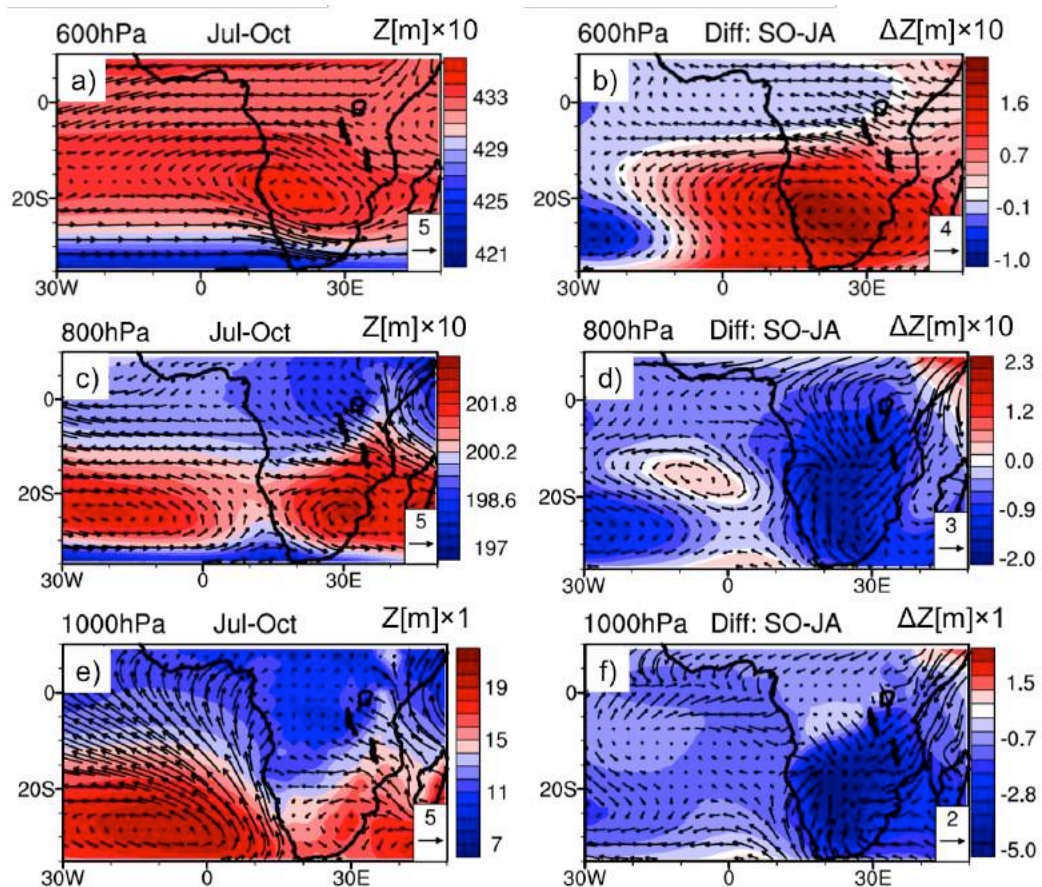


Figure 4.8 – ERA-Interim composite for July-October (left panels) and the September-October minus July-August (SO-JA) difference (right panels) for geopotential heights [m] and winds [$\text{m}\cdot\text{s}^{-1}$] for different pressure levels: (a-b) for 600 hPa, (c-d) for 800 hPa and (e-f) for 1000 hPa (Source: Adebisi et al. (2015)).

4.3 Aerosol effect at a local scale

The objective of this study is to analyze the statistical relationship between aerosols, clouds and meteorological parameters, which requires a large number of measurements. However, we need to account for the sensitivity of clouds to the meteorological variations.

Observations over long time spans and large areas (such as SAO) increase the sample size but, in the same time, they include meteorological variability that brings about different characteristics for clouds and the overlaid aerosols. Shorter intervals focused on different meteorological cycles contain statistically lower number of retrievals, but may exclude cloud natural variability due to meteorological factors and give more information of the cloud changes due to aerosol effects. Therefore, a compromise has to be made in order to keep a sufficiently large number of data, but to minimize the meteorological variability and its effects.

4.3.1 Strategy of observation and selection of a small area

In our study we selected a region close to the Angola's coast that expands from 15° to 10° S and 6° to 14° E, which is close to the main stratocumulus region identified by Klein and Hartmann (1993). The variability of meteorological parameters in this sample area is emphasized in Figure 4.9, which presents three meteorological parameters computed using the ERA-Interim reanalysis product, from June to October 2008. We can observe that the temperature profile doesn't much fluctuate throughout this period, while the relative humidity (RH) and the specific humidity (q_v) change from month to month. In June and July the moisture level is comparable, with values of q_v lower than 2.5 g.kg^{-1} at 700 hPa, in contrast with the retrievals from August and September where q_v is reaching 5 g.kg^{-1} at 700 hPa. In October, the RH shows a strong peak between 700 and 500 hPa, and the q_v is also larger compared to previous months.

Figure 4.10 illustrates the average monthly horizontal winds, from June to October 2008 over the zone. They show a significant difference between the months of SO compared to JJA. The winds are much stronger in SO and much more westwards above 800 hPa. The wind speed also increases above 800 hPa during these months. Winds in August differ from the winds in June/July, but not significantly below 800 hPa.

Knowing these temporal variations of mean meteorological parameters we chose to analyze the aerosol and cloud parameters and their correlation over the months of June to August 2008. Doing so, we select one main meteorological cycle characterized by few differences at the cloud altitudes in terms of wind, temperature and humidity and a moderate water vapor content at the aerosol layer. Moreover, we selected the area close to the coast because the frequency of detached aerosol layers from the underneath cloud is higher.

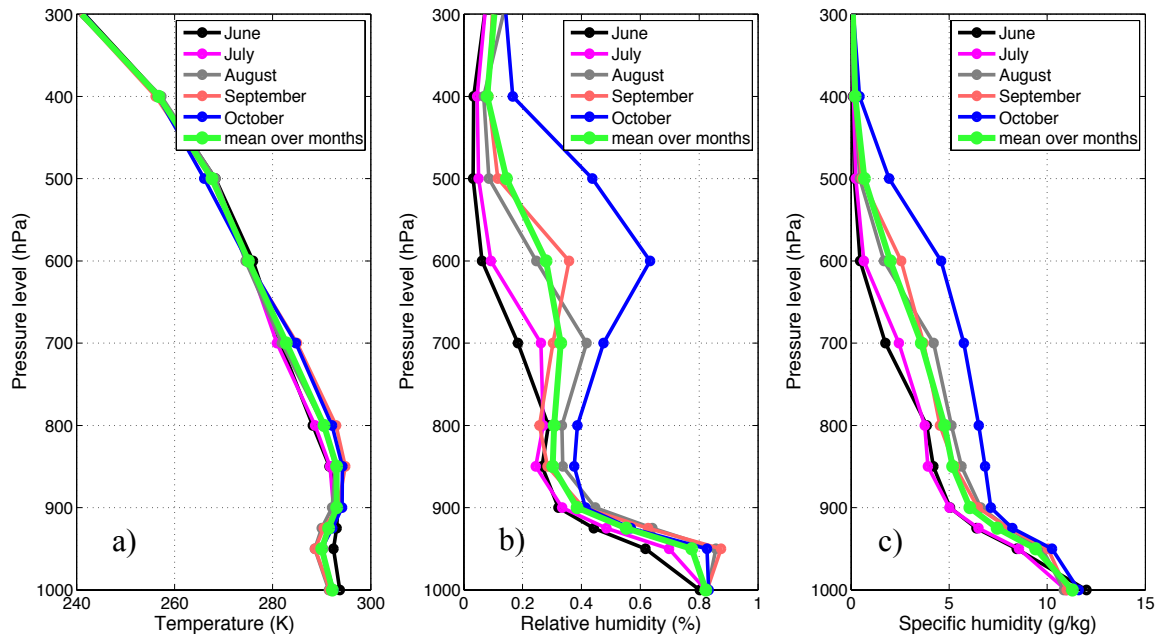


Figure 4.9 – Variation of the meteorological parameters computed with ERA-Interim model at 12h UTC, from June to October 2008, over the sampled area: (a) temperature (K), (b) relative humidity (%) and (c) specific humidity ($\text{g}\cdot\text{kg}^{-1}$)

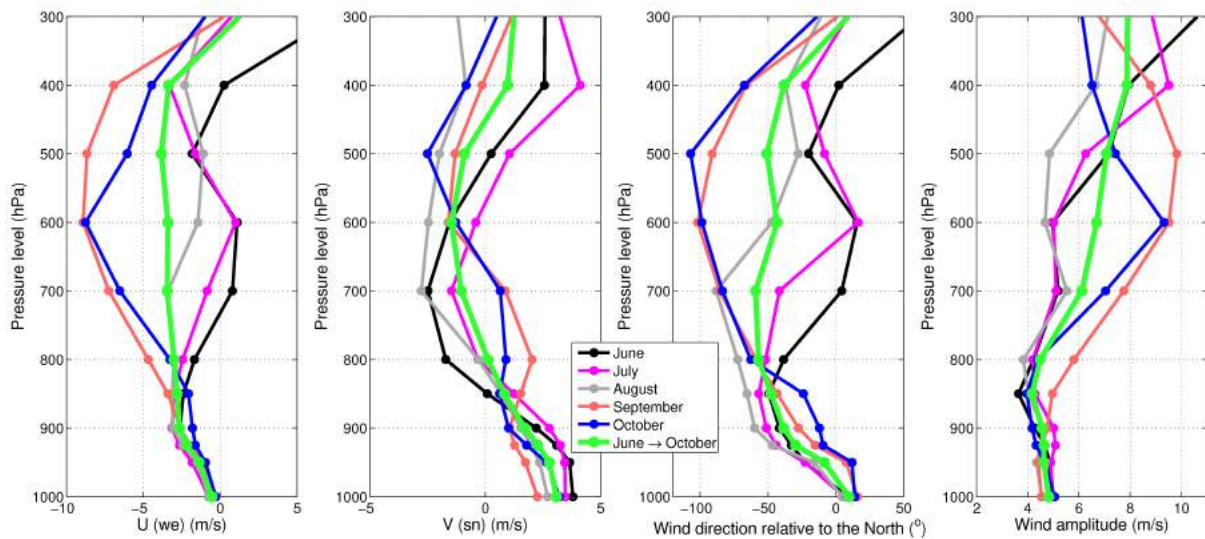


Figure 4.10 – Average monthly wind vectors U (easterlies) and V (northerlies) and derived wind direction and wind speed within the sample region, for June to October 2008.

4.3.2 Covariance between humidity and aerosol loadings

As a first step, we analyze the mean values of the specific humidity from June to August 2008 over the sampling area, at different pressure level as a function of the aerosol loading to identify any connection between these parameters. In Figure 4.11 we compare the ERA-Interim q_v values at 6 pressure levels, with POLDER AOT_{865nm} . The results show that at the surface and at 950 hPa, the q_v is almost constant, varying slightly with the AOT from 10 to 12 $g.kg^{-1}$ and from 7.5 and 10 $g.kg^{-1}$, respectively. Higher in altitude, at 500 and 400 hPa the mean values of q_v are very small, despite of the aerosol loading. On the other hand, at the smoke plume level, at 850 and 700 hPa we notice a strong increase of the q_v with the AOT, from 2 to 7 $g.kg^{-1}$ and from 1 to 5 $g.kg^{-1}$, respectively. An interpretation of the humidity reinforcement with larger biomass-burning AOT could originate from combustion processes.

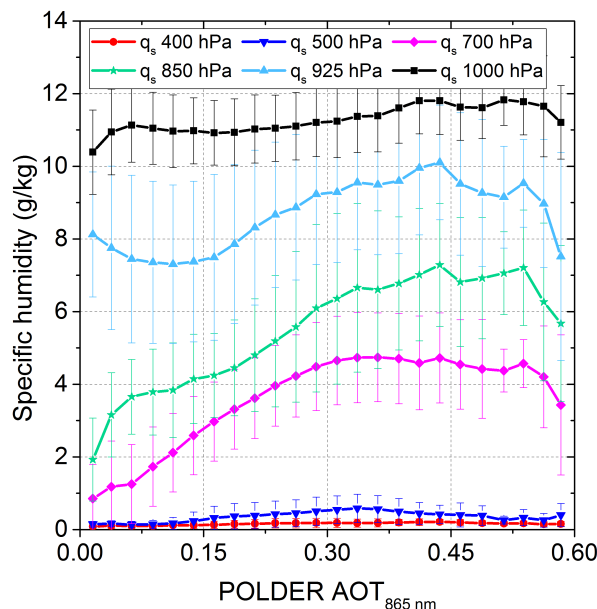


Figure 4.11 – Mean specific humidity as a function of POLDER AOT_{865nm} retrieved within the selected region over June-August 2008. The vertical bars represent the standard deviation for the specific humidity.

Depending on the fire intensity and the meteorological conditions, smoke parcels can be saturated with water vapor and the latent heat resulted from the condensation of the water vapor can enhance the vertical development of convection due to additional buoyancy. It is possible that smoke and water vapor released during biomass combustion are advected at higher altitudes, which contributes to the humidity in the aerosol plumes. Through laboratory measurements and experimental studies scientists have attempted to confirm that water vapor from wild-land or grass fires can significantly modify the dynamic of the lower troposphere. Some of their results suggested that the fuel moisture could make a significant contribution to

the humidity within the aerosol plumes resulted from biomass combustion (Clements et al., 2006; Parmar et al., 2008; Potter, 2005) while others consider that the released amount is unimportant to be taken into account (Luderer et al., 2006, 2007; Trentmann et al., 2006). Another hypothesis, however less probable, implies two different air masses, one moist and the other one carrying the smoke particles, may merge in one atmospheric parcel due to air mixing and circulation.

This result suggests a strong connection between the increase of aerosol loading and the increase in moisture at higher altitudes. Therefore, when investigating the aerosol effects one has to take into account the presence of water vapor with the aerosol or it may introduce biases in the estimation. In our study, this separation is one of the main objectives.

4.3.3 Strategy for an insight: the thread of thought

Our observation, based on Figure 4.7, is that the aerosol layer is mostly distant from the low-level cloud cover. Our hypothesis is that the smoke layer has an effect – at distance – on the cloud below. It has to be through an energetic forcing, that necessarily involves radiative processes. They will act directly or indirectly on the lower cloud cover. As an example, one could think about a solar shadowing effect, or about an infrared greenhouse (blanket) effect.

More precisely, the presence of a layer-containing aerosol within a moisture profile will modify the radiative heating rates in the atmospheric column, as a consequence of radiative processes that are absorption, scattering and emission of radiation. It is also the case for high-level clouds (Christensen et al., 2013). Heating rate's variation - if at the cloud layers – will directly impact cloud processes. We know that clouds experience generally a cooling at their cloud tops, which is the results of a radiative cooling and an evaporative cooling. Both act as drivers to create cloud top turbulence, mixing in the cloud layer, and small-scale dry air entrainment (Zuidema et al., 2009).

Moreover, the heating rate's variation at the layers surrounding the cloud (i.e. its environment) will modify the thermodynamic state of this environment, and so indirectly the cloud through a modification of his behavior. Indeed the atmospheric stability of this environment will be modified, which will affect the cloud ascent and its air entrainment capacity (Bretherton et al., 2004).

In the next section, we will perform radiative transfer calculation, and compute the solar radiative forcing caused by smoke episodes, as well as the associated profiles of heating rates. We note that smoke episodes consist of above cloud absorbing aerosols with a profile of water vapor, that both absorb radiation and are a very efficient greenhouse gas.

4.3.4 Calculation of radiative forcing of aerosols above clouds

We give below the detailed information about the radiative transfer study we performed, whose objective is to compute the radiative impact of aerosol above clouds in the studied area and the time period considered. The radiative quantities we show first are in the shortwave domain and are the aerosol radiative forcing at the top-of atmosphere, the warming rate within the aerosol layer, and the perturbation of the downwelling flux at the cloud top. Then we show the heating rate in the visible and infrared spectrum, and the total heating rate. These quantities are important, as they will indicate the magnitude of aerosol forcing over this area in this period. The level of perturbation of the chosen radiative quantities might be determinant for cloud processes.

Firstly, we describe the inputs of our RT calculation, and our strategy to describe in the more realistic way the atmospheric composition and its radiative properties. For this we realized a synergy between POLDER retrievals of aerosol and cloud properties, CALIOP vertical profiles and meteorological parameters derived from the ERA-Interim product. These parameters are then used as input in the GAME radiative transfer code, with which we simulated the effect of aerosols and water vapor in the shortwave spectrum, and only the water vapor radiative forcing in the longwave spectrum, as we considered a negligible effect of aerosols.

An initial study is the computation of heating rates for a biomass-burning case retrieved on 4 August 2008 off the coast of Namibia, for which we will show the input and the output parameters of GAME radiative transfer code. Afterwards, we will present the results of the heating rates computed over the South Atlantic sampling area.

4.3.4.1 Biomass-burning study case

Initially, POLDER data were collocated with the CALIOP retrievals of aerosol and cloud vertical profiles to gain information about the aerosol position relative to the cloud and their optical properties. The CALIOP altitude retrievals at 532 nm show that the aerosol layer is clearly detached from the cloud, with cloud top altitude decreasing from 1.25 to 0.75 km with latitude, the aerosol base altitude between 1.75 and 4 km and the cloud top altitude at around 4.6 km. As mentioned in Chapter 3, the CALIOP method can underestimate the geometrical thickness of the aerosol layer when the optical thickness is large enough, due to the attenuation of the backscattered signal (Jethva et al., 2014). A recent study that uses independent lidar backscattering measurements at 1064 nm of the Cloud-Aerosol Transport System (CATS), shown that the CALIOP algorithm probably overestimate the base of the aerosol layer by 500 m (Rajapakshe et al., 2017). Therefore, it is likely that the ABA values are slightly lower than the ones presented in Figure 4.12a. The majority of cloud optical and microphysical properties are typical for low-level stratocumulus clouds. The MODIS r_{eff} and the POLDER COT corrected for above-cloud aerosol effects are varying between 6 and 11 μm , respectively between 5 and 40 (Figure 4.12b). The MODIS COT is shown only for comparison, as it is not used in the radiative forcing computation.

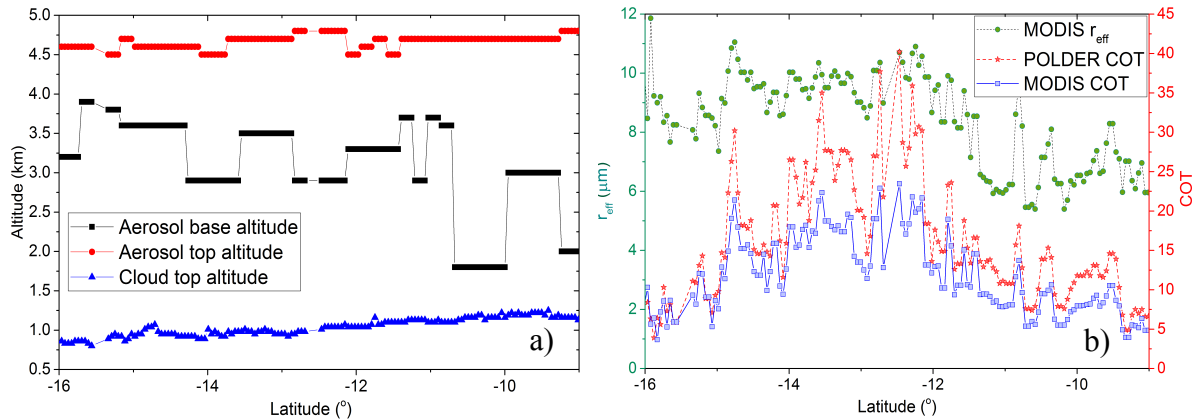


Figure 4.12 – Biomass-burning study case on 4 August 2008: (a) cloud top altitude and aerosol base and top altitudes as a function of latitude; (b) MODIS COT and r_{eff} and POLDER COT corrected for absorption as a function of latitude.

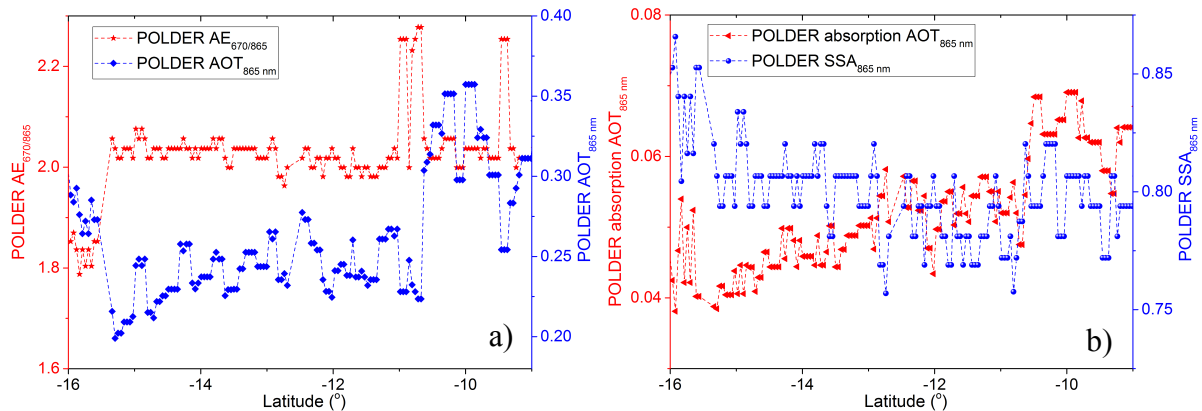


Figure 4.13 – Same as Fig. 4.6: (a) POLDER AOT_{865} nm and $AE_{670/865}$ nm as a function of latitude; (b) POLDER absorption AOT_{865} nm and SSA_{865} nm as a function of latitude.

The aerosol optical properties retrieved with POLDER method are presented in Figure 4.13. The measurements show that the smoke layer has large values of AOT with values ranging between 0.2 and 0.35 at 865 nm, and values for the $AE_{670/865}$ (> 2.0) characteristic for fine mode particles (Dubovik et al., 2002). POLDER $SSA_{865\text{nm}}$ is varying between 0.75 and 0.86 and the absorption $AOT_{865\text{nm}}$ has values between 0.04 and 0.07, representative for highly absorbing aerosols.

In addition to the vertical distribution of aerosol and clouds and their optical and microphysical properties, GAME model requires information on the vertical structure of the atmosphere. The vertical profile of meteorological parameters that are temperature and humidity, play a determinant role in the radiative computation in the longwave spectrum, as the water vapor is the main acting gas in the infrared domain. The temperature profiles were generated using ECMWF reanalysis. The water vapor content profile (wv) was calculated using the specific humidity (q_v) profile with the following equation:

$$wv = \frac{q_v \times \Delta P \times 10}{g} \quad (\text{Eq. 4.2})$$

where wv is the water vapor content (g.cm^{-2}), q_v is the specific humidity (kg.kg^{-1}), ΔP is the atmospheric pressure (hPa) between two altitudes, 10 is a conversion factor and g is the gravitational acceleration ($\approx 9.81 \text{ m.s}^{-2}$).

In GAME the computation is made for plane-parallel layers of atmosphere, each layer characterized by particular values of aerosol (or cloud) and meteorological parameters. We have divided the lower troposphere into 100 m-thick layers from the surface up to 8 km. Above this altitude (up to 100 km) the layers are more roughly distributed, as the upper atmosphere is not under the influence of biomass-burning aerosols and less our field of interest. For each 100 m-aerosol layer we provided the CALIOP extinction coefficient (σ_e , $\text{km}^{-1}.\text{sr}^{-1}$).

However, the CALIOP miscalculation of the aerosol bottom altitude would implicitly underestimate the aerosol extinction profile (i.e. the AOT), hence the aerosol radiative forcing. Therefore, in our study we will use the POLDER AOT_{865nm} retrieved under the CALIOP track to normalize the CALIOP σ_e profile used in GAME. As the POLDER AOT is retrieved at 865 nm and the CALIOP σ_e is at 532 nm, the σ_e normalization firstly requires an extrapolation of POLDER AOT at 532 nm. Afterwards, we infer the resulted CALIOP $\sigma_{e,\text{normalized}}$ at 550 nm, which is the wavelength used for AOT in the radiative transfer model. This procedure may bias the $\sigma_{e,\text{normalized}}$ profile. Nonetheless, the obtained values are more accurately describing the optical properties of the aerosol layer that the initial CALIOP σ_e . The extinction coefficient will be larger for the same geometrical thickness of the aerosol layer; therefore the mid-tropospheric shortwave absorption due to aerosols will be confined in this layer.

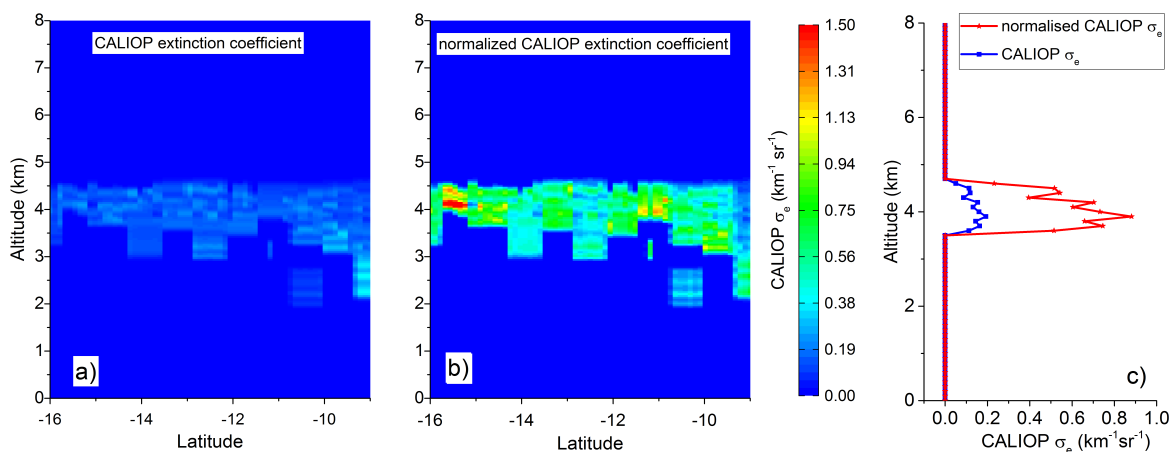


Figure 4.14 – Biomass-burning study case: (a) CALIOP original extinction coefficient (m^{-1}) at 532 nm ($\sigma_{e,532\text{nm}}$), (b) CALIOP normalized $\sigma_{e,532\text{nm}}$ as a function of latitude; (c) example of CALIOP extinction coefficient profile at 532 nm (blue) and the result of normalization (red) with the POLDER AOT extrapolated at 532 nm.

The left panel of Figure 4.14 shows the initial aerosol CALIOP σ_e at 532 nm along the lidar track, while the middle panel displays the CALIOP $\sigma_{e,normalized}$ at 532 nm. We clearly observe the CALIOP underestimation of the layer's optical thickness and it is obvious that, if used, these values lead to misinterpretation of the aerosol effects in models.

The following figures display the GAME output parameters along the CALIOP track for the biomass-burning case. It is worth mentioning that the calculations were made for the CALIOP passing hour, around 13:30 h local time, therefore the incoming solar radiation is close to maximum, as the solar zenith angle is small.

The results of the radiative transfer model (Figure 4.15) in the shortwave spectrum consist in direct radiative effect (DRE) at the top of the atmosphere (TOA), warming rate within the aerosol layer and the perturbation of the solar downwelling flux reaching the cloud top in situations with and without aerosols. DRE at TOA is influenced by the absorbing characteristics of the aerosol layer as well as the cloud optical properties: it varies between 20 and 150 $W.m^{-2}$ along the track. We calculated a shortwave radiative warming rate in $W.m^{-3}$ that describes the mean radiative energy absorbed within the aerosol layer due to the absorption of the solar radiation by the aerosol and the water vapor. We notice that the aerosol layer warming rate values increase with the aerosol loading (see Figure 4.13a) from 120 to 270 $W.m^{-3}$. The so-called “perturbation at the cloud top” parameter ($W.m^{-2}$) is calculated by making the difference between the downwelling solar fluxes that reach the cloud top in situations with and without aerosols above clouds. The absolute value of the cloud top perturbation are highly positively correlated with the warming rate: the larger the energy trapped in the upper aerosol layer, the less downwelling solar radiation is reaching the cloud surface.

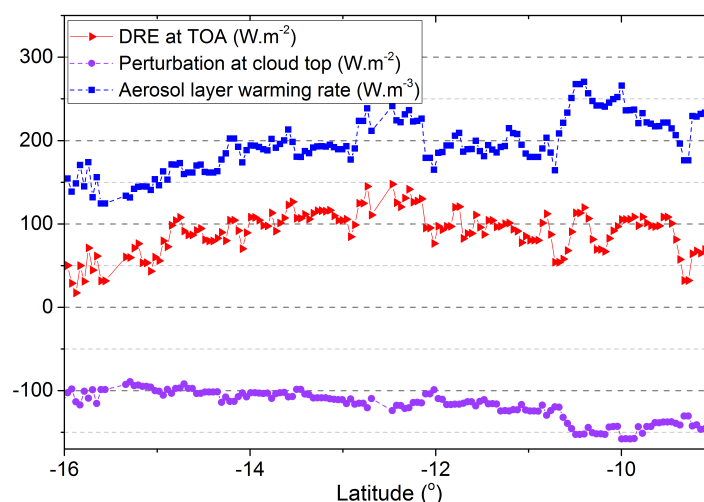


Figure 4.15 – Direct Radiative Forcing at the Top of the Atmosphere ($W.m^{-2}$), perturbation at the cloud top ($W.m^{-2}$), and aerosol layer warming rate ($W.m^{-3}$) as a function of latitude.

This computation shows a significant radiative effect of aerosols on important radiative quantities, along the track: the DRE at TOA is positive, with a mean value of $+86.5 \pm 29 \text{ W.m}^{-2}$ that depicts a warming of the Earth's atmosphere; the aerosol layer is warming on average with $+193.5 \pm 41.3 \text{ W.m}^{-3}$, and the cloud top receives with $-117.9 \pm 25.3 \text{ W.m}^{-2}$ less energy in case of aerosol above clouds. These values vary with the aerosol loading and the water vapor in the atmosphere.

To go further, we computed the instantaneous heating rate (HR) profiles (K/day) in the shortwave and in the longwave domains (HR_{SW} and HR_{LW}). The first is due to the vertical profiles of aerosols and water vapor. The second is the result of infrared absorption and emission processes, and depends mainly on the profile of atmospheric component, cloud and water vapor, with their temperatures. For the calculation of heating rates in both domains, the vertical location of the cloud layer and its radiative properties are, of course, important. The sum between HR_{SW} and HR_{LW} gives total heating rate (HR_{total}).

In an atmosphere with no aerosols, the heating rates depend only on the molecular and gaseous absorption of the shortwave and longwave radiation. Figure 4.16 shows an example of the HR_{SW} , HR_{LW} and HR_{total} for an atmosphere with clouds and water vapor but without aerosols. We observe a strong cooling at the cloud level ($\text{HR}_{\text{LW}} = -65 \text{ K/day}$) driven by the longwave emission at the cloud top and a cooling of about -5 K/day between 4.5 and 5.5 km, where the water vapor values are larger. The shortwave heating rate due to water vapor absorption shows: a gradual heating from the surface to the cloud top, where the maximum value is about 11 K/day , and a small heating of approximately 3 K/day at larger altitude. The total heating rate is mostly negative, except below the cloud to the surface level. This result underlines the importance of considering the shortwave absorption of water vapor separately from the aerosol absorption, when computing the shortwave heating rates.

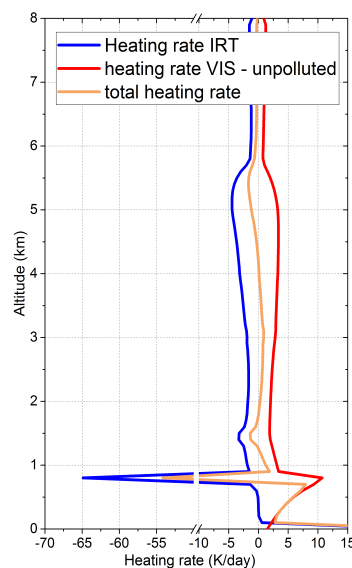


Figure 4.16 – Heating rate profiles (K/day) calculated for a “clean” atmosphere: shortwave heating rate (red line), longwave heating rate (purple line) and total heating rate (yellow line).

We now present the results for the biomass burning heating rates in shortwave, longwave and their balance. Figure 4.17a shows the values of HR_{SW} : at the altitude of the aerosol layer the values exceed 20 K/day (with a maximum of 25 K/day). They are mostly induced by aerosol absorption, as the previously computed water vapor contribution doesn't exceed 3 K/day; at cloud top the values reach 12 K/day mainly driven by the cloud droplets and water vapor absorption of shortwave radiation. We also notice small heating above the aerosol layer (around 3 K/day) that is due to the water vapor solar absorption.

In longwave (Figure 4.17b), once again we observe a strong cooling of the cloud top layer due to the loss of outgoing longwave radiation. The scale has been fixed between -8.0 and 1 K/day, but the true extremes of the HR_{LW} are between -65 K/day at the top of the cloud and 27 K/day at surface. The upper atmosphere is cooled up to a maximum HR_{LW} of -5 K/day at 5 km, right above the aerosol layer. At the altitude of the aerosol layer the cooling is connected to the increase in water vapor content with the aerosol loading (as seen in Figure 4.11). Also at 1.5 km the cooling can correspond to the temperature inversion usually observed above stratocumulus clouds, as the longwave HR depends also on the ambient conditions and not only on the emissivity of the water vapor.

The total heating rate (HR_{total}) is given in Figure 4.18. It shows that the atmosphere is heating where the aerosols reside mainly due to aerosol absorption of the shortwave radiation. The values range between -55 K/day at the top of the cloud layer and 27 K/day within the aerosol layer. The rest of the atmospheric column is slightly cooled (between -1 and -3 K/day). The cooling of the atmosphere partly compensates the shortwave warming, except under the cloud level where the water vapor and the clouds are heating the atmosphere. It might be worth noticing that at some locations a warming appears at the bottom part of the aerosol layers, while a cooling exists at its top. It could encourage mixing processes within the aerosol layer.

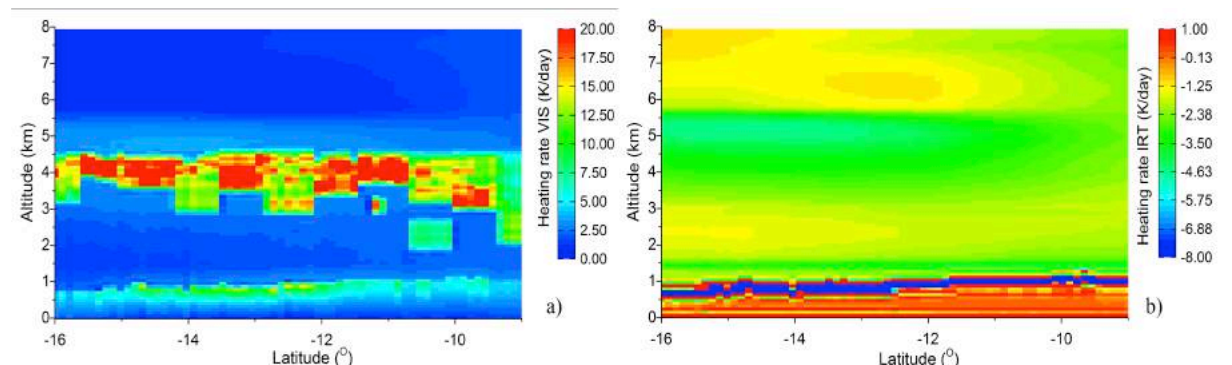


Figure 4.17 – Instantaneous heating rate (K/day) profiles calculated using GAME radiative transfer code in the shortwave spectrum, HR_{SW} (a), and in the longwave spectrum, HR_{LW} (b).

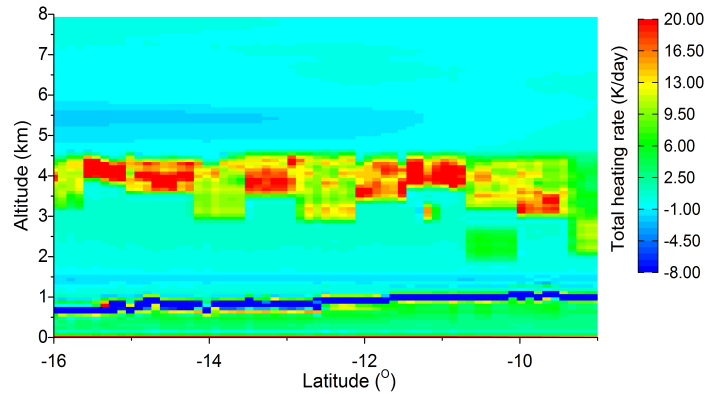


Figure 4.18 – Instantaneous heating rate budget HR_{total} (K/day) profile for the biomass-burning study case as a function of latitude.

4.3.4.2 Radiative effect over the sampled area

After having computed the profiles of heating rate under the CALIOP track, we now extend our study to the entire sample area close to Angola's coast and for the entire period of June to August 2008. It will provide information about the typical variability of the heating rates over the zone. The simulations were made initially for individual CALIOP tracks, thus taking into account the variability of aerosol and cloud properties, and then averaged for 0.5° bins of longitude.

Figure 4.19 shows the average POLDER AOT_{865nm} and COT per bin of longitude. In general, the AOT_{865nm} has values around $0.2 (\pm 0.5)$, except at 9.75° longitude where it reaches 0.4. POLDER COT varies between 6 and 22, the larger value corresponding to the highest value of AOT. Other aerosol and cloud properties that characterize this area are shown in Annex A.

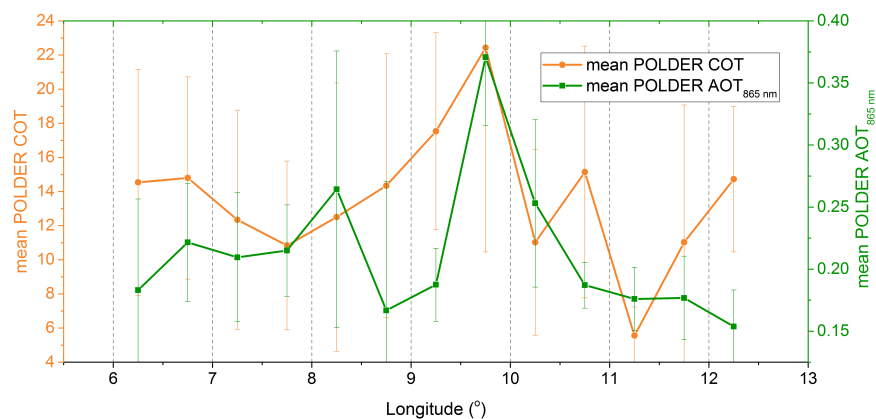


Figure 4.19 – Mean POLDER AOT_{865nm} and COT corrected for aerosol absorption as a function of longitude, over the sample area for June-August 2008. The mean was computed for 0.5° bin of longitude. The vertical bars represent the standard deviation.

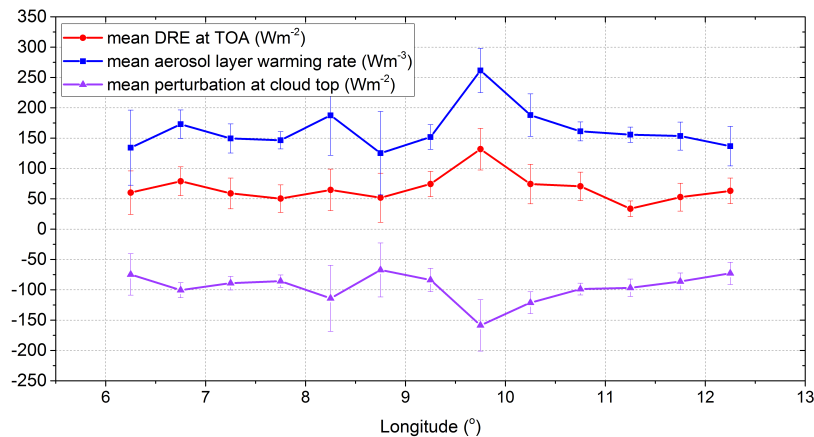


Figure 4.20 – Direct radiative effect at the top of the atmosphere ($\text{W}\cdot\text{m}^{-2}$), incident solar flux perturbation at the cloud top due to the presence of aerosols above clouds ($\text{W}\cdot\text{m}^{-2}$), and net radiative heating rate trapped in the aerosol layer ($\text{W}\cdot\text{m}^{-3}$), as a function of longitude.

The results of the radiative transfer model show values close to the ones obtained under one CALIOP track: the DRE at TOA and the warming rate within the aerosol layer are correlated, while the cloud top perturbation is anti-correlated with these two parameters. The instantaneous shortwave DRE at TOA (Figure 4.20) has values between 50 and $120 \text{ W}\cdot\text{m}^{-2}$, with an average of $66.7 \pm 23.2 \text{ W}\cdot\text{m}^{-2}$. The maximum value corresponds to the largest POLDER $\text{AOT}_{865\text{nm}}$ and COT. These positive values of DRE show that the aerosols reduce the local albedo by absorbing solar radiation, generating a warming of the atmospheric column. This is portrayed also by the aerosol layer warming rate, with values that vary as a function of the aerosol loading from 150 to $250 \text{ W}\cdot\text{m}^{-3}$, with a mean of $163.5 \pm 35 \text{ W}\cdot\text{m}^{-3}$. The negative values of the perturbation at the cloud top (between -70 and $-150 \text{ W}\cdot\text{m}^{-2}$, and a mean of $-96 \pm 24.4 \text{ W}\cdot\text{m}^{-2}$) suggest that there is less downwelling solar flux reaching the lower atmospheric layers and the cloud top. As expected, the lowest values appear where the POLDER AOT is largest. We observe interdependence between the three retrieved parameters and the aerosol loading in the atmosphere.

Figure 4.21 presents the mean profile of the heating rates (K/day) computed in shortwave, longwave and their budget, for “clean” situations (in which we disabled the aerosol loading for the same water vapor content, panel a) and for smoke events (panel b). This helps having a better appreciation of the average aerosol and water vapor contribution on the radiative budget in the area.

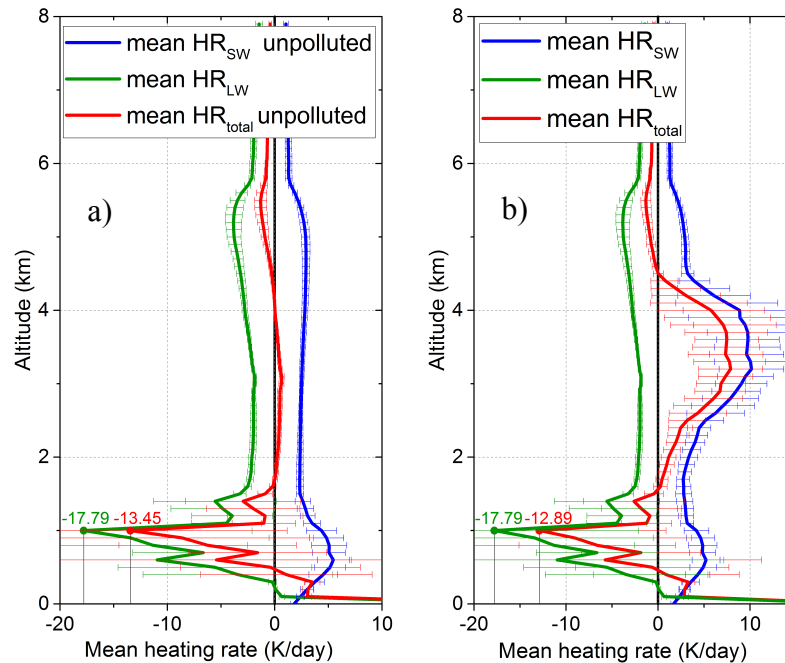


Figure 4.21 – Average heating rate for “clean” cases (a) and polluted situations (b), over the sample area, from June to August 2008: shortwave HR (blue line), longwave HR (green line) and total HR (red line). The horizontal bars represent the standard deviation.

We observe that most of the warming in the atmosphere occurs where the smoke resides (between 2.5 and 4.5 km). The HR_{SW} maximum value is 9 K/day, of which the water vapor contributes with 3 K/day (seen in panel a). The heating observed above 4.5 km is due to the shortwave radiation absorbed by the water vapor; at the cloud level the warming comes from solar absorption by water vapor and cloud droplets. There is a longwave cooling at the cloud level, with mean HR_{LW} of approximately -18 K/day and in the upper atmosphere a mean cooling up to -5 K/day. In case of polluted situations, the budget of the heating rates at the aerosol level shows that the aerosols warm the layer with an average HR_{total} of 6 K/day, while water vapor has an overall effect close to null over the cloud layer, with a compensation between its induced solar heating and infrared cooling. At the cloud level the mean HR_{total} has negative values: in the “clean” cases the HR_{total} at cloud top reaches -13.5 K/day, while in the presence of above cloud aerosols, the value decreases to -12.9 K/day. This difference represents the average effect of aerosol above cloud on the cloud top heating rate, as they act as a blanket, blocking the radiation to reach the cloud’s surface. At surface the longwave absorption leads to a strong warming, with values larger than 20 K/day.

In Annex A we attached the mean heating rate profiles determined for 0.5° bins of longitude within the sampled area, that show the variability of HR with the aerosol loading and longitude.

Overall, we can conclude that the sample area is globally under the energetic influence of absorbing aerosols. Indeed, generally there is a warming at the altitude where aerosols

reside that is mainly due to aerosols. While they create also a global positive shortwave direct effect at the top of the atmosphere, they produce also a global decrease of the cloud illumination. Finally, we observe that over the sample area there is a radiative cooling at the cloud top layers, slightly different between the case “clean” and the case with aerosols. This difference, of 0.56 K/day, is the average aerosol contribution at the cloud top in shortwave.

Actually, by removing aerosol radiative effects in our calculation, we did not really get an idea of the difference between radiative forcing for atmospheric columns loaded or less loaded in aerosols. To reach this goal, we have to account for the covariance between humidity and aerosol, not just turn off the aerosol loading and compare. Below we will use the observations to analyze the sensitivity of cloud parameters to a difference between two scenarios of aerosol and water vapor loadings: high and low.

4.4 High and low aerosol loading approach

In order to better understand the aerosol-cloud-radiation interactions, and to disentangle the aerosol effects on clouds from the meteorological impacts, we will investigate the variation of cloud properties and meteorological parameters for two aerosol scenarios: polluted and quasi-pristine cases.

For this study we chose to make the analysis over the same sample area and period as in the previous section, because of all previous reasons and because we have a comparable number of data between the pristine and polluted cases. Our strategy is to separate the situations of aerosols above stratocumulus clouds into two categories: cases that present low absorption AOT_{865nm} , which are close to pristine scenes, and are mainly retrieved during June-July, and cases with high absorption AOT_{865nm} that are typical for pollution events, mainly during August.

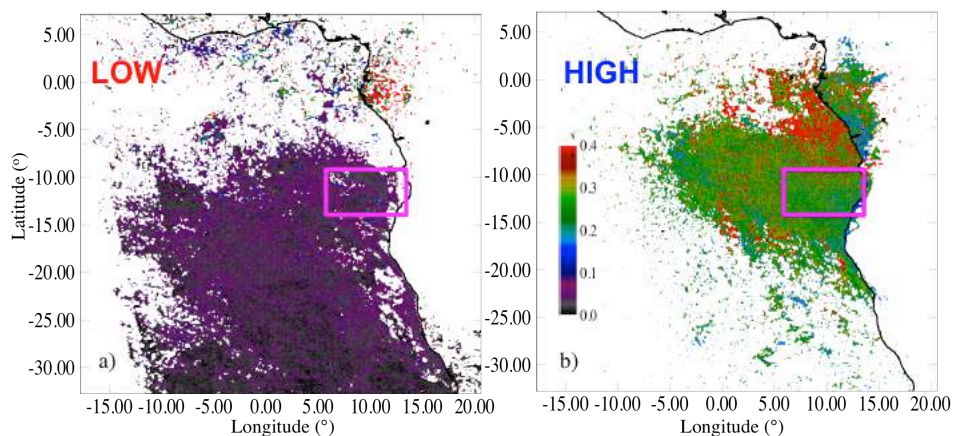


Figure 4.22 – POLDER AOT_{865nm} retrievals over the South Atlantic Ocean, for the period June-August 2008 for two categories: (a) absorption AOT smaller than 0.01 (LOW) and (b) absorption AOT larger than 0.04 (HIGH). The box illustrates the sampled area for our study.

The two panels of Figure 4.22 show the POLDER AOT_{865nm} retrievals of aerosols above clouds for which the absorption AOT_{865nm} is lower than 0.01 (labeled LOW), and for absorption AOT_{865nm} larger than 0.04 (labeled HIGH). We observe that, in the sampled region (illustrated by the box), the LOW cases are mostly characterized by AOTs lower than 0.1 at 865 nm while the HIGH situations are defined by AOTs larger than 0.2.

Hereinafter, we will use the POLDER aerosol and cloud retrievals together with ERA-Interim meteorological information to investigate any relationship between the aerosol loading (i.e. LOW and HIGH absorption AOTs) and the variability of meteorological and cloud parameters, over the sampled area.

4.4.1 Meteorological parameters in the absence and presence of aerosols

Firstly, we investigate the mean specific humidity and the temperature provided by ERA-Interim, over JJA 2008, for cases with and without absorbing aerosols above clouds. In Figure 4.23a) we observe that the temperature profile is almost stable along the atmospheric column. Above cloud, at 850 hPa we note a temperature inversion, called subsidence inversion that occurs when high-pressure systems sink the upper air layers, therefore a temperature inversion at lower altitudes can develop as a result of adiabatic compression. A moderate to strong temperature inversion almost always caps stratocumulus clouds located under a high-pressure center (such as the South Atlantic anticyclone). When smoke layers heated by the solar radiation cover low-level stratocumulus clouds, the temperature inversion is strengthened (Kaufman et al., 2005). In our case, we can observe a small increase by 1 K at 850 hPa when the absorbing aerosols have high values.

The humidity profiles show some significant differences between the two cases. The humidity is higher (up to 2.5 g.kg^{-1}) everywhere throughout the air column for the HIGH case. For these cases the average relative humidity (RH) is almost saturated at the cloud level – it has to be saturated – and presents a strong peak at 700 hPa ($RH \approx 40 \%$). The RH difference between HIGH and LOW situations is highest between 750 and 600 hPa, where the smoke layer resides.

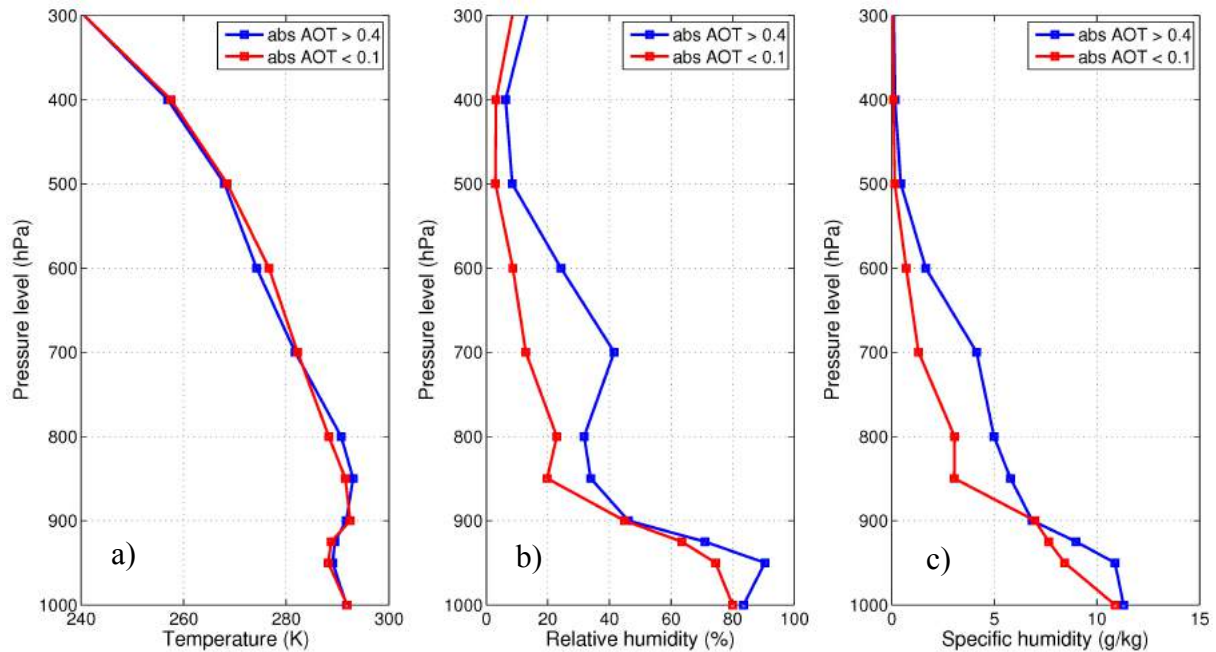


Figure 4.23 – Mean values of (a) temperature profile and (b) relative humidity profile and (c) specific humidity profile, within the sample region, from June to August 2008 selected for two situations: POLDER absorption $AOT_{865\text{nm}}$ smaller than 0.01 (red lines) and POLDER absorption $AOT_{865\text{nm}}$ larger than 0.04 (blue lines).

The meteorological database allows us to compute wind speed roses and specific humidity roses, representative for HIGH and LOW aerosol situations. This will give information of the circulation of air masses (e.g. wind direction) that put in motion the humidity and the aerosols close to the coast. Figure 4.24 to Figure 4.27 present these parameters for four pressure levels (1000 hPa, 925 hPa, 850 hPa and 700 hPa). We are most interested on the results at 700 hPa.

At surface (Figure 4.24) we notice that both HIGH and LOW situations are characterized by south-easterlies, with wind speeds of 6 to $9\text{ m}\cdot\text{s}^{-1}$ for more than 50 % of the cases and with specific humidity that is usually larger than $10\text{ g}\cdot\text{kg}^{-1}$. Similar wind and humidity patterns are observed at 950 hPa (Figure 4.25). The wind pattern at these pressure levels is similar with the MODIS cloud droplet effective radius pattern observed in Figure 4.5, with direction from SE to NW. It is possible that the surface wind speed activates the sea salt as CCN, resulting in the first indirect effect that leads to a decrease of r_{eff} .

At 850 hPa (Figure 4.26) we observe a slight change in the wind direction compared to surface, and also some differences between cases with and without aerosols. For low absorption AOT the wind is primarily coming from SE with few occurrences from NE, the wind speed is generally lower than $6\text{ m}\cdot\text{s}^{-1}$ and the specific humidity is lower than $6\text{ g}\cdot\text{kg}^{-1}$. In case of larger absorption AOT the wind direction is more westwards with similar values of wind speed but with larger values of q_v ($> 6\text{ g}\cdot\text{kg}^{-1}$).

Figure 4.27 shows that the meteorological parameters at 700 hPa are, however, very different for the two conditions. It is obvious that the air masses carrying high loads of aerosols are predominantly coming from the land (direction E-NE), while the air circulation responsible for low absorption AOT is originating from the open ocean (main direction W-NW). Even if it was expected, it can be considered as an interesting result because it shows the coherence between the POLDER AOT retrievals and the ERA-Interim meteorological parameters. The wind speed is generally 1-2 $\text{m}\cdot\text{s}^{-1}$ higher in case of larger absorption AOT and the q_v is 4 to 6 times larger for these cases.

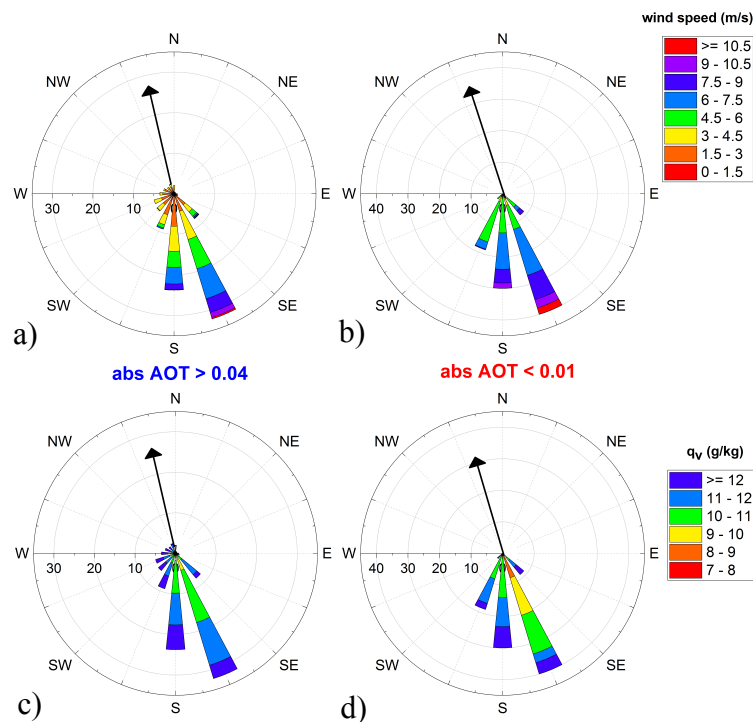


Figure 4.24 – Wind speed rose (a-b) and specific humidity rose (c-d) at 1000 hPa for situations with absorption AOT larger than 0.04 (a-c) and with absorption AOT smaller than 0.01 (b-d). The radius shows the frequency of wind direction. The arrow represents the main wind direction.

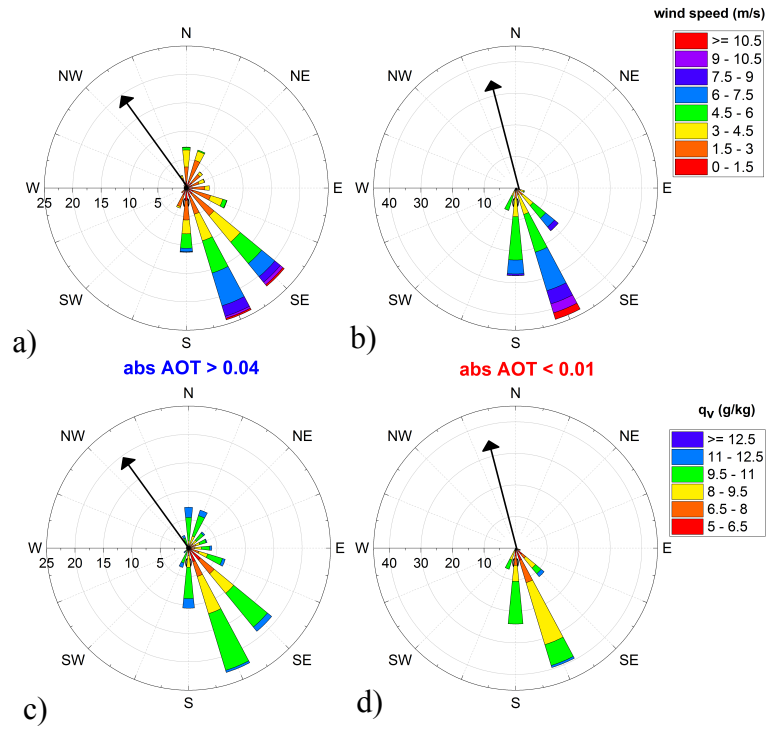


Figure 4.25 – Same as Figure 4.24, for 925 hPa.

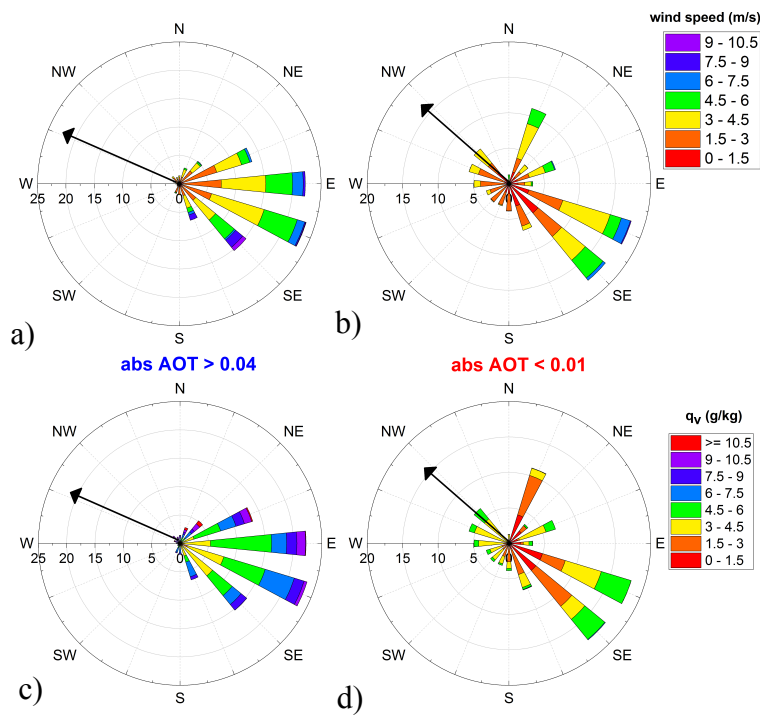


Figure 4.26 – Same as Figure 4.24, for 850 hPa.

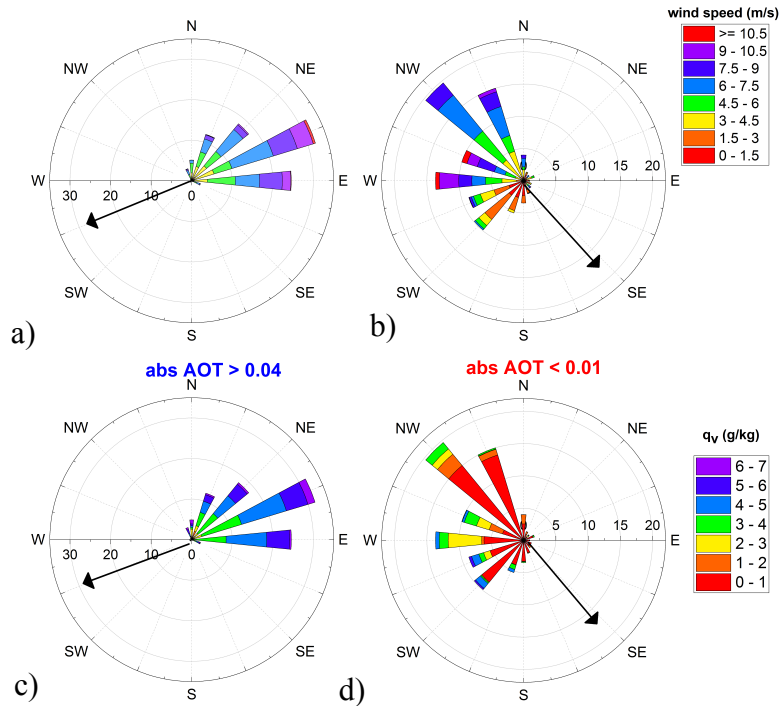


Figure 4.27 – Same as Figure 4.24, for 700 hPa.

A synthesis of these results highlights that few meteorological differences are found at lower altitudes and where the clouds reside (1000 and 925 hPa) between the HIGH and LOW situations: similar temperature inversion, similar wind direction and specific humidity. At 850 hPa we noticed some changes in the meteorological parameters with the increase in AOT (more humidity at higher AOTs), while at 750 hPa the wind direction and moisture are very different for the two situations: easterlies are associated to larger AOTs and larger humidity values, while the wind coming from the open ocean is characterized by low values of AOT and humidity.

4.4.2 Co-variation between cloud parameters, aerosol loads and meteorological parameters

Following our strategy to make a distinction between LOW and HIGH aerosol loads over the sample area, for June-August 2008, we analyzed the variation of cloud parameters, and their differences between LOW and HIGH cases, having in mind that the above-cloud aerosol load and the meteorological parameters might affect cloud properties. The variation of cloud parameters is analyzed as a function of longitude, and as a function of surface meteorological parameters.

The cloud parameters we analyzed are the POLDER COT, corrected for above-cloud aerosol effect, the MODIS r_{eff} , the POLDER ZO_2 and the LWP computed with the adiabatic assumption, using the POLDER COT and MODIS r_{eff} :

$$LWP = \frac{2\rho_w}{3} \times COT \times r_{eff} \quad (\text{Eq. 4.3})$$

where ρ_w is the water density. The MODIS r_{eff} bias of $\pm 2 \mu\text{m}$ in case dust (Haywood et al., 2004) and 2 % of mean monthly error for biomass-burning aerosols above clouds (Meyer et al., 2015) should have a small effect on the LWP computation.

Figure 4.28 presents the POLDER and MODIS cloud retrievals as a function of longitude for the two situations of absorbing AOT. We observe an evolution of some parameters that vary fundamentally in the same way with longitude, regardless of the HIGH or LOW situation, which may be linked to the transport effect. The POLDER COT, MODIS r_{eff} and the LWP increase westwards (panels a, b and c). This might be a result of the evolution of the clouds optical and microphysical properties, as they are driven further away from the coast by the air masses (it is consistent with the fact that the winds are mostly westwards).

Additionally, most of the parameters display a difference between the LOW and HIGH situations, as there is a visible gap between the values corresponding to the two situations, independently on longitude. MODIS r_{eff} increases from E to W from 6.5 to 11 μm when the aerosol loading is low. One can also observe an increase when the aerosol loading is high, but the increase is weaker, from 8 to 10 μm (Figure 4.28b). This difference suggests that the cloud microphysics is different for the situations with and without aerosols. We notice thicker clouds when the absorption AOT is larger than 0.04, as POLDER COT increases by approximately 3 (Figure 4.28a) and the LWP is systematically larger for these situations, by approximately 20 $\text{g}\cdot\text{m}^{-2}$ (Figure 4.28c).

The last cloud parameter we analyzed is the POLDER cloud altitude ZO_2 (Figure 4.28d). In case of LOW AOT situations, ZO_2 increases with longitude that may be the result of enhanced convection as the clouds move further away from the coast. In the case of HIGH AOT situations, we observe slightly lower cloud altitudes that remain under 1 km. The difference in altitude is very weak, and the effect of an upper level of aerosol on the cloud oxygen altitude is questionable. But a hypothetical mechanism could be that the above-cloud aerosols in the HIGH situations may inhibit the cloud vertical development through radiative mechanisms. These results are consistent with the observations of Wilcox (2010), who found an increase of LWP with 20 $\text{g}\cdot\text{m}^{-2}$ and a decrease of the cloud top altitude retrieved with CALIOP by around 200 m (see Figure 5 of Wilcox (2010)).

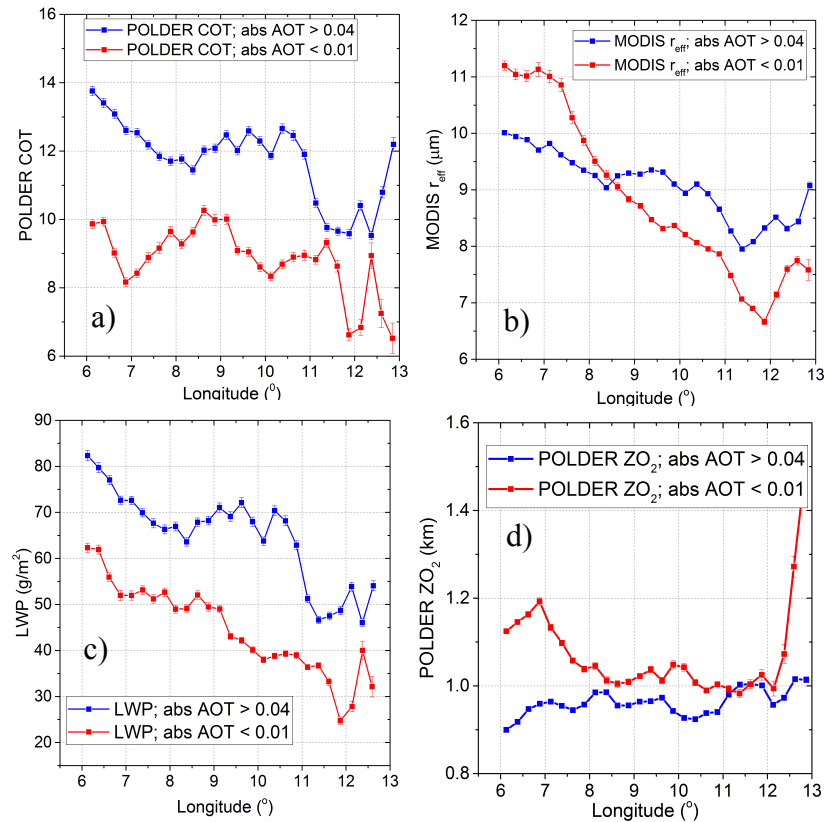


Figure 4.28 – Mean values of POLDER COT (a), MODIS r_{eff} (b) and Liquid Water Path (LWP) and POLDER ZO_2 (d) as a function of longitude. The data are separated into situations with POLDER absorption $\text{AOT}_{865 \text{ nm}}$ smaller than 0.01 (red lines) and with POLDER absorption $\text{AOT}_{865 \text{ nm}}$ larger than 0.04 (blue lines).

After the analysis of the cloud parameter variation with longitude, we analyzed the variation of LWP as a function of meteorological parameters for LOW and HIGH cases. The meteorological parameters we consider are the sea surface temperature (SST) and the surface wind speed. Both of them vary over the zone, as shown on Figure 4.29. We find lower values of SST for the HIGH cases, which might be explained by the presence of thicker clouds (larger LWP and COT, lower cloud altitude) that reduce the amount of solar radiation reaching the ocean's surface. The surface wind speed is also lower for HIGH cases, by approximately $2 \text{ m}\cdot\text{s}^{-1}$.

As shown on Figure 4.30a, LWP is increasing with surface wind speed, which is expected from Figure 4.28c and Figure 4.29a, as both LWP and wind speed are increasing going West. LWP is behaving very differently as a function of SST for the LOW and HIGH cases (Figure 4.30b). For the low case, LWP is clearly decreasing with SST, while a tendency is much less clear in the HIGH case. Again, one can observe that in almost all situations, LWP is larger for the HIGH compared with LOW cases.

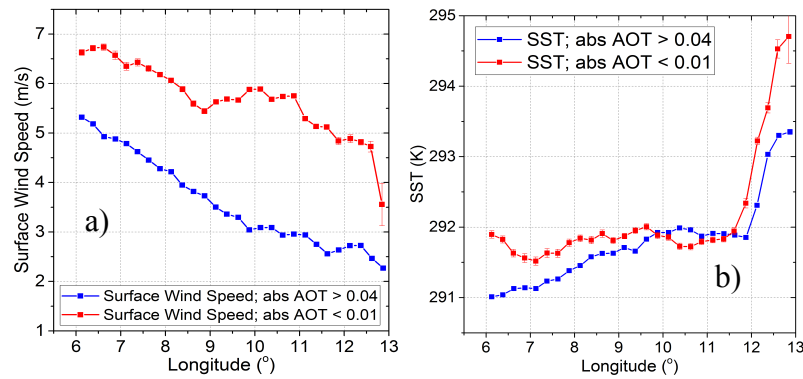


Figure 4.29 – Same description as for Figure 4.28, but for surface wind speed (a) and SST (b).

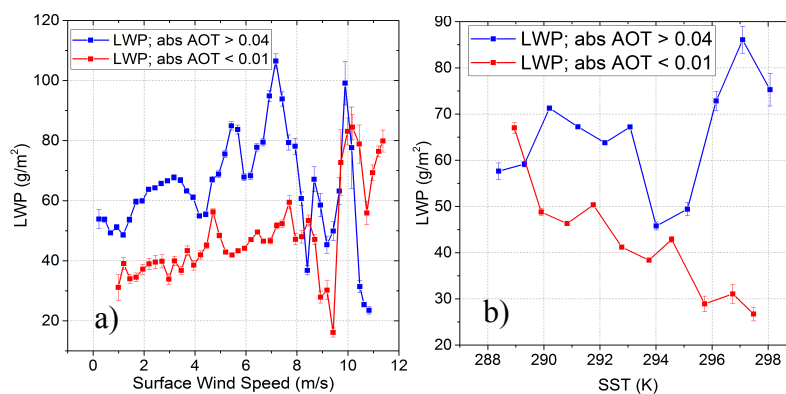


Figure 4.30 – Mean LWP values as a function of surface wind speed (a) and LWP as a function of SST (b), for HIGH (blue lines) and LOW (red lines) situations.

In the end, one could say that this analysis of the cloud parameters variation over the zone shows a significant difference between the LOW and HIGH aerosol situations, and that this difference remains for different meteorological conditions. These results do not contradict a cloud “thickening” effect forwarded by Wilcox (2010), that would be based on the absorption of solar radiation by aerosol layer (and water vapor), causing a warming of the air above the cloud, reducing the entrainment of dry air into it, and preserving its humidity. On the other hand, Adebisi et al. (2016) warns that there might be a cooling instead of a warming in the aerosol layer due to the water vapor emission in the infrared. In order to make our contribution to these studies, we performed radiative transfer simulations where we were interested by the radiative and distinct effects of aerosol and water vapor, not only at the aerosol layer and above the lower cloud cover, but also at the cloud top. In the last part of our study will be focused on the study of the radiative effects of above cloud aerosols and water vapor on the surrounding atmosphere and cloud top. For this, we will analyze the difference in the cloud top radiative cooling and above cloud layer heating rates between the LOW and HIGH smoke loadings, check if they are significant and how they typically vary during the day.

4.5 Typical radiative transfer simulations of polluted and quasi-pristine scenarios

The radiative study from Section 4.3.4 over the sampled area, has already given us information of the average aerosol and water vapor contribution to the heating rates, mainly at the aerosol level. Even if we could make a similar exercise in this section, by separating the HIGH and the LOW situations along the CALIOP track, we chose to analyze the aerosol and water vapor effects from a different perspective: we realized two different simulations by taking into account the diurnal variability of the meteorological parameters, for average HIGH and LOW loadings of aerosol / water vapor. This strategy's objective is to be able to separate in the end the different contributions and effects.

Firstly, we will shortly present the diurnal variability of the shortwave radiative forcing and the heating rates in both visible and infrared. Afterwards, we will simulate a case with HIGH aerosol amount and water vapor versus LOW aerosol loading and water vapor. Lastly, the AOT will be held constant, for two different water vapor contents.

4.5.1 Diurnal variation of radiative forcing and heating rates

Average diurnal variation of the aerosol forcing

We mentioned previously that the DRE and the heating rates were calculated at a certain time during the day (instantaneous), when the satellite is passing over the sampling area (i.e. around 13:30 local time). At this time and latitude, the solar zenith angle (Θ_s) is small. As we will see, the radiative quantities vary with time; it is interesting to have the amplitude of this time variation. Using different values of Θ_s and the mean values of aerosol, cloud and meteorological parameters (see Table 4.1) retrieved from June to August 2008 over the sampled region, we calculated the average diurnal variation of the radiative forcing and heating rates.

Table 4.1 – Mean values of meteorological parameters: specific humidity – q_v (g/kg), and temperature – T (K), mean aerosol and cloud properties calculated over the specific area from June to August 2008.

	Pressure (hPa)										
	1000	950	925	900	850	800	700	600	500	400	300
q_v	11.12	9.53	8.17	6.89	4.43	4.04	2.78	1.23	0.31	0.12	0.08
T	291.6	289.5	288.9	290.2	292.1	289.2	281.8	275.3	268.0	257.1	240.7
POLDER absorption			POLDER		POLDER		POLDER		POLDER		MODIS τ_{eff}
AOT _{865 nm}			AOT _{865 nm}		SSA _{865 nm}		AE _{670/865}		COT		
0.04			0.21		0.80		2.01		10		10

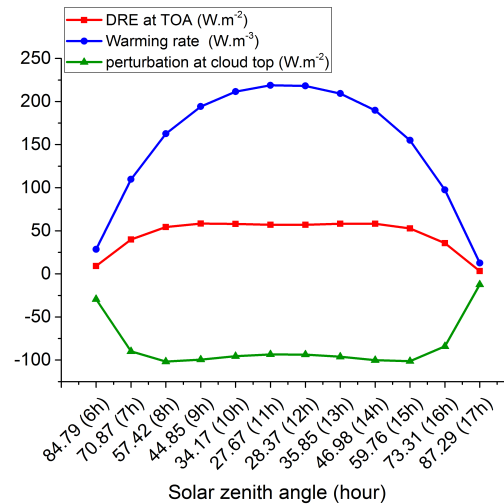


Figure 4.31 – DRE at TOA, net radiative heating rate within the aerosol layer and radiative perturbation at the cloud top as a function of the solar zenith angle/ hour over the selected area.

In Figure 4.31 we observe how the sun elevation plays a role in the direct radiative forcing and cloud top radiative perturbation. At sunrise and sunset the values of the DRE at TOA and the aerosol layer warming rate are minimal. The warming of the aerosol layer reaches the largest value around noon ($\approx 220 \text{ W.m}^{-3}$), when the solar zenith angle is lowest ($\Theta_s \approx 28^\circ$). The DRE at TOA remains almost constant ($\approx 50 \text{ W.m}^{-2}$) between 8 h and 15 h. Also, the cloud perturbation (W.m^{-2}) is minimum during the early morning and evening and varies slightly during the day.

Average diurnal variation of shortwave and longwave heating rates

Using the mean values of the aerosol, cloud and meteorological parameters presented in Table 4.1, we can calculate the diurnal variation of the heating rate profile (K/day) in the shortwave and longwave spectrum, as well as their total balance (Figure 4.32). We notice that in the shortwave spectrum the warming between 3 and 4.5 km increases from 2 K/day in the morning (at 6 h) to approximately 8 K/day around noon, and after 14 h the heating rate starts to decrease. Similar variation in shortwave spectrum is observed at the cloud top. In longwave we do not observe a dependence of the heating rate with the hour, because the water vapor longwave absorption/emission is not affected by the solar zenith angle. We notice more cooling (around -4 K/day) between 3.5 and 5.5 km due to the water vapor content in the atmospheric column, and a strong cooling at the cloud top. The scale is fixed between -8.0 and 0.0 K/day, but the true value goes down to -70 K/day. The total heating rate also varies during the day; the longwave cooling only partially compensates the shortwave heating between 8 h and 16 h. We observe a maximum heating of 5 K/day at noon at 4 km; early in the morning and late in the afternoon we notice, however, a total cooling of -1.7 K/day. The cloud top remains under strong cooling.

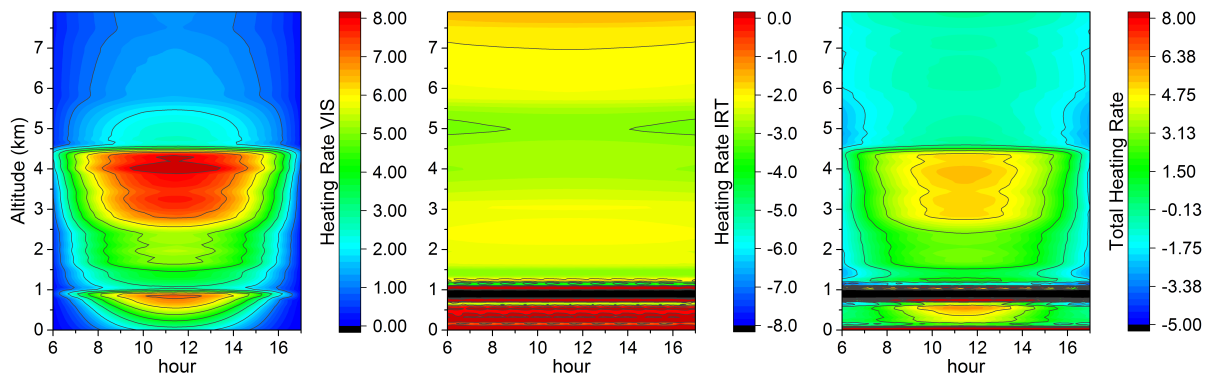


Figure 4.32 – Average diurnal variation of heating rate profiles calculated in shortwave spectrum (VIS), in longwave spectrum (IRT) and total heating rate, within the selected area.

4.5.2 Temporal variation of the heating rate profiles for HIGH and LOW simulations

Now that we have shown how the radiative forcing and heating rate profiles vary during the day, we want to investigate how different aerosol loadings and meteorological parameters can influence the computation of the direct radiative effect and the associated heating rates. Previous results showed that meteorological parameters modify with the aerosol loading, especially between 850 and 600 hPa, where the aerosol layer is usually located. But meteorological parameters also vary during the day, as shown in Figure 4.34. The three upper panels present a typical 24 h variation of the atmospheric temperature, relative humidity and specific humidity at 10 pressure levels (from 1000 hPa to 400 hPa). It was obtained from ECMWF reanalyzed data given every 6 hour (0, 6 12 and 18h UTC time). The variations given are a mean over the zone in terms of time tendency and amplitude. The additional point at 13h corresponds to the mean meteorological parameters sampled under the CALIOP track for the HIGH and LOW cases. The below panels show the same parameters, but for low absorption AOT. We notice that the temperature profile is characterized by a minimum value in the morning, which increases during the day. There are few differences between the typical temperatures of the HIGH situations compared to the LOW ones. The relative humidity and specific humidity show large variability during the day, and also we observe differences between their profiles retrieved for HIGH and LOW cases.

These meteorological profiles and average aerosol properties characteristic for HIGH and LOW situations (see Table 4.2) are used to study the diurnal variations of the radiative forcing (Figure 4.33) and heating rates (Figure 4.35). For this analysis we chose to define one cloud type for both HIGH and LOW situations, characterized by a cloud effective radius of 10 μm and a cloud optical thickness of 10. Thus, we consider the same contribution of the cloud droplets multiple scattering in both situations and their respective heating rate computations.

Table 4.2 – Mean values of aerosol properties over the specific area from June to August 2008, in case of HIGH values of absorption AOT (> 0.04) and in case of LOW values of absorption AOT (< 0.01), respectively.

	POLDER absorption AOT_{865nm}	POLDER AOT_{865nm}	POLDER SSA_{865nm}	POLDER $AE_{670/865}$
HIGH	0.05	0.26	0.80	2.03
LOW	0.005	0.06	0.86	1.75

The results of the computation (Figure 4.33) show that the DRE at TOA, the aerosol layer warming rate and the cloud top radiative perturbation still present similar diurnal variability with the ones shown in Section 4.5.1, but have very different values for the two HIGH and LOW situations. The DRE at TOA is around 70 W.m^{-2} for large values of absorbing AOT, compared to only 15 W.m^{-2} in more pristine cases. Similar differences are observed for the warming rate, which is reaching 250 W.m^{-3} in the HIGH cases and only 100 W.m^{-3} when calculated for low aerosol absorption; accordingly, the cloud top perturbation is more negative for large AOTs. We notice that for an aerosol loading almost 5 times larger in the polluted cases (0.26 compared to 0.06 in AOT) the direct radiative effect and the cloud top perturbation increase 5 times, and the warming rate only 2.5 times. Therefore, the DRE seems directly proportional to the AOT.

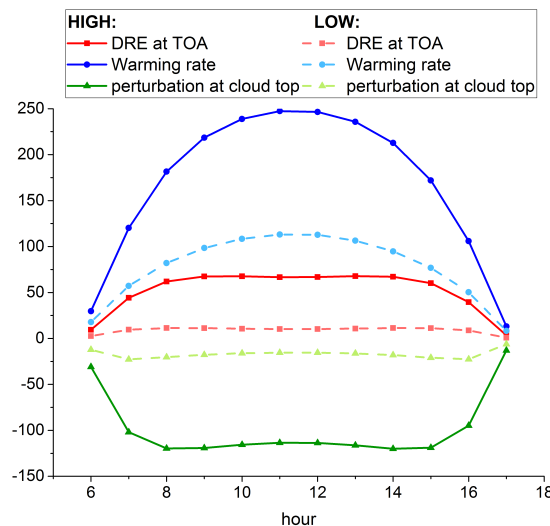


Figure 4.33 – Diurnal variation of the DRE at TOA (W.m^{-2}), net radiative heating rate within the aerosol layer (W.m^{-3}) and radiative perturbation at the cloud top (W.m^{-2}), over the selected region: in case of HIGH absorption AOT_{865nm} (solid line) and in case of LOW absorption AOT_{865nm} (dashed line).

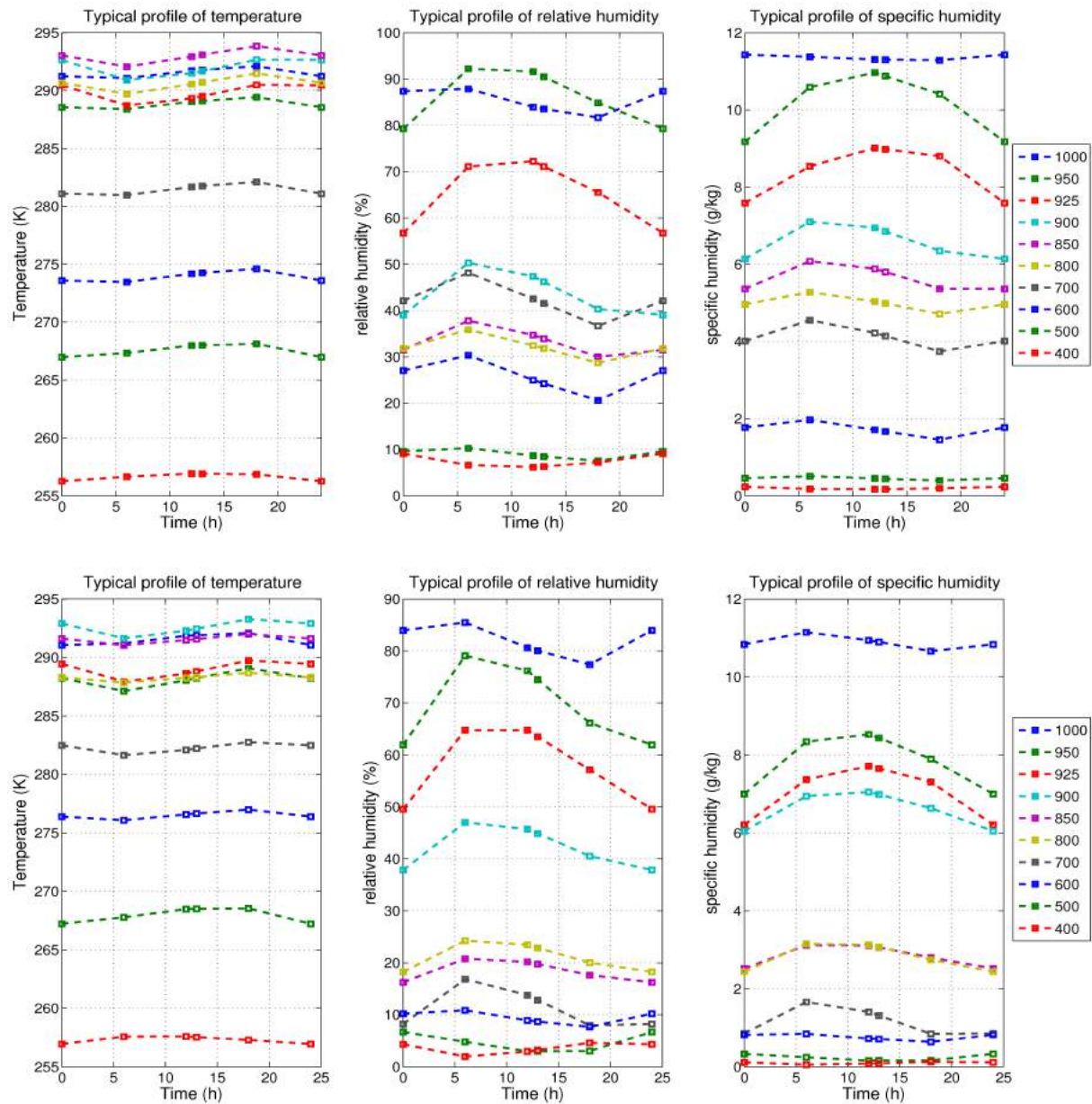


Figure 4.34 – Temporal variation of temperature profile, relative humidity and specific humidity profiles at 10 pressure levels, for situations with absorption AOT larger than 0.04 (upper panels), and for cases with low absorption AOT (bottom panels), within the sample area.

The diurnal variation of the heating rate profiles, for the HIGH and LOW situations, is shown in Figure 4.35. The upper panels present the HR in the shortwave and longwave spectrum along with their total budget, for the polluted cases. The middle panels show the results for the pristine cases and the bottom ones represent the HR differences between the polluted and unpolluted situations. In the following we will describe each set of results.

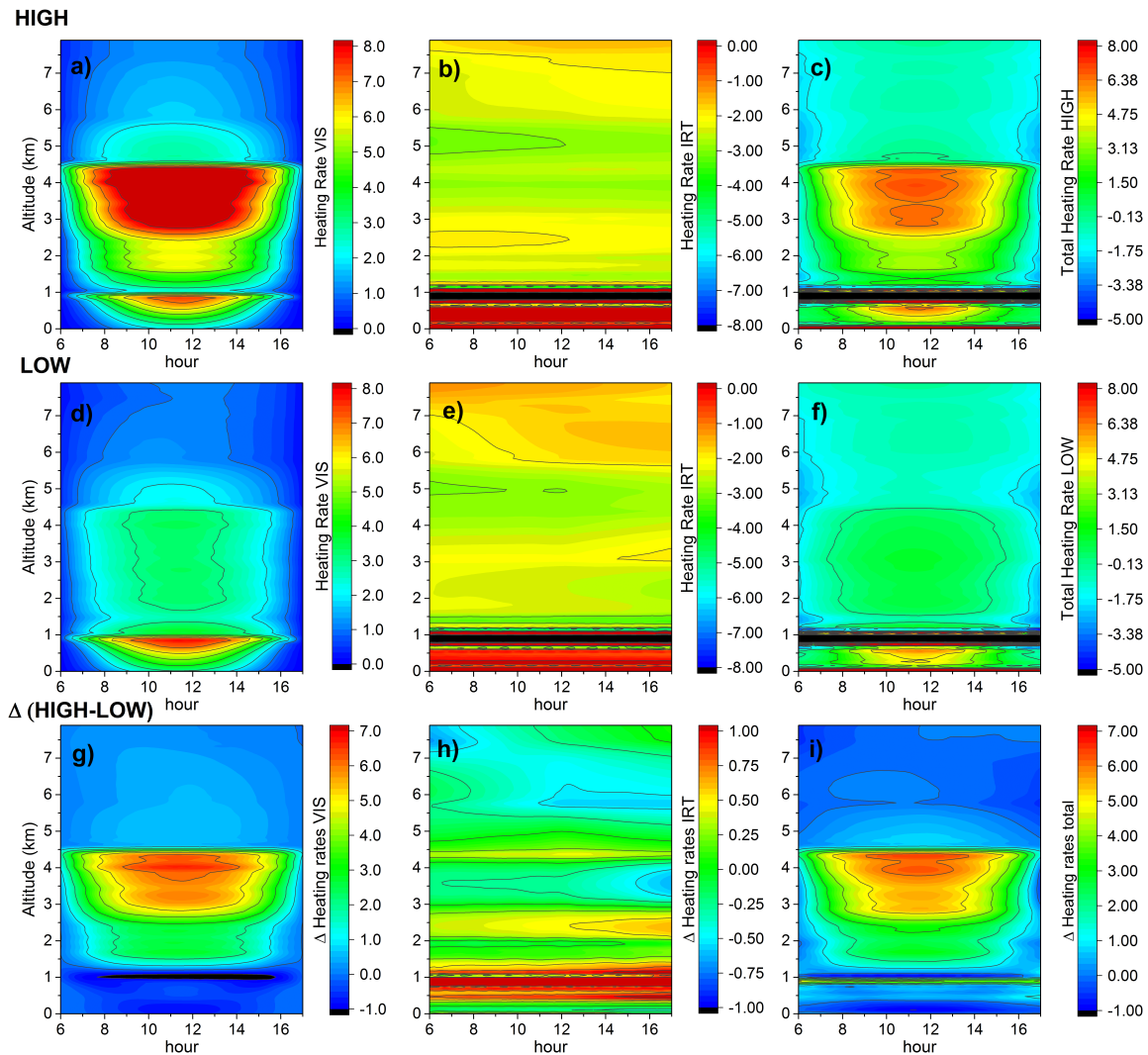


Figure 4.35 – Calculated heating rates in shortwave, longwave and total budget as a function of the hour, in case of HIGH absorption $AOT_{865\text{ nm}}$ ((a),(b) and (c)) and LOW absorption $AOT_{865\text{ nm}}$ ((d),(e) and (f)). Last row of the panel presents the difference between the heating rate of HIGH and LOW situations, for visible (g), thermic (h) and total (i), respectively.

In case of polluted cases, the HR_{SW} values exceed 8 K/day (maximum value of 9.95 K/day) between 3 and 4.5 km (panel a), which is due to the local absorption of the shortwave radiation by the aerosols and water vapor. One can observe a second local maximum just below the cloud top, which is due to the absorption by the cloud droplets along the radiation path within the cloud. Panel b shows that the longwave-heating rate is everywhere negative along the atmospheric column, except locally just above the cloud top and at the surface. Actually, the color scale has been fixed between -8.0 and 0.0 K/day, but the true extremes of the heating rate are + 24 K/day at the surface and - 73.K/day at the highest cloud layer. As a balance between shortwave and longwave heating rate, the HR_{total} still shows a warming within the aerosol layer (panel c), that reaches 7 K/day at noon. The cooling in the cloud top layers is slightly reduced.

The shortwave heating rate profile for the quasi-pristine cases show a very different feature compared to the polluted cases (panel d). The lower amounts of atmospheric aerosols and water vapor content heat the layer between 2 and 4.5 km with only 4 K/day at noon. At the cloud top, however, the heating is higher, as the solar illumination is higher. The longwave cooling shows a slightly different diurnal variation compared to the previous case. The cloud top cooling is stronger, down to -79 K/day. This difference will be discussed below. The sum of the HR_{SW} and HR_{LW} computed for the LOW situation shows less warming between 2 and 4.5 km of about 2 K/day, as there is less shortwave heating.

The last set of panels (Figure 4.35 g, h and i) describe the differences between the HIGH and LOW situations. It shows that the polluted case induce more warming between 2 and 4.5 km (up to + 7 K/day) and less cooling at the cloud top layer (+ 4 K/day). The difference is negligible everywhere else.

Figure 4.35 provides a general idea of the diurnal variation and magnitude of both shortwave and longwave heating rates, for HIGH and LOW situations. To help synthetizing and highlighting the radiative effects of aerosol and/or water vapor effect at the cloud top and at the aerosol location, we give in Table 4.3 more specific shortwave and longwave heating rate values for polluted and less-polluted cases, obtained at the cloud top altitude (between 0.9 and 1 km) and within the aerosol layer (at 4 km).

The HR values are given for three distinct hours: in the morning (7h), at noon (12h) and in the evening (17h), that show their diurnal variability. For example, at noon, the difference between the polluted and “clean” scenarios at the aerosol layer gives a heating of 6.45 K/day in the shortwave domain, and a cooling of -0.14 K/day due to water vapor in the longwave spectrum (which increases towards the evening). In case of more water vapor and aerosol in the atmosphere, there is less longwave cooling at the cloud top by + 6.26 K/day, which is partly compensated by less insolation reaching the cloud top, by - 1.79 K/day that is the shadowing effect. We will discuss in more details these results and their contribution to our knowledge in the following section.

Table 4.3 – Shortwave and longwave heating rate (K/day) values for polluted (HIGH) and less-polluted (LOW) cases, obtained at the cloud top level (between 0.9 and 1 km) and at 4 km (within the aerosol layer). The values are given for 3 different hours to show the diurnal variation. The difference between HIGH and LOW for each hour and level is also shown.

HIGH (AOT and q_v) or LOW (AOT and q_v)		7h		12h		17h	
		HR _{SW}	HR _{LW}	HR _{SW}	HR _{LW}	HR _{SW}	HR _{LW}
Cloud top altitude (0.9-1 km)	HIGH	2.57	-67.44	6.09	-67.53	0.11	-72.82
	LOW	3.51	-74.14	7.88	-73.79	0.20	-79.04
	In SW: aerosol + water vapor contribution. In LW only water vapor						
	HIGH-LOW	-0.94	6.7	-1.79	6.26	-0.09	6.22
Aerosol layer (4 km)	HIGH	5.82	-2.87	9.86	-2.86	0.83	-2.89
	LOW	1.95	-2.72	3.41	-2.72	0.36	-2.43
	In SW: aerosol + water vapor contribution. In LW only water vapor						
	HIGH-LOW	3.87	-0.15	6.45	-0.14	0.47	-0.46

4.5.3 Distinction between aerosol versus water vapor radiative effects

This last analysis has the objective to distinguish between the effect of aerosol and that of water vapor on the shortwave heating rate computation. We performed a second radiative transfer simulation, with a LOW and HIGH scenario, except that we consider the same aerosol profile for the two cases, described by the mean aerosol properties from Table 4.1. By this way and after a subtraction of the two resulting heating rate values, we obtain a close estimation of the contribution of water vapor only in the shortwave. Figure 4.36 and Table 4.4 present the results. The longwave HR profiles are identical to the previous ones, as the two infrared simulations are equal.

In the shortwave, the HR computation shows that the increase of water vapor between LOW and HIGH situations has a warming effect in the aerosol layer, due to higher humidity, and a cooling in the cloud layer, due to a shadowing effect. The synthesis between the shortwave heating rates computed in the first simulation (Table 4.3), water vapor and aerosol contribution) and those computed in the second scenario (Table 4.4), water vapor only after the subtraction), provides the distinct contribution of water vapor and aerosol in the heating rate difference between HIGH and LOW (Table 4.5).

Table 4.4 – Shortwave and longwave heating rate (K/day) values for a constant AOT and for large (HIGH) and small (LOW) values of the specific humidity profile (q_v), obtained at the cloud top level and at 4 km. The values are given for 3 different hours to show the diurnal variation. The difference between HIGH and LOW for each hour and level is also shown.

Constant AOT and HIGH q_v or LOW q_v		7h		12h		17h	
		HR _{SW}	HR _{LW}	HR _{SW}	HR _{LW}	HR _{SW}	HR _{LW}
Cloud top altitude (0.9-1 km)	HIGH	2.54	-67.44	6.13	-67.53	0.12	-72.82
	LOW	3.16	-74.14	7.69	-73.79	0.15	-79.04
	HIGH-LOW	-0.62	6.7	-1.56	6.26	-0.03	6.22
Aerosol layer (4 km)	HIGH	5.19	-2.87	8.78	-2.86	0.80	-2.89
	LOW	4.93	-2.72	8.02	-2.72	0.78	-2.43
	HIGH-LOW	0.26	-0.15	0.76	-0.14	0.02	-0.46

For example, at noon, within the aerosol layer we notice that when the water vapor content is HIGH, the shortwave computation gives a HR_{SW} with 0.76 K/day larger than for the LOW case. This value represents the contribution of water vapor in shortwave, from the 6.45 K/day, which was the cumulated effect of aerosol and water vapor in Table 4.3. It results that the increase of the aerosol only is increasing the heating by 5.69 K/day, meaning that 88 % of the heating rate between LOW and HIGH is attributable to aerosols. The morning and evening results follow in the same way, but at a smaller magnitude. If we consider the longwave cooling at the aerosol layer, the total heating rate difference between HIGH and LOW is 6.31 K/day due to water vapor and aerosol, of which 0.62 K/day is the contribution of water vapor.

On the contrary, at the cloud top we find larger shortwave heating when the water vapor content is small, with 1.56 K/day at 12h. By making the difference between this value and the one obtained in Table 4.3, we get the aerosol contribution at the cloud top of 0.23 K/day in shortwave. In the same time, the cloud top is cooler with - 6.26 K/day when there is less water vapor in the upper column, therefore, the total amount of cooling at the cloud top is with - 4.47 K/day more than in the polluted cases (see Table 4.5).

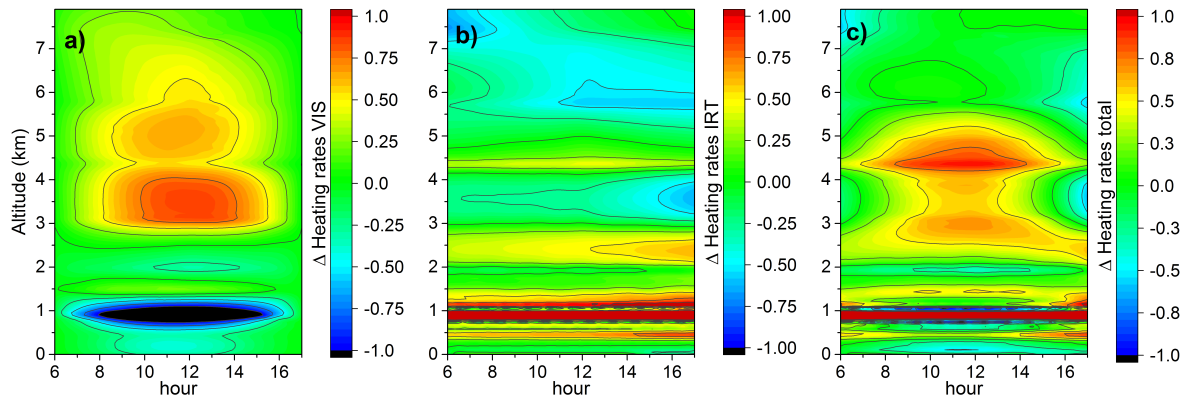


Figure 4.36 – Difference between the heating rate of high and low specific humidity situations, for shortwave (a), longwave (b) and total (c), as a function of hour.

These simulations helped us understand the significance of water vapor contribution in the shortwave and longwave spectrum, and to separate its effects from those of the aerosol loading in the visible domain. We demonstrate that the aerosols accompanied by water vapor impact not only the layer where they reside, by heating or cooling their environment, but also have a distant effect on the underlying cloud systems. We showed that aerosols drive the warming within the aerosol layer, while the water vapor (or lack of) is responsible for reduction of the cloud top radiative cooling, which could lead to less cloud top turbulence, mixing and dry air entrainment. These effects eventually affect the cloud evolution in a way that could lead to a cloud thickening.

Table 4.5 – Synthesis of aerosol and water vapor contribution within the aerosol layer and at the cloud top level, at noon, as a difference between the polluted and “clean” cases.

		In case of polluted situations	
		Aerosol layer (4 km)	Cloud top layer (0.9 – 1 km)
Total heating rate (K/day)	More heating in SW with:	+ 5.69 (due to aerosols) +0.76 (due to water vapor)	Less heating in SW with: + 0.23 (due to aerosols) + 1.56 (due to water vapor)
	More cooling in LW:	- 0.14 (due to water vapor)	Less cooling in LW: - 6.26 (due to water vapor)
	=> more heating: + 6.31 K/day, of which + 0.62 K/day is due to water vapor and + 5.69 K/day due to aerosols	=> less cooling: - 4.47 K/day, of which - 4.7 K/day is due to water vapor and + 0.23 K/day due to aerosols	

As mentioned in Section 4.3.3, the warming of the atmosphere above the cloud layer due to smoke can lead to an increased atmospheric stability, which will affect the cloud vertical development and its entrainment of environmental air. Furthermore, in case of polluted situations the cloud top cooling, which is another cloud engine, is less strong, adding a supplementary impact on the cloud evolution. Our study showed the importance of the contribution of water vapor in a possible cloud thickening effect observed in Section 4.4.2.

Final synthesis of this study

In our study, the main objective was to disentangle the effect of aerosols on clouds from the meteorological effect, and to calculate their radiative impact.

We began by characterizing the aerosols and cloud properties over the South Atlantic Ocean region, which gave us information on the average aerosol loading and their absorbing properties, as well as the stratocumulus main characteristics: r_{eff} of 10~15 μm , COT of 10~15 and a cloud top altitude around 1.2 km. Along the longitude, the clouds develop vertically as they are transported further westwards. The aerosols are mainly detached close to the coast and afterwards they lose altitude due to deposition processes. A strong anticyclone characterizes this area during June to October, which brings about easterlies at 600 hPa and south-easterlies at surface.

In our analysis we selected a small area, close to Angola's coast and a period of time between June and August 2008, in order to limit the meteorological variability. For this, we observed a strong correlation between the increase of the specific humidity with the increase of AOT, at 850 and 700 hPa (where the aerosols usually reside). Therefore, the necessity of separating the water vapor radiative effect from the aerosol effect has emerged.

A radiative study over the sampled area has revealed positive average values of the DRE at TOA (an average of approximately 66.6 W.m^{-2}), which are linked to a warming of the atmospheric column; the aerosol layer mean warming rate also has high values, of about 163.5 W.m^{-3} and the cloud top shows a perturbation in the energy intake of -96 W.m^{-2} . The DRE at TOA is directly correlated to the aerosol loading, and respectively to the warming rate, while the cloud top perturbation is in anti-correlation with these parameters.

The shortwave heating rate shows a warming of 9 K/day at the aerosol layer, of which 3 K/day are due to the water vapor shortwave absorption. However, the total effect of water vapor is almost null, as the shortwave heating is compensated by its longwave radiative cooling. In the total balance between shortwave and longwave heating rates, we notice a small effect of the presence of aerosols above clouds (of 0.56 K/day), which is explained by the shadowing effect of aerosols, that act as a blanket stopping the solar radiation to reach the cloud top.

For the same area and period we analyzed the cloud and meteorological parameters for two distinct scenarios: with HIGH amount of absorbing aerosols, and with LOW amount. This study revealed also two different specific humidity profiles, characteristic to the HIGH

and LOW situations. At 700 hPa we found a direct link between the aerosol loading, the wind direction and the water vapor content: the HIGH loads of aerosols are coming from the land (direction East-West), with high amounts of water vapor, while the LOW cases originate from the open ocean, with lower moisture quantities.

The study on the cloud parameters as a function of longitude and aerosol loading do not contradict a “thickening” effect, with lower cloud top altitudes and higher COT and LWP, regarding of the meteorological conditions. This effect may be due to the warming induced by the presence of aerosols above clouds, which can stabilize the atmosphere and affect the cloud development.

In order to separate even more the aerosol and meteorological effects for the HIGH and LOW situations, we calculated the radiative effect of aerosols and water vapor, by taking into account the diurnal variability of meteorological parameters. At the aerosol layer, the analysis of the two radiative transfer simulations at noon shows: (i) that in the pristine case the heating rate is low, and equal to 0.69 K/day, and (ii) that the smoke is responsible for additionally heating the layer where it resides by 6.31 K/day, of which 0.62 K/day are due to the water vapor. The additional heating varies significantly during the day: at 7 h and 17 h it is +3.72 and +0.01 K/day, respectively. At the cloud top upper layers, there is less cooling compared to pristine cases, by - 4.47 K/day mainly driven by the water vapor above the cloud. This cooling perturbation equals +6.1 % at noon, and 7.8 % at 7 h and 17 h, which seems significant.

Chapter 5

Conclusions and Perspectives

Intercomparison of active and passive AAC measurements

The first part of this thesis focused on the intercomparison of above-cloud aerosol retrievals from active and passive methods. The objective was to assess the consistency and limitations of the POLDER polarization method, the CALIOP operational method (CALIOP_{OM}) and the CALIOP Depolarization Method (DRM).

The main conclusion resulted from this study is that the above-cloud aerosol optical thickness (AOT) retrievals of POLDER and DRM are in good agreement, for most of the situations. Given the fact that the two techniques are based on very different physical concepts, our results highlight the fact that a remarkable coherence between active and passive inferences of aerosol above clouds (AAC) properties can be obtained.

Another important result is that CALIOP_{OM} is highly underestimating the above cloud AOT_{532nm}, mainly because the height of the aerosol layer is wrongly estimated in case of optically thick layers of absorbing aerosols. As results, there is a very poor correlation between CALIOP_{OM} and the other two methods. Previous studies based on CALIOP_{OM} retrievals are potentially biased, as aerosol above cloud radiative effects are probably underestimated.

When comparing POLDER and DRM AOT_{532nm} retrievals, the global analysis showed a mean difference of about ± 0.07 , and a correlation of $R^2 = 0.68$ when the aerosol and cloud layers are detached. Good correlations were also found when the aerosol microphysics is dominated by fine-mode particles of biomass-burning aerosols ($R^2 = 0.83$) or coarse-mode aerosols of dust ($R^2 = 0.82$). These results give confidence in our ability to monitor the aerosol load above clouds on a global scale. Nonetheless, differences arise when the aerosol microphysics is complex (such as mixtures from East Asia), and when the above-cloud aerosol layer is in contact with the below cloud. We considered two different hypotheses to explain how aerosols within clouds can affect the two methods, and we found that they:

- can create an additional polarized signal that impacts the POLDER AOT retrievals;
- can modify the ability of cloud droplets to backscatter light when absorbing aerosols are internally mixed with the droplets, which will affect the DRM AOT retrievals.

Another assumption that may explain a part of the differences observed between DRM and POLDER is that the passive method can be limited in detecting fractionated cloud covers. We cannot ignore the possibility that heterogeneous clouds not well detected generate biases in the POLDER retrievals (as shown with the 3D simulations in Chapter 3).

We consider that more efforts have to be done to increase the accuracy of the methods developed for AAC retrievals. A better description of the aerosol model used in the POLDER algorithm, by introducing additional dust or mixture models, would indeed improve the AOT and AE retrievals in more complex situations (such as East Asia region). Another possibility is to use more complex algorithms, such as GRASP (Generalized Retrieval of Aerosol and Surface Properties, Dubovik et al., (2014)) adapted for AAC scenes.

Airborne measurements are extremely useful in providing information on aerosols above cloud properties, and they can be used to validate the satellite observations. Measurements from AEROCLO-sA field campaign in Namibia combined an airborne sun-photometer and the OSIRIS sensor (3MI prototype instrument), which can be used to validate the CALIOP DRM and POLDER above-cloud aerosol products. Moreover, this mission employed a high-resolution lidar, which measured the backscattered signal in the 1064 nm channel. So, it should give correct information on the aerosol altitude in the region, and also where aerosols and clouds are in contact. These measurements would help improving the CALIOP estimation of the aerosol geometrical thickness and its retrievals, and could increase our understanding of aerosol within clouds situations, which are very interesting in the frame of aerosol-cloud interactions.

The combination of POLDER and CALIOP methods showed the potential to detect aerosols within or partially within the clouds. This synergy could bring closer the CALIOP and POLDER measurements for situations of contact. Data obtained by the CLARIFY-2016 field campaign that measured aerosols within the clouds, can be used to estimate the amount of biomass-burning aerosols within the stratocumulus clouds, and then validate our results.

Study on the aerosol radiative effects, and their potential semi-direct impact on clouds

The second part of this work focused on the impact of aerosol layers overlying a lower cloud layer, their associated radiative forcing and their potential effects on the underlying clouds. The region of interest was the South Atlantic Ocean due to the large loads of African biomass-burning absorbing aerosols that are frequently transported over the main South Atlantic stratocumulus deck.

We used our database to realize a synergy between CALIOP and POLDER measurements of aerosol above clouds, at which we added meteorological parameters provided by the ERA-Interim reanalysis. We gave the detailed properties of aerosol and clouds for the period May - October 2006 to 2009, and in particular information about the

vertical distance between the two layers. Aerosol and cloud layers are preponderantly at a larger distance closer to the coast, and in August - October, which is explained by the atmospheric circulation over the South of Africa and Southeast Ocean.

For a more detailed analysis we selected a small area close to the coast of Angola that is near the main stratocumulus deck identified in the region, and where large loads of aerosol are transported at higher altitudes, mainly detached from the clouds below. The study was limited to three months (June to August 2008), in order to constrain the meteorological variability that can affect the clouds and the overlaid aerosols, and also to maintain a sufficiently large number of data for a proper statistical analysis.

For this area and period, we found an important correlation between the aerosol loading (above cloud AOT) and the specific humidity between 850 and 600 hPa; we were able to deduce that the biomass-burning plumes come with more humidity.

A result in itself is that we are able to compute the aerosol radiative forcing and the vertical heating rate profiles when aerosol layers are above lower clouds in the visible and in thermal infrared domains, using the CALIOP / POLDER/ ERA-Interim synergy and a radiative transfer model.

Over the area, we estimated that smoke layers located above clouds significantly perturb TOA net flux and the solar illumination of clouds. They also warm the atmospheric layer where they reside by a mean maximum value of 6 K/day, while water vapor has an overall effect close to null over the cloud layer, with a compensation between its induced solar heating and infrared cooling. Another estimate is the heating rate at the cloud top layers. We observed a net cloud top radiative cooling dominated by infrared transfer, which is expected, around -60 K/day for each pixel under the CALIOP track, and a mean of -13 K/day over the area, as clouds are diversely vertically located. Removing aerosol in the calculation show a slight increased cooling.

In order to reach our objective, which was to analyze the possible effect over the zone of aerosol loading on cloud properties, we analyzed the cloud properties for two scenarios: large and low amounts of above-cloud absorbing aerosols. Our findings confirmed previous satellite observations and studies that showed that the clouds are lower and brighter when large loads of absorbing aerosols are located above clouds. These results do not contradict a cloud “thickening” effect caused by a warming of the air above the cloud, which reduces the entrainment of dry air into it, and preserves its humidity. As consequence, the Liquid Water Path increases, tendency that remains regarding the meteorological conditions.

Being aware of the possible effect of meteorological variation on the two cloud populations, and that aerosol loading is correlated with humidity loading above the cloud, we analyzed the meteorological conditions for the two scenario, and we performed two radiative transfer simulations with two typical covariant loadings of aerosol and humidity. The analysis of meteorological conditions at the surface and up to the first layer above the cloud cover show some differences, but mainly common feature of wind directions, temperature inversion

and humidity. The larger differences were observed above the cloud layers, at 850 and 700 hPa and where aerosol layer resides.

The results of the radiative transfer simulations show that aerosols are 88 % responsible for heating the layer where they reside, while the water vapor may impact the cloud processes, by affecting the cloud top cooling: more water vapor in the mid-troposphere leads to less cooling at the cloud top. Thus, the presence of smoke layers in the scene impacts significantly its radiative budget and modifies the heating rates. These are identified mechanisms for AAC semi-direct effects on clouds. However, we are still cautious in attributing the observed effects on clouds to aerosols.

Following these results, some questions arise that make the object of a future study: would a further analysis over the months of September and October show similar results with the ones observed from June to August? Taking into account the fact that the amount of aerosols and water vapor increase in these months, are we to expect a larger warming of the aerosol layer and a stronger impact at the cloud top?

Using our large database we can further calculate the heating rates of aerosol above clouds for a larger region to better study the transport effect, or even at a global scale. We could also calculate the heating rates of high and low situations by considering the CALIOP and POLDER observations with different aerosol and cloud spatial features. We can afterwards validate our computed heating rates by comparing them with the AEROCLO-sA data, as the mission also performed flux measurements within the smoke layers and simultaneously retrieved the water vapor content.

We also propose to combine our database with a climate or regional model to check the consistency of our data. The model can be constrained using observations (aerosol and cloud parameters, water vapor content, meteorological profiles), and can provide simulations made with and without aerosols. We have to account for the covariance between humidity, aerosol and temperature profiles in order to better separate the meteorology and the aerosol effects; this is not really possible using only observation.

The use of a model provides many advantages: (i) it could help disentangling the effects of meteorology versus the aerosol and water vapor effects with the smoke layers; (ii) it allows the calculation of cloud sensitivity to the presence of aerosols and to compare with sensitivities obtained from observations; (iii) it can help understand the diurnal variation (evolution of cloud properties – LWP, CTA) as a response to boundary layer characteristics; (iv) it can clarify the link between cloud processes and the perturbations of the radiative budget (does warming of aerosol layer and reduction of cloud top cooling produce effects that go in the same way?); (v) LES (large-eddy simulation) modeling could be used to reproduce the entire scene, that would give interesting possible comparison with our observations, with ECMWF data or with AEROCLO-sA observations. If a good agreement between data and the models is found, our results would be confirmed, and indeed the effects observed on clouds could definitely be attributed to a semi-direct effect of aerosols.

Annex A

- Average aerosol and cloud properties over the sample area
- Heating rate profiles in shortwave and longwave spectrum, and their total

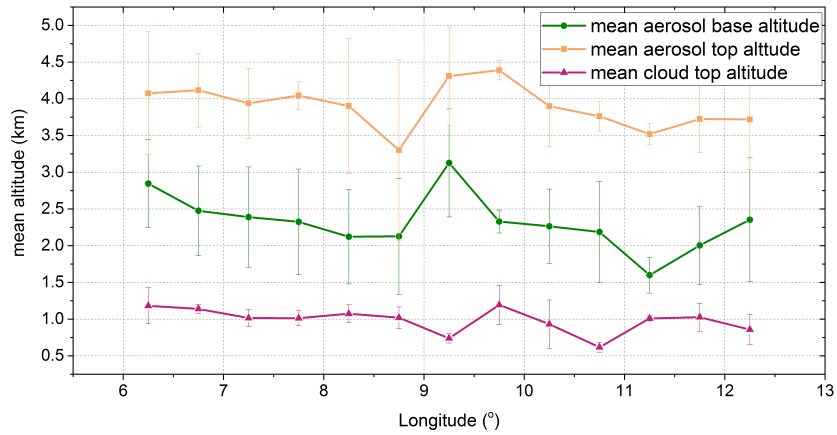


Figure. A.1 – Mean cloud top altitude, aerosol base altitude and aerosol top altitude as a function of longitude, over the sample region for June-August 2008. Vertical bars represent the standard deviation

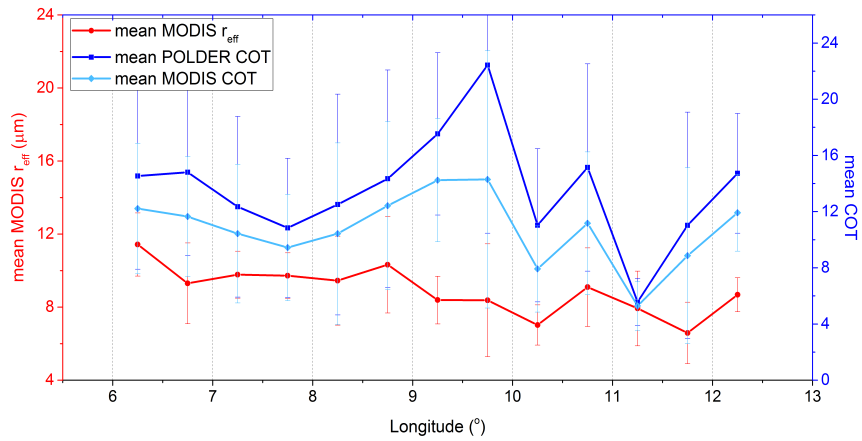


Figure. A.2 – Mean MODIS effective radius, mean MODIS COT and mean POLDER COT as a function of longitude, over the sample area from June to August 2008.

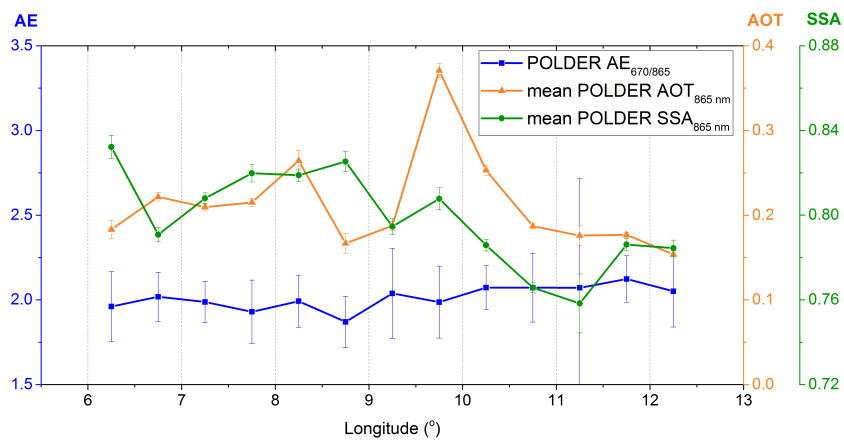


Figure. A.3 – Mean POLDER AOT and SSA at 865 nm; mean POLDER AE_{670/865nm} over the sample area, from June to August 2008.

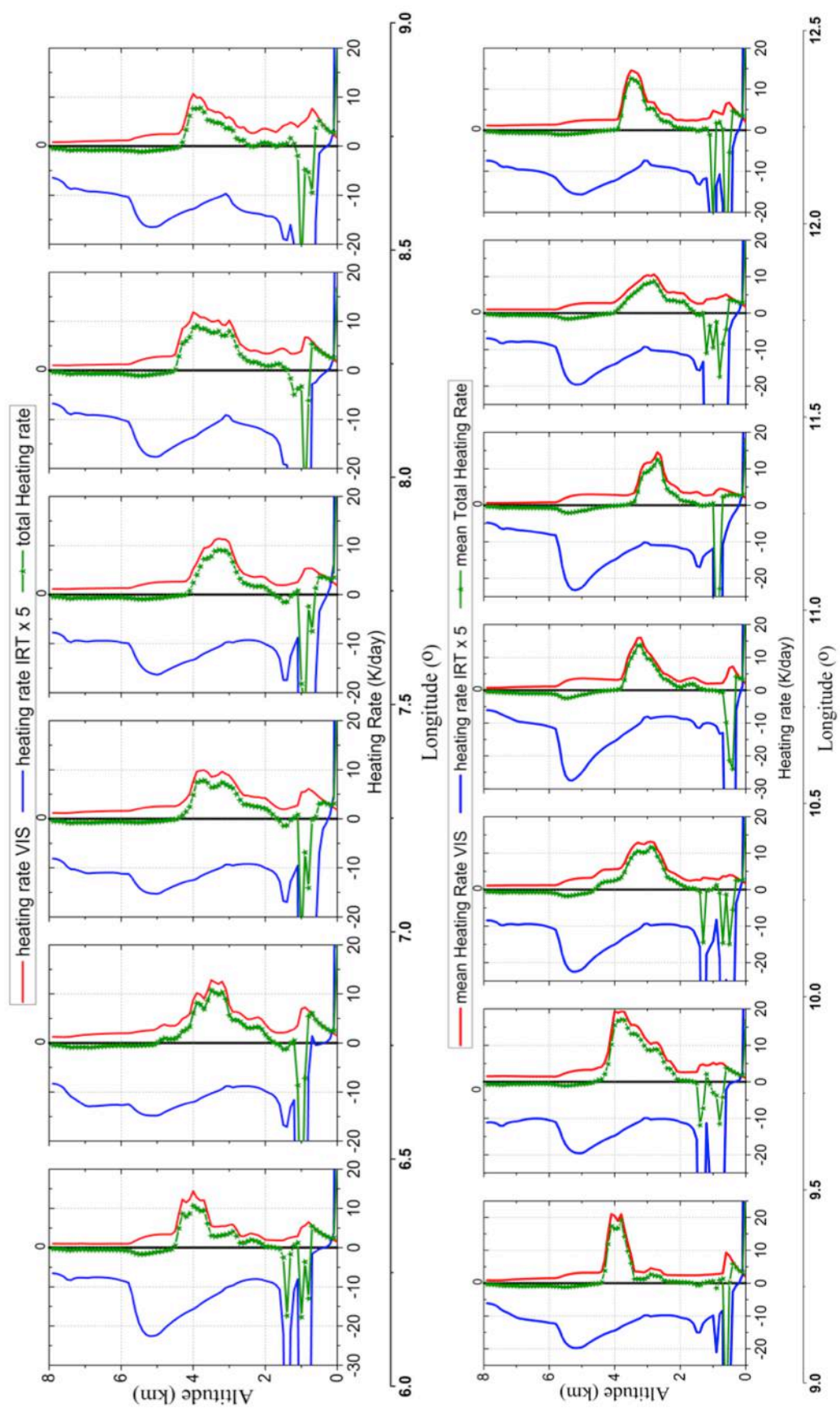


Figure. A.4— Average shortwave heating rate (red line), average longwave heating rate (blue line) multiplied with 5, and total heating rate (green stars) (K/day) profiles per 0.5 degree of longitude from June to August 2008 within the selected region.

Annex B

- Consistency of aerosols above clouds characterization from A-Train active and passive measurements



Consistency of aerosols above clouds characterization from A-Train active and passive measurements

Lucia T. Deaconu¹, Fabien Waquet¹, Damien Josset², Nicolas Ferlay¹, Fanny Peers³, François Thieuleux¹, Fabrice Ducos¹, Nicolas Pascal⁴, Didier Tanré¹, Jacques Pelon⁵, and Philippe Goloub¹

¹Université de Lille, CNRS, UMR 8518, LOA – Laboratoire d’Optique Atmosphérique, 59000 Lille, France

²US Naval Research Laboratory, NASA Stennis Space Center, 39529, Mississippi, USA

³College of Engineering, Mathematics and Physical Sciences, University of Exeter, Exeter, UK

⁴ICARE Data and Services Center, University of Lille, Villeneuve d’Ascq, 59655, France

⁵LATMOS, Université Paris, (CNRS-UVSQ), Paris 75005, France

Correspondence to: Lucia T. Deaconu (lucia-timea.deaconu@ed.univ-lille1.fr)
and Fabien Waquet (fabien.waquet@univ-lille1.fr)

Received: 10 February 2017 – Discussion started: 13 March 2017

Revised: 20 July 2017 – Accepted: 1 August 2017 – Published: 22 September 2017

Abstract. This study presents a comparison between the retrieval of optical properties of aerosol above clouds (AAC) from different techniques developed for the A-Train sensors CALIOP/CALIPSO and POLDER/PARASOL. The main objective is to analyse the consistency between the results derived from the active and the passive measurements. We compare the aerosol optical thickness (AOT) above optically thick clouds (cloud optical thickness (COT) larger than 3) and their Ångström exponent (AE). These parameters are retrieved with the CALIOP operational method, the POLDER operational polarization method and the CALIOP-based depolarization ratio method (DRM) – for which we also propose a calibrated version (denominated DRM_{SODA}, where SODA is the Synergized Optical Depth of Aerosols). We analyse 6 months of data over three distinctive regions characterized by different types of aerosols and clouds. Additionally, for these regions, we select three case studies: a biomass-burning event over the South Atlantic Ocean, a Saharan dust case over the North Atlantic Ocean and a Siberian biomass-burning event over the North Pacific Ocean. Four and a half years of data are studied over the entire globe for distinct situations where aerosol and cloud layers are in contact or vertically separated. Overall, the regional analysis shows a good correlation between the POLDER and the DRM_{SODA} AOTs when the microphysics of aerosols is dominated by fine-mode particles of biomass-burning aerosols from southern Africa (correlation coefficient (R^2) of 0.83) or

coarse-mode aerosols of Saharan dust (R^2 of 0.82). A good correlation between these methods (R^2 of 0.68) is also observed in the global treatment, when the aerosol and cloud layers are separated well. The analysis of detached layers also shows a mean difference in AOT of 0.07 at 532 nm between POLDER and DRM_{SODA} at a global scale. The correlation between the retrievals decreases when a complex mixture of aerosols is expected (R^2 of 0.37) – as in the East Asia region – and when the aerosol–cloud layers are in contact (R^2 of 0.36). The correlation coefficient between the CALIOP operational method and POLDER is found to be low, as the CALIOP method largely underestimates the aerosol loading above clouds by a factor that ranges from 2 to 4.

Potential biases on the retrieved AOT as a function of cloud properties are also investigated. For different types of scenes, the retrieval of above-cloud AOT from POLDER and from DRM are compared for different underlying cloud properties (droplet effective radius (r_{eff}) and COT retrieved with MODIS). The results reveal that DRM AOT vary with r_{eff} . When accounting for r_{eff} in the DRM algorithm, the consistency between the methods increases. The sensitivity study shows that an additional polarized signal coming from aerosols located *within* the cloud could affect the polarization method, which leads to an overestimation of the AOT retrieved with POLDER algorithm. In addition, the aerosols *attached* to or *within* the cloud can potentially impact the DRM retrievals through the modification of the cloud droplet

chemical composition and its ability to backscatter light. The next step of this work is to combine POLDER and CALIOP to investigate the impacts of aerosols on clouds and climate when these particles are transported above or within clouds.

1 Introduction

By interacting with radiations and by modifying the cloud reflectivity and microphysics, aerosols have important impacts on the Earth's radiative budget and water cycle (IPCC, 2013). These atmospheric particles absorb and scatter the sunlight, resulting in the so-called direct radiative effect (DRE). Although aerosols always produce a cooling effect at the Earth's surface, the sign and the amplitude of the DRE of aerosols at the top of the atmosphere depend not only on the aerosol properties but also on the reflective properties of underlying surface. For instance, in cases where absorbing aerosol layers are located above clouds, the DRE of aerosols is predominantly positive as a result of the reduction of the local planetary albedo (Keil and Haywood, 2003). By absorbing sunlight, aerosols also warm the layer of the atmosphere where they reside. This modifies the vertical profile of temperature in the atmosphere, which may affect the process of evaporation and cloud formation. This effect is called the semi-direct effect (Hansen et al., 1997; Ramanathan et al., 2001). Aerosols also impact the cloud properties by acting as cloud condensation nuclei and ice nuclei. They may modify the cloud microphysics and cloud brightness with potential impacts on precipitation and cloud lifetime (Rosenfeld, 2000; Twomey, 1974). These effects are referred as aerosol indirect effects and tend to cool the Earth.

The lack of knowledge of aerosol properties in cases of scenes of aerosols above clouds (AAC) has been recently highlighted as a source of uncertainty for the estimation of all-sky DRE of aerosols (Peers et al., 2016). Different approaches have been developed to quantify the DRE of AAC using satellite observations (Chand et al., 2009; Feng and Christopher, 2015; Meyer et al., 2013). But despite recent observational and modelling studies (De Graaf et al., 2014; Peers et al., 2015, 2016; Zhang et al., 2016), the aerosol DRE for AAC remains a subject of large uncertainty. In the process of quantification and interpretation of the aerosol impact on climate, the aerosol interactions with clouds constitute the largest uncertainty in global climate models (Myhre et al., 2013a, b). The study of AAC may also contribute to reduce those uncertainties. For instance, in case of absorbing AAC, the warming of the atmosphere occurring above stratocumulus clouds might reduce the strength of the convection and consequently impact the vertical development and the cloud properties. This warming might inhibit the entrainment of dry air at the top of the cloud, preserving the humidity of the cloud and increasing the liquid water content and the persistence of clouds (Johnson et al., 2004; Wilcox, 2010). Evi-

dence of the first indirect effect was also found over the South Atlantic region, where AAC events are frequently observed. Costantino and Bréon (2013) notably found a strong decrease in the droplet effective radius when the aerosol layers are in contact with the top altitude of the cloud deck.

The scientific community is working on better monitoring the load and microphysical properties of AAC in order to assess the influence of those particles on the Earth's radiative budget and clouds. The constellation of satellites called the A-Train provides different passive and active sensors for monitoring clouds and aerosols (<http://atrain.nasa.gov/publications/A-TrainFactSheet.pdf>). Passive imagers offer larger spatial coverage but have no direct information of the vertical distribution of particles in the atmosphere. Active methods offer unique capabilities, complementary to the passive methods, and are dedicated to the study of the vertical profiles of clouds and aerosols. The main retrieved optical properties for aerosols, in "clear-sky" conditions, are the aerosol optical thickness (AOT) and the Ångström exponent (AE), which is a parameter indicative of the particles size (Kaufman et al., 2002). Recent methods also allow retrieving the aerosol single scattering albedo (SSA) over clear-sky ocean scenes (Torres et al., 2013; Waquet et al., 2016).

The active sensor Cloud-Aerosol Lidar with Orthogonal Polarization (CALIOP) installed on CALIPSO (Cloud-Aerosol Lidar and Infrared Pathfinder Satellite Observation) satellite provides high-resolution vertical profiles of aerosols and clouds (Chand et al., 2008; Winker et al., 2010). CALIOP provides the total attenuated backscatter signal ($\text{km}^{-1} \text{sr}^{-1}$) at 532 and 1064 nm. From the backscatter measurements, an operational aerosol algorithm allows for retrieval of the vertical extinction profiles as well as the AOT in clear and cloudy skies by assuming an aerosol lidar ratio (extinction to backscatter) (Omar et al., 2009; Young and Vaughan, 2009). Moreover, two orthogonally polarized channels measure the parallel and perpendicular backscatter signal at 532 nm that allows calculating the depolarization ratio (i.e. the ratio of the two orthogonal polarization signals) (Hunt et al., 2009). Depolarization measurements are used for discrimination between spherical and non-spherical particles (Sassen, 1991). CALIOP provides exhaustive details on the vertical distribution of optical and microphysical properties of aerosols and clouds, including their shape, and a qualitative classification of aerosol type (via the wavelength dependence of the backscatter) (Winker et al., 2009; Young and Vaughan, 2009).

Alternative CALIOP-based research methods have also been introduced to retrieve above-cloud AOT (ACAOT). The depolarization ratio method (DRM) (Hu et al., 2007a) and the colour ratio method (CRM) (Chand et al., 2008) use fewer assumptions for the retrieval of aerosol properties. These methods are based on light transmission methods and treat the liquid water clouds situated underneath the aerosol layer as a target. Hu et al. (2007b) have shown that, in the case of opaque water clouds, the layer-integrated attenuated

backscatter at 532 nm and layer-integrated attenuated depolarization ratio at 532 nm can be used to retrieve the aerosol optical depth of the overlying aerosol or optically thin cloud layers. The CRM uses the layer-integrated attenuated colour ratio, which is the ratio of integrated attenuated backscatter at 1064 to 532 nm. Over the visible to near-infrared spectral region, fine-mode absorbing aerosols above clouds exhibit a strong wavelength dependence colour ratio (Chand et al., 2008). This makes possible the detection of absorbing biomass-burning aerosols transported above clouds. The colour ratio observed in the case of coarse-mode particles or purely scattering fine-mode aerosols transported above clouds exhibits little or no wavelength dependence and, thus, these particles can be less accurately detected with the CRM method.

Passive sensors have also been used to obtain information on aerosols above clouds. For example, Torres et al. (2012) have developed an algorithm to retrieve the ACAOT and the underlying aerosol-corrected cloud optical depth, using radiance measurements performed in the ultraviolet (UV) by the Ozone Monitoring Instrument (OMI). The method takes advantage of the ability of biomass-burning and mineral dust aerosols to strongly absorb UV radiations. Another method that can retrieve the ACAOT and, simultaneously, the aerosol-corrected cloud optical thickness (COT) is the “colour ratio” method proposed by Jethva et al. (2013) that employs measurements in visible and shortwave infrared channels from the Moderate Resolution Imaging Spectroradiometer (MODIS). Also, Meyer et al. (2015) developed an algorithm that employs reflectance measurements from six MODIS channels (from the visible to the shortwave infrared) to retrieve the ACAOT, as well as the COT and droplet effective radius (r_{eff}) of the underlying cloud.

The multi-directional polarization measurements have shown sensitivity to AAC scenes (Waquet et al., 2009; Hasekamp, 2010; Knobelspiesse et al., 2011). The Polarization and Directionality of Earth Reflectances (POLDER) instrument is measuring the directionality and polarization of light reflected by the Earth–atmosphere system. The aerosols generate an additional polarized light at forward and side scattering angles (70–130°) and reduce the polarized signal of the cloud bow (i.e. a strong polarized rainbow feature observed near 140° in scattering angle). Mineral dust particles do not much polarize light, but they strongly minimize the cloud bow magnitude. Based on these effects, Waquet et al. (2009) have developed a method for retrieving the properties of aerosols above clouds that relies on the polarized radiances measured by POLDER. Because polarized radiances are not affected by the optical thickness of the cloud (i.e. the polarized radiance reflected by the cloud is saturated when the cloud is optically thick enough), the method is able to retrieve the scattering ACAOT at two wavelengths (670 and 865 nm) without much assumption about cloud properties. An analysis of the global results obtained with the operational algorithm is given in Waquet et al. (2013a). Further-

more, Peers et al. (2015) have developed a complementary method that uses additional total multidirectional radiances measured by POLDER. The method provides the aerosol SSA and the aerosol-corrected COT. So far, the algorithm of Peers et al. (2015) is a research method, only applied for regional studies (Peers et al., 2016).

Jethva et al. (2014) performed an intercomparative analysis of the ACAOT retrieved with the aforementioned methods in order to assess the consistency (or lack thereof) between the two independently derived ACAOTs. The results were encouraging and, despite the use of different assumptions and measurements, a close agreement was reported over homogeneous clouds. Similar to this study, our paper will focus on the comparison between collocated active and passive AAC inversion products, improving our understanding of the ACAOT. But, compared to Jethva et al. (2014), who focused only on two study cases, we perform a global and multi-annual investigation to provide robust statistics results. The vertical distribution of the aerosol and cloud layer will be also considered. We will concentrate on the following methods: (a) the CALIOP operational method (CALIOP_{OM}) because of the numerous studies in which it was used, (b) the DRM developed by Hu et al. (2007a), (c) a calibrated version of the DRM algorithm and (d) the POLDER polarization method. The DRM and POLDER methods were chosen because both are measuring AAC properties above the same type of cloudy scenes (i.e. optically thick and homogeneous liquid water clouds). Moreover, both techniques are sensitive to all types of particles (scattering or absorbing particles, fine or coarse ones), which is not the case for CRM, which can operate only for absorbing aerosols. It is also interesting to compare these two approaches since the POLDER method requires a hypothesized aerosol microphysics, while DRM does not require any hypothesis for the aerosols but does require assumptions and an approximate model to estimate the signal backscattered by clouds.

To begin with, we briefly recall the principle of each algorithm and the data selection strategy. The results of AOT intercomparison are presented in Sects. 3 and 4. We first present a regional comparison and then describe a global comparison for a period of 4.5 years in function of the type of aerosols and AAC scenes (aerosol and cloud layers in contact or well separated). Discussions and conclusions will be drawn in Sects. 5 and 6.

2 Methodology and data selection

2.1 POLDER polarization method

POLDER, an instrument on the PARASOL (Polarization and Anisotropy of Reflectances for Atmospheric Science coupled with Observations from a Lidar) satellite, is a wide-field imaging radiometer/polarimeter (Tanré et al., 2011). This instrument measures the angular and spectral behaviour of

the normalized total and polarized radiances (Herman et al., 2005).

The method for retrieving the above-cloud scattering AOT developed by Waquet et al. (2013b) consists of a comparison between polarized radiances measured by POLDER at 670 and 865 nm and polarized radiances pre-computed with a successive order of scattering (SOS) code (Deuzé et al., 1989) for seven aerosol models that follow a single log-normal size distribution. Six models correspond to spherical aerosols (fine-mode particles) with radius from 0.06 to 0.16 μm , for which a complex refractive index of $1.47 - 0.01i$ is assumed. The seventh model is bimodal and characteristic of non-spherical aerosols (dust) with a refractive index of $1.47 - 0.0007i$. In the search for the best-fitting aerosol model, the operational algorithm follows the strategy described by Waquet et al. (2013b). After a first step, the algorithm produces an approximation of the AOT at 865 nm. As a function of this AOT value, a decision tree is applied: if the AOT is larger than 0.1 then the algorithm will search the best-fitting model within all the seven models without any angular constraint for the selection of the POLDER data (scattering angle ranging from 0 to 180°). Next, if the mineral dust model fails to reproduce the data or if the AOT retrieved in the first step is smaller than 0.1, then only fine-mode models are considered in the retrieval scheme and the viewing geometries are restricted to side or forward viewing geometries (scattering angles smaller than 130°). The AOT threshold of 0.1 at 865 nm is empirical and was introduced since the retrieval of the aerosol type (dust or fine-mode particles) becomes difficult for small AOT.

Collocated cloud properties retrieved from MODIS at high resolution ($1 \times 1 \text{ km}^2$ at nadir) are used to characterize and to select the cloudy scenes within a POLDER pixel ($6 \text{ km} \times 6 \text{ km}$ at nadir). We only consider fully covered cloudy pixels associated with optically thick liquid water clouds: the COT retrieved by MODIS has to be larger than 3 and a cloud phase algorithm is applied to select liquid water clouds (Riedi et al., 2010). Moreover, Waquet et al. (2013b) have introduced a mask to eliminate cirrus above liquid clouds that makes use of the MODIS brightness temperature difference (BTD) between 8.5 and 11 μm wavelength bands as well as MODIS and POLDER cloud top pressure estimates. Lastly, the AOT retrievals at the $6 \text{ km} \times 6 \text{ km}$ spatial resolution are aggregated to $18 \text{ km} \times 18 \text{ km}$ spatial grid. The retrieved solution is kept if the number of $6 \text{ km} \times 6 \text{ km}$ pixels is larger than 5 and if the standard deviation computed for the mean AOT is smaller than 0.1. This latter procedure allows to remove edges of clouds. In our study, we use the version 3.00 of the official output product PARASOL_PM02-L2 for AAC scenes available at ICARE website (<http://www.icare.univ-lille1.fr/parasol/products/>).

2.2 CALIOP methods

2.2.1 Operational method

The CALIPSO lidar (CALIOP) is a frequency-doubled Nd:YAG laser, dual-wavelength, dual-polarization, elastic backscatter lidar (Winker et al., 2009). The lidar returned signal is normalized and range-corrected to provide the total attenuated backscatter coefficient ($\text{km}^{-1} \text{ sr}^{-1}$).

In order to retrieve the attenuated backscatter data and the columnar AOT at 532 and 1064 nm, the operational CALIOP algorithm combines the feature and layer detection scheme (Vaughan et al., 2009) with the extinction retrieval algorithm (Young and Vaughan, 2009) that employs assumptions on the extinction-to-backscatter ratio of aerosols. There are several steps involved in the operational data processing: (1) cloud and aerosol layers are detected in the backscattered signal along with their altitudes; (2) the algorithm determines which layers have cloud or aerosol features; (3) the cloud ice-water phase is estimated and the aerosol lidar ratio is determined, using assumptions on the aerosol models; and finally (4) the extinction coefficients and AOT are retrieved at 532 and 1064 nm.

Lidar systems have a limited capability to determine the composition and size of aerosols. Hypotheses are then used on the aerosol phase function at 180° and on the aerosol SSA in order to calculate the aerosol lidar ratio. In the operational algorithm, the aerosol models consist in a mixture of aerosol components characteristic of a region or an air mass. It should be noted that an incorrect assumption for the lidar ratio could be a source of substantial errors in the AOT retrieved with this method.

For our study we use the level 2 version 3.01 of the inversion products, officially named CAL_LID_L2_05kmALay (ALay) and CAL_LID_L2_05kmCLay (CLay) (which can be found at <http://www.icare.univ-lille1.fr/calipso/products/>), which provide, respectively, the aerosol and cloud layer parameters at a nominal horizontal resolution of 5 km. From these products we used the AOTs retrieved at 532 and 1064 nm, the aerosol base and top altitudes, the cloud top altitude, the ice-water cloud phase and the feature type. We also use CALIOP level 1 dataset, labelled CAL_LID_L1-ValStage1 (link above), which provides the attenuated backscatter coefficient calculated at a vertical resolution of 30 m from -0.5 to 8.2 km altitude and at 333 m horizontal resolution (Winker et al., 2007).

2.2.2 Depolarization ratio method

For retrieving the optical thickness of a thin high layer (aerosols or clouds) above a lower and optically thick water cloud layer, Hu et al. (2007a) and Chand et al. (2008) describe the depolarization ratio method applied to CALIOP measurements. An opaque cloud with a minimum optical depth of 3 will attenuate the lidar beam completely. For op-

tically thick clouds, we estimate the optical thickness of the above thin aerosol or cloud layer by treating the opaque cloud as a target and by using the Beer–Lambert law to estimate the direct transmission of light above this cloud layer. We will refer to this product hereafter as DRM_{Hu} .

The physical properties used in this method are the cloud attenuated backscatter coefficient (γ'_{water}) integrated from the base to the top of the cloud layer at 532 nm and the integrated attenuated depolarization ratio (δ') at 532 nm. When Rayleigh scattering contribution has been corrected for, the definition of γ'_{water} is given by the following equation:

$$\gamma'_{\text{water}} = \int_{z_{\text{top}}}^{z_{\text{base}}} \beta'(z) dz, \quad (1)$$

where β' is the total attenuated backscatter coefficient ($\text{km}^{-1} \text{sr}^{-1}$).

In situations where the cloud is optically thick and there are no aerosols above the cloud, the lidar equation simplifies to the following definition, expressed as a function of the lidar ratio (S_c) and layer-effective multiple scattering factor (η_c) (Platt, 1979):

$$\gamma'_{\text{water, calc}} = \int_{z_{\text{top}}}^{z_{\text{base}}} \beta'(z) dz = (2\eta_c S_c)^{-1}. \quad (2)$$

S_c is narrowly constrained to about 19 sr at a wavelength of 532 nm. This value is typically used for liquid water clouds with droplets smaller than about 50 μm (O'Connor et al., 2004; Pinnick et al., 1983). η_c , which takes a value between 0 and 1, is strongly related to the cloud depolarization ratio δ' (defined as the ratio of the parallel and perpendicular polarization signals), since multiple scattering processes tend to depolarize light. An approximate relation was derived from Monte Carlo simulations (Hu et al., 2006):

$$\eta_c = \left(\frac{1 - \delta'}{1 + \delta'} \right)^2. \quad (3)$$

After γ'_{water} is corrected for molecular and gaseous attenuation, the ratio between γ'_{water} and $\gamma'_{\text{water, calc}}$ should be equal to 1 in the absence of higher aerosol or cloud layer and have an accurate lidar calibration. Instead, in case of an overlying aerosol or cloud layer, this ratio can be written as

$$\frac{\gamma'_{\text{water}}}{\gamma'_{\text{water, calc}}} = T^2 = \exp(-2\tau_{\text{top, DR}}), \quad (4)$$

where T^2 is the transmission of light after a two-way propagation between the sensor and the targeted cloud, and $\tau_{\text{top, DR}}$ is the higher layer's optical thickness. It follows from Eq. (4) that the optical depth ($\tau_{\text{top, DR}}$) is given by

$$\tau_{\text{top, DR}} = \frac{-1}{2} \ln(2S_c \gamma'_{\text{water}} \eta_c). \quad (5)$$

DRM_{Hu} differs from the operational method by the fact that it does not rely on assumptions related to aerosol microphysical properties (aerosol phase function and SSA) and does not require accurate layer detection for the overlying aerosol layer in order to estimate the AOT integrated over the atmospheric column. The main uncertainties of the DRM_{Hu} are linked to the calibration of the lidar, which impact the estimate of the parameters in Eq. (5).

Providing a robust, self-calibrated method at global scale and for the whole CALIPSO dataset is not trivial and, in order to improve the estimate of the AOT with the DR method, the developers of the Synergized Optical Depth of Aerosols and ICE clouds (SODA & ICE, available at the ICARE thematic centre), Josset et al. (2010, 2012), modified the original formalism of DRM_{Hu} . The main reason for these modifications is that the relationship between the multiple scattering factor and the depolarization by the cloud shows a systematic deviation from the theory (see Fig. 2 in Hu, 2007). The multiple scattering–depolarization relationship has been confirmed by laboratory experiments (Cao et al., 2009). Even if it has to be modified in the presence of submicrometer or non-spherical particles, the origin of the discrepancy between theory and observation points towards an instrumental issue. The long transient response of the receiver has been proposed as an explanation and a correction was also proposed (Hu et al., 2007b). There are, however, other issues related to the calibration of the polarization channel that could explain the discrepancy. The low gain–high gain merging scheme and the day–night calibration transfer are a significant source of uncertainty. Previous research (Sassen and Zhu, 2009) found a bias in the linear depolarization of cirrus clouds of around 30 %.

In order to overcome these difficulties and improve the accuracy of the method, SODA takes advantage of the high number of CALIOP observations of liquid water clouds in the absence of AAC. Practically, the SODA algorithm introduces global-scale correction factors in the multiple scattering coefficient to depolarization relationship and a recalibrated value of the liquid water cloud lidar ratio as a function of latitudes. These two corrections come from the fact that, when the liquid water clouds are optically dense and in absence of AAC, the lidar equation can be reduced to Eq. (2). Over the ocean, the lidar ratio of most liquid water clouds is relatively constant (Hu et al., 2006) and the multiple scattering coefficient can be measured directly if the lidar is well calibrated. This correction follows the original intent of DRM_{Hu} (Hu et al., 2007a), which has always been to be a self-calibrated method, unaffected by instrumental or geophysical uncertainties (see Eq. 4 of Hu et al., 2007a, and related discussion). However, because the discrepancy between theory and observations is due to an instrumental artefact linked to the receiver electronics, SODA introduces a clearer separation between the parallel and perpendicular channel than in DRM_{Hu} (Hu et al., 2007b). DRM_{Hu} relates the total backscatter coefficient to the ratio of perpendicu-

lar and parallel backscatter coefficient while SODA links the parallel backscatter coefficient to this ratio. This approach is supported by the theory of light propagation in dense medium where the contribution of multiple scattering in the perpendicular and parallel channel is identical (Xu and Alfano, 2005) and by the analysis of CALIOP data.

A preliminary and mandatory step of the calibration procedure is to select optically opaque liquid water clouds with no AAC. The calibration modules of SODA use the following criteria. Note that there is some level of redundancy in order to increase data quality selection.

a. Criteria of optical density:

- The top and bottom of the cloud is given by the 333 m CALIPSO cloud product. This ensures a minimum level of signal strength and the presence of a transparent atmosphere above it. Note that SODA corrects the molecular attenuation above the cloud but does not contain an explicit correction of it within the cloud because of the high scattering ratio of liquid water clouds. Nonetheless, the molecular contribution is statistically taken into account by the calibration procedure.
- The maximum of the lidar signal is above the base of the cloud. This ensures an adequate level of attenuation of the surface return.
- The ocean surface integrated attenuated backscatter is below a detectability threshold of $7.5 \times 10^{-6} \text{ sr}^{-1}$ for nighttime data and $1 \times 10^{-3} \text{ sr}^{-1}$ for daytime data. This corresponds to a COT of around 2 during daytime and 4–5 during nighttime, which is when this filter is the most useful. The intent of this threshold is the same as the previous criteria. More specifically, the goal is to use a threshold such that half the shots are below the noise sensitivity of the instrument.

b. Criteria of cloud in liquid phase:

- The temperature at the top of the cloud is higher than 0°C . The isotherm is defined by the GMAO (Global Modelling and Assimilation Office) temperature when interpolated on the CALIPSO vertical grid.
- The total cloud liquid water contained in a vertical column of atmosphere retrieved from collocated pixels of AMSR-E/AMSR2 is larger than 0 mm.

c. Criteria of clear air above the cloud:

- The total 532 nm integrated attenuated backscatter coefficient from 20 km of altitude to the top of the cloud is below the following threshold:

$$\int_{z_{\text{top}}}^{20 \text{ km}} \beta'(z) dz < \frac{1 - \exp(-2\tau_{\text{air,mol}})}{2 \frac{8\pi}{3} 1.5}, \quad (6)$$

where $\tau_{\text{air,mol}}$ is the optical depth due to air Rayleigh scattering and ozone absorption. The factor of 1.5 allows the reduction of occurrences of false positives due to noise. It also allows us to simplify the formalism as the King factor (Bates, 1984; King, 1923) can be neglected with no expected impact on the results. As this filter introduces more aerosol contamination during daytime (similar to Josset et al., 2010, Fig. 4), it could be desirable to consider the shot-to-shot CALIOP cloud mask for future version of the algorithm as SODA already uses this information for the scene classification flag.

As previously mentioned, even if the multiple scattering–depolarization relationship has been confirmed by laboratory experiments (Cao et al., 2009), the relationship between the multiple scattering factor and the depolarization by the cloud shows a systematic deviation from the theory. It has to be corrected, as it would introduce a bias in aerosol optical depth with the particularly undesirable trait to correlate with cloud microphysical properties. As a first step, SODA calibrates the multiple scattering to depolarization relationship for nighttime data on a monthly basis. The data of interest are based on Eq. (2) and can be written as

$$\eta_{\text{geo}} = \frac{1}{2 \times 19 \times \gamma'_{\text{water,parallel}}}, \quad (7)$$

where $\gamma'_{\text{water,parallel}}$ is the parallel-integrated backscatter coefficient. This equation provides a direct measurement of the multiple scattering coefficient of liquid water clouds (η_{geo}) when their lidar ratio is constant. The constant value of 19 sr used in the SODA algorithm is based on Hu et al. (2006), who found a lidar ratio equal to 19.1 ± 0.21 sr when the 41 droplet size distributions of Miles et al. (2000) are used as inputs of a Mie scattering code.

For all opaque liquid water clouds defined with the above criteria, SODA then compares the direct measurement of the multiple scattering coefficient (η_{geo}) and the theory (η_c) to find the second-order polynomial that best fit the data in the least-squares fit sense. This defines the calibrated multiple scattering coefficient (η_{calibr}):

$$\eta_{\text{calibr}} = \text{fit}[\eta_{\text{geo}}(\eta_c)] = A\eta_c + B\eta_c^2. \quad (8)$$

This procedure allows us to use a relationship between depolarization and multiple scattering that fits the observation.

Using Eq. (3) instead of Eq. (8) would create an aerosol optical depth bias that would typically range between 0.02 and 0.08. Although this is not always significant, this correction is necessary as the resulting ACAOT bias does correlate with the cloud's microphysical properties. This is particularly undesirable as the link between aerosol and cloud microphysical properties is an active topic of research.

As a second step, SODA calculates the apparent lidar ratio $S_{c,lat}$ of all opaque liquid water clouds as a function of each degree of latitude and for both 532 and 1064 nm. This procedure is done separately for daytime and nighttime data. The latitudinal dependency aims to correct the calibration inaccuracies of CALIOP, which are dependent on latitude (Powell et al., 2010) and possible geophysical variations of cloud microphysical properties between the northern and southern hemispheres.

$$S_{c,lat} = \frac{1}{2 \times \eta_{calibr} \times \gamma'_{water,parallel}} \quad (9)$$

For the 4.5 years of data we considered in this study, the median of $S_{c,lat}$ for the nighttime data is 19.36 sr, which is interestingly close from the theoretical value determined by Hu et al. (2006). For daytime data, $S_{c,lat}$ is systematically higher and with a median of 20.64 sr. The systematic daytime–nighttime difference could be geophysical. However, it is premature to reach such conclusion until all nighttime–daytime differences in the CALIPSO data have been addressed.

Lastly, all these coefficients are finally integrated in the AOT retrieval equation:

$$\tau_{top,DRcalibr} = -\frac{1}{2} \ln(2S_{c,lat} \eta_{calibr} \gamma'_{water,parallel}), \quad (10)$$

Throughout this study, we will refer to this product as DRM_{SODA} , which can be found at ICARE Data and Services Center (<http://www.icare.univ-lille1.fr/projects/soda/>).

2.3 Data selection

2.3.1 Collocation

The A-Train satellites pass through close orbits within several minutes, providing coincident observations of POLDER, MODIS and CALIOP instruments. Using the nearest pixel approximation, CALIOP files are used as a space reference for sampling POLDER and MODIS products. CALTRACK is the output dataset and can be found at ICARE. It contains coincident data from POLDER at $18 \text{ km} \times 18 \text{ km}$ and MODIS, extracted under the CALIOP track at 5 km horizontal resolution. The DRM_{Hu} and DRM_{SODA} optical depth retrievals are processed at the CALIOP native resolution of 333 m and aggregated afterwards at 5 km horizontal resolution. Moreover, for a better consistency of the AOT comparison, the POLDER AOT was extrapolated at 532 nm using the AE retrieved with the POLDER algorithm.

We also limited the cloud top altitude at 5 km because we are interested in low-level clouds. Likewise, we eliminated from our data analysis all situations in which the aerosol top altitude exceeds 10 km. This maximal value should be sufficient, since most of the biomass-burning and dust aerosol layers are typically observed between 0.5 and 4.0 km over ocean (Torres et al., 2013).

2.3.2 Distinction between vertical profiles

Additionally, we have employed an approach that is similar to the concept of Costantino and Bréon (2013) to classify the type of AAC scenes. The respective positions of the aerosol and cloud layers are defined using the CALIOP ALay and CLay products. We classify the AAC scenes into three categories: “attached”, “detached” and “undetermined”. The so-called “attached cases” correspond to situations where the aerosol layer touches the top of the beneath cloud layer. For these cases, we assume that the vertical distance of the aerosol bottom altitude from cloud top altitude must be lower than 100 m, without penetrating the cloud layer for more than 50 m. Inversely, the “detached cases” correspond to aerosol and cloud layers that are considered well separated, considering a distance higher than 500 m between the aerosol base altitude and the cloud top. Aerosol layers with the base altitude within a distance between 100 and 500 m above the cloud layer are considered too uncertain and are excluded from our study. We also removed the situations for which the detected CALIOP aerosol top and/or bottom altitudes are located below the cloud top, assuming that these data are highly uncertain. Practically, we rejected the CALIOP data for which the aerosol layer penetrates the cloud layer by more than 50 m. The third category, “undetermined”, corresponds to situations for which the respective position of the aerosol or cloud layer is not identified by the CALIOP layer detection algorithm (i.e. missing data), even though POLDER and DRM_{AAC} AOT retrievals are valid. We chose to keep these data in our analysis as they cover the majority of POLDER AAC detected cases with a non-negligible AOT (even if CALIOP classifies them as invalid or noise), as the purpose of the paper is to better understand the differences between the methods.

We also distinguish the “two-layer situation” (i.e. one aerosol layer and one cloud layer) from the “multiple-layer situations” (more than one aerosol layer and/or more than one cloud layer). These latter situations are filtered in our analysis for the sake of simplicity (see Sects. 3.4 and 4).

3 Regional analysis and case studies

The results presented in this section were acquired from May to October 2008. We selected three distinctive regions (see Fig. 2) that are under the influence of various aerosol species and different types of clouds: (a) an area that extends from

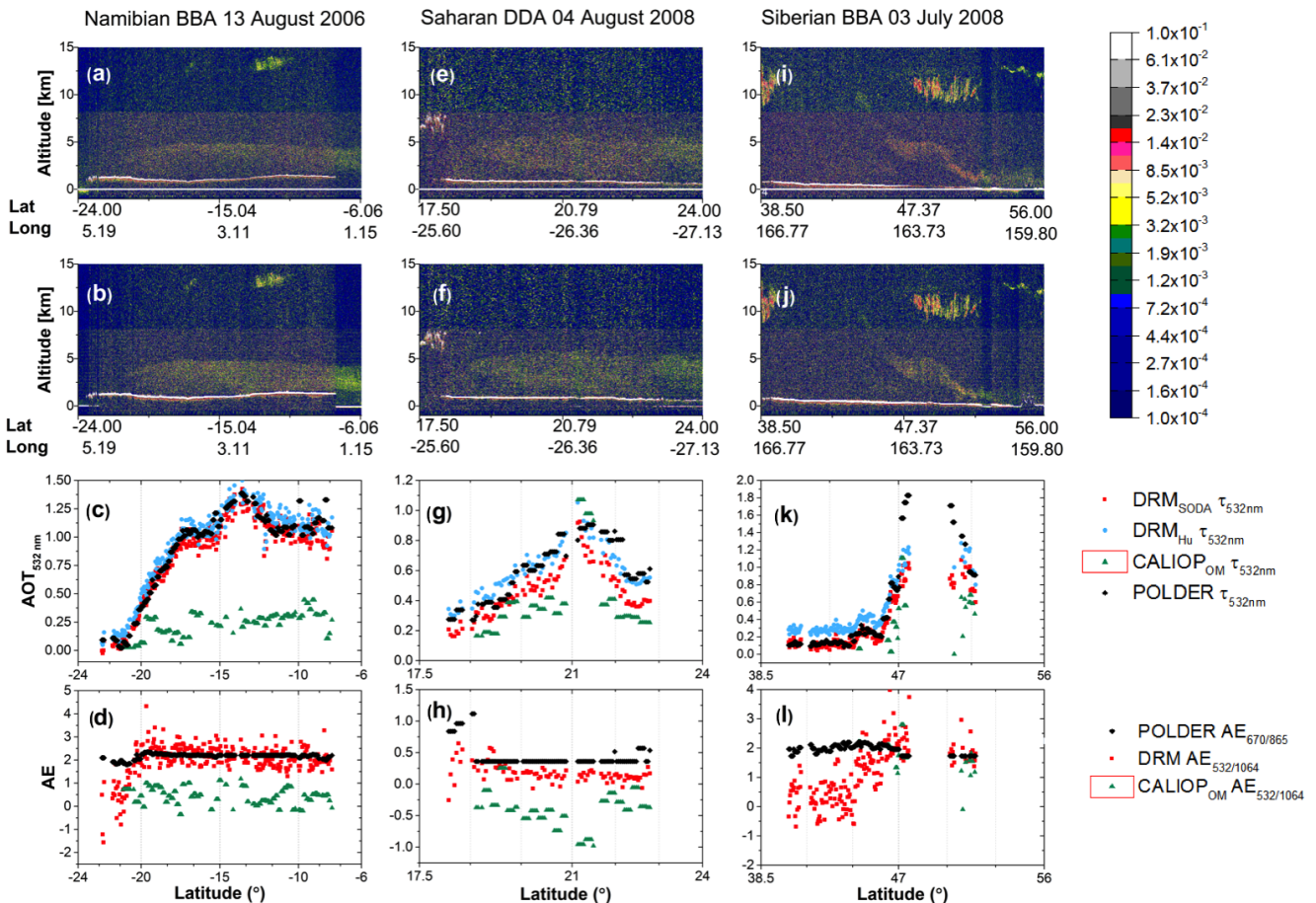


Figure 1. The first row of the panel shows the lidar CALIOP attenuated backscatter coefficients at 532 nm ($\text{km}^{-1} \text{sr}^{-1}$) and the second row presents the CALIOP attenuated backscatter coefficients at 1064 nm for three case studies: African biomass-burning aerosols (BBA) above clouds on 13 August 2006 (a–d), Saharan dust (DDA) on 4 August 2008 (e–h) and Siberian biomass-burning aerosols over the Okhotsk Sea on 3 July 2008 (i–l). For these cases, the above-cloud AOT at 532 nm and the Ångström exponent (AE) as a function of latitude, measured with several techniques, are displayed.

30° S to 5° N and 12° W to 14° E over the South Atlantic Ocean (SAO), (b) an area between 10 and 35° N and 10 and 40° W over the North Atlantic Ocean (NAO) and (c) an area located between 35 and 60° N and 140 and 170° E over the North Pacific Ocean (NPO). The south of the African continent is the main contributor to biomass-burning aerosols above clouds, originating from manmade crops fires (Waquet et al., 2013b). These aerosols are highly absorbing (SSA of approximately 0.84 at 865 nm) and associated with high AE values; they mainly contribute to the fine mode. The NAO area is mainly under the influence of dust aerosols originating from the Sahara for the time period of interest. These particles are mainly non-spherical and contribute primary to the coarse mode. They are moderately absorbing at the wavelength of CALIOP (532 nm) and almost non-absorbing at 865 nm (SSA of approximately 0.98) (Balkanski et al., 2007; Dubovik et al., 2002; Peers et al., 2015). The NPO is associated with various types of particles: fine-mode aerosols with

rather scattering properties originating from manmade pollution (Waquet et al., 2013a; Yu et al., 2008), biomass burning from forest fires (Peers et al., 2015; Zhang et al., 2003) and dust originated from the Asian deserts. Potential mixture of these different species is also possible for this area (Yu et al., 2006).

Cloud types and their associated optical and microphysical properties are expected to be different in these three regions (Warren et al., 1988). Low-level stratocumulus clouds typically cover the SAO, with some occurrences of cumulus and altostratus clouds. Cumulus, altostratus clouds and some stratocumulus clouds generally cover the NAO. The cloud cover is generally fractional over this part of the Atlantic Ocean. Stratocumulus clouds also frequently cover the NPO. Higher altostratus and cumulus clouds are also often observed over this area. Cirrus clouds can be frequently found at mid-latitudes and also in the intertropical convergence zone, which includes the NPO and the NAO regions.

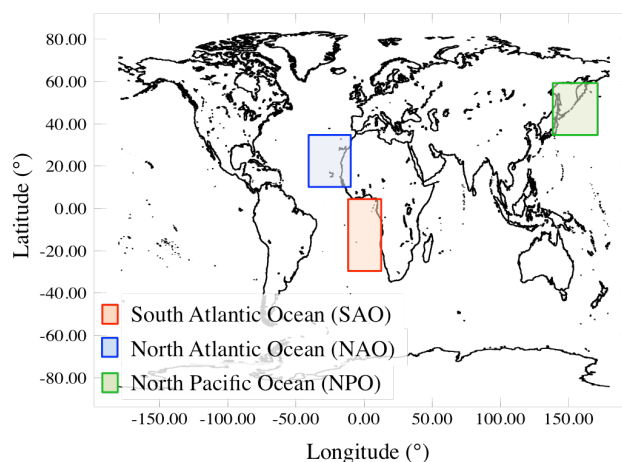
Table 1. Linear regressions of AOT calculated between different methods for three case studies: African biomass-burning aerosols (BBA), Saharan dust aerosols (DDA) and Siberian BBA. R^2 represents the coefficient of determination (COD) between the two sets of data.

Linear regressions		African BBA (13 Aug 2006)	Saharan DDA (4 Aug 2008)	Siberian BBA (3 Jul 2008)
DRM _{SODA} vs. POLDER	Slope	0.89 ± 0.01	0.74 ± 0.04	0.56 ± 0.01
	Intercept	0.04 ± 0.01	0.01 ± 0.02	0.07 ± 0.009
	R^2 (COD)	0.93	0.79	0.90
DRM _{Hu} vs. POLDER	Slope	0.91 ± 0.01	0.74 ± 0.03	0.60 ± 0.01
	Intercept	0.11 ± 0.01	0.15 ± 0.02	0.23 ± 0.009
	R^2 (COD)	0.93	0.82	0.89
CALIOP _{OM} vs. POLDER	Slope	0.19 ± 0.01	0.86 ± 0.11	0.47 ± 0.08
	Intercept	0.05 ± 0.01	-0.16 ± 0.07	-0.04 ± 0.08
	R^2 (COD)	0.35	0.41	0.45

We studied 6 months of data over each region to observe the consistency between different techniques for various types of aerosols. For this part of the study, we mixed the two-layer and multiple-layer situations and we analysed all the data, disregarding the position of the aerosol and cloud layers. A case study was selected for each region in order to show the spatial variability of the AOT at 532 nm retrieved along the CALIOP transect. The first case is related to a biomass-burning event detected off the coast of Namibia on 13 August 2006. The second event concerns Saharan dust lifted above clouds westwards over the NAO on 4 August 2008, and the third case concerns Siberian biomass-burning aerosols transported over the Okhotsk Sea on 3 July 2008.

Figure 1 presents the backscatter profile at 532 nm and at 1064 nm ($\text{km}^{-1} \text{sr}^{-1}$) of the lidar CALIOP for the three case studies, which directly provides information on the aerosol and cloud vertical distribution. In addition, the AOT and AE values measured by different techniques are presented along the CALIOP track. Additional results for the study cases comparison are shown in Table 1.

Figure 3 shows the regional comparison between the AOT and AE retrieved with POLDER and DRM_{SODA} for a period of 6 months in 2008. The retrieval of aerosol type becomes difficult at small AOT. Therefore the AE comparison was performed only when the values of POLDER AOT at 865 nm and DRM_{SODA} AOT at 532 nm were larger than 0.1. The AE mean value is shown with a dashed blue line. The lateral histograms show the data distribution. For the AOT comparison the colour scale represents the POLDER AE_{670/865}. In the case of AE comparison, the POLDER AOT_{532 nm} was also reported with a colour scale. The above-mentioned description is also considered in Fig. 4, which presents the regional comparison between the AOT and AE retrieved with POLDER and CALIOP_{OM} for the same period. Additional results for the regional intercomparison are reported in Table 2.

**Figure 2.** The map presents the latitudinal and longitudinal boundaries of the three regions used in the regional study (Sect. 3): South Atlantic Ocean (SAO) extends from 30° S to 5° N and 12° W to 14° E, North Atlantic Ocean (NAO) is situated between 10 and 35° N and 10 and 40° W and North Pacific Ocean (NPO) is located between 35 and 60° N and 140 and 170° E.

3.1 African biomass-burning aerosols

According to the CALIOP vertical profile at 532 nm of the biomass-burning case (Fig. 1a), the cloud top is at around 1.5 km and the aerosol layer is located between 3 and 5 km. The 1064 nm backscatter profile (Fig. 1b) exhibits an aerosol layer with a larger vertical extent, showing more potential contact area with the underlying cloud. We observe a thin cirrus cloud between 10 and 12° S that was not filtered, probably because the cirrus is optically too thin (Fig. 1c and d). In general, there is an excellent agreement between POLDER, DRM_{Hu} and DRM_{SODA} AOT retrievals with a square correlation $R^2 = 0.93$ (see Table 1). High values of AOT are retrieved by the different methods, with AOT values as large as 1.5. The retrieved POLDER AE_{670/865} is larger

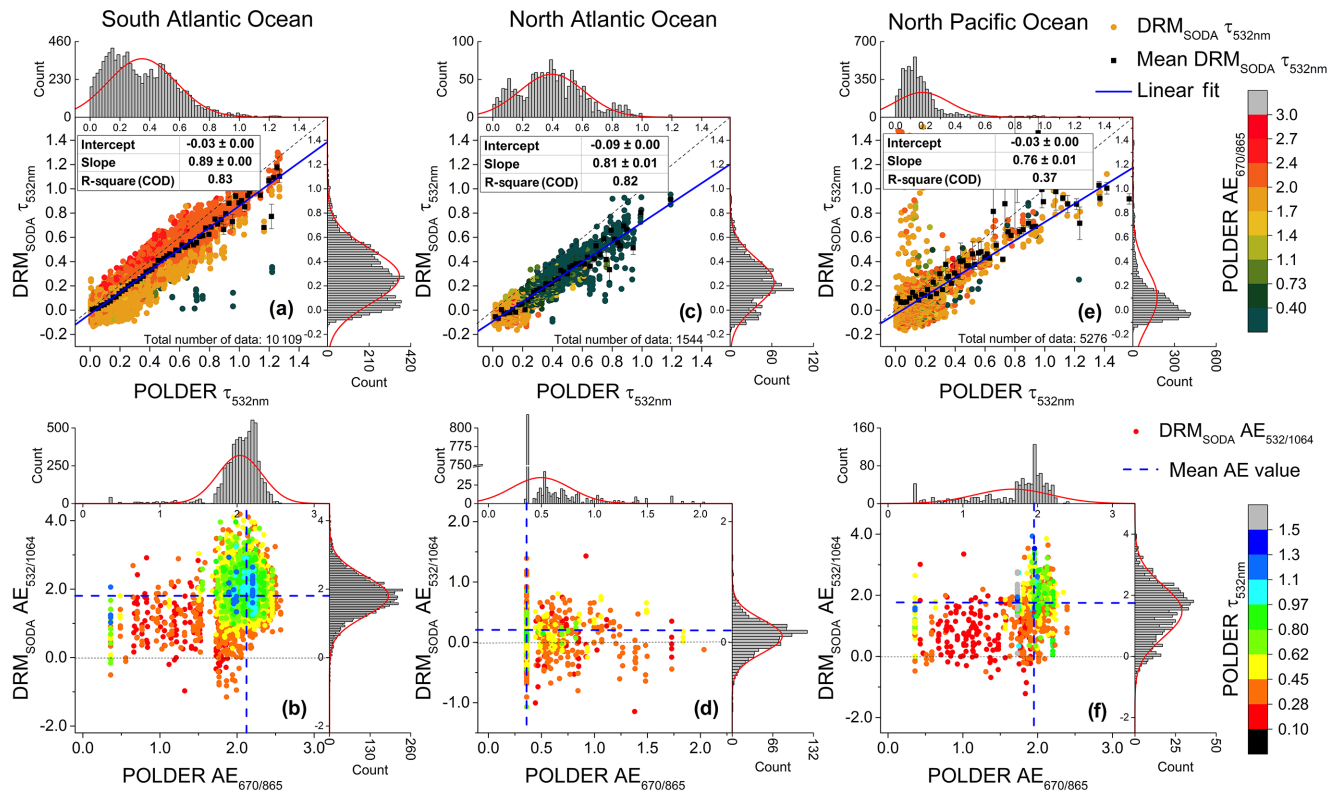


Figure 3. The first row of the panel shows the comparison of AOT at 532 nm retrieved from DRM_{SODA} and POLDER methods, with the corresponding POLDER AE colour scale, computed between 670 and 865 nm. The second row presents the Ångström exponent comparison for AOTs larger than 0.1, retrieved from DRM_{SODA} and POLDER methods, with the corresponding POLDER AOT at 532 nm colour scale. The measurements were made over a period of 6 months (May to October 2008) and over three distinctive regions: South Atlantic Ocean, between 30° S and 5° N and 12° W and 14° E (a, b); North Atlantic Ocean, between 10 and 35° N and 10 and 40° W (c, d); and North Pacific Ocean, between 35 and 60° N and 140 and 170° E (e, f). The histograms present the data distribution. The error bars in (a), (c) and (e) represent the standard error of the mean (SEM).

Table 2. Linear regressions of AOT calculated between different methods for data acquired over 6 months (May to October 2008), over three different regions: South Atlantic Ocean (SAO), North Atlantic Ocean (NAO) and North Pacific Ocean (NPO).

Linear regressions		SAO	NAO	NPO
DRM_{SODA} vs. POLDER	Slope	0.89 ± 0.004	0.81 ± 0.009	0.76 ± 0.01
	Intercept	-0.03 ± 0.001	-0.09 ± 0.004	-0.03 ± 0.003
	R^2 (COD)	0.83	0.82	0.37
DRM_{Hu} vs. POLDER	Slope	0.90 ± 0.004	0.86 ± 0.01	0.76 ± 0.01
	Intercept	0.05 ± 0.001	0.04 ± 0.004	0.13 ± 0.003
	R^2 (COD)	0.82	0.82	0.44
$\text{CALIOP}_{\text{OM}}$ vs. POLDER	Slope	0.34 ± 0.004	0.52 ± 0.02	0.28 ± 0.02
	Intercept	-0.04 ± 0.002	-0.01 ± 0.01	0.01 ± 0.01
	R^2 (COD)	0.43	0.42	0.24
$\text{CALIOP}_{\text{OM}}$ vs. DRM_{SODA}	Slope	0.34 ± 0.002	0.62 ± 0.01	0.35 ± 0.01
	Intercept	-0.01 ± 0.002	0.04 ± 0.006	0.01 ± 0.007
	R^2 (COD)	0.42	0.48	0.28

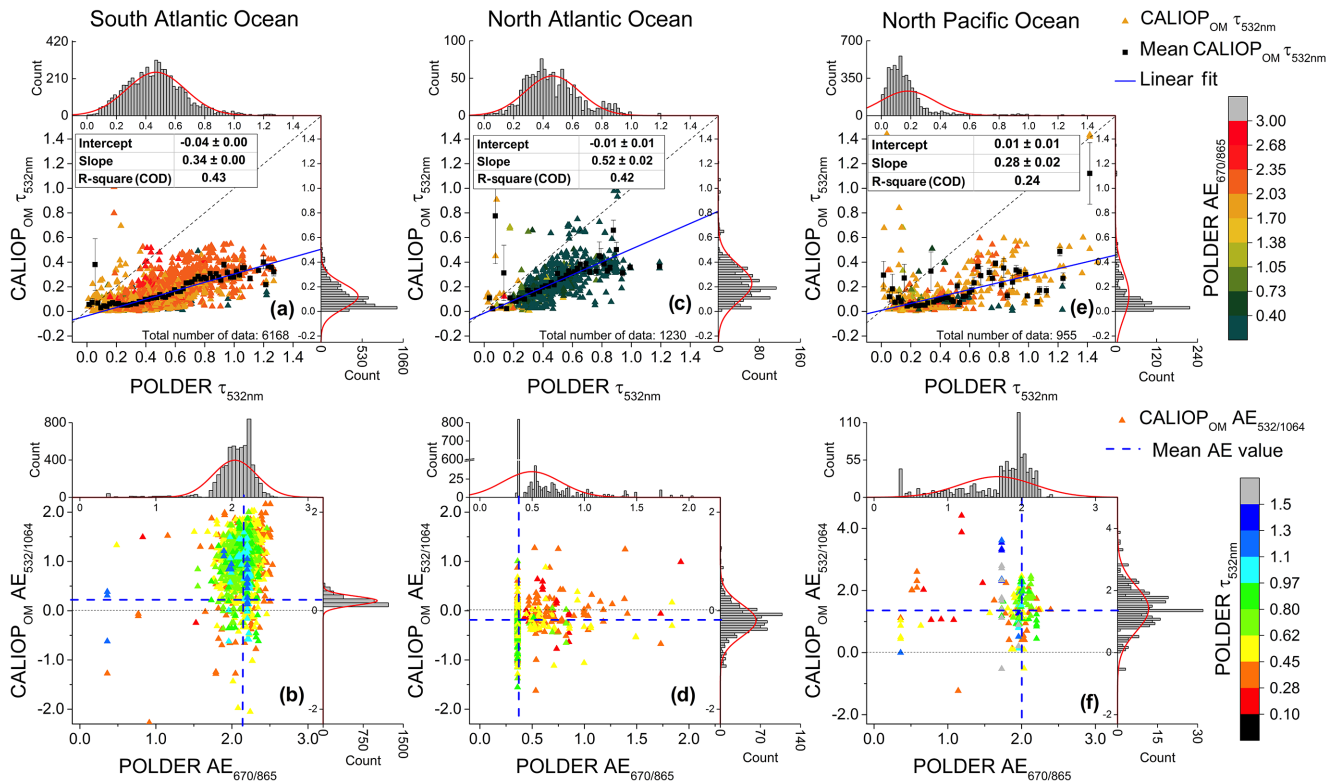


Figure 4. Same as Fig. 3, retrieved from CALIOP operational method and POLDER method.

than 1.8 (Fig. 1d), which is characteristic of fine-mode particles (Dubovik et al., 2002). The $DRM_{SODA} AE_{532/1064}$ is consistent with the POLDER AE, with values higher than 1.5. AOT values retrieved by $CALIOP_{OM}$ are much lower than the ones retrieved by the three other techniques. The maximal AOT retrieved by $CALIOP_{OM}$ at 532 nm is 0.5. A possible explanation for this potential low bias was proposed by Jethva et al. (2014): in case of optically thick aerosol layer, the sensitivity of the backscattered signal to the altitude of the base of the aerosol layer would be reduced or lost, being strongly attenuated by the two-way transmission term. As a result, the operational algorithm may overestimate the aerosol base altitude and so underestimate the geometrical thickness of the aerosol layer and consequently the AOT. The selection of an inappropriate aerosol model (i.e. aerosol lidar ratio S_a for biomass burning varies between 70 ± 28 at 532 nm and 40 ± 24 sr at 1064 nm; Catrall et al., 2005; Omar et al., 2005) or the significant biases found in the V3.01 CALIOP 1064 nm calibration might also contribute to the underestimation of the AOT for this case study. The $CALIOP_{OM}$ mean $AE_{532/1064}$ seems quite low for fine-mode particles (AE values are lower than 1). The selection of an inappropriate aerosol model might also contribute to the underestimation of the AOT for this case study.

Regional analysis shows that South Atlantic region is mostly characterized by biomass-burning aerosols with large

AOT and AE (Fig. 3a and b). On average, the cloud top height is located below 1.5 km, while the aerosol layers are frequently located between 2.5 and 4 km (see Table 3). The AOT_{532nm} measured by DRM_{SODA} and POLDER may reach values as large as 1.30 (Fig. 3a), with 80% of the retrieved AOTs ranging between 0.05 and 0.8. This AOT intercomparison shows close correlation between DRM_{SODA} and POLDER ($R^2 = 0.83$). The mean value of POLDER $AE_{670/865}$ is 2.05, whereas the mean $DRM_{SODA} AE_{532/1064}$ is 1.79 (Table 5) (both typical for BBA). DRM_{Hu} and DRM_{SODA} give rather same results. From the linear regressions performed (see Table 2) we can observe that the offset is always positive for DRM_{Hu} and systematically larger than the absolute value for DRM_{SODA} when compared to POLDER method. The AOT estimated by POLDER is constantly between DRM_{Hu} and DRM_{SODA} .

We do not find a good correlation between the $CALIOP_{OM}$ and POLDER AOT and AE retrievals. The $CALIOP_{OM}$ mean AOT_{532nm} is 0.12 and the mean $AE_{532/1064}$ is 0.97. Comparing with POLDER and DRM_{SODA} , $CALIOP_{OM}$ is underestimating the ACAOT by a factor of 2.92.

3.2 Saharan dust aerosols

For the mineral dust case (Fig. 1e), the cloud top altitude is located at approximately 1 km altitude whereas the aerosol layer is located between 2 and 5 km for latitudes be-

tween 18 and 23° N. Figure 1g shows that the POLDER, DRMS_{SODA} and DRM_{Hu} AOT_{532 nm} increase up to 0.92, following the same gradient. The correlation coefficients between POLDER parameters and DRM_{Hu} and DRMS_{SODA} parameters are close (Table 1). The majority of POLDER AE_{670/865} and DRMS_{SODA} AE_{532/1064} is associated with values lower than 0.4 (Fig. 1h), which indicates that coarse-mode particles are predominant (Dubovik et al., 2002). Except for few retrievals associated with an abrupt change in the AE and AOT measured by CALIOP_{OM} (around 21° N in latitude), 90 % of the CALIOP_{OM} AOT_{532 nm} is lower than 0.45, being once again underestimated with respect to the other estimates. Most of CALIOP_{OM} AE_{532/1064} values are underestimated (i.e. overestimation of the particles size) in comparison with the AE retrieved by the two other algorithms. These low values of AOT and AE may be explained once more by a biased CALIOP calibration at 1064 nm combined with an unfitted model selection (i.e. for desert dust, S_a is equal to 40 ± 20 sr at 532 nm and 55 ± 17 sr at 1064 nm; Catrall et al., 2005; Omar et al., 2005).

A regional study shows similar AOT and AE results over the North Atlantic region (Fig. 3c). On average, the aerosol layers are located between 3 and 4.5 km and the cloud top heights are typically around 1.4 km (see Table 3). The values of AOT₅₃₂ retrieved from POLDER and DRMS_{SODA} are well correlated ($R^2 = 0.82$), with maximum values of, respectively, 1.19 and 0.95. Nonetheless, we observe a larger offset between DRMS_{SODA} and POLDER AOT_{532 nm} for this region (-0.09) compared to the South Atlantic Ocean region (-0.03). The use of only one dust model in the LUT algorithm used for POLDER remains a limitation that might explain this larger offset. The introduction of additional dust models with larger or smaller effective radius values may contribute to improve the AOT retrievals for dust AAC events. Regarding the POLDER AE_{670/865} retrievals, most of the values are lower than 0.4, which is expected for desert dust aerosols (Fig. 3c and d). However, for AOT values lower than 0.2, the AE_{670/865} retrieved by POLDER is between 1.4 and 2.2. This is explained by the fact that the selection of the dust model is not permitted in the POLDER algorithm in case of low AOTs. Nonetheless, all three methods are consistent in revealing the predominance of the coarse mode. The mean values for the AE are 0.49 for POLDER, 0.10 for DRMS_{SODA} and -0.19 for CALIOP_{OM}. The AOT_{532 nm} correlation between CALIOP_{OM} and POLDER is low, with $R^2 = 0.42$.

3.3 East Asian mixture of aerosols

The CALIOP transect shows that Siberian biomass-burning case is located between 40 and 52° N, the cloud top altitude is constantly around 1 km and the base of the aerosol layer decreases from 10 km in the south (at 45° N) to around 2 km in the north (at 54° N) (Fig. 1i). We notice also cirrus clouds at high altitude (around 10 km) between 47 and 51° N, which were efficiently eliminated from the retrievals (Fig. 1k). The

Table 3. Regional analysis using CALIOP measurements over 6 months (May to October 2008), over South Atlantic Ocean (SAO), North Atlantic Ocean (NAO) and North Pacific Ocean (NPO): mean cloud altitude for altitudes smaller than 5 km, mean aerosol base and top altitudes for altitudes smaller than 10 km.

	SAO	NAO	NPO
Mean cloud top altitude (km)	1.24 ± 0.43 Min: 0.30 Max: 4.95	1.35 ± 0.5 Min: 0.20 Max: 3.25	1.09 ± 0.84 Min: 0.05 Max: 5.0
Mean aerosol top altitude (km)	3.83 ± 0.093 Min: 0.50 Max: 6.73	4.50 ± 1.03 Min: 0.44 Max: 6.67	2.74 ± 1.68 Min: 0.47 Max: 9.85
Mean aerosol base altitude (km)	2.90 ± 0.97 Min: 0.02 Max: 5.80	2.97 ± 1.12 Min: 0.02 Max: 5.74	3.48 ± 1.78 Min: 0.05 Max: 9.31

Table 4. Calculated mean, minimum value and maximum value of AOT_{532 nm} over 6 months in 2008, for three regions (SAO, NAO, NPO) and for different methods.

AOT _{532 nm}		SAO	NAO	NPO
POLDER	Mean	0.35 ± 0.23	0.39 ± 0.21	0.18 ± 0.21
	Min	0.005	0.005	0.005
	Max	1.27	1.19	2.17
DRMS _{SODA}	Mean	0.28 ± 0.22	0.23 ± 0.19	0.15 ± 0.38
	Min	-0.13	-0.16	-0.16
	Max	1.30	0.95	3.26
DRM _{Hu}	Mean	0.37 ± 0.23	0.38 ± 0.20	0.32 ± 0.40
	Min	-0.07	-0.06	-0.06
	Max	1.50	1.17	3.68
CALIOP _{OM}	Mean	0.12 ± 0.11	0.23 ± 0.18	0.14 ± 0.23
	Min	0.001	0.005	0.001
	Max	1.88	2.38	2.01

maximum POLDER AOT value is as large as 1.9, while DRM reaches 1.3 in AOT. Nonetheless, Table 1 shows that POLDER and DRM methods AOT_{532 nm} retrievals are consistent ($R^2 = 0.90$). POLDER AE_{670/865} values are between 1.7 and 2.3, indicating small particles of smoke, while DRMS_{SODA} AE_{532/1064} has a large range of values (Fig. 11). The number of sampled ACAOT events by CALIOP_{OM} is 4.5 times less than of POLDER and DRMS_{SODA}. For these, the CALIOP_{OM} AOTs are underestimated by a factor of 1.5 compared to ones retrieved by the other methods. Also, the correlation coefficient with POLDER is 0.45.

On a regional scale, this area is under the influence of various aerosols (BBA, DDA, pollution) and elevated cirrus clouds are frequent. The mean cloud top altitude is around 1 km and the aerosols are between 2.5 km and 4.0 km. As indicated in Table 3, the maximum aerosol altitude is 9.85 km, which might suggest cirrus misclassification. In some cases,

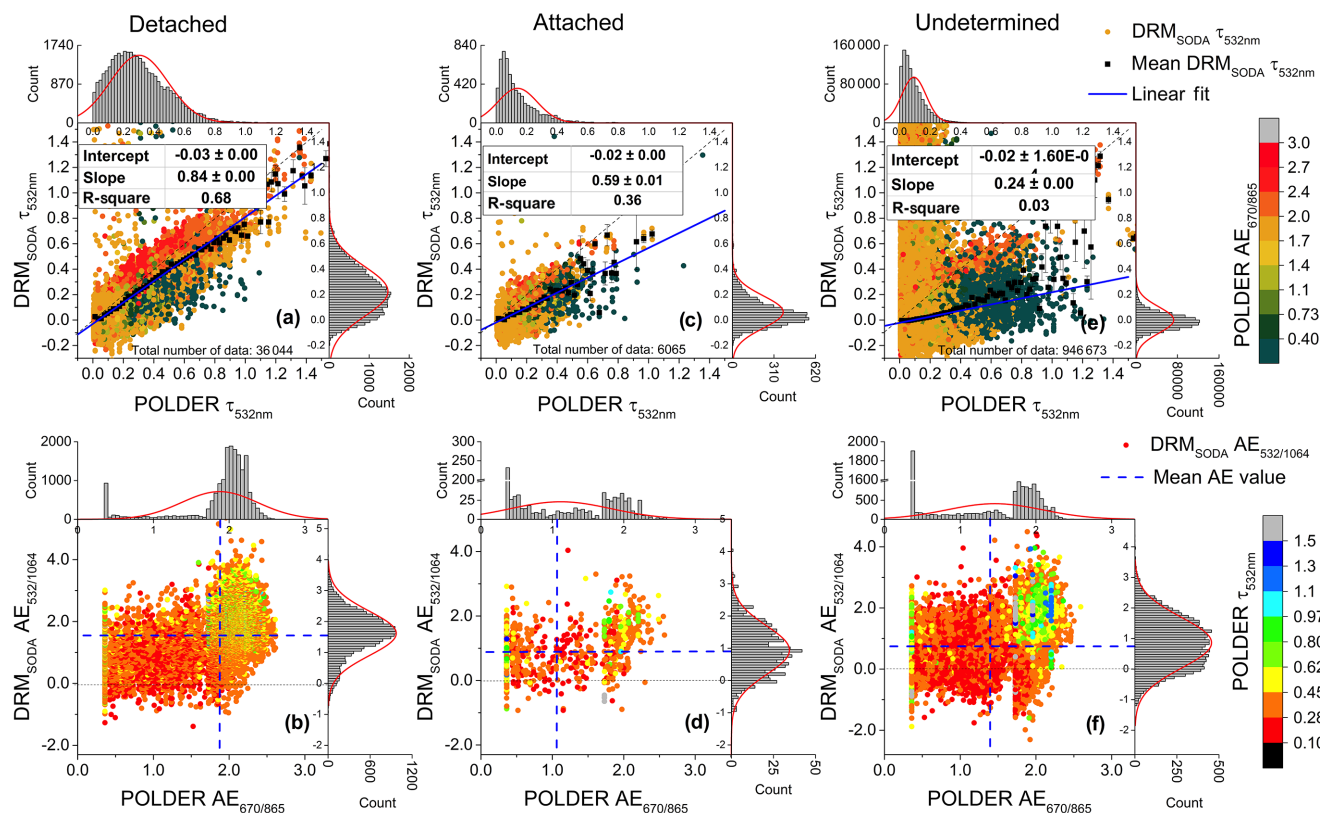


Figure 5. Global comparison over a period of 4.5 years (June 2006–December 2010) for situations with aerosol layer well separated from the cloud top (“detached”; **a**, **b**), for cases where the aerosol layer is in contact with the cloud (“attached”; **c**, **d**) and for “undetermined” situations (**e**, **f**). The comparison of AOT at 532 nm retrieved from DRM_{SODA} and POLDER methods is shown in the first row. The colour scale represents the corresponding POLDER AE computed between 670 and 865 nm. The second row presents the Ångström exponent for AOTs larger than 0.1, with a POLDER AOT at 532 nm colour scale. The histograms present the data distribution. The error bars in (**a**), (**c**) and (**e**) represent the standard error of the mean (SEM).

DRM_{SODA} gives large values of $\text{AOT}_{532\text{nm}}$ (larger than 1) whereas the POLDER estimates $\text{AOT}_{532\text{nm}}$ smaller than 0.2. These situations could be explained by a misinterpretation of thin cirrus clouds as aerosols. Otherwise, the POLDER mean $\text{AOT}_{532\text{nm}}$ and DRM_{SODA} $\text{AOT}_{532\text{nm}}$ are in rather close agreement (0.18 and 0.15, respectively; see Table 4), but the correlation between them is low ($R^2 = 0.37$, Table 2). All methods show a large variability for the retrieved AE, with values that correspond to particle size distributions dominated by coarse or fine modes and mixtures (Table 5). As previously mentioned, the algorithm developed for POLDER uses a bimodal aerosol model for dust. However, the possibility of mixing different fine and coarse aerosol models in various proportions is not yet included. This might explain why we found a lower correlation between the POLDER and DRM retrievals for this region. As for above, the $\text{CALIOP}_{\text{OM}}$ and POLDER $\text{AOT}_{532\text{nm}}$ are not correlated ($R^2 = 0.24$).

In general, there is a good agreement between POLDER and DRM_{SODA} AOTs, especially when the fine mode or coarse mode dominates the particle size distribution (i.e. BBA and DDA). Overall, DRM_{SODA} and DRM_{Hu} give sim-

ilar results. However, the AOTs retrieved with DRM_{Hu} are generally larger than those of DRM_{SODA} for all the three regions (i.e. 0.37 compared to 0.28 for SAO; see Table 4). While DRM_{SODA} has a constant negative offset when compared to POLDER, DRM_{Hu} rarely retrieves null AOT values (offsets always larger than 0; see Table 2). This is likely to be a consequence of the calibration performed for the DRM_{SODA} method. Also, there is no obvious correlation between the $\text{CALIOP}_{\text{OM}}$ and POLDER $\text{AOT}_{532\text{nm}}$ retrievals for all regions.

Finally, in addition to the 6-month regional study, we also examined the impact of the vertical aerosol–cloud profiles over the three regions using data acquired from May to October between 2006 and 2010. We systematically found higher correlation coefficients between the DRM_{SODA} and POLDER AOTs when the layers were well separated than when they were in contact (see Table 6). These results have led us to consider the vertical distribution of aerosols and clouds in the global comparison.

Table 5. Mean value of AE over 6 months in 2008 for three regions (SAO, NAO, NPO) for different methods after filtering the POLDER $AOT_{865\text{ nm}} > 0.1$ and $DRM_{SODA} AOT_{532\text{ nm}} > 0.1$ and the $CALIOP_{OM} AOT_{532\text{ nm}} > 0.1$.

		SAO	NAO	NPO
POLDER	Mean $AE_{670/865}$	2.05 ± 0.27	0.49 ± 0.27	1.67 ± 0.50
	Min	0.36	0.36	0.36
	Max	2.56	2.03	2.39
DRM_{SODA}	Mean $AE_{532/1064}$	1.79 ± 0.58	0.10 ± 0.27	1.47 ± 0.84
	Min	-1.15	-1.14	-1.21
	Max	4.19	1.43	3.93
$CALIOP_{OM}$	Mean $AE_{532/1064}$	0.97 ± 0.51	-0.19 ± 0.32	0.41 ± 0.72
	Min	-2.27	-1.62	-2.63
	Max	3.16	1.27	4.41

Table 6. Linear regression calculated between $DRM_{SODA} AOT_{532\text{ nm}}$ and $POLDER AOT_{532\text{ nm}}$ for situations when the aerosol layer is attached to the cloud top and when the aerosol layer is well separated from the cloud over three regions (South Atlantic Ocean, North Atlantic Ocean and North Pacific Ocean) and for a period of 4.5 years.

	SAO		NAO		NPO	
	Attached	Detached	Attached	Detached	Attached	Detached
Slope	0.60 ± 0.02	0.77 ± 0.003	0.63 ± 0.07	0.59 ± 0.01	0.78 ± 0.12	0.80 ± 0.02
Intercept	0.04 ± 0.006	0.02 ± 0.001	-0.005 ± 0.02	-0.011 ± 0.006	-0.04 ± 0.02	-0.015 ± 0.007
R^2 (COD)	0.54	0.715	0.39	0.57	0.19	0.435

4 Global analysis on different types of scenes

4.1 Detached, attached, undetermined

Figure 5a shows the global comparison between the $AOT_{532\text{ nm}}$ and AE retrieved with POLDER and DRM_{SODA} for the detached cases. The AE comparison was only performed when the POLDER AOT at 865 nm and DRM_{SODA} AOT at 532 nm are larger than 0.1. The colour scales used in Fig. 5 represent either the POLDER $AE_{670/865}$ for the AOT comparison (Fig. 5a) or the POLDER $AOT_{532\text{ nm}}$ for the AE comparison (Fig. 5d). Considering the large amount of selected data (85.6 % of the two-layer cases) in terms of both spatial and temporal coverage, the comparison shows a good correlation between the two methods ($R^2 = 0.68$). A better agreement between the methods is found when the values of DRM_{SODA} and POLDER AE are larger than 1.8. This is likely due to the fact that the POLDER method is more sensitive to fine-mode aerosols, due to polarization measurements, and also because an improved description of the fine-mode properties was included in the LUT (i.e. six fine-mode aerosol models are used).

Events for which the aerosol layer is attached to the cloud top represent 14.4 % of the total number of two-layer cases. They are associated with lower AOT and the correlation between the two retrievals largely decreases (compared to the detached events). The correlation between the two AOT retrievals also decreases ($R^2 = 0.36$, Fig. 5c). The POLDER

AOT is larger by a coefficient of 1.7 than the DRM_{SODA} AOT on average. The AE given by both methods is approximately 1.0 (when considering only AE values associated with $AOT > 0.1$). The lateral histogram shows that the POLDER method identifies AAC events associated with both low and high AE values, resulting in a mean AE of about 1.0.

The undetermined situations correspond to retrievals when CALIOP does not give all the information regarding the layer altitudes. The number of cases is significant (approximately 92 % of the total number of global retrievals) but most of data (95 %) correspond to $AOT_{532\text{ nm}}$ lower than 0.2. This probably explains why the layer detection algorithm has difficulties in estimating the base and top of the aerosol layer. For the undetermined cases, we observe that there is not much correlation between POLDER and DRM_{SODA} measurements. On average, the DRM_{SODA} AOTs are centred around zero for this category whereas POLDER has a non-negligibly low AOT for most cases. In this category, the AE comparison shows a better consistency between the methods for $AOT_{532\text{ nm}} > 0.5$ and for AE of approximately 2.0.

Table 7 shows the results of the linear regressions performed between the AOTs retrieved with POLDER and the other active methods considered in our study for each category (i.e. detached, attached and undetermined). We recapture the systematically larger offsets of $DRM_{Hu} AOT_{532\text{ nm}}$ compared to DRM_{SODA} and the underestimation of $CALIOP_{OM} AOT$ with respect to the other methods.

Table 7. Linear regressions calculated between different methods for data acquired over June 2006 to December 2010, on a global scale above the ocean in the case of aerosol attached to the cloud top, detached from the cloud and undetermined situations for AOT smaller than 1.5.

Linear regressions		Detached	Attached	Undetermined
DRM _{SODA} vs. POLDER	Slope	0.84 ± 0.003	0.59 ± 0.01	0.24 ± 0.001
	Intercept	−0.03 ± 0.001	−0.02 ± 0.002	−0.02
	R ² (COD)	0.68	0.36	0.03
DRM _{Hu} vs. POLDER	Slope	0.78 ± 0.002	0.55 ± 0.001	0.28 ± 0.001
	Intercept	0.10 ± 0.001	0.12 ± 0.002	0.09
	R ² (COD)	0.68	0.36	0.05
CALIOP _{OM} vs. POLDER	Slope	0.17 ± 0.002	0.12 ± 0.007	0.06 ± 0.008
	Intercept	0.013	0.02 ± 0.001	0.14 ± 0.002
	R ² (COD)	0.15	0.047	0.003
CALIOP _{OM} vs. DRM _{SODA}	Slope	0.17 ± 0.002	0.1 ± 0.007	0.21 ± 0.01
	Intercept	0.029	0.04 ± 0.001	0.14 ± 0.001
	R ² (COD)	0.15	0.03	0.01

4.2 Evolution of the above-cloud AOT retrievals with cloud properties

In principle, the retrieval of AAC properties from the methods considered in this study should not depend on the properties of the underlying clouds. However, hypotheses and empirical relations used in the retrieval methods to exploit the signal backscattered by the underlying cloud cover obviously have their limitations. In order to understand potential issues linked with diversity of cloud properties, we analyse in this section the difference between the AOT retrievals of POLDER, DRM_{SODA} and DRM_{Hu} by classes of cloud properties (COT and r_{eff} retrieved with MODIS). We considered global measurements acquired for 4.5 years of data and used the classification defined in Sect. 2.3.2.

Figure 6 presents POLDER and DRM_{SODA} AOT₅₃₂ retrievals as a function of the MODIS droplets effective radius (r_{eff}), while Fig. 8 displays POLDER and DRM_{SODA} AOT_{532nm} as a function of the MODIS COT. Histograms of the cloud properties are also reported in Figs. 6, 7 and 8. The results of the POLDER and DRM_{Hu} AOT₅₃₂ comparison as a function of the effective radius are shown in Fig. 7. DRM_{SODA} and DRM_{Hu} AOT_{532nm} generally exhibit rather similar behaviour, at least qualitatively. Therefore, we did not report the results found for the DRM_{Hu} AOT₅₃₂ as a function of MODIS COT.

4.2.1 AOT vs. r_{eff}

The lateral histograms plotted in Figs. 6 and 8 show that most of the AAC scenes correspond to cloud droplets effective radius values between 8 and 15 μm (mean r_{eff} equal to 12 μm) and COT ranging from 5 to 15 (mean COT of 10). These mean values are expected since most of the of AAC events are generally associated with low-level non-

precipitating clouds, such as stratocumulus ones, which typically show rather small droplets (approximately 10 μm) and optical thickness values of approximately 10.

Figure 6a shows the POLDER and DRM_{SODA} AOTs for the detached situations. For the two methods, the retrieved AOTs are maximal for the smallest values of r_{eff} and progressively decrease with r_{eff} . Same tendencies are observed for the DRM_{Hu} (see Fig. 7a). The two curves have an offset, however. The histogram of the differences between POLDER and DRM_{SODA} AOT ($\Delta\tau$) is presented in Fig. 6d. The mean $\Delta\tau$ value computed over the entire range of r_{eff} is equal to 0.073. This offset is not constant and slightly increases with r_{eff} , suggesting a sensitivity of one of the two methods to the cloud droplets effective radius. The DRM algorithm does not use an explicit parameterization of the lidar ratio as a function of the cloud droplets effective radius. An implicit dependence will arise from the latitudinal correction (Eq. 9) when clouds at different latitudes exhibit different microphysical properties. In order to understand the usefulness of adding an explicit parameterization, we recalculated the DRM_{SODA} AOT_{532nm}, taking into account the dependence of S_c on r_{eff} . This calculation assumes a simplified and unique droplet size distribution and is based on MODIS r_{eff} retrieval. We expect that even if the cloud droplet size distribution is variable (Miles et al., 2000) and the ACAOT creates a bias in r_{eff} , the results will still provide guidance for future algorithm development. As defined in Josset et al. (2011), S_c was computed using a Mie code with the following equation:

$$S_c = \frac{4\pi}{\omega_0 \times p(180^\circ)}, \quad (11)$$

where $p(180^\circ)$ is the average value of the phase function in the backscatter direction computed over the size distribution. ω_0 is the SSA of the particles, defined as the ratio

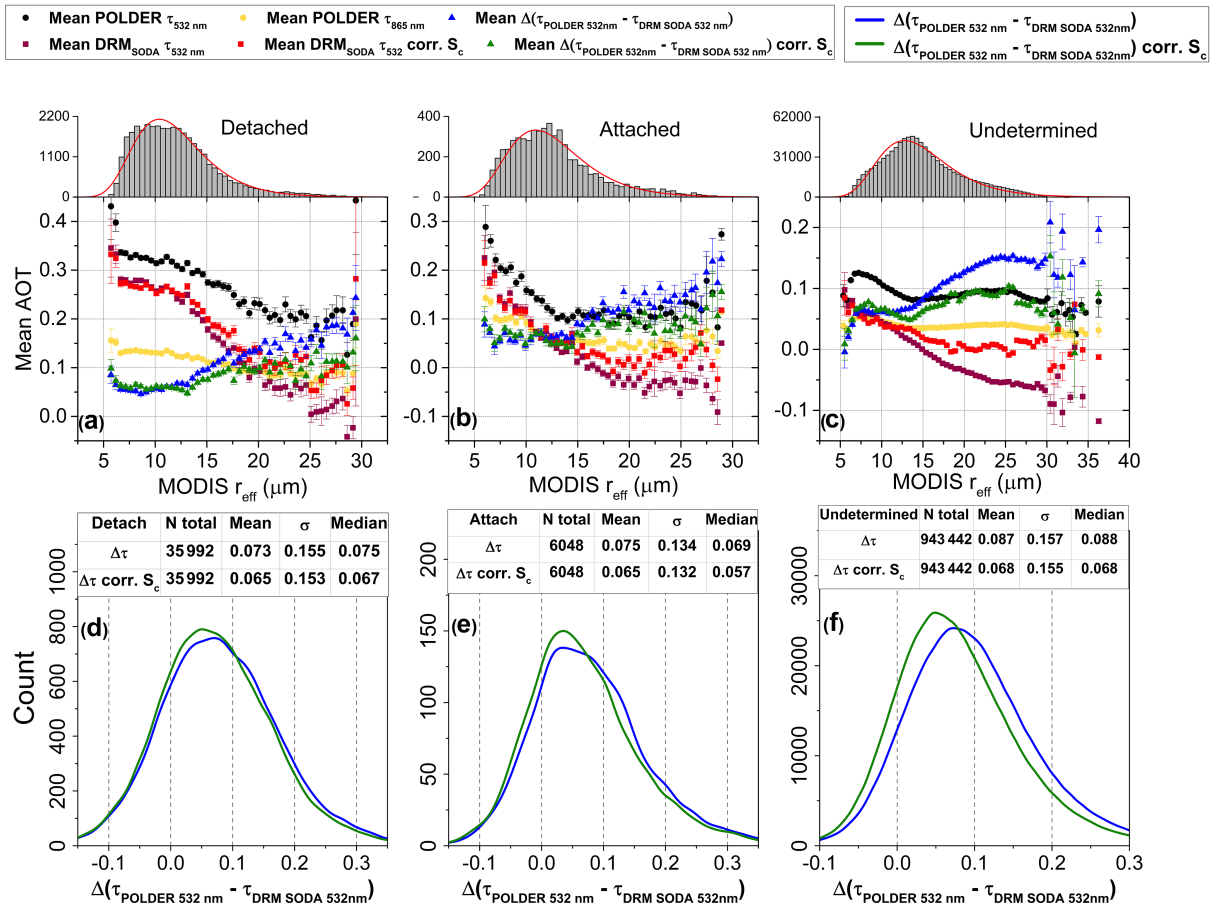


Figure 6. Four and a half years of global study on the evolution of POLDER and DRMSODA above-cloud AOT retrievals as a function of MODIS effective radius (r_{eff} , μm) for situations where the aerosol layer is detached from the cloud top (a, d), for cases where the aerosol layer is attached to the cloud top (b, e) and for undetermined situations (c, f). The histograms in (a)–(c) represent the distribution of r_{eff} . The histograms in (d)–(f) present the difference between POLDER and DRMSODA mean AOTs, before the correction of DRMSODA AOT with r_{eff} ($\Delta\tau$) and after this correction ($\Delta\tau \text{ corr. } S_c$). The associated tables indicate the number of cases, mean, standard deviation (σ) and median values of these differences. The error bars in (a)–(c) represent the standard error of the mean (SEM).

between the mean scattering coefficient and the mean extinction coefficient computed over the particle size distribution. We used a two-parameter gamma size distribution with an effective variance of 0.088. The real refractive index was set to 1.337. Liquid water droplets do not significantly absorb at 532 nm and the imaginary part of the complex refractive index was set to 0. As shown in Fig. 9, S_c slightly decreases with r_{eff} from 19.5 to 15.5 as the effective radius values increases from 5 to 40 μm . With this correction, the mean difference between POLDER and the DRMSODA AOT_{532 nm} ($\Delta\tau \text{ corr. } S_c$ in Fig. 6d) decreases from 0.073 to 0.065. We found equivalent results for the attached and undetermined cases (Fig. 6b and c). After correction of S_c , the difference between POLDER and DRMSODA decreases on average by 0.01 for the attached cases and by 0.019 for the undetermined cases. We also observe that most of the negative AOT values retrieved by the DRMSODA shift either to null values or weakly positive values when this correction is included

(Fig. 6a–c). We are aware that MODIS effective radius may be affected by the presence of aerosols above clouds. For example, Haywood et al. (2004) found biases of $\pm 2 \mu\text{m}$ for r_{eff} in case of strong dust events above clouds and Meyer et al. (2015) found an increase in the r_{eff} monthly mean of 2 % in case of above-cloud absorbing aerosols. We expect that large biases on r_{eff} could be possible in case of high aerosol loading for detached cases. However, we consider that the impact of the biases on the retrieved r_{eff} on our findings and conclusions can be neglected, since the analysis hold for (i) a wide range of droplets effective radius (from 5 to 40 μm) and (ii) AAC events associated with low aerosol loadings (see the results for the undetermined cases), where the impacts of the aerosols on the cloud retrievals are expected to be minimized or negligible.

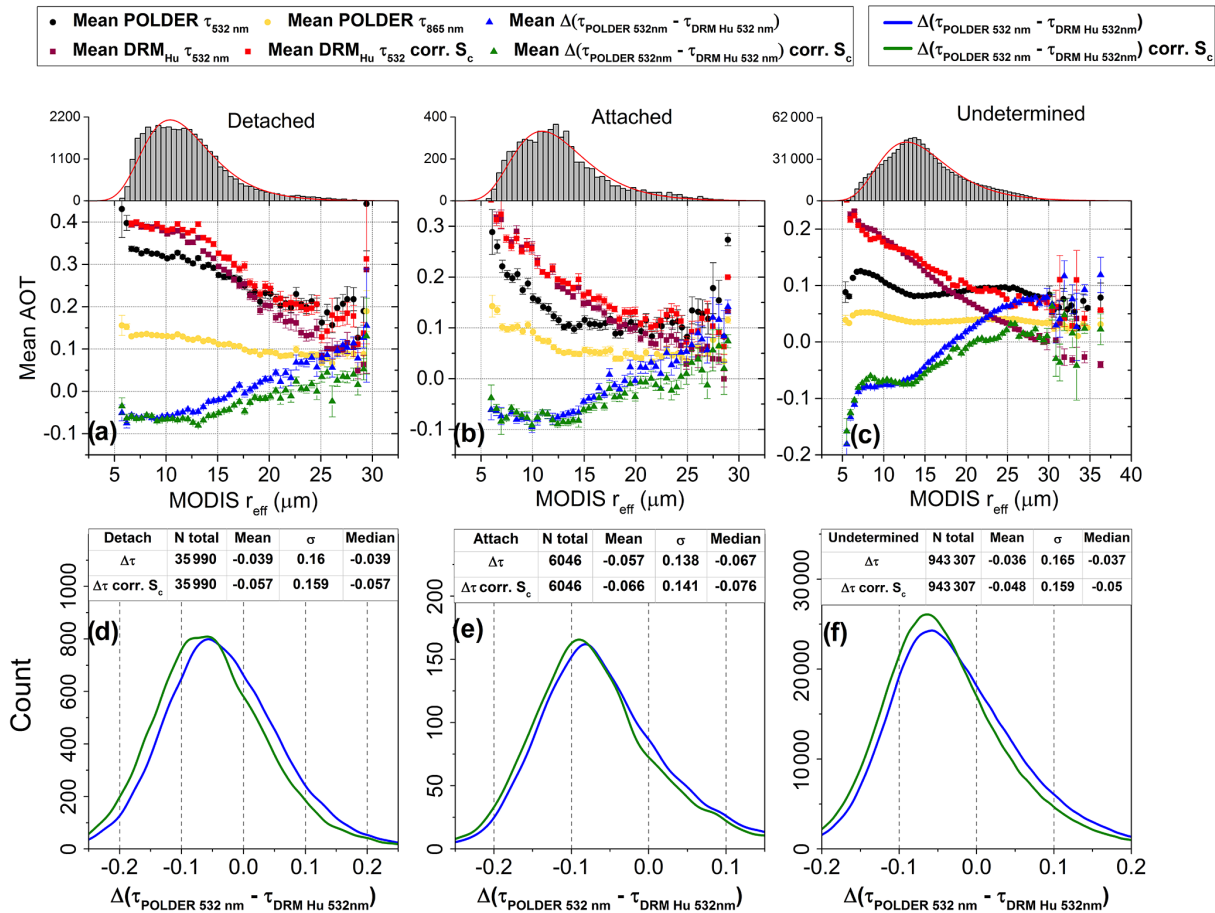


Figure 7. Same as Fig. 6: POLDER and DRM_{Hu} above-cloud AOT retrievals as a function of MODIS effective radius (r_{eff} , μm).

4.2.2 AOT vs. COT

The two methods were developed to detect AAC events in the case of optically thick and homogeneous liquid water clouds. In the following, we only discuss results obtained for large values of COT (larger than 5). If the clouds are optically thinner, the two methods are potentially less accurate since they become sensitive to the surface contribution. Hu et al. (2007a) noticed the surface impact on DRM_{Hu} when the underlying cloud is not entirely opaque; therefore the assumptions used in the DRM_{Hu} AOT retrievals are not met. For COTs ranging between 5 and 30 and for detached cases, the POLDER AOTs are almost constant and reach 0.3 on average at 532 nm (see Fig. 8a). Most of the associated COT values then range between 5 and 10. For these cases, DRM_{SODA} and POLDER AOTs are offset by around 0.07 on average, as noted above. However, the DRM_{SODA} AOT progressively increases with the COT, which is not observed for the POLDER AOT. Consequently, the differences in AOT between the two methods become almost negligible for the largest (and less frequent) values of COT (larger than 20). For COTs larger than 3, the polarized signal reflected by the

cloud is saturated and the POLDER method should be insensitive to COT. DRM_{SODA} is sensitive to the multiple scattering processes occurring within the cloud layers and might be impacted by the COT since multiple scattering increases with the optical thickness. The measured depolarization (δ') and the multiple scattering factor (η_{calibr}) plotted as a function of the COT are shown in Fig. 8d. As expected, the depolarization and the multiple scattering factor respectively increase and decrease as COT increases. The increase in the DRM_{SODA} AOT observed at large COTs might be due to an increase in the multiple scattering. We recall that DRM_{SODA} uses a relationship to connect the depolarization and the multiple scattering factor and that this relation is calibrated based on CALIOP data. The calibration might be less accurate in the case of AAC events associated with clouds for which the properties are statistically less representative. Again, we presume that our conclusions are not impacted by the fact that the MODIS COTs can be potentially biased in case of AAC events since the tendencies we observed hold for a large range of variability in COT (5 to 30) and also for AAC events associated with low AOT above clouds (see the results for the undetermined cases).

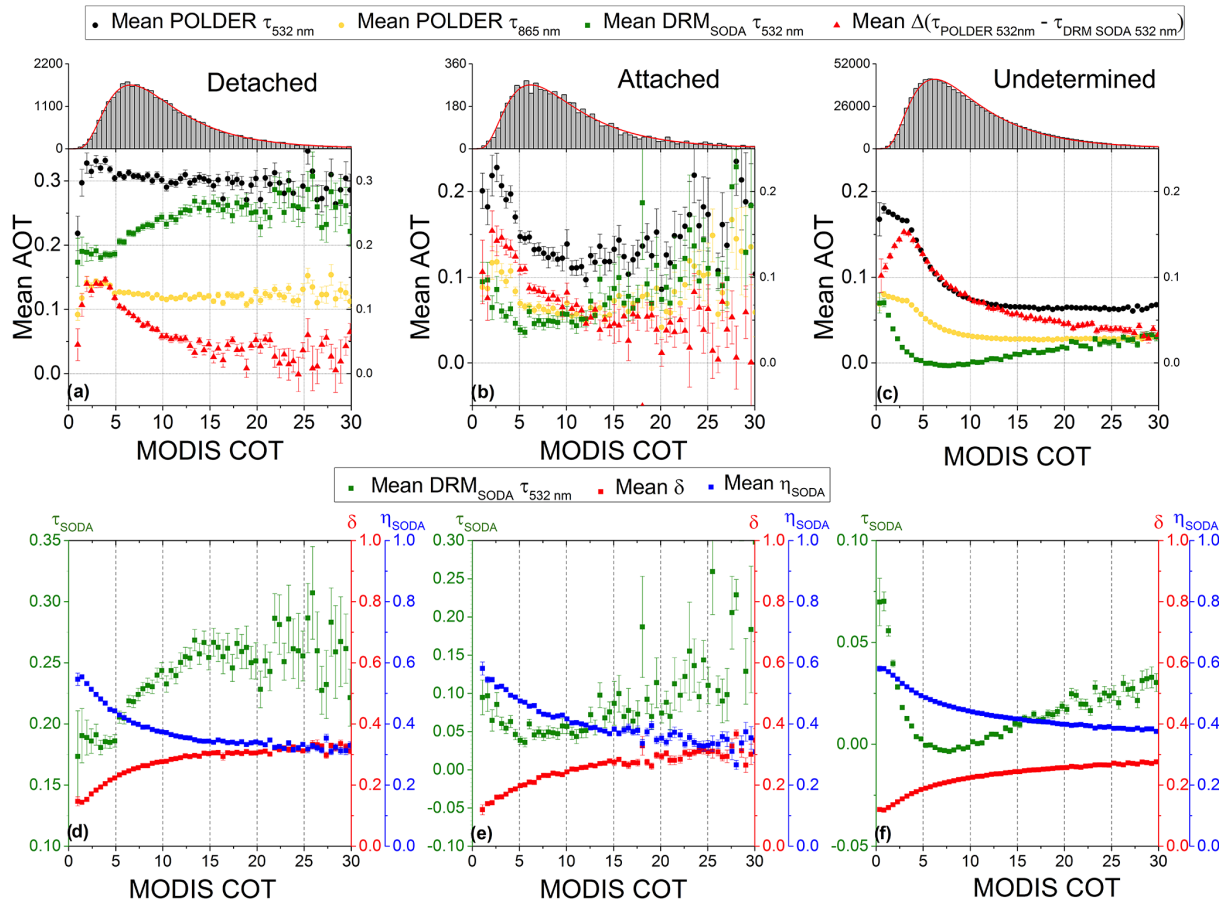


Figure 8. Four and a half years of global study of the evolution of POLDER and DRM_{SODA} above-cloud AOT retrievals, as well as the difference of these two methods as a function of MODIS cloud optical thickness (COT), for situations where the aerosol layer is detached from the cloud top (a), for cases where the aerosol layer is attached to the cloud top (b) and for undetermined situations (c). The histograms represent the distribution of COT. The error bars show the standard error of the mean (SEM). Panels (d)–(f) display the evolution of DRM_{SODA} AOT (τ_{SODA}), depolarization ratio (δ) and multiple scattering factor (η_{SODA}) as a function of MODIS COT, for the abovementioned situations.

5 Discussion

In the first part of this section, we quantify and discuss the overall differences found between the active and passive methods in terms of the retrieved AOT. In the second part, we address more specifically the attached cases and make hypotheses regarding the meaning of these results.

On average, the difference between POLDER and DRM_{SODA} AOTs at 532 nm is equal to 0.073 for the detached cases and 0.087 for the undetermined cases. These differences slightly decrease to 0.065 and 0.068, respectively, when we account for the dependency of the cloud droplets lidar ratio (S_c) to r_{eff} in Eq. (10). The POLDER AOTs are systematically smaller than the ones retrieved with DRM_{Hu}. On average, these differences between these two methods are equal to -0.039 and -0.057 , for the detached cases, and reach -0.036 and -0.048 for the undetermined cases, respectively without and with corrections for S_c . Thereby, the POLDER AOT estimates range, on average, between the

DRM_{Hu} and DRM_{SODA} ones. The differences in AOTs found between the POLDER method and the two DRM ones could be set to zero by modifying the lidar calibration by roughly $\pm 10\%$. One another main difference between the three methods is their different responses in terms of AOT when the atmosphere above the clouds becomes pristine. The majority of AOT (94 %) is lower than 0.1 at 865 nm for the undetermined cases. For these cases, the POLDER algorithm retrieves a mean AOT of about 0.04 at 865 nm. The accuracy of the POLDER AOT product is on the same order of magnitude. For an AOT_{865 nm} of 0.2, the error for a real refractive index uncertainty of ± 0.06 would be about 0.05; for an imaginary refractive index uncertainty of ± 0.01 , the error would be of 0.02 (Peers et al., 2015). The impact of the assumed refractive index is lower at smaller AOT (especially for an AOT of 0.04). The background of the extrapolated POLDER AOT at 532 nm for the undetermined cases reaches 0.09. This latter value is only reported for the sake of comparison with the two other methods since the Ångström ex-

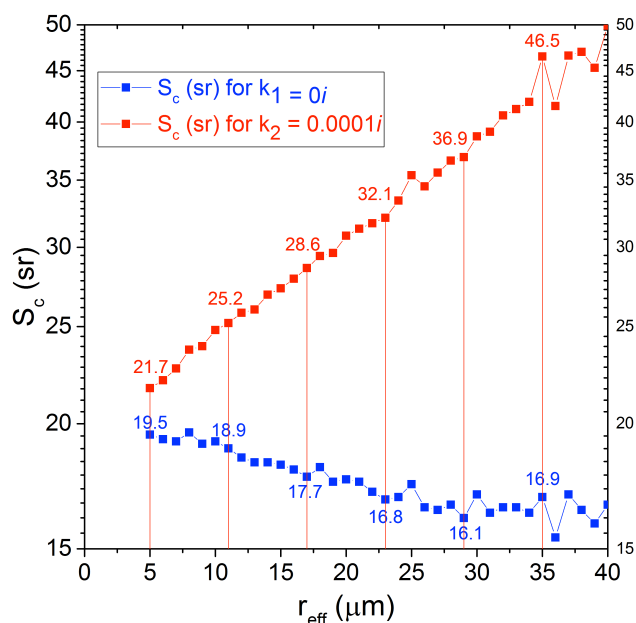


Figure 9. Sensitivity study of lidar ratio (S_c , sr) as a function of the cloud droplets effective radius, using a two-parameter gamma size distribution in Mie code. The effective variance, v_{eff} , is set to 0.088. The real part of the refractive index is fixed to 1.337, while the imaginary part, k , was set to 0 (blue) and to $0.0001i$ (red).

ponent retrieved by POLDER (and consequently the AOT extrapolated at 532 nm) cannot be accurately retrieved for low AOTs. DRM_{SODA} found a mean AOT of about 0.005 at 532 nm for the undetermined cases (see Fig. 6c). The result is likely due to the re-calibration process since DRM_{Hu} found a background even larger than that of POLDER: about 0.12 at 532 nm. It is difficult to assess the truthfulness of this background, considering the given level of accuracy of the POLDER method and the uncertainties associated with the lidar calibration. We assume that these background values are not physical and could be due to some inherent limitations of the retrieval methods. From our data, however, we cannot exclude the possibility that there is always a background loading of particles above clouds (e.g. aerosols or fine droplets in formation). Nevertheless, the main result of our investigation is that POLDER and DRM methods compare well for most situations with a mean difference of about ± 0.07 in AOT at 532 nm.

Although the number of cases is small, the results of the attached cases are interesting. They suggest that the lidar CALIOP and POLDER could be affected by layers of aerosols that physically and locally interact with the upper part of the cloud. In order to understand how the vertical profiles differ from one situation to another, we compared the CALIOP attenuated backscatter coefficient for attached and detached cases. We considered the period 2006–2010 and used data acquired over the entire globe. We only select the attached and detached cases where the cloud top

altitude is below 1.5 km, the COT is larger than 5 and the $\text{DRM}_{\text{SODA}} \text{AOT}_{532 \text{ nm}}$ is larger than 0.1. These criteria allow for selection of data that correspond to AAC events associated with similar cloud vertical extents and with significant AOTs. For these cases, we computed the average and median of the CALIOP level 1 attenuated backscatter coefficients at 532 nm. Figure 10 presents these results and some information concerning the mean and median values of CALIOP level 2 products: cloud top altitude, aerosol layer's base and top altitudes. The mean and median values computed for the AOTs retrieved by POLDER and DRM_{SODA} and the numbers of sampled events are also reported. Two different types of profiles can be observed for the detached and attached situations. For the detached cases, the aerosol and cloud backscattering profiles can be easily distinguished in both the median and mean profiles. The strong peaks in the backscatter profiles at around 1 km correspond to the top of the clouds, whereas the increase in the lidar backscatter signal observed between 2 and 4 km in altitude comes from the aerosols. For the attached situations, the backscatter profiles are noisier, which is likely due to the fact that the number of detected events is smaller compared to detached cases. The top of the cloud layer is still clearly visible in the mean and median backscattered lidar signals, but two maxima can be observed. We assume that we sampled two different regimes of clouds. In addition, there is a continuous transition in the backscatter signal between the top of the cloud and the above molecular atmosphere that is most clearly visible in the median profiles. This signal does not appear for the detached cases. This signal could explain the non-negligible above-cloud AOTs retrieved by POLDER and DRM_{SODA} for the attached cases (see Fig. 5). It is difficult to assess the origin of the signal. It might be due to aerosols layers that penetrate the cloud layers at the top of the clouds. Natural aerosol or fine droplets in formation, commonly present in the vicinity of the clouds, might also create this additional signal.

Another hypothesis that could explain the low AOT correlation for the attached cases is that the aerosols located within the cloud layer could affect the polarized radiances measured by POLDER. Note that the polarized radiance at 865 nm is not affected by the vertical position of the aerosol layer as long as there is no contact between the aerosol and the cloud. Since the operational algorithm developed for POLDER assumes that the entire aerosol layer is located above the clouds, an additional polarized signal coming from aerosol located within the cloud would lead to an overestimation of the above-cloud AOT retrieved from POLDER. To test this assumption, we modelled the polarized radiance measured by POLDER for AAC scenes, considering different vertical locations of the aerosol layer (Fig. 11). We used the SOS radiative transfer code (Lenoble et al., 2007) for this simulation. We considered a liquid water cloud located between 0 and 1 km. The particles (aerosol and cloud) are vertically homogeneously mixed. The COT is equal to 10 and the effective radius and variance are equal to $10 \mu\text{m}$ and 0.08,

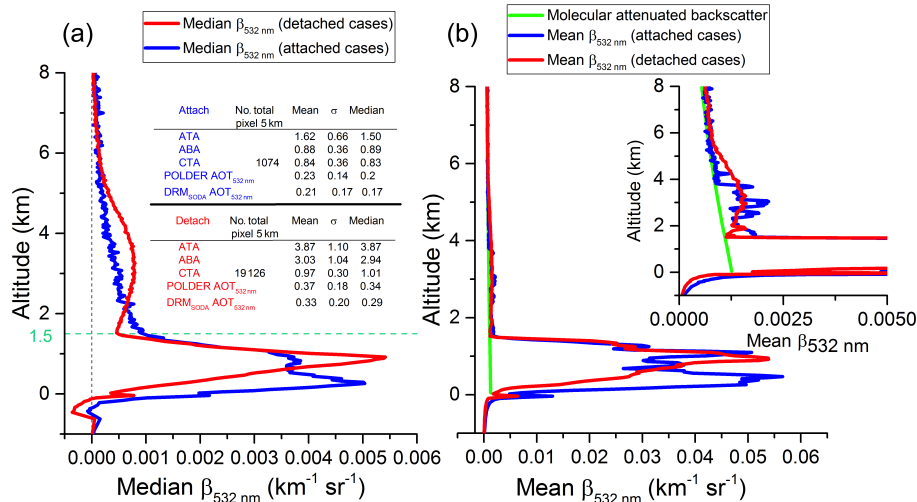


Figure 10. Median (a) and averaged (b) backscatter profiles ($\text{km}^{-1} \text{sr}^{-1}$) for aerosol layer detached from the cloud layer (red) and aerosols attached to the top of the cloud (blue), for a period of 4.5 years on the global scale. For comparison, the molecular attenuated backscatter profile is shown as a green line. The data were filtered for a cloud top altitude lower than 1.5 km, a cloud optical thickness (COT) larger than 5 and for a DRM_{SODA} AOT at 532 nm larger than 0.1. The number of 5 km horizontal-resolution pixels is also shown. The mean, standard deviation (σ) and median of aerosol top altitude (ATA), aerosol base altitude (ABA) and cloud top altitude (CTA) are given for each situation. Same values are shown for POLDER AOT at and DRM_{SODA} AOT at 532 nm.

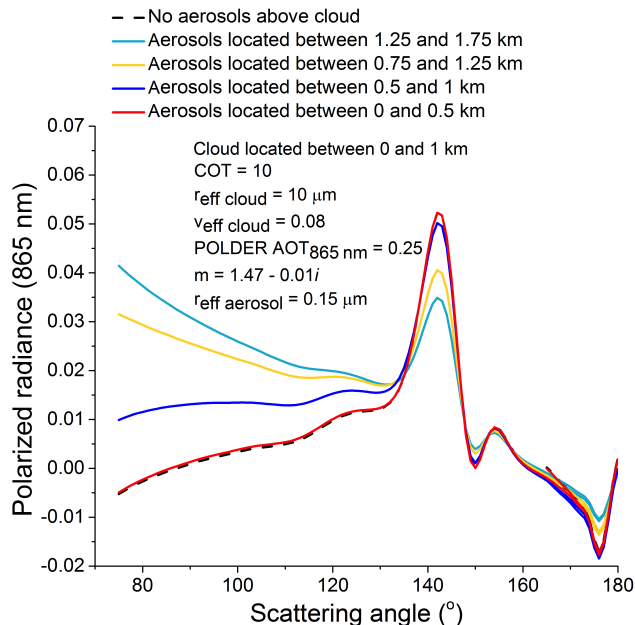


Figure 11. Sensitivity study of polarized radiance at 865 nm to the relative position of the aerosol layer above the cloud. Simulation performed for a cloud layer located between 0 and 1 km and aerosol layers varying at different altitudes. The cloud droplet effective radius is fixed to $10 \mu\text{m}$ and the effective variance is 0.08. The aerosol layer is characterized by an AOT of 0.25 at 865 nm, a refractive index of $1.47 - 0.01i$ and an aerosol effective radius of $0.15 \mu\text{m}$.

respectively. The aerosol layer is characterized by an AOT of 0.25 at 865 nm, a refractive index of $m = 1.47 - 0.01i$ and an effective radius of $0.15 \mu\text{m}$. Figure 11 shows the typical polarized feature for AAC events in case of detached situations (i.e. aerosols located between 1.25 and 1.75 km): a creation of polarization is observed at side and forward scattering angles, whereas the cloud bow magnitude decreases. For the attached case (aerosols between 0.75 and 1.25 km), the amount of polarization created at forward scattering angles decreases and the cloud bow attenuation is less significant in comparison with the detached scenario. When the aerosol layer is located within the upper part of the cloud layer (between 0.5 and 1 km) we still observe a weak polarized signal created at forward scattering angles. When the aerosol layer is located in the lower part of the cloud layer, the effects of the aerosols disappear since the polarized radiance scattered by the aerosols is lost due to multiple scattering occurring within the clouds. These simulations were processed with the POLDER algorithm (Waquet et al., 2013b). We recall that the LUTs used in this algorithm were built for detached situations. The algorithm retrieved an AOT of 0.09 at 865 nm when the aerosols are located within the upper part of the cloud layer. This demonstrates that polarized radiances are sensitive to aerosols situated within the clouds for the attached cases.

The DRM methods might also be impacted by the presence of aerosols within the clouds. Aerosols as a solution within the cloud droplets (i.e. internal mixture) might impact the chemical composition of the droplets and modify their ability to backscatter light. Figure 9 shows lidar ratio

computed for absorbing cloud droplets. We used an imaginary part of 0.0001 for the complex refractive index of the droplets. This might simulate, for instance, the properties of brown clouds contaminated by absorbing aerosols. The chosen value is in agreement with the refractive indices given for water containing soot inclusions with volume fractions ranging between 10^{-4} and 10^{-2} (Erlick, 2006). We observe a drastic increase of S_c with r_{eff} (from 21.7 sr at $5\ \mu\text{m}$ to 50 sr at $40\ \mu\text{m}$) when the water droplet is weakly absorbing. In the case of an external mixture, we assume that the presence of aerosols at the top of cloud might also modify the value of S_c . Any deviation from the 19 sr value assumed for the droplets lidar ratio in Eq. (9) will necessarily impact the retrieved AOT and the differences observed between the AOT estimates provided by the POLDER and DRM methods.

6 Conclusions

In this study, we compared and analysed the consistency of the AOT and AE retrievals above clouds from different passive and active techniques. We used the CALIOP operational algorithm (Winker et al., 2009), the POLDER polarization method (Waquet et al., 2013b) and the CALIOP-based depolarization ratio method (DRM_{Hu}) (Hu et al., 2007a), for which we proposed a re-calibrated version of the DRM algorithm (DRM_{SODA}). The observations were made for (a) three case studies corresponding to an African biomass-burning event, a Saharan dust event and a Siberian biomass-burning event; (b) a regional-scale analysis over South Atlantic Ocean, North Atlantic Ocean and North Pacific Ocean for a period of 6 months in 2008; and (c) a global-scale analysis for different vertical layer distributions for the period 2006–2010.

In the regional analysis, we observed that POLDER method and DRM are in good agreement when the microphysics of aerosols is dominated by fine-mode particles of biomass-burning aerosols (in the South Atlantic region, $R^2 = 0.83$) or coarse-mode aerosols of dust (in the North Atlantic region, $R^2 = 0.82$). A good correlation between these methods ($R^2 = 0.68$) is also noticed in the global treatment, when the aerosol and cloud layers are well separated. Nevertheless, some of the detached cases considered in our study, mainly the ones associated with optically thick smoke layers, are likely to be incorrectly classified as detached. As a future perspective, these misclassified detached cases (due to strong attenuation of the CALIOP 532 nm signal) could be detected by controlling the CALIOP 1064 nm signal, which was shown to provide more sensitivity to the entire vertical extent of these absorbing aerosol layers. The CALIOP operational method largely underestimates the AOT above clouds in all situations, with respect to other methods.

The differences between the DRM and POLDER retrievals increase when a complex mixture of aerosols is expected (such as in the East Asia region). This is probably due to the

fact that the current algorithm developed for POLDER uses a limited number of microphysical models of aerosols. Also, the relative position of the aerosol layer above the cloud impacts the AOT retrievals from both active and passive measurements: the correlation decreases when the layers are in contact ($R^2 = 0.36$), suggesting that aerosols at the top or within the cloud can affect the AOT retrievals. One hypothesis is that an additional polarized signal coming from aerosol located within the cloud could affect the polarization signal and method, which leads to an overestimation of the AOT retrieved with POLDER algorithm. The aerosols attached with or within the cloud also have the potential to impact the DRM retrievals by modifying the lidar ratio (and consequently the AOT) as a result of internal or external mixture.

Furthermore, we investigated potential biases in the retrieved AOT measured by POLDER and DRM_{SODA} as a function of MODIS cloud properties (i.e. droplet effective radius (r_{eff}) and COT). The tendencies show an increase in the difference between the two methods for larger r_{eff} , suggesting sensitivity to the cloud droplet effective radius. For this reason, we recalculated the DRM_{SODA} $\text{AOT}_{532\text{nm}}$, taking into account the dependence of lidar ratio on r_{eff} , as this method assumes a constant lidar ratio regarding the droplet effective radius. By doing so, we observed a decrease in the difference between POLDER and DRM methods and a shift of the DRM AOT values from negative to positive. For a better accuracy of DRM retrievals in future studies, this correction should be taken into account. The results show also that the multiple scattering processes, which are more pronounced in optically thick clouds, could also affect the DRM technique.

All of the aforementioned situations have revealed that DRM_{Hu} has larger mean AOT than that of DRM_{SODA} . This is likely to be a consequence of the re-calibration performed for the DRM_{SODA} method. Actually, POLDER $\text{AOT}_{532\text{nm}}$ values are consistently smaller than the ones of DRM_{Hu} and larger than those of DRM_{SODA} . The primary conclusion of our investigation is that POLDER and DRM techniques are comparable for the majority of cases, with a mean difference of about ± 0.07 in AOT at 532 nm, depending on lidar calibration.

Given the fact that each method relies upon different physical concepts, applied to different sensors and measurements, the high value of the correlation obtained for the AOT retrievals is a remarkable result that highlights the coherence between active and passive methods for aerosols above clouds. Nonetheless, more efforts have to be done to increase the accuracy of the methods in order to better understand aerosols above clouds and their related effects. Airborne measurements are extremely useful in providing information on aerosols' above-cloud properties. Several ongoing and planned airborne field campaigns will attempt to characterize the properties of biomass-burning aerosols over the South Atlantic Ocean (Zuidema et al., 2016). Planned measurements from the French Falcon 20 aircraft, equipped

with a high-resolution lidar, an airborne sun photometer and a POLDER-like sensor, will notably be considered for a future validation of CALIOP DRM and POLDER above-cloud aerosol products. Another perspective is to improve the POLDER algorithm by introducing additional dust or mixture models with larger or smaller effective radii values in the LUT. This would definitely improve the AOT and AE retrievals in more complex situations (such as East Asia region). Also, our results suggest that a combination of POLDER and DRM methods has the potential to detect aerosols within clouds. It is very relevant to study these situations, since they can affect the retrievals and provide important information regarding the cloud processes. A further perspective would be to exploit the synergy between CALIOP and POLDER to infer the direct aerosol radiative forcing, aerosol heating rates and the semi-direct effect of absorbing aerosols located above clouds.

Data availability. All data are available at ICARE website on-line archive: <http://www.icare.univ-lille1.fr/archive>.

Competing interests. The authors declare that they have no conflict of interest.

Acknowledgements. Lucia Deaconu's grant is provided by the CaPPA project (Chemical and Physical Properties of the Atmosphere), which is funded by the French National Research Agency (ANR) through the PIA (Programme d'Investissement d'Avenir) under contract ANR-11-LABX-0005-01 and by the Regional Council Hauts-de-France and the European Funds for Regional Economic Development (FEDER).

Edited by: Piet Stammes

Reviewed by: Hiren Jethva and two anonymous referees

References

- Balkanski, Y., Schulz, M., Claquin, T., and Guibert, S.: Reevaluation of Mineral aerosol radiative forcings suggests a better agreement with satellite and AERONET data, *Atmos. Chem. Phys.*, 7, 81–95, <https://doi.org/10.5194/acp-7-81-2007>, 2007.
- Bates, D. R.: Rayleigh scattering by air, *Planet. Space Sci.*, 32, 785–790, 1984.
- Cao, X., Roy, G., Roy, N., and Bernier, R.: Comparison of the relationships between lidar integrated backscattered light and accumulated depolarization ratios for linear and circular polarization for water droplets, fog oil, and dust, *Appl. Opt.*, 48, 4130–4141, <https://doi.org/10.1364/AO.48.004130>, 2009.
- Catrrall, C., Reagan, J., Thome, K., and Dubovik, O.: Variability of aerosol and spectral lidar and backscatter and extinction ratios of key aerosol types derived from selected Aerosol Robotic Network locations, *J. Geophys. Res.*, 110, D10S11, <https://doi.org/10.1029/2004JD005124>, 2005.
- Chand, D., Anderson, T. L., Wood, R., Charlson, R. J., Hu, Y., Liu, Z., and Vaughan, M.: Quantifying above-cloud aerosol using spaceborne lidar for improved understanding of cloudy-sky direct climate forcing, *J. Geophys. Res.*, 113, D13206, <https://doi.org/10.1029/2007JD009433>, 2008.
- Chand, D., Wood, R., Anderson, T. L., Satheesh, S. K., and Charlson, R. J.: Satellite-derived direct radiative effect of aerosols dependent on cloud cover, *Nat. Geosci.*, 2, 181–184, <https://doi.org/10.1038/ngeo437>, 2009.
- Costantino, L. and Bréon, F.-M.: Aerosol indirect effect on warm clouds over South-East Atlantic, from co-located MODIS and CALIPSO observations, *Atmos. Chem. Phys.*, 13, 69–88, <https://doi.org/10.5194/acp-13-69-2013>, 2013.
- Deuzé, J. L., Herman, M., and Santer, R.: Fourier series expansion of the transfer equation in the atmosphere-ocean system, *J. Quant. Spectrosc. Ra.*, 41, 483–494, [https://doi.org/10.1016/0022-4073\(89\)90118-0](https://doi.org/10.1016/0022-4073(89)90118-0), 1989.
- Dubovik, O., Holben, B., Eck, T. F., Smirnov, A., Kaufman, Y. J., King, M. D., Tanré, D., and Slutsker, I.: Variability of Absorption and Optical Properties of Key Aerosol Types Observed in Worldwide Locations, *J. Atmos. Sci.*, 59, 590–608, [https://doi.org/10.1175/1520-0469\(2002\)059<0590:VOAOP>2.0.CO;2](https://doi.org/10.1175/1520-0469(2002)059<0590:VOAOP>2.0.CO;2), 2002.
- Erlick, C.: Effective Refractive Indices of Water and Sulfate Drops Containing Absorbing Inclusions, *J. Atmos. Sci.*, 63, 754–763, <https://doi.org/10.1175/JAS3635.1>, 2006.
- Feng, N. and Christopher, S. A.: Measurement-based estimates of direct radiative effects of absorbing aerosols above clouds, *J. Geophys. Res.-Atmos.*, 120, 6908–6921, <https://doi.org/10.1002/2015JD023252>, 2015.
- De Graaf, M., Bellouin, N., Tilstra, L. G., Haywood, J., and Stammes, P.: Aerosol direct radiative effect of smoke over clouds over the southeast Atlantic Ocean from 2006 to 2009, *Geophys. Res. Lett.*, 41, 7723–7730, <https://doi.org/10.1002/2014GL061103>, 2014.
- Hansen, J., Sato, M., and Ruedy, R.: Radiative forcing and climate response, *J. Geophys. Res.-Atmos.*, 102, 6831–6864, <https://doi.org/10.1029/96JD03436>, 1997.
- Hasekamp, O. P.: Capability of multi-viewing-angle photopolarimetric measurements for the simultaneous retrieval of aerosol and cloud properties, *Atmos. Meas. Tech.*, 3, 839–851, <https://doi.org/10.5194/amt-3-839-2010>, 2010.
- Haywood, J. M., Osborne, S. R., and Abel, S. J.: The effect of overlying absorbing aerosol layers on remote sensing retrievals of cloud effective radius and cloud optical depth, *Q. J. Roy. Meteor. Soc.*, 130, 779–800, <https://doi.org/10.1256/qj.03.100>, 2004.
- Herman, M., Deuzé, J. L., Marchand, A., Roger, B., and Lallart, P.: Aerosol remote sensing from POLDER/ADEOS over the ocean: Improved retrieval using a nonspherical particle model, *J. Geophys. Res.-Atmos.*, 110, 1–11, <https://doi.org/10.1029/2004JD004798>, 2005.
- Hu, Y.: Depolarization ratio-effective lidar ratio relation: Theoretical basis for space lidar cloud phase discrimination, *Geophys. Res. Lett.*, 34, L11812, <https://doi.org/10.1029/2007GL029584>, 2007.
- Hu, Y., Liu, Z., Winker, D., Vaughan, M., Noel, V., Bissonnette, L., Roy, G., and McGill, M.: Simple relation between lidar multiple scattering and depolarization for water clouds, *Opt. Lett.*, 31, 1809, <https://doi.org/10.1364/OL.31.001809>, 2006.

- Hu, Y., Vaughan, M., Liu, Z., Powell, K., and Rodier, S.: Retrieving Optical Depths and Lidar Ratios for Transparent Layers Above Opaque Water Clouds From CALIPSO Lidar Measurements, *IEEE Geosci. Remote Sens.*, 4, 523–526, <https://doi.org/10.1109/LGRS.2007.901085>, 2007a.
- Hu, Y., Vaughan, M., Liu, Z., Lin, B., Yang, P., Flittner, D., Hunt, B., Kuehn, R., Huang, J., Wu, D., Rodier, S., Powell, K., Trepte, C., and Winker, D.: The depolarization – attenuated backscatter relation: CALIPSO lidar measurements vs. theory, *Opt. Express*, 15, 5327–5332, <https://doi.org/10.1364/OE.15.005327>, 2007b.
- Hunt, W. H., Winker, D. M., Vaughan, M. A., Powell, K. A., Lucker, P. L., Weimer, C., Hunt, W. H., Winker, D. M., Vaughan, M. A., Powell, K. A., Lucker, P. L., and Weimer, C.: *CALIPSO* Lidar Description and Performance Assessment, *J. Atmos. Ocean. Tech.*, 26, 1214–1228, <https://doi.org/10.1175/2009JTECHA1223.1>, 2009.
- IPCC: Climate Change 2013: The Physical Science Basis, Contribution of Working Group I to the Fifth Assessment Report of the Intergovernmental Panel on Climate Change, edited by: Stocker, T. F., Qin, D., Plattner, G.-K., Tignor, M., Allen, S. K., Boschung, J., Nauels, A., Xia, Y., Bex, V., and Midgley, P. M., Cambridge University Press, Cambridge, UK, New York, NY, USA, 1535 pp., <https://doi.org/10.1017/CBO9781107415324>, 2013.
- Jethva, H., Torres, O., Remer, L. A., and Bhartia, P. K.: A color ratio method for simultaneous retrieval of aerosol and cloud optical thickness of above-cloud absorbing aerosols from passive sensors: Application to MODIS measurements, *IEEE T. Geosci. Remote*, 51, 3862–3870, <https://doi.org/10.1109/TGRS.2012.2230008>, 2013.
- Jethva, H., Torres, O., Waquet, F., Chand, D., and Hu, Y.: How do A-train sensors intercompare in the retrieval of above-cloud aerosol optical depth? A case study-based assessment, *Geophys. Res. Lett.*, 41, 186–192, <https://doi.org/10.1002/2013GL058405>, 2014.
- Johnson, B. T., Shine, K. P., and Forster, P. M.: The semi-direct aerosol effect: Impact of absorbing aerosols on marine stratocumulus, *Q. J. Roy. Meteor. Soc.*, 130, 1407–1422, <https://doi.org/10.1256/qj.03.61>, 2004.
- Josset, D., Hu, Y., Pelon, J., Zhai, P., Tanré, D., Rogers, R., Lucker, P., Trepte, C., Powell, K., Rodier, S., Pascal, N., and Team, T. I.: Advances in Research Products From CALIPSO: Optical Depth Direct Retrieval Over Ocean, Water Clouds and Land, 25th International Laser Radar Conference (ILRC), Curran Associates, Inc., Curran Associates, Inc., 1280–1283, 2010.
- Josset, D., Rogers, R., Pelon, J., Hu, Y., Liu, Z., Omar, A., Zhai, P.-W., Fernald, F. G., Herman, B. M., Reagan, J. A., Winker, D. M., Pelon, J., Coakley, J. A., Ackerman, S. A., Charlson, R. J., Colarco, P. R., Flamant, P., Fu, Q., Hoff, R., Kittaka, C., Kubar, T. L., LeTret, H., McCormick, M. P., Megie, G., Poole, L., Powell, K., Trepte, C., Vaughan, M. A., Wielicki, B. A., Stephens, G. L., Vane, D. G., Tanelli, S., Im, E., Durden, S., Rokey, M., Reinke, D., Partain, P., Mace, G. G., Austin, R., Haynes, J., Lebsack, M., Suzuki, K., Waliser, D., Wu, D., Kay, J., Gettelman, A., Wang, Z., and Marchand, R.: CALIPSO lidar ratio retrieval over the ocean, *Opt. Express*, 19, 18696–18706, <https://doi.org/10.1364/OE.19.018696>, 2011.
- Josset, D., Pelon, J., Hu, Y., Rogers, R., Liu, Z., Omar, A., Vaughan, M., Zhai, P., and Team, I.: Global scale lidar ratio retrieval over the ocean, 26th International Laser Radar Conference (ILRC 26), Porto Heli, Greece, 25–29 June, 2012.
- Kaufman, Y. J., Tanré, D., and Boucher, O.: A satellite view of aerosols in the climate system, *Nature*, 419, 215–23, <https://doi.org/10.1038/nature01091>, 2002.
- Keil, A. and Haywood, J. M.: Solar radiative forcing by biomass burning aerosol particles during SAFARI 2000: A case study based on measured aerosol and cloud properties, *J. Geophys. Res.-Atmos.*, 108, 8467, <https://doi.org/10.1029/2002JD002315>, 2003.
- King, L. V.: On the Complex Anisotropic Molecule in Relation to the Dispersion and Scattering of Light, *P. Roy. Soc. A-Math. Phys.*, 104, 333–357, 1923.
- Knobelspiesse, K., Cairns, B., Ottaviani, M., Ferrare, R., Hair, J., Hostetler, C., Obland, M., Rogers, R., Redemann, J., Shinozuka, Y., Clarke, A., Freitag, S., Howell, S., Kapustin, V., and McNaughton, C.: Combined retrievals of boreal forest fire aerosol properties with a polarimeter and lidar, *Atmos. Chem. Phys.*, 11, 7045–7067, <https://doi.org/10.5194/acp-11-7045-2011>, 2011.
- Lenoble, J., Herman, M., Deuzé, J. L., Lafrance, B., Santer, R., and Tanré, D.: A successive order of scattering code for solving the vector equation of transfer in the earth's atmosphere with aerosols, *J. Quant. Spectrosc. Ra.*, 107, 479–507, <https://doi.org/10.1016/j.jqsrt.2007.03.010>, 2007.
- Meyer, K., Platnick, S., Oreopoulos, L., and Lee, D.: Estimating the direct radiative effect of absorbing aerosols overlying marine boundary layer clouds in the southeast Atlantic using MODIS and CALIOP, *J. Geophys. Res.-Atmos.*, 118, 4801–4815, <https://doi.org/10.1002/jgrd.50449>, 2013.
- Meyer, K., Platnick, S., and Zhang, Z.: Simultaneously inferring above-cloud absorbing aerosol optical thickness and underlying liquid phase cloud optical and microphysical properties using MODIS, *J. Geophys. Res.-Atmos.*, 120, 5524–5547, <https://doi.org/10.1002/2015JD023128>, 2015.
- Miles, N. L., Verlinde, J., Clothiaux, E. E., Miles, N. L., Verlinde, J., and Clothiaux, E. E.: Cloud Droplet Size Distributions in Low-Level Stratiform Clouds, *J. Atmos. Sci.*, 57, 295–311, [https://doi.org/10.1175/1520-0469\(2000\)057<0295:CDSIDL>2.0.CO;2](https://doi.org/10.1175/1520-0469(2000)057<0295:CDSIDL>2.0.CO;2), 2000.
- Myhre, G., Shindell, D., Bréon, F.-M., Collins, W., Fuglestedt, J., Huang, J., Koch, D., Lamarque, J.-F., Lee, D., Mendoza, B., Nakajima, T., Robock, A., Stephens, G., Takemura, T., and Zhang, H.: Anthropogenic and Natural Radiative Forcing, Intergovernmental Panel on Climate Change (IPCC), Cambridge University Press, 659–740, <https://doi.org/10.1017/CBO9781107415324.018>, 2013a.
- Myhre, G., Samset, B. H., Schulz, M., Balkanski, Y., Bauer, S., Bernsten, T. K., Bian, H., Bellouin, N., Chin, M., Diehl, T., Easter, R. C., Feichter, J., Ghan, S. J., Hauglustaine, D., Iversen, T., Kinne, S., Kirkevåg, A., Lamarque, J.-F., Lin, G., Liu, X., Lund, M. T., Luo, G., Ma, X., van Noije, T., Penner, J. E., Rasch, P. J., Ruiz, A., Seland, Ø., Skeie, R. B., Stier, P., Takemura, T., Tsigaridis, K., Wang, P., Wang, Z., Xu, L., Yu, H., Yu, F., Yoon, J.-H., Zhang, K., Zhang, H., and Zhou, C.: Radiative forcing of the direct aerosol effect from AeroCom Phase II simulations, *Atmos. Chem. Phys.*, 13, 1853–1877, <https://doi.org/10.5194/acp-13-1853-2013>, 2013b.
- O'Connor, E. J., Illingworth, A. J., and Hogan, R. J.: A Technique for Autocalibration of Cloud Lidar, *J. At-*

- mos. Ocean. Tech., 21, 777–786, [https://doi.org/10.1175/1520-0426\(2004\)021<0777:ATFAOC>2.0.CO;2](https://doi.org/10.1175/1520-0426(2004)021<0777:ATFAOC>2.0.CO;2), 2004.
- Omar, A. H., Won, J.-G., Winker, D. M., Yoon, S.-C., Dubovik, O., and McCormick, M. P.: Development of global aerosol models using cluster analysis of Aerosol Robotic Network (AERONET) measurements, *J. Geophys. Res.*, 110, 10–14, <https://doi.org/10.1029/2004JD004874>, 2005.
- Omar, A. H., Winker, D. M., Vaughan, M. A., Hu, Y., Trepte, C. R., Ferrare, R. A., Lee, K.-P., Hostetler, C. A., Kittaka, C., Rogers, R. R., Kuehn, R. E., Liu, Z., Omar, A. H., Winker, D. M., Vaughan, M. A., Hu, Y., Trepte, C. R., Ferrare, R. A., Lee, K.-P., Hostetler, C. A., Kittaka, C., Rogers, R. R., Kuehn, R. E., and Liu, Z.: The CALIPSO Automated Aerosol Classification and Lidar Ratio Selection Algorithm, *J. Atmos. Ocean. Tech.*, 26, 1994–2014, <https://doi.org/10.1175/2009JTECHA1231.1>, 2009.
- Peers, F., Waquet, F., Cornet, C., Dubuisson, P., Ducos, F., Goloub, P., Szczap, F., Tanré, D., and Thieuleux, F.: Absorption of aerosols above clouds from POLDER/PARASOL measurements and estimation of their direct radiative effect, *Atmos. Chem. Phys.*, 15, 4179–4196, <https://doi.org/10.5194/acp-15-4179-2015>, 2015.
- Peers, F., Bellouin, N., Waquet, F., Ducos, F., Goloub, P., Mollard, J., Myhre, G., Skeie, R. B., Takemura, T., Tanré, D., Thieuleux, F., and Zhang, K.: Comparison of aerosol optical properties above clouds between POLDER and AeroCom models over the South East Atlantic Ocean during the fire season, *Geophys. Res. Lett.*, 43, 3991–4000, <https://doi.org/10.1002/2016GL068222>, 2016.
- Pinnick, R. G., Jennings, S. G., Chýlek, P., Ham, C., and Grandy, W. T.: Backscatter and extinction in water clouds, *J. Geophys. Res.*, 88, 6787, <https://doi.org/10.1029/JC088iC11p06787>, 1983.
- Platt, C. M. R.: Remote Sounding of High Clouds: I. Calculation of Visible and Infrared Optical Properties from Lidar and Radiometer Measurements, *J. Appl. Meteorol.*, 18, 1130–1143, [https://doi.org/10.1175/1520-0450\(1979\)018<1130:RSOHC1>2.0.CO;2](https://doi.org/10.1175/1520-0450(1979)018<1130:RSOHC1>2.0.CO;2), 1979.
- Powell, K., Vaughan, M., Winker, D., Lee, K. P., Pitts, M., Trepte, C., Detweiler, P., Hunt, W., Lambeth, J., and Lucker, P.: Cloud–Aerosol LIDAR Infrared Pathfinder Satellite Observations (CALIPSO), *Data Manag. Syst. Data, Prod. Cat. Doc. No. PC-SCI-503*, Release, 3, 2010.
- Ramanathan, V., Crutzen, P. J., Kiehl, J. T., and Rosenfeld, D.: Aerosols, climate, and the hydrological cycle., *Science*, 294, 2119–2124, <https://doi.org/10.1126/science.1064034>, 2001.
- Riedi, J., Marchant, B., Platnick, S., Baum, B. A., Thieuleux, F., Oudard, C., Parol, F., Nicolas, J.-M., and Dubuisson, P.: Cloud thermodynamic phase inferred from merged POLDER and MODIS data, *Atmos. Chem. Phys.*, 10, 11851–11865, <https://doi.org/10.5194/acp-10-11851-2010>, 2010.
- Rosenfeld, D.: Suppression of Rain and Snow by Urban and Industrial Air Pollution, *Science*, 287, 1793–1796, <https://doi.org/10.1126/science.287.5459.1793>, 2000.
- Sassen, K.: The Polarization Lidar Technique for Cloud Research: A Review and Current Assessment, *B. Am. Meteorol. Soc.*, 72, 1848–1866, [https://doi.org/10.1175/1520-0477\(1991\)072<1848:TPLTFC>2.0.CO;2](https://doi.org/10.1175/1520-0477(1991)072<1848:TPLTFC>2.0.CO;2), 1991.
- Sassen, K. and Zhu, J.: A global survey of CALIPSO linear depolarization ratios in ice clouds: Initial findings, *J. Geophys. Res.-Atmos.*, 114, D00H07, <https://doi.org/10.1029/2009JD012279>, 2009.
- Tanré, D., Bréon, F. M., Deuzé, J. L., Dubovik, O., Ducos, F., François, P., Goloub, P., Herman, M., Lifermann, A., and Waquet, F.: Remote sensing of aerosols by using polarized, directional and spectral measurements within the A-Train: the PARASOL mission, *Atmos. Meas. Tech.*, 4, 1383–1395, <https://doi.org/10.5194/amt-4-1383-2011>, 2011.
- Torres, O., Jethva, H., and Bhartia, P. K.: Retrieval of Aerosol Optical Depth above Clouds from OMI Observations: Sensitivity Analysis and Case Studies, *J. Atmos. Sci.*, 69, 1037–1053, <https://doi.org/10.1175/JAS-D-11-0130.1>, 2012.
- Torres, O., Ahn, C., and Chen, Z.: Improvements to the OMI near-UV aerosol algorithm using A-train CALIOP and AIRS observations, *Atmos. Meas. Tech.*, 6, 3257–3270, <https://doi.org/10.5194/amt-6-3257-2013>, 2013.
- Twomey, S.: Pollution and the planetary albedo, *Atmos. Environ.*, 8, 1251–1256, [https://doi.org/10.1016/0004-6981\(74\)90004-3](https://doi.org/10.1016/0004-6981(74)90004-3), 1974.
- Vaughan, M. A., Powell, K. A., Winker, D. M., Hostetler, C. A., Kuehn, R. E., Hunt, W. H., Getzewich, B. J., Young, S. A., Liu, Z., and McGill, M. J.: Fully Automated Detection of Cloud and Aerosol Layers in the CALIPSO Lidar Measurements, *J. Atmos. Ocean. Tech.*, 26, 2034–2050, <https://doi.org/10.1175/2009JTECHA1228.1>, 2009.
- Waquet, F., Riedi, J., Labonnote, L. C., Goloub, P., Cairns, B., Deuzé, J.-L., and Tanré, D.: Aerosol Remote Sensing over Clouds Using A-Train Observations, *J. Atmos. Sci.*, 66, 2468–2480, <https://doi.org/10.1175/2009JAS3026.1>, 2009.
- Waquet, F., Peers, F., Ducos, F., Goloub, P., Platnick, S., Riedi, J., Tanré, D., and Thieuleux, F.: Global analysis of aerosol properties above clouds, *Geophys. Res. Lett.*, 40, 5809–5814, <https://doi.org/10.1002/2013GL057482>, 2013a.
- Waquet, F., Cornet, C., Deuzé, J.-L., Dubovik, O., Ducos, F., Goloub, P., Herman, M., Lapyonok, T., Labonnote, L. C., Riedi, J., Tanré, D., Thieuleux, F., and Vanbauce, C.: Retrieval of aerosol microphysical and optical properties above liquid clouds from POLDER/PARASOL polarization measurements, *Atmos. Meas. Tech.*, 6, 991–1016, <https://doi.org/10.5194/amt-6-991-2013>, 2013b.
- Waquet, F., Péré, J.-C., Peers, F., Goloub, P., Ducos, F., Thieuleux, F., and Tanré, D.: Global detection of absorbing aerosols over the ocean in the red and near-infrared spectral region, *J. Geophys. Res.-Atmos.*, 121, 10902–10918, <https://doi.org/10.1002/2016JD025163>, 2016.
- Warren, S. G., Hahn, C. J., London, J., Chervin, R. M., and Jenne, R. L.: Global Distribution of Total Cloud Cover and Cloud Amounts over the Ocean, *NCAR Tech. Note, NCAR/TN-27*, <https://doi.org/10.2172/5415329>, 1988.
- Wilcox, E. M.: Stratocumulus cloud thickening beneath layers of absorbing smoke aerosol, *Atmos. Chem. Phys.*, 10, 11769–11777, <https://doi.org/10.5194/acp-10-11769-2010>, 2010.
- Winker, D. M., Hunt, W. H., and McGill, M. J.: Initial performance assessment of CALIOP, *Geophys. Res. Lett.*, 34, L19803, <https://doi.org/10.1029/2007GL030135>, 2007.
- Winker, D. M., Vaughan, M. A., Omar, A., Hu, Y., Powell, K. A., Liu, Z., Hunt, W. H., and Young, S. A.: Overview of the CALIPSO Mission and CALIOP Data Pro-

- cessing Algorithms, *J. Atmos. Ocean. Tech.*, 26, 2310–2323, <https://doi.org/10.1175/2009JTECHA1281.1>, 2009.
- Winker, D. M., Pelon, J., Jr., J. A. C., Ackerman, S. A., Charlson, R. J., Colarco, P. R., Flamant, P., Fu, Q., Hoff, R. M., Kittaka, C., Kubar, T. L., Trepte, H. Le, McCormick, M. P., Mégie, G., Poole, L., Powell, K., Trepte, C., Vaughan, M. A. and Wielicki, B. A.: The CALIPSO Mission: A Global 3D View of Aerosols and Clouds, *B. Am. Meteorol. Soc.*, 91, 1211–1229, <https://doi.org/10.1175/2010BAMS3009.1>, 2010.
- Xu, M. and Alfano, R. R.: Random Walk of Polarized Light in Turbid Media, *Phys. Rev. Lett.*, 95, 213901, <https://doi.org/10.1103/PhysRevLett.95.213901>, 2005.
- Young, S. A. and Vaughan, M. A.: The Retrieval of Profiles of Particulate Extinction from Cloud-Aerosol Lidar Infrared Pathfinder Satellite Observations (CALIPSO) Data: Algorithm Description, *J. Atmos. Ocean. Tech.*, 26, 1105–1119, <https://doi.org/10.1175/2008JTECHA1221.1>, 2009.
- Yu, H., Kaufman, Y. J., Chin, M., Feingold, G., Remer, L. A., Anderson, T. L., Balkanski, Y., Bellouin, N., Boucher, O., Christopher, S., DeCola, P., Kahn, R., Koch, D., Loeb, N., Reddy, M. S., Schulz, M., Takemura, T., and Zhou, M.: A review of measurement-based assessments of the aerosol direct radiative effect and forcing, *Atmos. Chem. Phys.*, 6, 613–666, <https://doi.org/10.5194/acp-6-613-2006>, 2006.
- Yu, H., Remer, L. A., Chin, M., Bian, H., Kleidman, R. G., and Diehl, T.: A satellite-based assessment of transpacific transport of pollution aerosol, *J. Geophys. Res.*, 113, D14S12, <https://doi.org/10.1029/2007JD009349>, 2008.
- Zhang, Y. H., Wooster, M. J., Tutubalina, O., and Perry, G. L. W.: Monthly burned area and forest fire carbon emission estimates for the Russian Federation from SPOT VGT, *Remote Sens. Environ.*, 87, 1–15, [https://doi.org/10.1016/S0034-4257\(03\)00141-X](https://doi.org/10.1016/S0034-4257(03)00141-X), 2003.
- Zhang, Z., Meyer, K., Yu, H., Platnick, S., Colarco, P., Liu, Z., and Oreopoulos, L.: Shortwave direct radiative effects of above-cloud aerosols over global oceans derived from 8 years of CALIOP and MODIS observations, *Atmos. Chem. Phys.*, 16, 2877–2900, <https://doi.org/10.5194/acp-16-2877-2016>, 2016.
- Zuidema, P., Redemann, J., Haywood, J., Wood, R., Piketh, S., Hipondoka, M., Formenti, P., Zuidema, P., Redemann, J., Haywood, J., Wood, R., Piketh, S., Hipondoka, M., and Formenti, P.: Smoke and Clouds above the Southeast Atlantic: Upcoming Field Campaigns Probe Absorbing Aerosol's Impact on Climate, *B. Am. Meteorol. Soc.*, 97, 1131–1135, <https://doi.org/10.1175/BAMS-D-15-00082.1>, 2016.

Bibliography

- Ackerman, A. S., Toon, O. B., Stevens, D. E., Heymsfield, A. J., Ramanathan, V. and Welton, E. J.: Reduction of tropical cloudiness by soot, *Science* (80-), 288(5468), 1042–1047, doi:10.1126/science.288.5468.1042, 2000.
- Adebiyi, A. A., Zuidema, P. and Abel, S. J.: The Convolution of Dynamics and Moisture with the Presence of Shortwave Absorbing Aerosols over the Southeast Atlantic, *J. Clim.*, 28(5), 1997–2024, doi:10.1175/JCLI-D-14-00352.1, 2015.
- Ahrens, C. D.: *Essentials of Meteorology: An Invitation to the Atmosphere*, Cengage Learning., 2011.
- Albrecht, B. A.: Aerosols, Cloud Microphysics, and Fractional Cloudiness, *Science* (80-), 245(4923), 1227–1230, doi:10.1126/science.245.4923.1227, 1989.
- Andreae, M. O. and Merlet, P.: Emission of trace gases and aerosols from biomass burning, *Global Biogeochem. Cycles*, 15(4), 955–966, doi:10.1029/2000GB001382, 2001.
- Babenko, V. A. (Viktor A., Astafyeva, L. G. (Ludmila G. . and Kuz'min, V. N. (Vladimir N.: *Electromagnetic scattering in dispersed media : inhomogeneous and anisotropic particles*, Springer., 2003.
- Balkanski, Y., Schulz, M., Claquin, T. and Guibert, S.: Reevaluation of Mineral aerosol radiative forcings suggests a better agreement with satellite and AERONET data, *Atmos. Chem. Phys.*, 7(1), 81–95, doi:10.5194/acp-7-81-2007, 2007.
- Bates, D. R.: *Rayleigh scattering by air.*, 1984.
- Berrisford, P., Dee, D. P., Poli, P., Brugge, R., Fielding, K., Fuentes, M., Kallberg, P. W., Kobayashi, S., Uppala, S. and Simmons, A.: The ERA-Interim archive Version 2.0, *ERA Rep. Ser.*, (1), 23, 2011.
- Boucher, O.: *Atmospheric aerosols.*, 2015.
- Boucher, O., Randall, D., Artaxo, P., Bretherton, C., Feingold, G., Forster, P., Kerminen, V.-M. V.-M., Kondo, Y., Liao, H., Lohmann, U., Rasch, P., Satheesh, S. K., Sherwood, S., Stevens, B., Zhang, X. Y. and Zhan, X. Y.: Clouds and Aerosols, *Clim. Chang. 2013 Phys. Sci. Basis. Contrib. Work. Gr. I to Fifth Assess. Rep. Intergov. Panel Clim. Chang.*, 571–657, doi:10.1017/CBO9781107415324.016, 2013.
- Bréon, F.-M. and Goloub, P.: Cloud droplet effective radius from spaceborne polarization measurements, *Geophys. Res. Lett.*, 25(11), 1879–1882, doi:10.1029/98GL01221, 1998.

- Bretherton, C. S., Uttal, T., Fairall, C. W., Yuter, S. E., Weller, R. A., Baumgardner, D., Comstock, K., Wood, R. and Raga, G. B.: The EPIC 2001 stratocumulus study, *Bull. Am. Meteorol. Soc.*, 85(7), 967–977, doi:10.1175/BAMS-85-7-967, 2004.
- Brioude, J., Cooper, O. R., Feingold, G., Trainer, M., Freitas, S. R., Kowal, D., Ayers, J. K., Prins, E., Minnis, P., McKeen, S. A., Frost, G. J. and Hsie, E.-Y.: Effect of biomass burning on marine stratocumulus clouds off the California coast, *Atmos. Chem. Phys.*, 9(22), 8841–8856, doi:10.5194/acp-9-8841-2009, 2009.
- Buriez, J. C., Vanbauce, C., Parol, F., Goloub, P., Herman, M., Bonnel, B., Fouquart, Y., Couvert, P. and Seze, G.: Cloud detection and derivation of cloud properties from POLDER, *Int. J. Remote Sens.*, 18(13), 2785–2813, doi:10.1080/014311697217332, 1997.
- Cao, X., Roy, G., Roy, N. and Bernier, R.: Comparison of the relationships between lidar integrated backscattered light and accumulated depolarization ratios for linear and circular polarization for water droplets, fog oil, and dust, *Appl. Opt.*, 48(21), 4130–4141, doi:10.1364/AO.48.004130, 2009.
- Catrrall, C., Reagan, J., Thome, K. and Dubovik, O.: Variability of aerosol and spectral lidar and backscatter and extinction ratios of key aerosol types derived from selected Aerosol Robotic Network locations, *J. Geophys. Res.*, 110(D10), D10S11, doi:10.1029/2004JD005124, 2005.
- Chand, D., Anderson, T. L., Wood, R., Charlson, R. J., Hu, Y., Liu, Z. and Vaughan, M.: Quantifying above-cloud aerosol using spaceborne lidar for improved understanding of cloudy-sky direct climate forcing, *J. Geophys. Res.*, 113(D13), D13206, doi:10.1029/2007JD009433, 2008.
- Chandrasekhar, S.: Radiative transfer. By S. Chandrasekhar. London (Oxford University Press) 1950. 8vo. Pp. 393, 35 figures. 35s, *Q. J. R. Meteorol. Soc.*, 76(330), 498–498, doi:10.1002/qj.49707633016, 1950.
- Chepfer, H., Goloub, P., Spinhirne, J., Flamant, P. H., Lavorato, M., Sauvage, L., Brogniez, G., Pelon, J., Chepfer, H., Goloub, P., Spinhirne, J., Flamant, P. H., Lavorato, M., Sauvage, L., Brogniez, G. and Pelon, J.: Cirrus Cloud Properties Derived from POLDER-1/ADEOS Polarized Radiances: First Validation Using a Ground-Based Lidar Network, *J. Appl. Meteorol.*, 39(2), 154–168, doi:10.1175/1520-0450(2000)039<0154:CCPDFP>2.0.CO;2, 2000.
- Chiapello, I.: Apport des observations satellitaires pour l'étude des aérosols et de leurs impacts, *Habilitation à Diriger des Recherches.*, 2011.
- Christensen, M. W., Carrió, G. G., Stephens, G. L. and Cotton, W. R.: Radiative Impacts of Free-Tropospheric Clouds on the Properties of Marine Stratocumulus, *J. Atmos. Sci.*, 70(10), 3102–3118, doi:10.1175/JAS-D-12-0287.1, 2013.
- Clements, C. B., Potter, B. E. and Zhong, S.: In situ measurements of water vapor, heat, and CO₂ fluxes within a prescribed grass fire, *Int. J. Wildl. Fire*, 15, 299–306, doi:10.1071/WF05101, 2006.
- Cornet, C., C-Labonnote, L. and Szczap, F.: Using a 3-D radiative transfer Monte-Carlo model to assess radiative effects on polarized reflectances above cloud scenes, in *Light Scattering Reviews 5*, pp. 81–104, Springer Berlin Heidelberg, Berlin, Heidelberg, 2010.
- Costantino, L. and Bréon, F.-M.: Aerosol indirect effect on warm clouds over South-East Atlantic, from co-located MODIS and CALIPSO observations, *Atmos. Chem. Phys. Discuss.*, 12(6), 14197–14246, doi:10.5194/acpd-12-14197-

2012, 2012.

- Costantino, L. and Bréon, F. M.: Aerosol indirect effect on warm clouds over South-East Atlantic, from co-located MODIS and CALIPSO observations, *Atmos. Chem. Phys.*, 13(1), 69–88, doi:10.5194/acp-13-69-2013, 2013.
- Deaconu, L. T., Waquet, F., Josset, D., Ferlay, N., Peers, F., Thieuleux, F., Ducos, F., Pascal, N., Tanré, D., Pelon, J. and Goloub, P.: Consistency of aerosols above clouds characterization from A-Train active and passive measurements, *Atmos. Meas. Tech*, 10, 3499–3523, doi:10.5194/amt-10-3499-2017, 2017.
- Dee, D. P., Uppala, S. M., Simmons, A. J., Berrisford, P., Poli, P., Kobayashi, S., Andrae, U., Balmaseda, M. A., Balsamo, G., Bauer, P., Bechtold, P., Beljaars, A. C. M., van de Berg, L., Bidlot, J., Bormann, N., Delsol, C., Dragani, R., Fuentes, M., Geer, A. J., Haimberger, L., Healy, S. B., Hersbach, H., Hólm, E. V., Isaksen, I., Kållberg, P., Köhler, M., Matricardi, M., McNally, A. P., Monge-Sanz, B. M., Morcrette, J. J., Park, B. K., Peubey, C., de Rosnay, P., Tavolato, C., Thépaut, J. N. and Vitart, F.: The ERA-Interim reanalysis: Configuration and performance of the data assimilation system, *Q. J. R. Meteorol. Soc.*, 137(656), 553–597, doi:10.1002/qj.828, 2011.
- Deuzé, J. L., Herman, M. and Santer, R.: Fourier series expansion of the transfer equation in the atmosphere-ocean system, *J. Quant. Spectrosc. Radiat. Transf.*, 41(6), 483–494, doi:10.1016/0022-4073(89)90118-0, 1989.
- Dubovik, O., Holben, B., Eck, T. F., Smirnov, A., Kaufman, Y. J., King, M. D., Tanré, D. and Slutsker, I.: Variability of Absorption and Optical Properties of Key Aerosol Types Observed in Worldwide Locations, *J. Atmos. Sci.*, 59(3), 590–608, doi:10.1175/1520-0469(2002)059<0590:VOAAOP>2.0.CO;2, 2002.
- Dubovik, O., Sinyuk, A., Lapyonok, T., Holben, B. N., Mishchenko, M., Yang, P., Eck, T. F., Volten, H., Muñoz, O., Veihermann, B., van der Zande, W. J., Leon, J. F., Sorokin, M. and Slutsker, I.: Application of spheroid models to account for aerosol particle nonsphericity in remote sensing of desert dust, *J. Geophys. Res. Atmos.*, 111(11), D11208, doi:10.1029/2005JD006619, 2006.
- Dubovik, O., Lapyonok, T., Kaufman, Y. J., Chin, M., Ginoux, P., Kahn, R. A. and Sinyuk, A.: Retrieving global aerosol sources from satellites using inverse modeling, *Atmos. Chem. Phys.*, 8(2), 209–250, doi:10.5194/acp-8-209-2008, 2008.
- Dubovik, O., Herman, M., Holdak, A., Lapyonok, T., Tanré, D., Deuzé, J. L., Ducos, F., Sinyuk, A. and Lopatin, A.: Statistically optimized inversion algorithm for enhanced retrieval of aerosol properties from spectral multi-angle polarimetric satellite observations, *Atmos. Meas. Tech.*, 4(5), 975–1018, doi:10.5194/amt-4-975-2011, 2011.
- Dubovik, O., Lapyonok, T., Litvinov, P., Herman, M., Fuertes, D., Ducos, F., Torres, B., Derimian, Y., Huang, X., Lopatin, A., Chaikovskiy, A., Aspöck, M. and Federspiel, C.: GRASP: a versatile algorithm for characterizing the atmosphere, *SPIE Newsroom*, 2–5, doi:10.1117/2.1201408.005558, 2014.
- Dubuisson, P., J. C. Roger, M. Mallet, and O. D.: A code to compute the direct solar radiative forcing: Application to anthropogenic aerosols during the Escompte experiment, in *IRS 2004: Current Problems in Atmospheric Radiation*, edited by H. Fischer and B.-J. Sohn, pp. 127–130, Hampton, Va., 2006.
- Erlick, C.: Effective Refractive Indices of Water and Sulfate Drops Containing Absorbing Inclusions, *J. Atmos. Sci.*, 63(2), 754–763, doi:10.1175/JAS3635.1, 2006.

- Feingold, G., Jiang, H. and Harrington, J. Y.: On smoke suppression of clouds in Amazonia, *Geophys. Res. Lett.*, 32(2), L02804, doi:10.1029/2004GL021369, 2005.
- Ferlay, N., Thieuleux, F., Cornet, C., Davis, A. B., Dubuisson, P., Ducos, F., Parol, F., Riédi, J. and Vanbauce, C.: Toward new inferences about cloud structures from multidirectional measurements in the oxygen a band: Middle-of-cloud pressure and cloud geometrical thickness from POLDER-3/PARASOL, *J. Appl. Meteorol. Climatol.*, 49(12), 2492–2507, doi:10.1175/2010JAMC2550.1, 2010.
- Fishman, J., Fakhruzzaman, K., Cros, B. and Nganga, D.: Identification of widespread pollution in the southern hemisphere deduced from satellite analyses., *Science*, 252(5013), 1693–6, doi:10.1126/science.252.5013.1693, 1991.
- Goloub, P., Herman, M., Chepfer, H., Riedi, J., Brogniez, G., Couvert, P. and Séze, G.: Cloud thermodynamical phase classification from the POLDER spaceborne instrument, *J. Geophys. Res. Atmos.*, 105(D11), 14747–14759, doi:10.1029/1999JD901183, 2000.
- de Graaf, M., Tilstra, L. G., Wang, P. and Stammes, P.: Retrieval of the aerosol direct radiative effect over clouds from spaceborne spectrometry, *J. Geophys. Res. Atmos.*, 117(D7), n/a-n/a, doi:10.1029/2011JD017160, 2012.
- De Graaf, M., Tilstra, L. G., Wang, P. and Stammes, P.: Retrieval of the aerosol direct radiative effect over clouds from spaceborne spectrometry, *J. Geophys. Res. Atmos.*, 117(7), n/a-n/a, doi:10.1029/2011JD017160, 2012.
- De Graaf, M., Bellouin, N., Tilstra, L. G., Haywood, J. and Stammes, P.: Aerosol direct radiative effect of smoke over clouds over the southeast Atlantic Ocean from 2006 to 2009, *Geophys. Res. Lett.*, 41(21), 7723–7730, doi:10.1002/2014GL061103, 2014.
- Hansen, J., Sato, M. and Ruedy, R.: Radiative forcing and climate response, *J. Geophys. Res. Atmos.*, 102(D6), 6831–6864, doi:10.1029/96JD03436, 1997.
- Hasekamp, O. P.: Capability of multi-viewing-angle photo-polarimetric measurements for the simultaneous retrieval of aerosol and cloud properties, *Atmos. Meas. Tech.*, 3(4), 839–851, doi:10.5194/amt-3-839-2010, 2010.
- Haywood, J. M., Osborne, S. R., Francis, P. N., Keil, A., Formenti, P., Andreae, M. O. and Kaye, P. H.: The mean physical and optical properties of regional haze dominated by biomass burning aerosol measured from the C-130 aircraft during SAFARI 2000, *J. Geophys. Res. Atmos.*, 108(D13), n/a-n/a, doi:10.1029/2002JD002226, 2003.
- Haywood, J. M., Osborne, S. R. and Abel, S. J.: The effect of overlying absorbing aerosol layers on remote sensing retrievals of cloud effective radius and cloud optical depth, *Q. J. R. Meteorol. Soc.*, 130(598), 779–800, doi:10.1256/qj.03.100, 2004.
- Herman, M., Deuzé, J. L., Marchand, A., Roger, B. and Lallart, P.: Aerosol remote sensing from POLDER/ADEOS over the ocean: Improved retrieval using a nonspherical particle model, *J. Geophys. Res. D Atmos.*, 110(10), 1–11, doi:10.1029/2004JD004798, 2005.
- Hill, A. A., Dobbie, S. and Yin, Y.: The impact of aerosols on non-precipitating marine stratocumulus. I: Model description and prediction of the indirect effect, *Q. J. R. Meteorol. Soc.*, 134(634 A), 1143–1154, doi:10.1002/qj.278, 2008.
- Hu, Y.: Depolarization ratio-effective lidar ratio relation: Theoretical basis for space

- lidar cloud phase discrimination, *Geophys. Res. Lett.*, 34(11), L11812, doi:10.1029/2007GL029584, 2007.
- Hu, Y., Liu, Z., Winker, D., Vaughan, M., Noel, V., Bissonnette, L., Roy, G. and McGill, M.: Simple relation between lidar multiple scattering and depolarization for water clouds, *Opt. Lett.*, 31(12), 1809, doi:10.1364/OL.31.001809, 2006.
- Hu, Y., Vaughan, M., Liu, Z., Powell, K. and Rodier, S.: Retrieving Optical Depths and Lidar Ratios for Transparent Layers Above Opaque Water Clouds From CALIPSO Lidar Measurements, *IEEE Geosci. Remote Sens. Lett.*, 4(4), 523–526, doi:10.1109/LGRS.2007.901085, 2007a.
- Hu, Y., Vaughan, M., Liu, Z., Lin, B., Yang, P., Flittner, D., Hunt, B., Kuehn, R., Huang, J., Wu, D., Rodier, S., Powell, K., Trepte, C. and Winker, D.: The depolarization - attenuated backscatter relation: CALIPSO lidar measurements vs. theory, *Opt. Express*, 15(9), 5327–5332, doi:10.1364/OE.15.005327, 2007b.
- van de Hulst, H. C. (Hendrik C.: Light scattering by small particles, Dover Publications., 1957.
- Hunt, W. H., Winker, D. M., Vaughan, M. A., Powell, K. A., Lucker, P. L., Weimer, C., Hunt, W. H., Winker, D. M., Vaughan, M. A., Powell, K. A., Lucker, P. L. and Weimer, C.: *CALIPSO Lidar Description and Performance Assessment*, *J. Atmos. Ocean. Technol.*, 26(7), 1214–1228, doi:10.1175/2009JTECHA1223.1, 2009.
- Ichoku, C., Remer, L. A., Kaufman, Y. J., Levy, R., Chu, D. A., Tanré, D. and Holben, B. N.: MODIS observation of aerosols and estimation of aerosol radiative forcing over southern Africa during SAFARI 2000, *J. Geophys. Res. Atmos.*, 108(D13), n/a-n/a, doi:10.1029/2002JD002366, 2003.
- Jacobson, M. Z.: Isolating nitrated and aromatic aerosols and nitrated aromatic gases as sources of ultraviolet light absorption, *J. Geophys. Res.*, 104(D3), 3527, doi:10.1029/1998JD100054, 1999.
- Jethva, H., Torres, O., Remer, L. A. and Bhartia, P. K.: A color ratio method for simultaneous retrieval of aerosol and cloud optical thickness of above-cloud absorbing aerosols from passive sensors: Application to MODIS measurements, *IEEE Trans. Geosci. Remote Sens.*, 51(7), 3862–3870, doi:10.1109/TGRS.2012.2230008, 2013.
- Jethva, H., Torres, O., Waquet, F., Chand, D. and Hu, Y.: How do A-train sensors intercompare in the retrieval of above-cloud aerosol optical depth? A case study-based assessment, *Geophys. Res. Lett.*, 41(1), 186–192, doi:10.1002/2013GL058405, 2014.
- Johnson, B. T., Shine, K. P. and Forster, P. M.: The semi-direct aerosol effect: Impact of absorbing aerosols on marine stratocumulus, *Q. J. R. Meteorol. Soc.*, 130(599), 1407–1422, doi:10.1256/qj.03.61, 2004a.
- Johnson, B. T., Shine, K. P. and Forster, P. M.: The semi-direct aerosol effect: Impact of absorbing aerosols on marine stratocumulus, *Q. J. R. Meteorol. Soc.*, 130(599), 1407–1422, doi:10.1256/qj.03.61, 2004b.
- Johnson, B. T., Osborne, S. R., Haywood, J. M. and Harrison, M. A. J.: Aircraft measurements of biomass burning aerosol over West Africa during DABEX, *J. Geophys. Res.*, 113(D23), D00C06, doi:10.1029/2007JD009451, 2008.
- Josset, D., Hu, Y., Pelon, J., Zhai, P., Tanré, D., Rogers, R., Lucker, P., Trepte, C., Powell, K., Rodier, S., Pascal, N. and Team, T. I.: Advances in Research Products From CALIPSO: Optical Depth Direct Retrieval Over Ocean, Water

- Clouds and Land, in International Coordination Group on Laser Atmospheric Studies (ICLAS). 25th International Laser Radar Conference (ILRC), St. Petersburg, Russia. Curran Associates, Inc., pp. 1280–1283, Curran Associates, Inc., 2010.
- Josset, D., Rogers, R., Pelon, J., Hu, Y., Liu, Z., Omar, A., Zhai, P.-W., Fernald, F. G., Herman, B. M., Reagan, J. A., Winker, D. M., Pelon, J., Coakley, J. A., Ackerman, S. A., Charlson, R. J., Colarco, P. R., Flamant, P., Fu, Q., Hoff, R., Kittaka, C., Kubar, T. L., LeTreut, H., McCormick, M. P., Megie, G., Poole, L., Powell, K., Trepte, C., Vaughan, M. A., Wielicki, B. A., Stephens, G. L., Vane, D. G., Tanelli, S., Im, E., Durden, S., Rokey, M., Reinke, D., Partain, P., Mace, G. G., Austin, R., Haynes, J., Lebsock, M., Suzuki, K., Waliser, D., Wu, D., Kay, J., Gettelman, A., Wang, Z. and Marchand, R.: CALIPSO lidar ratio retrieval over the ocean, *Opt. Express*, 19(19), 18696, doi:10.1364/OE.19.018696, 2011.
- Josset, D., Pelon, J., Hu, Y., Rogers, R., Liu, Z., Omar, A., Vaughan, M., Zhai, P. and Team, I.: Global scale lidar ratio retrieval over the ocean, in 26th International Laser Radar Conference (ILRC 26), Porto Heli, Greece., 2012.
- Kaufman, Y. J., Tanré, D. and Boucher, O.: A satellite view of aerosols in the climate system., *Nature*, 419(6903), 215–23, doi:10.1038/nature01091, 2002.
- Kaufman, Y. J., Koren, I., Remer, L. A., Rosenfeld, D. and Rudich, Y.: The effect of smoke, dust, and pollution aerosol on shallow cloud development over the Atlantic Ocean, *Proc. Natl. Acad. Sci.*, 102(32), 11207–11212, doi:10.1073/pnas.0505191102, 2005.
- Kawata, Y.: Circular polarization of sunlight reflected by planetary atmospheres, *Icarus*, 33(1), 217–232, doi:10.1016/0019-1035(78)90035-0, 1978.
- Keil, A. and Haywood, J. M.: Solar radiative forcing by biomass burning aerosol particles during SAFARI 2000: A case study based on measured aerosol and cloud properties, *J. Geophys. Res. Atmos.*, 108(D13), n/a-n/a, doi:10.1029/2002JD002315, 2003.
- King, L. V: On the Complex Anisotropic Molecule in Relation to the Dispersion and Scattering of Light, *Proc. R. Soc. London. Ser. A, Contain. Pap. a Math. Phys. Character*, 104(726), 333–357, 1923.
- King, M., Tsay, S., Platnick, S., Wang, M. and Liou, K.-N.: Cloud retrieval algorithms for MODIS: Optical thickness, effective particle radius, and thermodynamic phase., 1997.
- Kinne, S., Schulz, M., Textor, C., Guibert, S., Balkanski, Y., Bauer, S. E., Berntsen, T., Berglen, T. F., Boucher, O., Chin, M., Collins, W., Dentener, F., Diehl, T., Easter, R., Feichter, J., Fillmore, D., Ghan, S., Ginoux, P., Gong, S., Grini, A., Hendricks, J., Herzog, M., Horowitz, L., Isaksen, I., Iversen, T., Kirkevåg, A., Kloster, S., Koch, D., Kristjansson, J. E., Krol, M., Lauer, A., Lamarque, J. F., Lesins, G., Liu, X., Lohmann, U., Montanaro, V., Myhre, G., Penner, J., Pitari, G., Reddy, S., Seland, O., Stier, P., Takemura, T. and Tie, X.: An AeroCom initial assessment – optical properties in aerosol component modules of global models, *Atmos. Chem. Phys.*, 6(7), 1815–1834, doi:10.5194/acp-6-1815-2006, 2006.
- Klein, S. A. and Hartmann, D. L.: The seasonal cycle of low stratiform clouds, *J. Clim.*, 6(8), 1587–1606, doi:10.1175/1520-0442(1993)006<1587:TSCOLS>2.0.CO;2, 1993.
- Knobelspiesse, K., Cairns, B., Ottaviani, M., Ferrare, R., Hair, J., Hostetler, C., Obland, M., Rogers, R., Redemann, J., Shinozuka, Y., Clarke, A., Freitag, S.,

- Howell, S., Kapustin, V. and McNaughton, C.: Combined retrievals of boreal forest fire aerosol properties with a polarimeter and lidar, *Atmos. Chem. Phys.*, 11(14), 7045–7067, doi:10.5194/acp-11-7045-2011, 2011.
- Koch, D. and Del Genio, A. D.: Black carbon semi-direct effects on cloud cover: Review and synthesis, *Atmos. Chem. Phys.*, 10(16), 7685–7696, doi:10.5194/acp-10-7685-2010, 2010.
- Koren, I., Kaufman, Y. J., Remer, L. A. and Martins, J. V.: Measurement of the Effect of Amazon Smoke on Inhibition of Cloud Formation, *Science* (80-.), 303(5662), 1342–1345, doi:10.1126/science.1089424, 2004.
- Labonne, M., Bréon, F. M. and Chevallier, F.: Injection height of biomass burning aerosols as seen from a spaceborne lidar, *Geophys. Res. Lett.*, 34(11), L11806, doi:10.1029/2007GL029311, 2007.
- Labonnote, L., Brogniez, G., Doutriaux-Boucher, M., Buriez, J. C., Gayet, J. F. and Chepfer, H.: Modeling of light scattering in cirrus clouds with inhomogeneous hexagonal monocrystals. Comparison with in-situ and ADEOS-POLDER measurements, *Geophys. Res. Lett.*, 27(1), 113–116, doi:10.1029/1999GL010839, 2000.
- Lamb, D. and Verlinde, J.: *Physics and Chemistry of Clouds*, Cambridge University Press., 2011.
- Leahy, L. V., Anderson, T. L., Eck, T. F. and Bergtrom, R. W.: A synthesis of single scattering albedo of biomass burning aerosol over southern Africa during SAFARI 2000, *Geophys. Res. Lett.*, 34(12), L12814, doi:10.1029/2007GL029697, 2007.
- Lelieveld, J., Berresheim, H., Borrmann, S., Crutzen, P. J., Dentener, F. J., Fischer, H., Feichter, J., Flatau, P. J., Heland, J., Holzinger, R., Kormann, R., Lawrence, M. G., Levin, Z., Markowicz, K. M., Mihalopoulos, N., Minikin, A., Ramanathan, V., De Reus, M., Roelofs, G. J., Scheeren, H. A., Sciare, J., Schlager, H., Schultz, M., Siegmund, P., Steil, B., Stephanou, E. G., Stier, P., Traub, M., Warneke, C., Williams, J. and Ziereis, H.: Global Air Pollution Crossroads over the Mediterranean, *Science* (80-.), 298(5594), 794–799, doi:10.1126/science.1075457, 2002.
- Lenoble, J., Tanre, D., Deschamps, P. Y. and Herman, M.: A Simple Method to Compute the Change in Earth-Atmosphere Radiative Balance Due to a Stratospheric Aerosol Layer, *J. Atmos. ...*, 39(11), 2565–2576, doi:10.1175/1520-0469(1982)039<2565:ASMTCT>2.0.CO;2, 1982.
- Lenoble, J., Herman, M., Deuzé, J. L., Lafrance, B., Santer, R. and Tanré, D.: A successive order of scattering code for solving the vector equation of transfer in the earth's atmosphere with aerosols, *J. Quant. Spectrosc. Radiat. Transf.*, 107(3), 479–507, doi:10.1016/j.jqsrt.2007.03.010, 2007.
- Levine, J. S.: *Global biomass burning: atmospheric, climatic, and biospheric implications*, MIT Press., 1991.
- Luderer, G., Trentmann, J., Winterrath, T., Textor, C., Herzog, M., Graf, H. & Andreae, M. O.: Modeling of biomass smoke injection into the lower stratosphere by a large forest fire (Part II): sensitivity studies, *Atmos. Chem. Phys.*, 6(12), 5261–5277, doi:10.5194/acp-6-5261-2006, 2006.
- Luderer, G., Trentmann, J., Hungershofer, K., Herzog, M., Fromm, M. and Andreae, M. O.: Small-scale mixing processes enhancing troposphere-to-stratosphere transport by pyro-cumulonimbus storms, *Atmos. Chem. Phys. Atmos. Chem. Phys.*, 7, 5945–5957, 2007.

- Marshak, A. (Alexander) and Davis, A. B. (Anthony B.): 3D radiative transfer in cloudy atmospheres, Springer-Verlag., 2005.
- Metropolis, N. and Ulam, S.: The Monte Carlo Method, *J. Am. Stat. Assoc.*, 44(247), 335, doi:10.2307/2280232, 1949.
- Meyer, K., Platnick, S., Oreopoulos, L. and Lee, D.: Estimating the direct radiative effect of absorbing aerosols overlying marine boundary layer clouds in the southeast Atlantic using MODIS and CALIOP, *J. Geophys. Res. Atmos.*, 118(10), 4801–4815, doi:10.1002/jgrd.50449, 2013.
- Meyer, K., Platnick, S. and Zhang, Z.: Simultaneously inferring above-cloud absorbing aerosol optical thickness and underlying liquid phase cloud optical and microphysical properties using MODIS, *J. Geophys. Res. Atmos.*, 120(11), 5524–5547, doi:10.1002/2015JD023128, 2015.
- Mie, G.: Beiträge zur Optik trüber Medien, speziell kolloidaler Metallösungen, *Ann. Phys.*, 330(3), 377–445, doi:10.1002/andp.19083300302, 1908.
- Miles, N. L., Verlinde, J., Clothiaux, E. E., Miles, N. L., Verlinde, J. and Clothiaux, E. E.: Cloud Droplet Size Distributions in Low-Level Stratiform Clouds, *J. Atmos. Sci.*, 57(2), 295–311, doi:10.1175/1520-0469(2000)057<0295:CDSDIL>2.0.CO;2, 2000.
- Mishchenko, M. I., Travis, L. D. and Lacis, A. A.: Scattering, absorption, and emission of light by small particles, Cambridge University Press., 2002.
- Mortier, A.: Tendances et Variabilités de l'aérosol atmosphérique à l'aide du couplage LiDAR/Photomètre sur les sites de Lille et Dakar, University of Lille 1., 2014.
- Müller, D., Ansmann, A., Mattis, I., Tesche, M., Wandinger, U., Althausen, D. and Pisani, G.: Aerosol-type-dependent lidar ratios observed with Raman lidar, *J. Geophys. Res.*, 112(D16), D16202, doi:10.1029/2006JD008292, 2007.
- Myhre, G., Shindell, D., Bréon, F.-M., Collins, W., Fuglestedt, J., Huang, J., Koch, D., Lamarque, J.-F., Lee, D., Mendoza, B., Nakajima, T., Robock, A., Stephens, G., Takemura, T. and Zhang, H.: Anthropogenic and Natural Radiative Forcing, *Clim. Chang. 2013 Phys. Sci. Basis. Contrib. Work. Gr. I to Fifth Assess. Rep. Intergov. Panel Clim. Chang.*, 659–740, doi:10.1017/CBO9781107415324.018, 2013a.
- Myhre, G., Samset, B. H., Schulz, M., Balkanski, Y., Bauer, S., Bernsten, T. K., Bian, H., Bellouin, N., Chin, M., Diehl, T., Easter, R. C., Feichter, J., Ghan, S. J., Hauglustaine, D., Iversen, T., Kinne, S., Kirkev??g, A., Lamarque, J. F., Lin, G., Liu, X., Lund, M. T., Luo, G., Ma, X., Van Noije, T., Penner, J. E., Rasch, P. J., Ruiz, A., Seland, Skeie, R. B., Stier, P., Takemura, T., Tsigaridis, K., Wang, P., Wang, Z., Xu, L., Yu, H., Yu, F., Yoon, J. H., Zhang, K., Zhang, H. and Zhou, C.: Radiative forcing of the direct aerosol effect from AeroCom Phase II simulations, *Atmos. Chem. Phys.*, 13(4), 1853–1877, doi:10.5194/acp-13-1853-2013, 2013b.
- O'Connor, E. J., Illingworth, A. J. and Hogan, R. J.: A Technique for Autocalibration of Cloud Lidar, *J. Atmos. Ocean. Technol.*, 21(5), 777–786, doi:10.1175/1520-0426(2004)021<0777:ATFAOC>2.0.CO;2, 2004.
- Omar, A. H., Won, J.-G., Winker, D. M., Yoon, S.-C., Dubovik, O. and McCormick, M. P.: Development of global aerosol models using cluster analysis of Aerosol Robotic Network (AERONET) measurements, *J. Geophys. Res.*, 110, 10–14, doi:10.1029/2004JD004874, 2005.
- Omar, A. H., Winker, D. M., Vaughan, M. A., Hu, Y., Trepte, C. R., Ferrare, R. A., Lee, K.-P., Hostetler, C. A., Kittaka, C., Rogers, R. R., Kuehn, R. E., Liu, Z.,

- Omar, A. H., Winker, D. M., Vaughan, M. A., Hu, Y., Trepte, C. R., Ferrare, R. A., Lee, K.-P., Hostetler, C. A., Kittaka, C., Rogers, R. R., Kuehn, R. E. and Liu, Z.: The CALIPSO Automated Aerosol Classification and Lidar Ratio Selection Algorithm, *J. Atmos. Ocean. Technol.*, 26(10), 1994–2014, doi:10.1175/2009JTECHA1231.1, 2009.
- Parmar, R. S., Welling, M., Andreae, M. O. and Helas, G.: Water vapor release from biomass combustion, *Atmos. Chem. Phys. Atmos. Chem. Phys.*, 8, 6147–6153, doi:10.5194/acp-8-6147-2008, 2008.
- Peers, F., Waquet, F., Cornet, C., Dubuisson, P., Ducos, F., Goloub, P., Szczap, F., Tanré, D. and Thieuleux, F.: Absorption of aerosols above clouds from POLDER/PARASOL measurements and estimation of their direct radiative effect, *Atmos. Chem. Phys.*, 15(8), 4179–4196, doi:10.5194/acp-15-4179-2015, 2015.
- Peers, F., Bellouin, N., Waquet, F., Ducos, F., Goloub, P., Mollard, J., Myhre, G., Skeie, R. B., Takemura, T., Tanré, D., Thieuleux, F. and Zhang, K.: Comparison of aerosol optical properties above clouds between POLDER and AeroCom models over the South East Atlantic Ocean during the fire season, *Geophys. Res. Lett.*, 43(8), 3991–4000, doi:10.1002/2016GL068222, 2016.
- Piketh, S. J., Annegarn, H. J. and Tyson, P. D.: Lower tropospheric aerosol loadings over South Africa: The relative contribution of aeolian dust, industrial emissions, and biomass burning, *J. Geophys. Res.*, 104(D1), 1597, doi:10.1029/1998JD100014, 1999.
- Pinnick, R. G., Jennings, S. G., Chýlek, P., Ham, C. and Grandy, W. T.: Backscatter and extinction in water clouds, *J. Geophys. Res.*, 88(C11), 6787, doi:10.1029/JC088iC11p06787, 1983.
- Platt, C. M. R.: Remote Sounding of High Clouds: I. Calculation of Visible and Infrared Optical Properties from Lidar and Radiometer Measurements, *J. Appl. Meteorol.*, 18(9), 1130–1143, doi:10.1175/1520-0450(1979)018<1130:RSOHC1>2.0.CO;2, 1979.
- Potter, B. E.: The role of released moisture in the atmospheric dynamics associated with wildland fires, *Int. J. Wildl. Fire*, 14(1), 77, doi:10.1071/WF04045, 2005.
- Powell, K., Vaughan, M., Winker, D., Lee, K. P., Pitts, M., Trepte, C., Detweiler, P., Hunt, W., Lambeth, J. and Lucker, P.: Cloud–Aerosol LIDAR Infrared Pathfinder Satellite Observations (CALIPSO), *Data Manag. Syst. Data Prod. Cat. Doc. No PC-SCI-503*, Release, 3, 2010.
- Rajapakshe, C., Zhang, Z., Yorks, J. E., Yu, H., Tan, Q., Meyer, K., Platnick, S. and Winker, D. M.: Seasonally Transported Aerosol Layers over Southeast Atlantic are Closer to Underlying Clouds than Previously Reported, *Geophys. Res. Lett.*, doi:10.1002/2017GL073559, 2017.
- Rayleigh, Lord: On the scattering of light by small particles, *Philos. Mag.*, 41(4), 447–454, 1871.
- Reid, J. S., Hobbs, P. V., Ferek, R. J., Blake, D. R., Martins, J. V., Dunlap, M. R. and Liousse, C.: Physical, chemical, and optical properties of regional hazes dominated by smoke in Brazil, *J. Geophys. Res. Atmos.*, 103(D24), 32059–32080, doi:10.1029/98JD00458, 1998.
- Riedi, J., Marchant, B., Platnick, S., Baum, B. A., Thieuleux, F., Oudard, C., Parol, F., Nicolas, J. M. and Dubuisson, P.: Cloud thermodynamic phase inferred from merged POLDER and MODIS data, *Atmos. Chem. Phys.*, 10(23), 11851–11865, doi:10.5194/acp-10-11851-2010, 2010.
- Rosenfeld, D.: Suppression of Rain and Snow by Urban and Industrial Air Pollution,

- Science (80-.), 287(5459), 1793–1796, doi:10.1126/science.287.5459.1793, 2000.
- Sakaeda, N., Wood, R. and Rasch, P. J.: Direct and semidirect aerosol effects of southern African biomass burning aerosol, *J. Geophys. Res. Atmos.*, 116(12), D12205, doi:10.1029/2010JD015540, 2011.
- Sassen, K.: The Polarization Lidar Technique for Cloud Research: A Review and Current Assessment, *Bull. Am. Meteorol. Soc.*, 72(12), 1848–1866, doi:10.1175/1520-0477(1991)072<1848:TPLTFC>2.0.CO;2, 1991.
- Sassen, K. and Zhu, J.: A global survey of CALIPSO linear depolarization ratios in ice clouds: Initial findings, *J. Geophys. Res. Atmos.*, 114(21), doi:10.1029/2009JD012279, 2009.
- Scott, N. A.: A direct method of computation of the transmission function of an inhomogeneous gaseous medium- I: Description of the method, *J. Quant. Spectrosc. Radiat. Transf.*, 14(8), 691–704, doi:10.1016/0022-4073(74)90116-2, 1974.
- Stamnes, K., Tsay, S. C., Wiscombe, W. and Jayaweera, K.: Numerically stable algorithm for discrete-ordinate-method radiative transfer in multiple scattering and emitting layered media., *Appl. Opt.*, 27(12), 2502–2509, doi:10.1364/AO.27.002502, 1988.
- Stokes, G. G.: On the change of refrangibility of light, *Philos. Trans. R. Soc. London*, 142, 463–562, 1852.
- Sullivan, R. C., Moore, M. J. K., Petters, M. D., Kreidenweis, S. M., Roberts, G. C. and Prather, K. A.: Effect of chemical mixing state on the hygroscopicity and cloud nucleation properties of calcium mineral dust particles, *Atmos. Chem. Phys.*, 9(10), 3303–3316, doi:10.5194/acp-9-3303-2009, 2009.
- Swap, R., Garstang, M., Macko, S. A., Tyson, P. D., Maenhaut, W., Artaxo, P., Kållberg, P. and Talbot, R.: The long-range transport of southern African aerosols to the tropical South Atlantic, *J. Geophys. Res.*, 101(D19), 23777–23791, doi:10.1029/95JD01049, 1996.
- Szczap, F., Gour, Y., Fauchez, T., Cornet, C., Faure, T., Jourdan, O., Penide, G. and Dubuisson, P.: A flexible three-dimensional stratocumulus, cumulus and cirrus cloud generator (3DCLOUD) based on drastically simplified atmospheric equations and the fourier transform framework, *Geosci. Model Dev.*, 7(4), 1779–1801, doi:10.5194/gmd-7-1779-2014, 2014.
- Szczodrak, M., Austin, P. H. and Krummel, P. B.: Variability of Optical Depth and Effective Radius in Marine Stratocumulus Clouds, *J. Atmos. Sci.*, 58(19), 2912–2926, doi:10.1175/1520-0469(2001)058<2912:VOODAE>2.0.CO;2, 2001.
- Tang, M., Cziczo, D. J. and Grassian, V. H.: Interactions of Water with Mineral Dust Aerosol: Water Adsorption, Hygroscopicity, Cloud Condensation, and Ice Nucleation, *Chem. Rev.*, 116(7), 4205–4259, doi:10.1021/acs.chemrev.5b00529, 2016.
- Tanré, D., Kaufman, Y. J., Herman, M. and Mattoo, S.: Remote sensing of aerosol properties over oceans using the MODIS/EOS spectral radiances, *J. Geophys. Res. Atmos.*, 102(D14), 16971–16988, doi:10.1029/96JD03437, 1997.
- Tanré, D., Bréon, F. M., Deuzé, J. L., Herman, M., Goloub, P., Nadal, F. and Marchand, A.: Global observation of anthropogenic aerosols from satellite, *Geophys. Res. Lett.*, 28(24), 4555–4558, doi:10.1029/2001GL013036, 2001.
- Tanré, D., Bréon, F. M., Deuzé, J. L., Dubovik, O., Ducos, F., François, P., Goloub, P., Herman, M., Lifermann, A. and Waquet, F.: Remote sensing of aerosols by

- using polarized, directional and spectral measurements within the A-Train: the PARASOL mission, *Atmos. Meas. Tech.*, 4(7), 1383–1395, doi:10.5194/amt-4-1383-2011, 2011.
- Textor, C., Schulz, M., Guibert, S., Kinne, S., Balkanski, Y., Bauer, S., Bernsten, T., Berglen, T. and Boucher, O.: and Physics Analysis and quantification of the diversities of aerosol life cycles within AeroCom, *Atmos. Chem. Phys.*, 6(7), 1777–1813, doi:10.5194/acp-6-1777-2006, 2006.
- Torres, O., Tanskanen, A., Veihelmann, B., Ahn, C., Braak, R., Bhartia, P. K., Veefkind, P. and Levelt, P.: Aerosols and surface UV products from Ozone Monitoring Instrument observations: An overview, *J. Geophys. Res. Atmos.*, 112(24), 24–47, doi:10.1029/2007JD008809, 2007.
- Torres, O., Jethva, H. and Bhartia, P. K.: Retrieval of Aerosol Optical Depth above Clouds from OMI Observations: Sensitivity Analysis and Case Studies, *J. Atmos. Sci.*, 69(3), 1037–1053, doi:10.1175/JAS-D-11-0130.1, 2012.
- Torres, O., Ahn, C. and Chen, Z.: Improvements to the OMI near-UV aerosol algorithm using A-train CALIOP and AIRS observations, *Atmos. Meas. Tech.*, 6(11), 3257–3270, doi:10.5194/amt-6-3257-2013, 2013.
- Trentmann, J., Luderer, G., Winterrath, T., Fromm, M. D., Servranckx, R., Textor, C., Herzog, M., Graf, H.-F. and Andreae, M. O.: Modeling of biomass smoke injection into the lower stratosphere by a large forest fire (Part I): reference simulation, *Atmos. Chem. Phys.*, 6(12), 5247–5260, doi:10.5194/acp-6-5247-2006, 2006.
- Twomey, S.: Pollution and the planetary albedo, *Atmos. Environ.*, 8(12), 1251–1256, doi:10.1016/0004-6981(74)90004-3, 1974.
- Unga, F.: Investigation of atmospheric aerosol mixing state effect on measured and retrieved optical characteristics: an approach integrating individual particle analysis, remote sensing and numerical simulations, University of Lille 1., 2017.
- Vanbauce, C., Cadet, B. and Marchand, R. T.: Comparison of POLDER apparent and corrected oxygen pressure to ARM/MMCR cloud boundary pressures, *Geophys. Res. Lett.*, 30(5), n/a-n/a, doi:10.1029/2002GL016449, 2003.
- Vaughan, M. A., Powell, K. A., Winker, D. M., Hostetler, C. A., Kuehn, R. E., Hunt, W. H., Getzewich, B. J., Young, S. A., Liu, Z. and McGill, M. J.: Fully Automated Detection of Cloud and Aerosol Layers in the CALIPSO Lidar Measurements, *J. Atmos. Ocean. Technol.*, 26(10), 2034–2050, doi:10.1175/2009JTECHA1228.1, 2009.
- Waquet, F., Riedi, J., Labonnote, L. C., Goloub, P., Cairns, B., Deuzé, J.-L. and Tanré, D.: Aerosol Remote Sensing over Clouds Using A-Train Observations, *J. Atmos. Sci.*, 66, 2468–2480, doi:10.1175/2009JAS3026.1, 2009.
- Waquet, F., Peers, F., Ducos, F., Goloub, P., Platnick, S., Riedi, J., Tanré, D. and Thieuleux, F.: Global analysis of aerosol properties above clouds, *Geophys. Res. Lett.*, 40(21), 5809–5814, doi:10.1002/2013GL057482, 2013a.
- Waquet, F., Cornet, C., Deuzé, J.-L., Dubovik, O., Ducos, F., Goloub, P., Herman, M., Lapyonok, T., Labonnote, L. C., Riedi, J., Tanré, D., Thieuleux, F. and Vanbauce, C.: Retrieval of aerosol microphysical and optical properties above liquid clouds from POLDER/PARASOL polarization measurements, *Atmos. Meas. Tech.*, 6(4), 991–1016, doi:10.5194/amt-6-991-2013, 2013b.
- Waquet, F., Péré, J.-C., Peers, F., Goloub, P., Ducos, F., Thieuleux, F. and Tanré, D.: Global detection of absorbing aerosols over the ocean in the red and near-infrared spectral region, *J. Geophys. Res. Atmos.*, 121(18), 10,902–10,918,

- doi:10.1002/2016JD025163, 2016.
- Warren, S. G., Hahn, C. J., London, J., Chervin, R. M. and Jenne, R. L.: Global Distribution of Total Cloud Cover and Cloud Amounts over the Ocean, NCAR Tech. Note, NCAR/TN-27, 42, doi:10.2172/5415329, 1988.
- Wilcox, E. M.: Stratocumulus cloud thickening beneath layers of absorbing smoke aerosol, *Atmos. Chem. Phys.*, 10(23), 11769–11777, doi:10.5194/acp-10-11769-2010, 2010.
- Winker, D. M., Hunt, W. H. and McGill, M. J.: Initial performance assessment of CALIOP, *Geophys. Res. Lett.*, 34(19), L19803, doi:10.1029/2007GL030135, 2007.
- Winker, D. M., Vaughan, M. A., Omar, A., Hu, Y., Powell, K. A., Liu, Z., Hunt, W. H. and Young, S. A.: Overview of the CALIPSO Mission and CALIOP Data Processing Algorithms, *J. Atmos. Ocean. Technol.*, 26(11), 2310–2323, doi:10.1175/2009JTECHA1281.1, 2009.
- Winker, D. M., Pelon, J., Coakley, J. A., Ackerman, S. A., Charlson, R. J., Colarco, P. R., Flamant, P., Fu, Q., Hoff, R. M., Kittaka, C., Kubar, T. L., Le Treut, H., McCormick, M. P., Mégie, G., Poole, L., Powell, K., Treppe, C., Vaughan, M. A., Wielicki, B. A., Winker, D. M., Pelon, J., Jr., J. A. C., Ackerman, S. A., Charlson, R. J., Colarco, P. R., Flamant, P., Fu, Q., Hoff, R. M., Kittaka, C., Kubar, T. L., Treut, H. Le, McCormick, M. P., Mégie, G., Poole, L., Powell, K., Treppe, C., Vaughan, M. A. and Wielicki, B. A.: The CALIPSO Mission: A Global 3D View of Aerosols and Clouds, *Bull. Am. Meteorol. Soc.*, 91(9), 1211–1229, doi:10.1175/2010BAMS3009.1, 2010.
- Xu, M. and Alfano, R. R.: Random Walk of Polarized Light in Turbid Media, *Phys. Rev. Lett.*, 95(21), 213901, doi:10.1103/PhysRevLett.95.213901, 2005.
- Young, S. A. and Vaughan, M. A.: The Retrieval of Profiles of Particulate Extinction from Cloud-Aerosol Lidar Infrared Pathfinder Satellite Observations (CALIPSO) Data: Algorithm Description, *J. Atmos. Ocean. Technol.*, 26(6), 1105–1119, doi:10.1175/2008JTECHA1221.1, 2009.
- Yu, H., Kaufman, Y. J., Chin, M., Feingold, G., Remer, L. A., Anderson, T. L., Balkanski, Y., Bellouin, N., Boucher, O., Christopher, S., DeCola, P., Kahn, R., Koch, D., Loeb, N., Reddy, M. S., Schulz, M., Takemura, T. and Zhou, M.: A review of measurement-based assessments of the aerosol direct radiative effect and forcing, *Atmos. Chem. Phys.*, 6(3), 613–666, doi:10.5194/acp-6-613-2006, 2006.
- Yu, H., Remer, L. A., Chin, M., Bian, H., Kleidman, R. G. and Diehl, T.: A satellite-based assessment of transpacific transport of pollution aerosol, *J. Geophys. Res.*, 113(D14), D14S12, doi:10.1029/2007JD009349, 2008.
- Zhang, Y. H., Wooster, M. J., Tutubalina, O. and Perry, G. L. W.: Monthly burned area and forest fire carbon emission estimates for the Russian Federation from SPOT VGT, *Remote Sens. Environ.*, 87(1), 1–15, doi:10.1016/S0034-4257(03)00141-X, 2003.
- Zhang, Z., Meyer, K., Yu, H., Platnick, S., Colarco, P., Liu, Z. and Oreopoulos, L.: Shortwave direct radiative effects of above-cloud aerosols over global oceans derived from 8 years of CALIOP and MODIS observations, *Atmos. Chem. Phys.*, 16(5), 2877–2900, doi:10.5194/acp-16-2877-2016, 2016.
- Zuidema, P., Painemal, D., de Szoeko, S., Fairall, C., Zuidema, P., Painemal, D., Szoeko, S. de and Fairall, C.: Stratocumulus Cloud-Top Height Estimates and Their Climatic Implications, *J. Clim.*, 22(17), 4652–4666, doi:10.1175/2009JCLI2708.1, 2009.